THE FLOW OF RIVERS INTO LAKES: EXPERIMENTS AND MODELS

CHARLES ALAN RENSHAW HOGG

ROBINSON COLLEGE
UNIVERSITY OF CAMBRIDGE

A DISSERTATION SUBMITTED FOR THE DEGREE OF DOCTOR OF PHILOSOPHY

DEPARTMENT OF APPLIED MATHEMATICS AND THEORETICAL PHYSICS,

INSTITUTE OF THEORETICAL GEOPHYSICS,

AND

CENTRE FOR WATER RESEARCH, UNIVERSITY OF WESTERN AUSTRALIA

March 2014

For Monica, Mum and Dad.

The Flow of Rivers into Lakes: Experiments and Models

Charles Alan Renshaw Hogg

This study considers the motion of river water flowing into a lake. The study has two parts: field observations of an interflowing river in Lake Iseo (Italy); and laboratory experiments on basins fed by an underflow. In both, observations are compared to existing and new models. There is significant uncertainty in predicting contaminant transport from inflows to lakes. Reducing the uncertainty contributes both to understanding lake ecosystems and protecting water resources.

In field observations, the progressive stages of the inflow were interpreted as a laterally falling plunge region with little mixing, an underflow region with substantial mixing, and finally an intrusion. A simple theory for a laterally falling plunge region was developed, giving the ratio of offshore extent of the plunge region to river width as equal to the initial densimetric Froude number. This theory agreed with the observed plunge location better than existing models.

In laboratory experiments, the evolving density stratification in a basin fed by underflowing gravity currents was measured. The transport pathway of the inflowing fluid was visualised with dyes. Gravity currents underflowing uniform ambient fluid over an intermediate range of source Reynolds number (Re_s) at constant Richardson number (Ri) had entrainment coefficients (E) that varied linearly with Re_s. The values for E were within the previously observed range, but were lower than previously observed for the Ri used here, because Re_s was lower here than in previous studies. Dye pulses showed that gravity currents in stratified ambients did not only entrain, as occurs when in uniform ambient fluid, but also effluxed fluid over the whole depth of the stratified ambient. Analytical expressions were developed for the evolving stratification generated by efflux from the gravity current. The new efflux model predicted the observed stratifications more closely than existing entrainment models. The efflux model could better match observations by including the continued mixing that occurs within the stratified ambient and including the undiluted sublayer observed within the gravity current. Future work should quantify efflux from gravity currents and incorporate the efflux mechanism into full lake basin simulations.

Given the deviation of existing entrainment models from observations shown here, a better model of gravity current efflux would improve modelling of lakes and a variety of buoyancy driven flows, from building ventilation to ocean circulation.

PREFACE

As required by university regulations, this dissertation is the result of my own work and includes nothing which is the outcome of work done in collaboration except where specifically indicated in the text.

Specifically, the work in chapter 2 was done under the supervision of Jörg Imberger, Clelia Marti and Herbert Huppert and was published with them as "Mixing of an interflow into the ambient water of Lake Iseo" (Hogg *et al.*, 2013). The work in chapters 3 to 5 was done under the supervision of Herbert Huppert, Stuart Dalziel and Jörg Imberger.

No part of this thesis has been, or is being, submitted for any other qualification.

The reader is invited to send any comments to the author at chogg@cantab.net and may find corrigenda at `http://www.damtp.cam.ac.uk/user/carh5/`.

CONTENTS

List of Figures

Chapter 1

Introduction

Most of us know of a river that flows into a lake or reservoir, like that in figure 1.1. The importance of these waters is clear. They attract the curiosity and imagination of people across cultures and backgrounds: figure 1.2 shows some examples. The importance of managing water resources responsibly has also been stressed by government and academics in the recent UK National Ecosystem Assessment: “The water quality benefits of inland wetlands may be as high as £1,500 million p.a., while planned river quality improvements may generate values up to £1,100 million p.a.”(Bateman, 2011). Water quality is of the utmost importance for public health. Surprisingly, much about this everyday occurrence remains beyond our current understanding of fluid dynamics. The assessment underlined the challenge posed by understanding these processes and their interactions: “Understanding the linkages between physical, biogeochemical and ecological processes (from genes to ecosystems) that regulate the services of freshwater systems remains a scientific challenge.”(Maltby & Ormerod, 2011).

Figure 1.1: The northern basin of Lake Iseo. Source: Marco Pilotti.

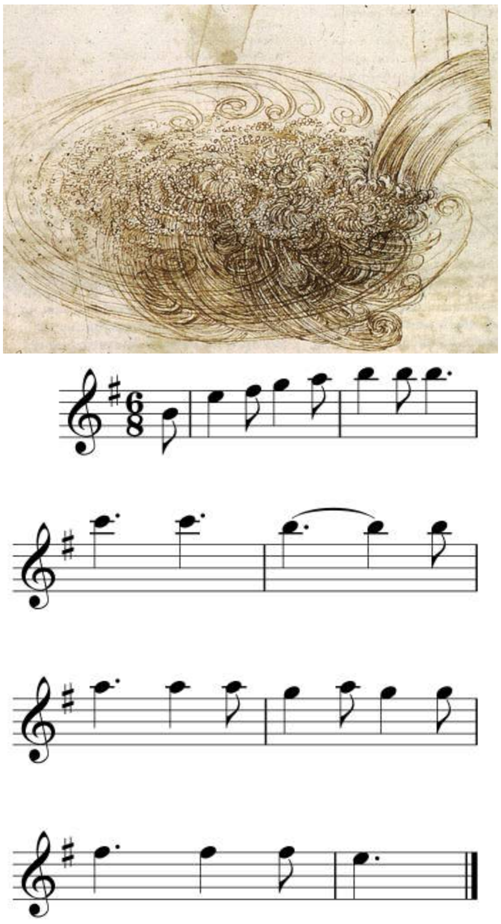

"A lake is the landscape's most beautiful and expressive feature. It is earth's eye; looking into which the beholder measures the depth of his own nature. The fluviatile trees next the shore are the slender eyelashes which fringe it, and the wooded hills and cliffs around are its overhanging brows."

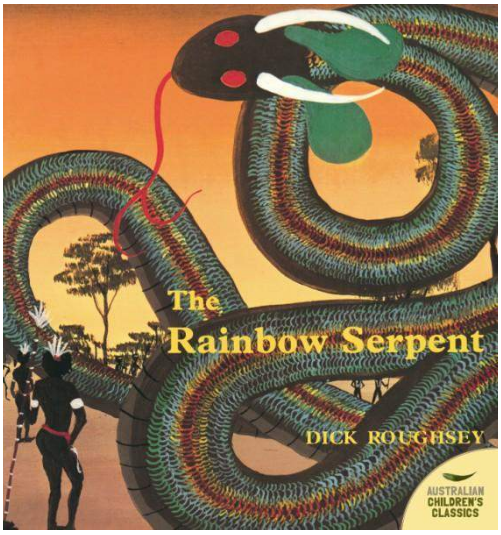

Figure 1.2: Some examples of the cultural influences of rivers and lakes. Clockwise from top left: detail from "Study of water falling into still water." (da Vinci, 1508); extract from "Walden; or Life in the Woods" (Thoreau, 1854); art from "The Rainbow Serpent" (Roughsey, 1988); "Song of the Moldau", theme from "Vltava" (Smetana, 1874).

This thesis studies the motion of water flowing from a river into a lake. First, we describe a field investigation, which observed the river inflow in the consecutive stages of its transition to forming an interflow. Secondly, we describe a laboratory investigation of an underflow, which drives the evolution of the basin stratification. To motivate our study of inflows, let us begin by reviewing a recent approach to managing water resources.

1.1 Water resource management

Real time management of water bodies has recently become technologically feasible and is starting to be implemented (Imberger, 2004). Under this management strategy, the state of a lake is predicted in real time to allow ongoing decision making. These predictions are made by hydrodynamic and ecological models. The models are calibrated for the given water body and driven by data measured at the site and meteorological forecast. This information can guide interventions on an ongoing basis. For example water resource managers can: predict the risks posed from pathogens and monitor pathogen concentrations more effectively (Antenucci *et al.*, 2005); control water extraction and recirculation with awareness of the impact to the ecological status of the lake (Morillo *et al.*, 2009; Fornarelli & Antenucci, 2011); predict sediment transport through the lake (Scheu, K. private communication); and predict the location within the water column of hazardous products deposited from wildfires (Smith *et al.*, 2011). Besides being used in real time management of water resources, understanding lake hydrodynamics also allows the benefits of design alternatives to be evaluated more reliably when new reservoirs are commissioned. Real time management strategies rely on accurate hydrodynamic models and a good understanding of lake function.

1.2 Hydrodynamic lake modelling

Hydrodynamic models of lakes have been developed over the last 50 years (Killworth & Carmack, 1979; Imberger & Patterson, 1981; Hodges *et al.*, 2000; Fringer *et al.*, 2006), paralleling the development of numerical models in many environmental systems (Richardson, 1922; Budyko, 1969). Early models of lakes incorporated heat and mass budgets, along with simple plume models of vertical mass circulation (Killworth & Carmack, 1979). These models successfully predicted the seasonal cycles of the lake stratification, such as the overturn when the lake water reaches the density maximum at 4°C. More recent and sophisticated models either resolve or parameterise many of the important mixing and advection processes in lakes (some of these processes are shown in figure 1.3). Current models are able to capture complex three dimensional (3D) motions and internal waves (Valerio *et al.*, 2012) and provide the basis for ecological models of interacting biological processes (Machado & Imberger, 2013). The ecological functioning of lakes is usually highly sensitive to the flow regime (Šimek *et al.*, 2010). It is therefore important that water motions are accurately represented in hydrodynamic models, which form the foundation for more complex lake models. Many important hydrodynamic processes, including many in inflows, can still only be modelled with significant inaccuracies (Rueda *et al.*, 2007). Recent observations suggest that in common regimes, common conceptual models of entrainment into underflows can be incorrect (Cortés *et al.*, 2014*a*).

Accurate modelling of the inflow is particularly important in a lake model because of the location of the inflow, upstream of the lake. Uncertainty introduced by the inflow model propagates through the rest of the lake simulation. Other model errors, for example modelling the outflow, do not have such a negative impact on the lake simulation because the fluid at the outflow has no further impact on the model.

We will now discuss some processes which are important throughout this thesis.

1.3 Inclined gravity currents

Gravity currents are primarily horizontal motions of fluid, driven by differences in density of the fluid. They were analysed in the seminal paper by Benjamin (1968) and later reviewed by Simpson (1987), Huppert (2006) and Linden (2013). Gravity currents are common structures in many geophysical settings, such as katabatic winds, submarine landslides, meltwater discharge from glaciers, lava flows, avalanches and rivers debouching into oceans or lakes.

Often gravity currents descend along surfaces inclined slightly from horizontal. These cases are termed, more specifically, *inclined gravity currents*. In this thesis they will also be referred to as gravity currents for brevity where the context is

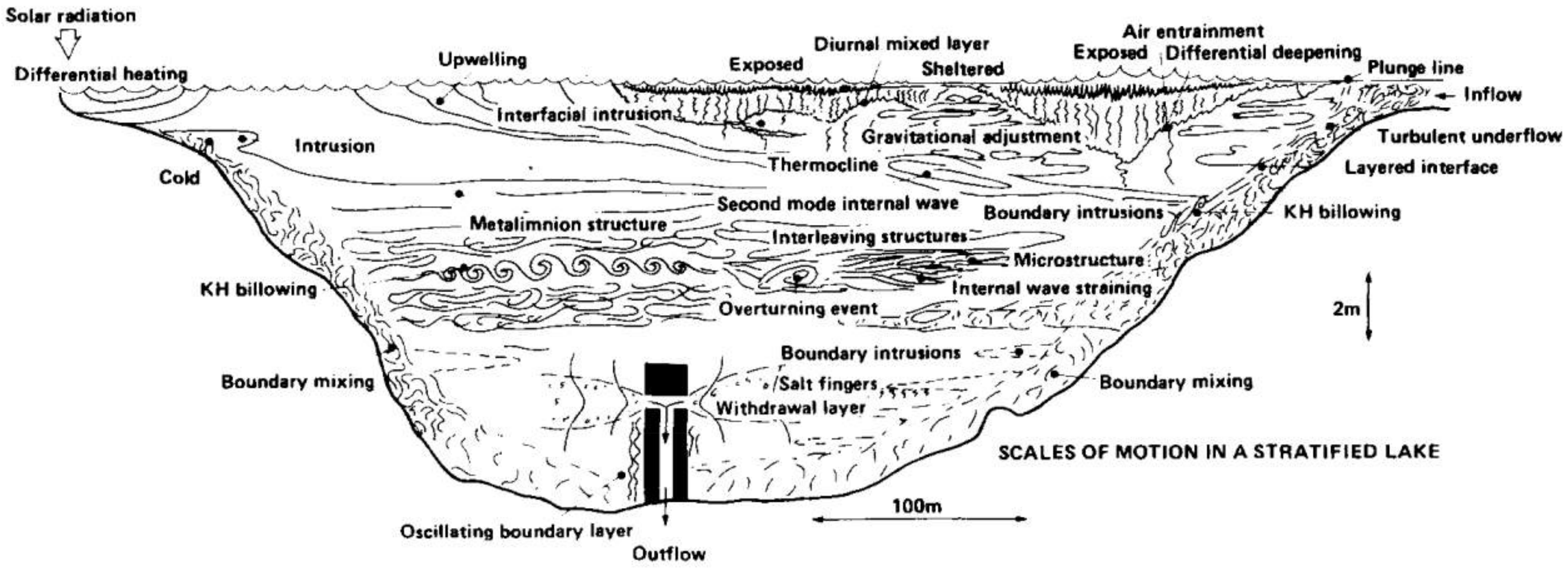

FIGURE 1.3: Mechanisms which lead to mixing in lakes. Source: Imberger (1985)

clear. In these cases, the source of energy is the potential energy released as the fluid descends the slope; a more familiar, similar situation is a ball rolling down a hill.

Gravity currents are distinct from plumes, which are primarily vertical fluid motions (Turner, 1973). These two types of currents have many similarities: in both cases buoyancy is transported by the bulk motion, and velocity shear causes turbulent entrainment of surrounding fluid. The literature sometimes uses the terms interchangeably, particularly when dealing with inclined cases. There is no agreed criteria to distinguish between the two phenomena in these intermediate cases. This is in part because some of the processes are not fully understood. For currents in steady state flowing down very shallow slopes, the buoyancy force is predominantly balanced by drag from bottom roughness. In this case, the majority of the turbulent kinetic energy is produced at the bottom surface. On steeper slopes, the buoyancy force is balanced by accelerating entrained fluid. In this case, the majority of turbulent kinetic energy is produced internally at the shear interface (Turner, 1973, pp. 117). Another important distinction is that, for a gravity current, the interface across which entrainment occurs is stabilised by gravity. In a vertically falling plume, the entrainment is horizontal and does not do any work against gravity.

The dynamics and mixing in the head of a gravity current are different from those in the continuous, quasi-steady following current which is far behind and unaffected by the head. At the head, the gravity current does not have the stable stratification of the following current and ambient fluid is entrained at a larger rate. Here we focus on steady flowing river inflows, so we refer to the following current where the influence of the head is not present.

1.4 Turbulent entrainment

Turbulent entrainment is the transport of fluid by a shear induced turbulent flux across an interface between two bodies of fluid (Turner, 1973, pp. 167). The entrainment process in an entraining gravity current is as follows. Fluid in the ambient far field is drawn towards the low pressure boundary layer comprised of the gravity current (Ellison & Turner, 1959). At the interface of the gravity current, shear instabilities cause irrotational fluid from one side of the interface to be engulfed within eddies and transferred across the interface (Turner, 1986; Baines, 2001; Woods, 2010). Holmboe instabilities have been identified by Baines (2001), Kelvin-Helmholtz instabilities have been identified by Turner (1986) and Taylor instabilities have been identified in theoretical analysis by Caulfield (1994). The fluid is then stirred by the turbulence, producing large surfaces with strong gradients. Diffusion finally acts to fully mix the fluids (Dimotakis, 2000).

1.5 Entrainment parameterisations

The entrainment hypothesis has been used widely in the literature to parameterise entrainment and provide a closure for the turbulent velocity field in a plume. The hypothesis states that the entrainment into a plume does not depend on small scales in the flow. This implies, on dimensional grounds, that the entrainment velocity is linearly proportional to the local average velocity of the bulk flow in the plume (Turner, 1986). The coefficient of linear proportionality, E, is known as the entrainment coefficient. When expressing the conservation of mass, volume and momentum for a plume, E remains as a free parameter in the equations that govern the plume evolution. As E increases, more irreversible mixing of ambient fluid into the plume occurs.

In the simple case of a buoyant plume in a uniform ambient, experiments have found that, approximately, $E = 0.1$ (Turner, 1973). This has been applied across a large range of scales, from centimetres in the lab to kilometres in the atmosphere, and would presumably hold at larger scales if turbulent plumes could be observed elsewhere in the solar system. The constancy of the value of E is striking and implies that in these cases there exists a limit on the amount of mixing in a plume. No theoretical prediction or bound for the value of E has as yet been put forward. In unconfined momentum jets, a slightly lower, but still constant, value of E is also observed. At low Reynolds number – the dimensionless number giving the ratio of viscous forces to inertia – plumes enter a laminar regime and do not turbulently entrain fluid. The manner in which the value of E for a plume reduces as the Reynolds number reduces to this limit has not received much research attention, but would be an interesting topic of study.

In wall bounded plumes, the meandering instabilities of the plume that involve motion perpendicular to the wall are inhibited by the rigid boundary. When the wall bounding the plume is inclined, the entrainment velocity into the current includes a vertical component. In this case, entrainment must do work against gravity, damping the shear instabilities by which entrainment occurs. Ellison & Turner (1959) did early work investigating this effect. They suggested that in inclined gravity currents, E varies as a function of the bulk Richardson number, Ri, the dimensionless ratio of the stabilising gravitational potential energy of the current to the destabilising kinetic energy. Different forms of the function $E(Ri)$ have been developed in the literature. Turner (1986) suggested a functional form that fitted to their laboratory measurements. Christodoulou (1986) combined a number of different functional forms over a large range of Ri, accounting for the different entrainment mechanisms occurring in regimes at different values of Ri. At low Ri, the entrainment parameterisation is the same as a vertically falling plume. At high Ri, the entrainment parameterisation is based on experiments on entrainment across a density interface driven by grid-generated turbulence or vortex rings incident on the interface (Turner, 1968; Linden, 1973).

Recently, the importance of entrainment parameterisations to climate models has spurred a renewed effort to improve such parameterisations (Legg *et al.*, 2009). Cenedese & Adduce (2010) have extended the parameterisation for E to account for the variation with the Reynolds number, Re. The form of the parameterisation is based on that given by Turner (1986). A fit to the very scattered data set is given by their expression

$$E_{CA} = \frac{E_{min} + AFr^{\alpha}}{1 + A[E_{max}^{-1} + (Re_{cr}/Re)^{\beta}](Fr + Fr_0)^{\alpha}} \tag{1.1}$$

where the constants, either found by a nonlinear regression from existing data or chosen somewhat arbitrarily, are $E_{min} = 4 \times 10^{-5}$, $A = 3.4 \times 10^{-3}$, $\alpha = 7.18$, $E_{max} = 1$, $Re_{cr} = 6 \times 10^{4}$, $\beta = 0.5$, and $Fr_0 = 0.51$; and $Fr = Ri^{-1/2}$ is the densimetric Froude number.

At steep inclines, bottom drag at the wall is negligible in the momentum balance for gravity currents, and may be neglected (Turner, 1986). At shallow inclines, bottom drag at the solid boundary modifies the gravity current behaviour. The inclination angle at which the bottom stress becomes significant depends on the drag coefficient. In previous literature, no consensus has been reached on the angle at which this transition occurs. Previous researchers have suggested that the transition occurs between 5 and 30° (Britter & Linden, 1980; Baines, 2005), where the transition occurs at higher angles within this range on surfaces with higher bottom drag. At very low inclinations the entrainment drag, associated with accelerating the entrained fluid, becomes negligible in the momentum balance of the gravity current. Lane-Serff (1993) showed that for drag coefficients typical of the ocean, the entrainment drag became negligible below approximately 0.05°.

When the bottom drag in a gravity current becomes significant, the turbulent kinetic energy budget in the gravity current changes (Sherman *et al.*, 1978). Over very rough surfaces, the main source of turbulent energy in the current becomes stirring by the bottom roughness rather than the shear layer at the interface between the current and the ambient fluid. Dallimore *et al.* (2001) measured the turbulent structure for a gravity current on an incline of 0.2° in Lake Ogowara (Japan) and found that turbulent kinetic energy was generated at the bottom of the current. The density profile within the gravity current was well mixed and homogeneous in density. There was a transport of the turbulent kinetic energy to the upper interface of the current, where eddies impinged on the density interface, scraping light fluid from the overlying fluid into the gravity current and giving rise to a buoyancy flux.

Bottom drag slows and thickens the current, giving a higher Richardson number, and increases the entrainment coefficient (Dallimore *et al.*, 2001; Fischer *et al.*, 1979). Empirically observed parameterisations of the effect of bottom drag on the Richardson number and the entrainment coefficient have been established through many inflow studies in lakes (Fernandez & Imberger, 2006; Dallimore *et al.*, 2001; Elder & Wunderlich, 1972; Hebbert *et al.*, 1979). Fernandez & Imberger (2006) found that, for limnological studies on shallow slopes with substantial drag, the empirical parameterisations of entrainment coefficient which account explicitly for bottom drag give better estimates of entrainment than parameterisations which do not treat bottom drag explicitly, such as those by Turner (1986) and Christodoulou (1986). There remains, none-the-less, a substantial error factor between the predictions of the empirical parameterisations and the observed entrainment rates, exceeding 40% in one station in the study of Fernandez & Imberger (2006). This may be because of the limited accuracy achievable in field measurements, or because the variation of E with the Reynolds number was not accounted for.

The exchange of fluid from an inclined gravity current to a surrounding ambient which is stratified is a current area of research. This exchange is called detrainment by Baines (2001, 2005, 2008) and others in the literature. A number of other studies have observed detrainment to stratified ambients in the laboratory (Wong, 1998), including in rotating experiments where the Coriolis force is significant (Lane-Serff & Baines, 2000). From laboratory experiments, in which gravity currents descend through a stratified ambient and the volume flux to the ambient is measured, Baines (2001) found an empirical parameterisation for a detrainment coefficient. This parameter describes the volume flux effluxing from the current into the ambient. Using this empirical observation, he stated a condition to determine when detrainment occurs, as will be used in section 5.4.

Mixing is not a reversible process, i.e., turbulent unmixing does not exist, and therefore an exactly inverse process to turbulent entrainment does not exist. Having said this, whether the term 'detrainment' is appropriate to describe the transfer of fluid out of a gravity current into its surroundings is to some extent a matter of definition. If the definition of entrainment only refers to a volume sink at a boundary layer drawing fluid out of the ambient, then it is reasonable to talk about a process inverse to this called detrainment. Detrainment then refers to a source at a boundary layer pushing fluid into an ambient. In this thesis, as is common elsewhere in the literature, we will define turbulent entrainment to include the irreversible mixing process. Under this definition, the term detrainment is inappropriate and shall not be used. Instead, the term 'gravity current efflux' will be used to describe the transfer of fluid across the boundary from the gravity current to the stratified ambient. The mechanism of gravity current efflux to a stratified ambient is substantially different to the mechanism of entrainment, as will be discussed in chapter 5.

Motion in the ambient fluid is common in many settings where gravity currents occur. Mean, turbulent or oscillatory motion in the ambient can change the amount of entrainment into a current (Ellison & Turner, 1959; Linden & Simpson, 1986; Baines, 2001; Cenedese & Adduce, 2010). Some methods of accounting for such ambient motions have been explored (Ellison & Turner, 1959; Linden & Simpson, 1986; Hubner, 2004), but widely applicable parameterisations have not been put forward.

1.6 The evolution of filling box stratifications

When a basin containing uniform ambient fluid is fed with fluid by convection through a plume or gravity current, the evolving stratification of the basin is known as a filling box stratification. Filling box models show how the entraining plumes and gravity currents discussed in the previous sections drive the evolution of the confined basin's stratification. Filling box models have been applied to many different situations: liquefied gas container ships (Germeles, 1975), convection of water in the Red Sea (Baines & Turner, 1969), building ventilation (Linden, 1999), and lakes (Killworth & Carmack, 1979; Imberger & Patterson, 1981).

In simple geometries, analytical expressions can be found which describe the evolving stratification (Baines & Turner, 1969; Worster & Huppert, 1983). To extend these models to more complex geometries and plume dynamics, numerical models have been used (Germeles, 1975; Imberger & Patterson, 1981). Both of these approaches will be used in chapter 3. For filling box models to be applicable to the stratification evolution, the entraining gravity current must be the dominant factor driving the convection in the basin.

1.7 Outline

This thesis is organised as follows. Chapter 2 discusses field measurements of the inflowing River Oglio as it enters Lake Iseo in its stratified summer condition. The length scales and amount of mixing of the consecutive stages of the inflow – the plunge region, underflow and intrusion – are observed and compared to existing models. A new model appropriate for the observed plunging regime is suggested.

In chapter 3 the evolution of the stratification in basins of different geometries receiving dense fluid are calculated under different theoretical mixing regimes. A simple numerical scheme for the evolving stratification in a triangular basin is found to compare well with asymptotic solutions. A novel filling box model is developed which allows fluid within the gravity current to be internally stratified and to peel away in a stratified ambient.

Chapter 4 describes the apparatus used to examine a gravity current fed filling box in the laboratory. Data processing algorithms used in the experiments are also described. Chapter 5 gives details of the experimental results which show that the rise of the first front in a triangular basin is captured well by the theory as long as account is taken of the trend for E to reduce at lower Reynolds numbers. Qualitative evidence will be given for gravity current efflux in a stratified ambient by the peeling away of the current outer layers. Using the trend for E with Reynolds number, the experimentally observed stratifications in the triangular basin typical for a lake are compared to the new peeling gravity current model and the previously existing (Germeles, 1975) persistently entraining gravity current model.

Finally, in chapter 6 the findings of this work will be summarised and the implications for river inflows and other convective processes will be outlined. Questions raised by this investigation which will require further investigation will be identified. A route to apply these findings to commercial, practical codes and validate their predictive abilities will be outlined.

CHAPTER 2

FIELD INVESTIGATION

2.1 Introduction

The passage of water from a river inlet to an intrusion can be the dominant driver of ecology within a lake, yet current quantitative understanding of this transport is not satisfactory (Rueda *et al.*, 2007). The motion of water entering a lake from a river can take various forms depending on the density of the inflow water relative to the density of the receiving lake surface water (Serruya, 1974). Inflowing water less dense than the lake surface water will flow along the surface of the lake as an overflow (Chen, 1980; Luketina & Imberger, 1987; Cáceres *et al.*, 2002). Inflowing water denser than the surface water of the lake will descend along the lake-bed to enter at a level of neutral buoyancy as an interflow (Imberger &

Patterson, 1989). If the inflow never becomes neutrally buoyant, the inflow will enter at the bottom of the lake as an underflow (Hebbert *et al.*, 1979).

The nutrient loading to a lake normally comes from river inflows, so the ecological response of the lake is very sensitive to changes in the inflow behaviour (Rueda & MacIntyre, 2009; Vilhena *et al.*, 2010; Marti *et al.*, 2011). Incorrect modeling of the dilution of an inflow can give rise to errors in both the intrusion depth and the availability of nutrients to the primary producers in the surface layer (Rueda *et al.*, 2007). In addition, the public health risk posed by pathogens that enter with the river depends on the dilution and horizontal extent of the inflow (Antenucci *et al.*, 2005). Knowledge of the behaviour of river inflows is still incomplete. The primary deficiencies addressed in this chapter are the dynamics of inflows in 3D inlet geometries and the amount of dilution in the plunge region.

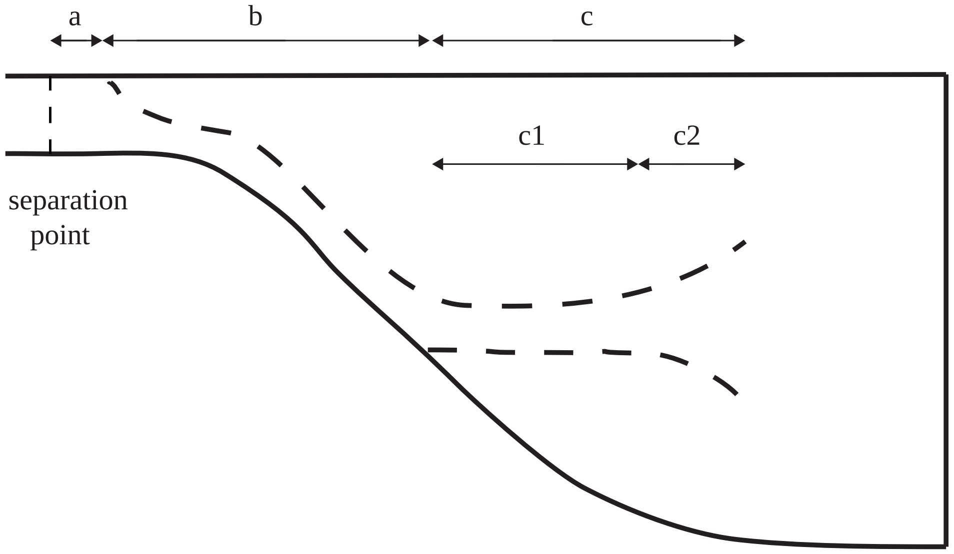

FIGURE 2.1: Schematic showing length scales of the consecutive stages of an interflow: (a) the plunging stage, (b) the underflow stage, (c1) the inertia-buoyancy intrusion stage, and (c2) the diffusion-buoyancy intrusion stage.

General reviews of inflows include those by Ford & Johnson (1983), Imberger & Patterson (1989), and Alavian *et al.* (1992). The consecutive stages along an inflow are governed by different dynamics. We consider here the three dynamical regimes of an interflow in turn: a) the plunge stage; b) the underflow stage; and

c) the intrusion stage. These stages are shown schematically in figure 2.1.

2.1.1 Plunge stage

When a relatively dense river flows into a lake, the river water flows as a uniform layer until the water reaches the plunge region. Four distinct, although not exhaustive, cases may be defined, depending upon the geometry and dynamics of the river.

1) A two dimensional (2D) plunge point occurs when the dynamic pressure of the inflowing river water, $\rho_r u_0^2/2$, becomes less than the hydrostatic pressure difference, $\rho_r g_0' H$, where, ρ_r is the reference density, u_0 the velocity of the water, $g_0' = g\Delta\rho/\rho_r$ the reduced gravity of the river water with respect to the lake surface water, g the acceleration due to gravity, $\Delta\rho$ the difference in density between the river water and the lake surface water and H the depth of the water column at the plunge region. This transition implies that the densimetric Froude number $Fr = u_0/\sqrt{g_0' H}$ is of order unity. As the inflow is no longer able to push back the lake water, the inflow plunges beneath the surface with an initial underflow depth of half the channel depth (Benjamin, 1968).

2) The case of a drowned river valley characterised by a sloping channel with a triangular cross-section was originally described and observed in the field by Hebbert *et al.* (1979). The triangular cross-section alters the vertical distribution of the force due to hydrostatic pressure. The slope causes the water depth to increase and the dynamic pressure to reduce along the river. At a critical depth, the dynamic pressure becomes less than the hydrostatic pressure difference and plunging occurs.

3) Johnson *et al.* (1987) examined plunge regions formed when a river suddenly widens and separates as it enters a lake, as shown in plan form in figure 2.2. Both the river and the lake had the same constant depth. They only considered the scenario where lateral turbulent mixing dominates lateral gravitational slumping. The inflowing river water forms a three dimensional (3D) plunge region. When the relative density difference between the river water and receiving water is small at the inlet (i.e., $Fr_0 \gg 1$), the mechanism for plunging is that the inflow forms a turbulent jet that entrains lake water horizontally inward across the shear layers on either side of the inflow. The entrainment decreases Fr to the critical value, $Fr_C \sim 1$, at which point the inflow plunges. The model for the evolution of Fr

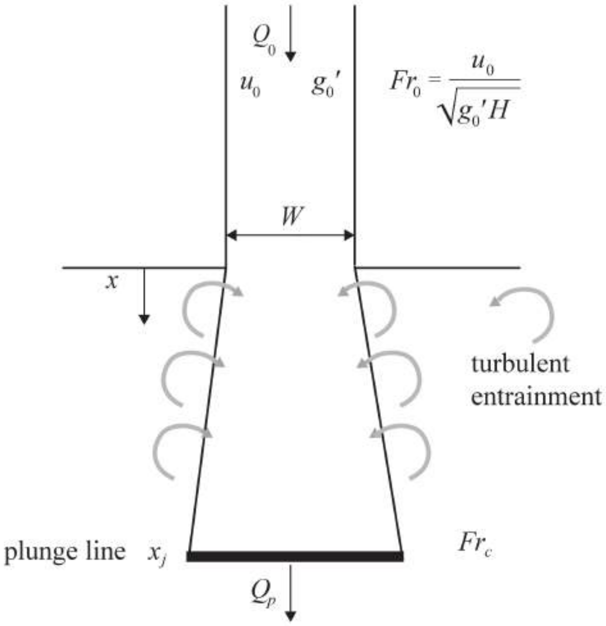

FIGURE 2.2: Plan view, from above, of a river entering a lake as an entraining jet, showing our interpretation of the analysis of Johnson et al. (1987).

along the jet is derived from conservation of volume, momentum, and buoyancy, and an entrainment law that the jet volume flow scales with the square root of the distance offshore (Fischer *et al.*, 1979). The jet reaches the critical value of Fr at the offshore extent of the plunge region, given by

$$x_j = 0.52WFr_0^4, \tag{2.1}$$

where W is the width of the channel and Fr_0 is the Froude number at the separation point (Morton *et al.*, 1956; Stefan & Johnson, 1989).

The mixing ratio in the plunge region, $\gamma_p = (Q_p - Q_0)/Q_0$, derived from the same entrainment model, is given by

$$\gamma_p = 0.5(x_j/W)^{1/2} - 1, \tag{2.2}$$

where Q_0 is the initial volume flow rate of the inflow and Q_p the flow rate after the plunge (Johnson *et al.*, 1989). The laboratory evidence of Johnson *et al.* (1989) supports this model in the parameter range $1 < \gamma_p < 3$, although their conclusions are based on only three data points.

4) When the river directly enters the lake, as in the third case, but the relative density differential between the river water and the receiving water is large and the inflow velocities are small (i.e., Fr_0 is only slightly larger than unity), the separated jet will slump laterally under gravity. When this occurs, the vertical stratification suppresses mixing, and the entering fluid spreads laterally as it flows into the receiving water. This case was observed in Lake Iseo, and a theory describing it is presented in section 2.2.

In field experiments in reservoirs in the Tennessee River Basin, Elder & Wunderlich (1972) measured the combined entrainment in the plunge region and underflow but did not isolate the separate contributions. The ratio of entrained water volume to initial water volume ranged from 0.02 up to 0.46. Fleenor (2001) carried out tracer dilution tests in the Whiskeytown river valley (in California), which had sharply diverging and converging riverbanks, and reported γ_p ranging from 0.2 to 0.7. For channels for which the half angle formed by the diverging channel walls is greater than 7°, a linear regression of his field results and the laboratory results of Johnson *et al.* (1989) gave

$$\gamma_p = 0.223 Fr_0 + 0.008\alpha, \tag{2.3}$$

where α is the divergence half angle formed by the channel walls, measured in degrees, at the separation point of the river (Fleenor, 2001). Spigel *et al.* (2005) measured γ_p for two inflows into Lake Taupo (New Zealand) using a tracer injection method and found that γ_p was 1.87 and 1.94 in the two inflows respectively. To find a linear relationship between γ_p and Fr_0, different site-specific coefficients were required for each inflow. These studies show that there are large variations in plunge region mixing.

2.1.2 Underflow stage

After the plunge region, a dense underflow will run along the lake-bed to the depth of neutral buoyancy (Hebbert *et al.*, 1979). If the bed slope varies only gradually, the bulk Richardson number quickly reaches a value that remains constant along the slope, a condition that is known as normal flow (Ellison & Turner, 1959) and is dynamically analogous to uniform open channel flow. The bulk Richardson number is defined as $Ri = g'_u h/U^2$, where g'_u is the reduced gravity of the underflow, h is the thickness of the underflow and U is the speed of the current along the slope. When normal flow theory is applied to the case of a triangular cross-sectional channel with a uniform density ambient, the evolution of the volume flow rate of the underflow along the slope, Q_u, is given by

$$Q_u = Q_0[6Es/(5h_0) + 1]^{5/3}, \tag{2.4}$$

where h_0 is the initial thickness of the underflow, Q_0 the underflow initial volume flow rate, and s the distance along the lake-bed (Hebbert *et al.*, 1979). The entrainment coefficient is $E = W/U$, where W is the entrainment velocity perpendicular to the slope. To calculate the evolution of an underflow where the ambient water is stratified, Antenucci *et al.* (2005) showed that (2.4) could be applied locally, which is again analogous to gradually varied open channel flow.

Entrainment into the underflow requires that turbulent kinetic energy (TKE) is converted into gravitational potential energy in order to mix the overlying lighter water into the underflow (Sherman *et al.*, 1978). The TKE may be generated either from stirring by the bottom roughness beneath the underflow or, at lower bulk Richardson numbers, from shear production at the upper interface of the underflow (Dallimore *et al.*, 2001; Fernandez & Imberger, 2006). A parameterisation of the entrainment that is valid in both the stirring or shear production regimes was used for E in (2.4). This entrainment parameterisation was

$$E = \frac{C_K C_D^{3/2} + C_s}{Ri + 10(C_K C_D^{3/2} + C_s)}, \tag{2.5}$$

where $C_K = 2.2$ and $C_S = 1 \times 10^{-4}$ are empirically observed parameters used in previous limnological studies (Sherman *et al.*, 1978; Dallimore *et al.*, 2001; Antenucci *et al.*, 2005), and C_D is the drag coefficient so that the bottom stress is given by $C_D \rho_r U^2$.

Dallimore *et al.* (2004) coupled the underflow model described in Sherman *et al.* (1978) with the 3D lake hydrodynamic Estuary Lake and Coastal Ocean Model (ELCOM) (Hodges *et al.*, 2000) and compared model results to field observations. The free surface height of the lake model was used to set the plunge location and to limit the depth of the underflow in the plunge region. The underflow was modelled by applying the vertically integrated conservation equations to the underflow. The model assumed that no mixing occurred within the plunge region. The absence of a parameterisation for mixing within the plunge region was highlighted as a remaining limitation in this and other inflow models (Rueda & MacIntyre, 2009).

2.1.3 Intrusion stage

At the depth of neutral buoyancy, the underflow stops descending, separates from the lake bed and intrudes into the ambient lake water at the isopycnal depth (Imberger, 1985). The intrusion is governed at first by an inertia-buoyancy force balance that extends to where inertia, buoyancy and vertical diffusion all balance (Imberger, 1972). At distances further from the source than the half-width of the basin, the intrusion may be modelled as 2D. The length scale of the inertia-buoyancy intrusion is given by

$$x_i = q^{3/2} N^{-1/2} \kappa^{-1}, \tag{2.6}$$

where q is the source volume flow per unit width, N the buoyancy frequency of the ambient (assumed locally constant), and κ the vertical turbulent diffusivity (Imberger *et al.*, 1976). The turbulent diffusivity represents an average of all the distinct mixing events occurring at the intrusion. In the inertia-buoyancy intrusion, the velocity has been shown in laboratory experiments and theory to be given by

$$u_i = N\delta_i \tag{2.7}$$

and the intrusion thickness to be constant and given by (Manins, 1976)

$$\delta_i = (q/N)^{1/2}. \tag{2.8}$$

A 2D intrusion in the diffusive-buoyancy regime moves with velocity

$$u_v = Ax^{-1/3}, \tag{2.9}$$

and has thickness

$$\delta_v = \beta(x\kappa/N)^{1/3}, \tag{2.10}$$

where $\beta = 7.1$ is an empirical constant and x the distance from the source (Koh, 1966). The position of a parcel of fluid is

$$x = [4(At + B)/3]^{3/4}, \tag{2.11}$$

where t is the time that the parcel has been in the diffusive-buoyancy regime, and both A and B are parameters set by the boundary conditions of the diffusive-buoyancy regime intrusion. The distance to the virtual origin, x_v, for the diffusive-buoyancy regime may be found from (2.10) by matching the thickness of the two intrusion regimes. The distance from the virtual origin to the start of the diffusive-buoyancy regime, when $t = 0$ in (2.11), yields the boundary parameter $B = 3x_v^{4/3}/4$. Additionally, continuity allows the velocity of the diffusive-buoyancy intrusion, given by (2.9), to be matched to the velocity of the inertia-buoyancy intrusion, to yield the boundary parameter $A = u_i x_v^{1/3}$. As the intrusion advances in the diffusive-buoyancy stage, the intrusion diffuses into the adjacent layers of ambient water. The diffusion occurs over a characteristic time scale $t_d \sim \delta_v^2/\kappa$. The characteristic length scale over which the intrusion diffuses into the background fluid is therefore given by

$$x_d \sim [4(3\beta) + 1/\beta^4]^{3/4} q^{3/2} N^{-1/2} \kappa^{-1}. \tag{2.12}$$

In this study, the influence of rotation has not been considered. The Rossby number in the plunge region and underflow observed in Lake Iseo is too large (> 10) for rotation to influence the dynamics. The impact of rotation on the intrusion, however, is more important. The Coriolis force will push the intrusion towards the western boundary of the lake. A detailed investigation of this effect is outside the scope of this study.

The main contribution of this chapter is to present field measurements of the length scales and mixing ratios in the three consecutive stages of an interflow. The measurements are then compared with the existing models of the dynamics of interflows. A novel model of the plunge region, not to our knowledge previously discussed in the literature, is presented and compared with field measurements. The rest of the chapter is structured as follows. Section 2.2 develops a theory for plunge regions in the regime of Fr_0 slightly larger than unity. Section 2.3 describes the field campaign. Section 2.4 provides calculations of the observed length scales and mixing ratios in the interflow. The final section of the chapter highlights the significance of our findings when analysing inflow behaviour.

2.2 Theory

The derivations of x_j and γ_p in (2.1) and (2.2) assume that an entrainment law can be applied to the inflow. At Fr_0 slightly larger than unity, however, buoyancy dominates before lateral entrainment can affect the inflow. Thus, because the stratification suppresses the turbulence, the entrainment law (Johnson *et al.*, 1989) used in turbulent jet theory is not applicable. Furthermore, because at Fr_0 slightly larger than unity the plunge region does not extend into the zone of established flow, which begins at a distance $O(W)$ from the inlet, the assumed entrainment law is not applicable (Fischer *et al.*, 1979). The mechanism applicable for the range of Fr_0 slightly larger than unity is that baroclinic generation of vorticity causes the inflow to fall away laterally such that the inflow water eventually plunges entirely below the lake surface. The progression of this falling motion is shown, schematically, in figures 2.3 and 2.4. This is similar to the mechanism proposed for buoyant surface trapped plumes (Chen, 1980).

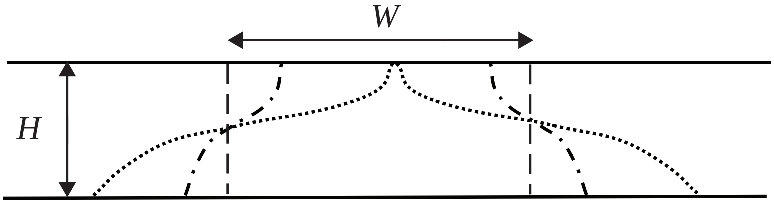

FIGURE 2.3: Three transverse sections of the plunge region showing the progression of the lateral falling mechanism. The plunge region begins at the point of separation from the riverbanks where the inflow has the shape of the river channel (dashed). Within the plunge region, the edges of the inflow fall laterally (dot-dashed), until the entire inflow falls below the surface (dotted).

To analyse this lateral falling motion, consider a box model of a transverse slice of river water entering the lake. When the river water separates from the riverbanks, the river water has lighter lake surface water on either side. The different densities of the horizontally adjacent water bodies give rise to lateral baroclinic forces that accelerate the river water downwards and laterally outwards. The lateral motion is similar to the initial slumping phase of a gravity current

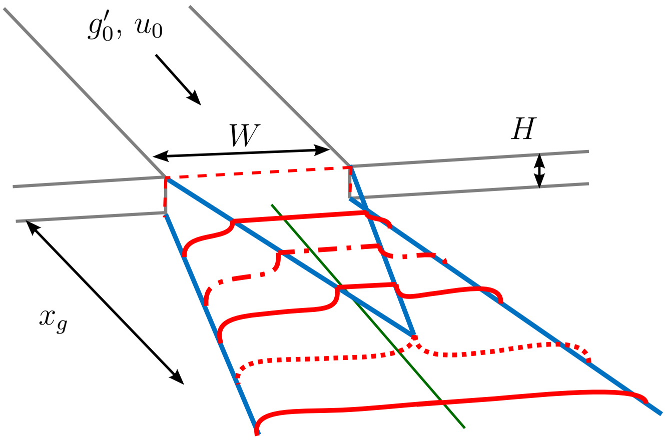

FIGURE 2.4: Schematic of lateral falling mechanism shown in perspective. Dashed lines correspond to the dashed lines in figure 2.3. The green line indicates a line on the lake bed along which the cross-section in figure 2.5 is taken.

after a lock release (Huppert & Simpson, 1980). As the river spreads laterally along the lake-bed, water from either side of the inflow travels along the surface of the lake towards the midpoint of the river at speed $u_r = \sqrt{g_0' H}/2$ (Shin *et al.*, 2004). On the surface of the lake, the curve that separates the river water from the lake water is defined as the plunge curve. The point on the surface at which the lake water from both sides meets, where the river water becomes fully submerged, defines the offshore extent of the plunge region, x_g. The ratio x_g/W is identical to the ratio of the lateral to axial velocity, where the axial velocity is assumed to remain constant at u_0. This analysis gives

$$x_g = (u_0 W)/\sqrt{g_0' H}. \tag{2.13}$$

When Fr_0 is only slightly larger than unity, entrainment is primarily caused by shear between the falling river water and the overlying stationary lake surface water. Entrainment at such a front is different to entrainment into an inclined gravity current described in section 1.4. The entrainment of the overlying lake water downwards by the falling river water is much less than the horizontal entrainment at the vertical lateral interfaces in the model of Johnson *et al.* (1989). This is because downwards entrainment has to work against gravity, and is thus inhibited. The limited amount of mixing in the kind of front present in the laterally slumping plunge region was measured in laboratory experiments by Britter & Simpson (1978). In this lab experiment: the inflowing river is analogous to

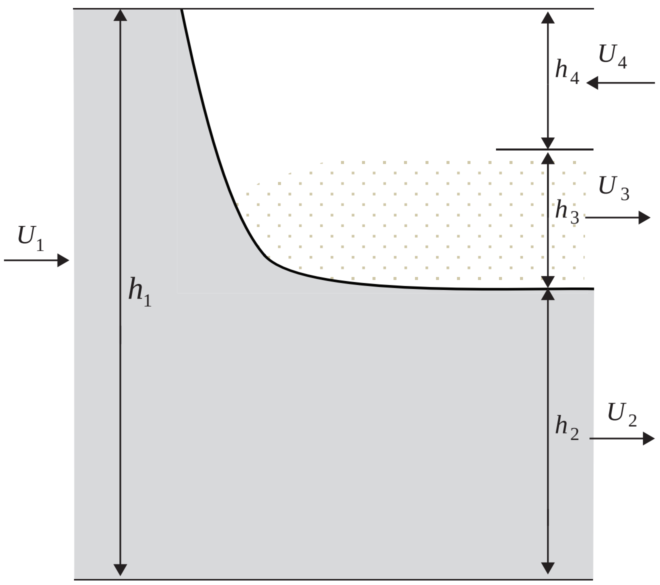

FIGURE 2.5: Laboratory configuration to measure entrainment into the head of a gravity current held stationary by an opposing flow. This is also the configuration of the surface lake water held stationary at the plunge region. The surface lake water mixes with the underflow and leaves the plunge region in layer 3. The layer numbers are indicated by the subscripts of the variables.

the fluid entering from the left in layer 1; the overlying lake water being drawn towards the plunge curve is analogous to layer 4; and the dense underflow downstream of the plunge point is analogous to layers 2 and 3 leaving to the right. The outflowing waters in both layers 2 and 3 are denser than the lake surface water in layer 4. This outflowing fluid, in layers 2 and 3, will remain below the surface water, going on downstream to form the underflow discussed in section 2.1.2. The section shown in figure 2.5 can be thought of as running along the green line shown in figure 2.4. In the laboratory experiments, the head of a saline gravity current was held stationary in a steady state by fluid flowing against the flow of the gravity current, as shown in figure 2.5. The current was in a 2D channel of constant depth. The experiments measured the volume entrained across the shear interface into the opposing flow. The experimental results of Britter & Simpson (1978) may be applied to the mixing of lake surface water into the inflow in the plunge region. Conservation of volume in their conceptual model of the flow implies that $U_1h_1 + U_4h_4 = U_3h_3 + U_2h_2$. In their experiments the relative layer thicknesses were $h_1 = 2h_2 = 4h_3 = 4h_4$ and the velocity ratio was

$\Upsilon = U_4/U_1 = 0.22$. These observations show that

$$\begin{aligned}\gamma_p &= \frac{U_4 h_4}{U_1 h_1} \\ &= \Upsilon/4 \\ &= 0.06.\end{aligned} \tag{2.14}$$

2.3 Methods

A multi-objective field campaign was undertaken in Lake Iseo, Italy (45.7 °N, 10.0 °E), from 14 to 28 July 2010 (ordinal date 195 to 209) (Valerio *et al.*, 2012). Only parts of the campaign relevant to the objective – determining the length scales and mixing in the consecutive stages of the interflow in the northern part of the lake – are reported in this thesis.

2.3.1 Field site

Lake Iseo, shown in figure 2.6, is a natural, meromictic, eutrophic, freshwater lake situated in the foothills of the Alps. The surface area is 62 km^2, maximum depth 250 m and volume 7.6 km^3. The lake geomorphology was reported by Bini *et al.* (2007). Lake Iseo is oriented along the north-south axis of a steep-sided valley. The main inflows, the Oglio River and the Canale Italsider, enter at the northern shore and would fill the lake in approximately 4 years (Salmaso *et al.*, 2003). These rivers bring snow-melt and run-off from a series of reservoirs from the catchment north of the lake. Industrial effluents are discharged into the Oglio River and Canale Italsider, which cause daily fluctuations in the salinity of both inflows. The meteorological and hydrological conditions over the period 1995 - 2012 are given by Pilotti *et al.* (2013).

During the field campaign, the temperature at the bottom of the lake was 6.4°C, and the peak surface temperature was 26.8°C. The density stratification throughout the lake was dominated by the temperature variations. Salinity had negligible effect on the density of river or lake water discussed in this chapter and was effectively a passive tracer. The metalimnion extended between 5 and 30 m. The wind over the lake generally oscillated between northerly katabatic winds at

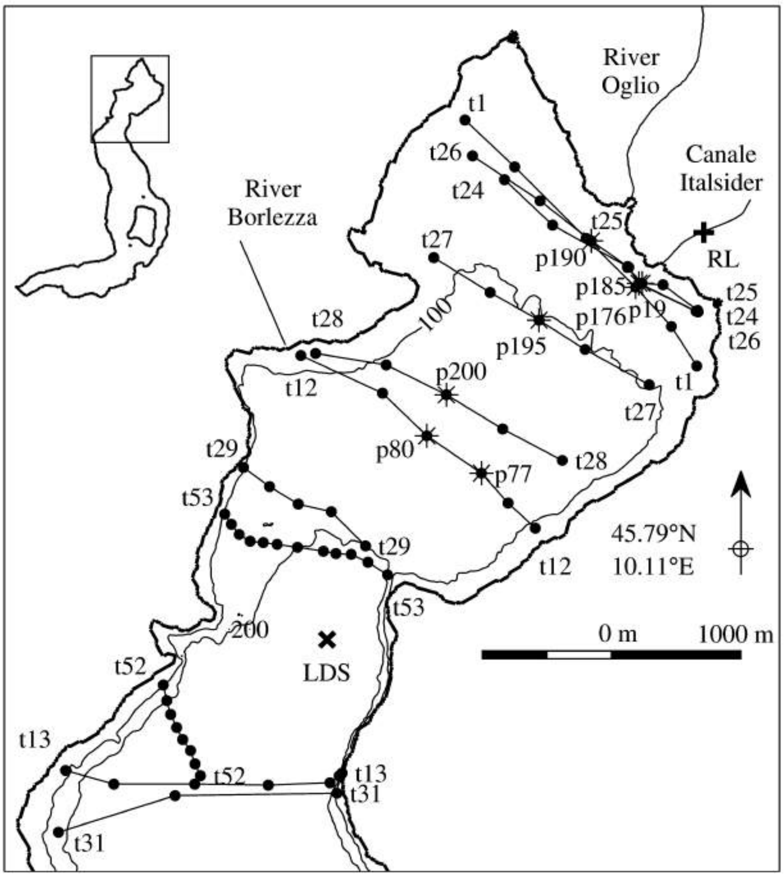

FIGURE 2.6: Map of the bathymetry of Lake Iseo. Location of the LDS is shown by × and the river logger by +. The Oglio River logger was located 10 km upstream from the lake, outside the frame. Profile stations are marked by filled circles apart from stations p19, p77, p80, p176, p185, p190, 195, and p200, which are marked by asterisks and identified individually. The transects are indicated with lines and named.

night and southerly anabatic winds in the day, which generated the internal wave field within the basin (Valerio *et al.*, 2012).

During the field campaign, the Oglio River had an average discharge of 9.8 m^3 s^{-1} (standard deviation: 3.8 m^3 s^{-1}; minimum: 2.3 m^3 s^{-1}; maximum: 22.1 m^3 s^{-1}), average salinity of 0.33 (standard deviation: 0.05; minimum: 0.17; maximum: 0.41), and average temperature of 14.6°C (standard deviation: 1.7°C; minimum: 11.6°C; maximum 19.0°C). Salinity will be reported in units of g kg^{-1} solution throughout this chapter. The Canale Italsider is located 500 m east of the Oglio River, as shown in figure 2.6. During the field campaign the Canale Italsider had an average discharge of 40 m^3 s^{-1} (standard deviation: 4.7 m^3 s^{-1}; minimum: 30.5 m^3 s^{-1}; maximum: 48 m^3 s^{-1}), average salinity of 0.13 and average temperature of 13.0°C (standard deviation: 0.7°C; minimum: 11.3°C; maximum: 14.9°C). The River Borlezza enters at the north-west of the lake, as shown in figure 2.6, and had a discharge of approximately 2 m^3 s^{-1} and a salinity of 0.44. This river had only a negligible hydrodynamic effect on the lake and provided a minor salinity tracer source. The Canale Italsider dominated the volume flow into the lake during the field campaign. This river had Fr_0 of 2.5 and sharply diverging riverbanks at the inlet to the lake, which suggests that the plunge region should be case 4 of the categorisation described in section 2.1.1.

2.3.2 Instrumentation

The location of instrumentation used in this study is shown in figure 2.6. A Lake Diagnostic System (LDS) deployed in open water in the northern part of the lake consisted of meteorological sensors (wind speed and direction, net total radiation, incoming short wave radiation, air temperature and relative humidity) located 2 m above the water surface and a thermistor chain equipped with 21 thermistors measuring the water temperature at different depths that varied from 0.25 to 49.75 m (Imberger, 2004). The sensors were sampled at 10 s intervals. River data loggers were installed on the two main inflows, the Oglio River and the Canale Italsider, sampling at 5 minute intervals. The logger in the Oglio River was located at a weir upstream of the lake and measured water level, temperature and conductivity. The inflow rates were estimated by applying the weir rating curve to the measured water level. The logger in the Canale Italsider measured temperature. The daily inflow rates were provided by the hydropower plant that controls the flow to the Canale Italsider. The conductivity within the Canale Italsider was measured on three occasions during the field experiment. Temperature and conductivity measurements taken after the field campaign at 3 minute intervals between 01 and 24 of June 2011 found the mean salinity to be 0.08. This supports the measurements taken during the field campaign, to within the expected interannual variability, showing that the Canale Italsider was lower in salinity than the Oglio River. The inflow conditions of the Canale Italsider and the thermal structure of the lake measured at the LDS are shown in figure 2.7.

The Multi-scale Profiler (MSP) comprises: a C6 Multi-Sensor Platform™ submersible fluorometer with six Cyclops-7™ fluorescence and turbidity sensors and the device's standard temperature and pressure sensors; a fine scale probe (Im-

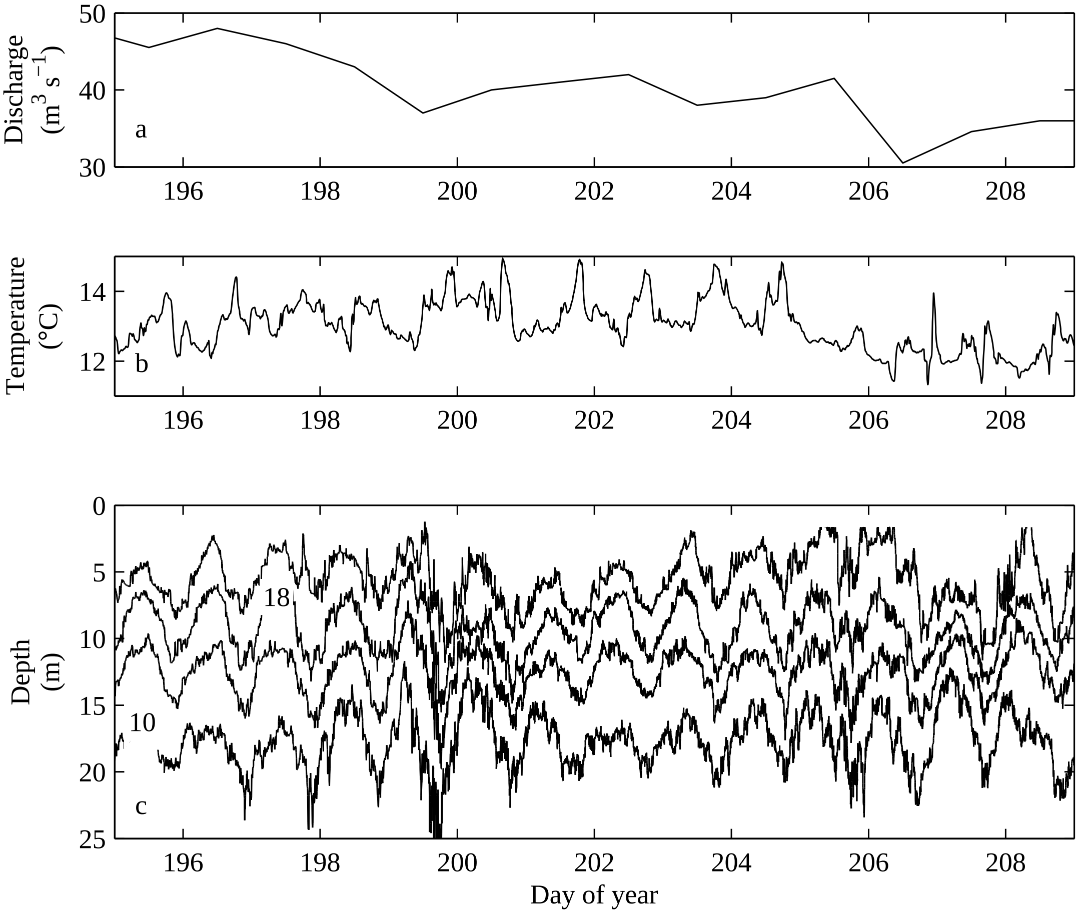

FIGURE 2.7: Time series of (a) discharge and (b) temperature of the Canale Italsider and (c) depths of isotherm at 4°C intervals measured by the thermistor chain.

berger & Head, 1994) measuring pressure, temperature (with accuracy better than 0.001°C), conductivity (with accuracy better than 0.001 S m^{-1}), dissolved oxygen (DO) (with accuracy better than 0.1 mg L^{-1}), pH, and photosynthetic active radiation (PAR); and a microstructure probe with pressure and fast temperature sensors. The MSP is a free-fall profiler, falling at about 0.15 m s^{-1}. The fine scale sensors were sampled at 50 Hz, the microstructure at 100 Hz, and the C6 at 1 Hz. Rhodamine WT, chlorophyll a (Chl-a), coloured fraction of dissolved organic matter (CDOM) and turbidity sensors were installed on the C6 unit. The fine scale sensor signals were digitally enhanced, as described by Fozdar *et al.* (1985), in order to match the sensor responses and avoid spiking in the quantities derived from multiple signals, e.g., salinity. The Chl-a fluorescence measurements were calibrated against laboratory determinations of Chl-a in water samples taken alongside profiles at 8 stations spanning the lake. Opportunistic MSP profiling was conducted over several days along longitudinal and cross transects taken throughout the lake.

The small differences in salinity between the river and lake waters allowed the dilution rate of the inflow to be calculated. The small salinity differences require an accurate method of calculating the salinity to achieve accurate dilution rate calculations. The relationship between the measured conductivity and salinity of water depends on the species of ions present in the water. The ionic species can be taken into account by using the method described by Pawlowicz (2008). The ionic content of water in Lake Iseo was 2.19 meq L^{-1} calcium, 1.89 meq L^{-1} bicarbonate, 0.67 meq L^{-1} magnesium and 1.04 meq L^{-1} sulphate (Ambrosetti & Barbanti, 2005). This ratio of ions was used to calculate salinity of all water in the lake, because all the water comes from the same catchment.

The dissipation of TKE was determined by analysis of the temperature microstructure profiles as described in Luketina & Imberger (2001). In brief, after filtering to correct for response time (Fozdar *et al.*, 1985) the profiles were partitioned into statistically stationary segments (Imberger & Boashash, 1986; Imberger & Ivey, 1991; Luketina & Imberger, 2001). The temperature gradient signal from each stationary signal was then analysed using a Batchelor curve fitting technique to evaluate the dissipation of TKE, ϵ. The upper bound of the vertical mixing coefficient was evaluated from the Osborn (1980) formula (Yeates *et al.*, 2013):

$$\kappa = 0.2\epsilon/N^2. \tag{2.15}$$

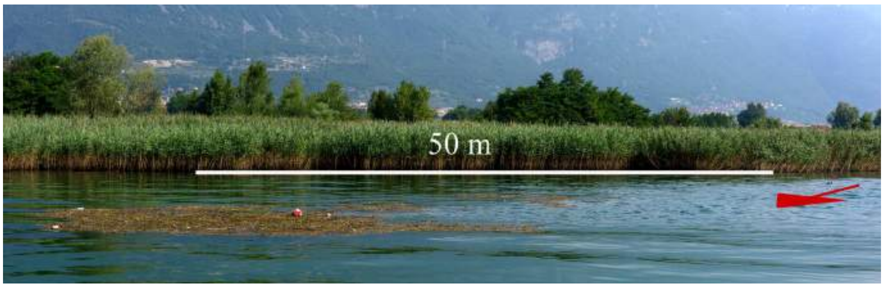

Figure 2.8: Photograph showing the size of the plunge region and the build-up of flotsam which identified the extent of the plunge region. The scale indicates 50 m along the bank of the river and the red arrow indicates the direction of inflow of the river.

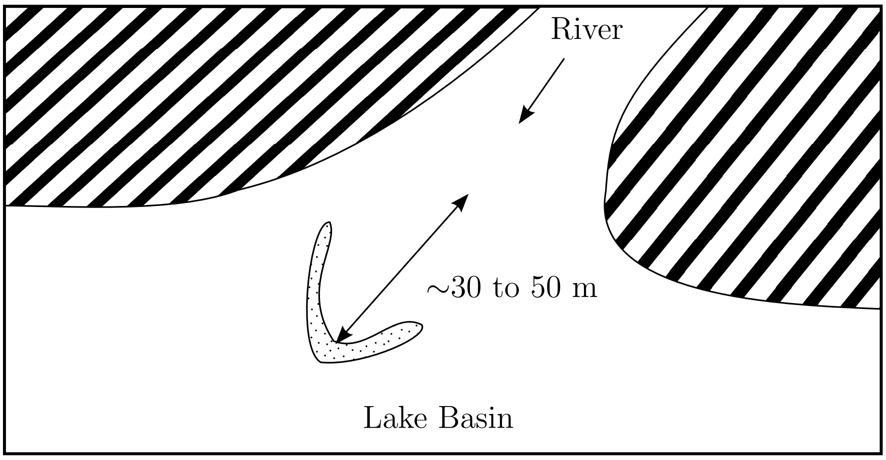

FIGURE 2.9: Plan view sketch of the photograph in figure 2.8. The dotted area shows the location of the build-up of flotsam on the lake surface and the diagonally striped areas show the shore.

2.4 Results

2.4.1 Plunge region

The plunge curve formed by the water issuing from the Canale Italsider was identified visually in the field by the build-up of flotsam at the convergence zone. The plunge curve reached approximately 30 to 50 m from the separation point, as shown in figures 2.8 and 2.9. The separation point was located at the start of the increase in the width of the river. The inflow characteristics measured during the field campaign are given in table 2.1. The river velocity was found by dividing the average volume flow rate during the campaign by the channel cross-sectional area upstream, where the river depth was uniform across the channel. The reduced gravity was calculated from the difference between the average temperature of the river during the experiment and the average temperature at the 0.25 m deep thermistor at the LDS during the experiment. The average entrance Froude number Fr_0 was 2.5 and indicated that lateral collapse (case 4) was the relevant plunging mechanism. The model for lateral collapse, (2.13), gave a distance to the plunge region vertex of 120 m, in reasonable agreement with the plunge curve visible in figure 2.8. The laboratory measurements show the mixing ratio in a plunge region undergoing lateral falling has a constant value of 0.06 (Britter & Simpson, 1978).

Parameter	Value
Inflow channel width	49 m
Inflow channel depth	1.7 m
Inflow velocity	0.48 m s^{-1}
Inflow reduced gravity	0.021 m s^{-2}
Inflow temperature	13.0°C
Lake surface temperature	24.2°C
Inflow density	999.4 kg m^{-3}
Lake surface density	997.3 kg m^{-3}

Table 2.1: Characteristics of the inflow used in calculating the plunge region length scale.

2.4.2 Underflow

The entrainment during the underflow and the depth at which the underflow lifts away from the lake bed were calculated using the assumption of gradually varied flow from (2.4) (Antenucci *et al.*, 2005). The lake stratification, inflow temperature, and volume flow rate were averaged over the duration of the experiment. The bathymetry around the river mouth was available from an echo sounder survey of the lake with a nominal horizontal resolution of 10 m (Bini *et al.*, 2007). The river channel was assumed to have a triangular cross-section with a bottom drag coefficient typical for a sandy bed (Fischer *et al.*, 1979). The bed slope was averaged over the first 100 m of the thalweg from the inlet. The base angle of the triangular cross-section of the river channel was found by averaging five cross-sections over the first 50 m from the river mouth. The bathymetry around the Canale Italsider inlet is shown in figure 2.10. Using the values given in table 2.2, the calculation of the underflow behaviour gives a neutral buoyancy depth of 9.9 m, corresponding to the 18°C isotherm, and a mixing ratio of 1.1. The bathymetry reaches this depth at a distance of the order of 100 m offshore from the inlet.

2.4.3 Measurement of underflow dilution

The mixing ratio during the underflow, γ_u, was calculated from the changes in concentration of conserved quantities between the upstream river and the beginning of the intrusion. The quantities used - salinity, temperature, DO, CDOM, and turbidity - were naturally present in the water and were assumed to be con-

Parameter	Value
Inflow temperature	13.0°C
Volume flow rate	40 $\mathrm{m^3\ s^{-1}}$
Bottom drag coefficient (C_D)	0.016
Average bed slope angle	4.6°
Valley half angle	86°

Table 2.2: Parameter values used in calculating underflow length scale for Canale Italsider.

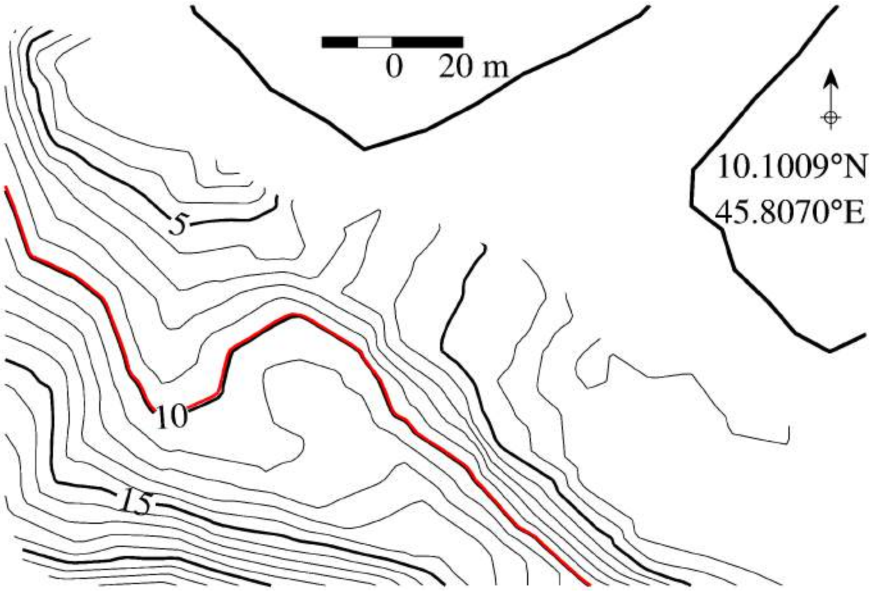

Figure 2.10: Bathymetry in the neighbourhood of the Canale Italsider inlet. The isobath of the neutral buoyancy level predicted by the numerical underflow model is given by the red line.

servative over the time taken for the water to pass through the underflow. DO, CDOM, and turbidity are quasi conservative over the time taken for the water to pass through the underflow, so they gave additional estimates of the mixing ratio, although less accurate than those obtained from salinity and temperature.

The underflow mixing ratio was calculated using

$$\gamma_u = (c_r - c_i)/(c_i - c_s), \tag{2.16}$$

where c_r is the concentration of a conserved quantity in the river water, c_s the average concentration in the lake surface water, and c_i the concentration in the intrusion. The river concentrations were measured in the river upstream of the

Profile station	Mixing ratio (γ_u) based on: salinity	temperature	DO	CDOM	turbidity	Average of estimates
p19	0.8	1.6	1.3	0.6	0.4	1.0
p185	2.0	1.5	0.6	1.2	4.0	1.9

Table 2.3: Mixing ratios measured from different natural tracers and averaged over the estimates.

plunge region, so the estimate of underflow mixing ratio includes the contribution of the plunge region mixing. The plunge region mixing caused by the lateral falling mechanism, calculated from laboratory observations in (2.14), was small relative to the underflow mixing.

In order to calculate c_i, the intrusion water was identified by the following method. Profiles in the northern basin were selected in which the Canale Italsider intrusion could be identified from anomalies in the salinity measurements. Anomalies that occurred in statically unstable regions were discarded because they were the result of turbulent overturns, not intrusions. The profiles selected were p19 and p185; the locations of these stations are shown in figure 2.6 and the profiles of salinity and temperature are shown in figure 2.11. The upper and lower extents of the intrusion were demarcated by sharp salinity and temperature changes bounding the intrusion. Such changes are apparent in figure 2.11 at depths of 6.8 m, 7.5 m, 10.6 m, and 11.2 m in p19 and 5.3 m, 8.6 m, and 11.1 m in p185. To choose between the alternative upper and lower extents present in the profile, the extents selected were those that were most self-consistent, i.e., led to the least variance between mixing ratios estimated from the different tracers. The calculated mixing ratios are shown in table 2.3. The average γ_u over both underflows was 1.5. The mixing rates measured in the two intrusions based on the strictly conserved quantities of temperature and salinity ranged from 0.8 to 2.0.

2.4.4 Intrusion

Intrusion waters from both the Oglio River and Canale Italsider were clearly apparent in the salinity, DO, and Chl-a fields of the transverse transect t1 taken 300 m from the shore, as shown in figure 2.12. The fresher water of the Canale Italsider intrusion can be seen 0.5 km along the transect, and the saltier water of

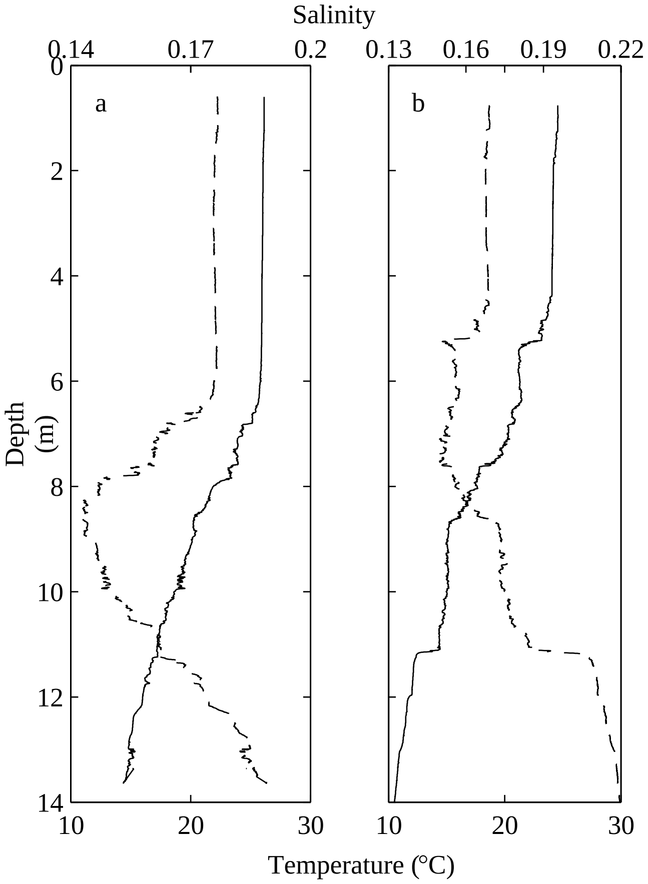

FIGURE 2.11: Profiles of salinity (dashed line) and temperature (solid line) at stations a) p19 and b) p185.

the Oglio intrusion can be seen 1.5 km along the transect. The inflows both had Chl-a concentrations of 0.8 g L^{-1}, significantly lower than the lake water. The Oglio River and Canale Italsider inflows had DO concentrations of 10.0 and 10.8 mg L^{-1} respectively, again significantly lower than the lake water. The regions of anomalies in the Chl-a and DO were collocated with each other and the salinity anomalies. At the same location, the isotherms, shown in figure 2.12, are spread apart by the intrusions which introduce water with a more uniform density than water at this depth in the lake. The collocation of the anomalies in all the different measured quantities supports the hypothesis that these two regions are intrusions consisting of water from the inlets. In transects further from the inlets than transect t1, the intrusion waters were harder to identify because the anomalies caused by the intrusions were weaker.

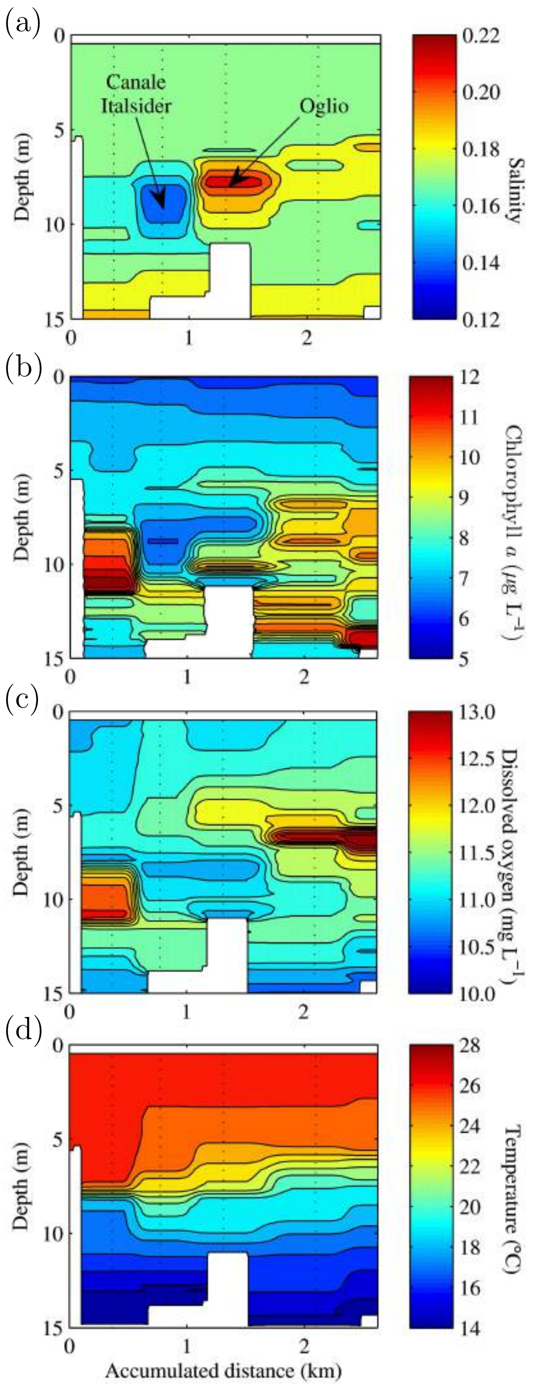

FIGURE 2.12: Transverse transect of (a) salinity, (b) Chl-a concentration, (c) DO concentration, and (d) temperature at transect t1, as viewed looking downstream. The profiles were taken between 17:06 h and 18:14 h on day 196. The plots show the fresher water intruding from the Canale Italsider and the saltier water intruding from the River Oglio. Signals of the intrusion are apparent at the same positions in other tracer measurements. The location of the profiles are indicated with dotted lines. Values were interpolated with a finite impulse response filter between profiles.

2.4.5 General salinity pattern in the northern basin

The salinity measurements at transect t1 show that both the surface and deep water were saltier than the intrusion from the Canale Italsider. Throughout the northern basin the water around the 20°C isotherm typically possessed a minimum in salinity, as shown in profile p176 in figure 2.13. This may be explained by noting that the Oglio River inflow was more buoyant than the Canale Italsider. The Oglio River intrusion therefore entered the lake slightly above the Canale Italsider. The surface mixed layer was therefore slightly saltier as it contained a larger proportion of the Oglio River water. The water around the 20°C isotherm contained the highest concentration of fresh Canale Italsider water, causing the minimum in salt content. At depths below the Canale Italsider intrusion, the proportion of the water retained from the previous winter increased. Water retained from the previous winter was saltier than the Canale Italsider intrusion because the upper part of the lake mixes during the winter, attaining a salinity between those of the Oglio River and Canale Italsider (Mosello *et al.*, 2010).

The horizontal extent of the relatively undiluted intrusion water from the two inflows is apparent in the horizontal section of salinity, averaged between the 18°C and 22°C isotherms, shown in figure 2.14. The values of the upper and lower bounding isotherms were selected to encompass the depths at which the salinity signals of the intrusions were observed most strongly. The resulting salinity distributions were insensitive to the exact values of these bounds. The inflow from the Canale Italsider may be considered steady over the time taken for the water to travel the length of the intrusion, as shown in figure 2.7. Within approximately 5 km of the inlets, the western part of the lake was dominated by higher salinity water and the eastern part of the lake was dominated by lower salinity water coming from the Canale Italsider. Further than 5 km from the inlets, the lake water at the depth of the intrusion became relatively homogeneous.

2.4.6 Intrusion dynamics

Calculation of the length scales of the intrusion from dynamical considerations requires measurement of the vertical turbulent diffusivity at the depth of the intrusions. The locations of the microstructure profiles used (p19, p77, p80, p176, p185, p190, 195, and p200) are shown in figure 2.6 and the TKE dissipation

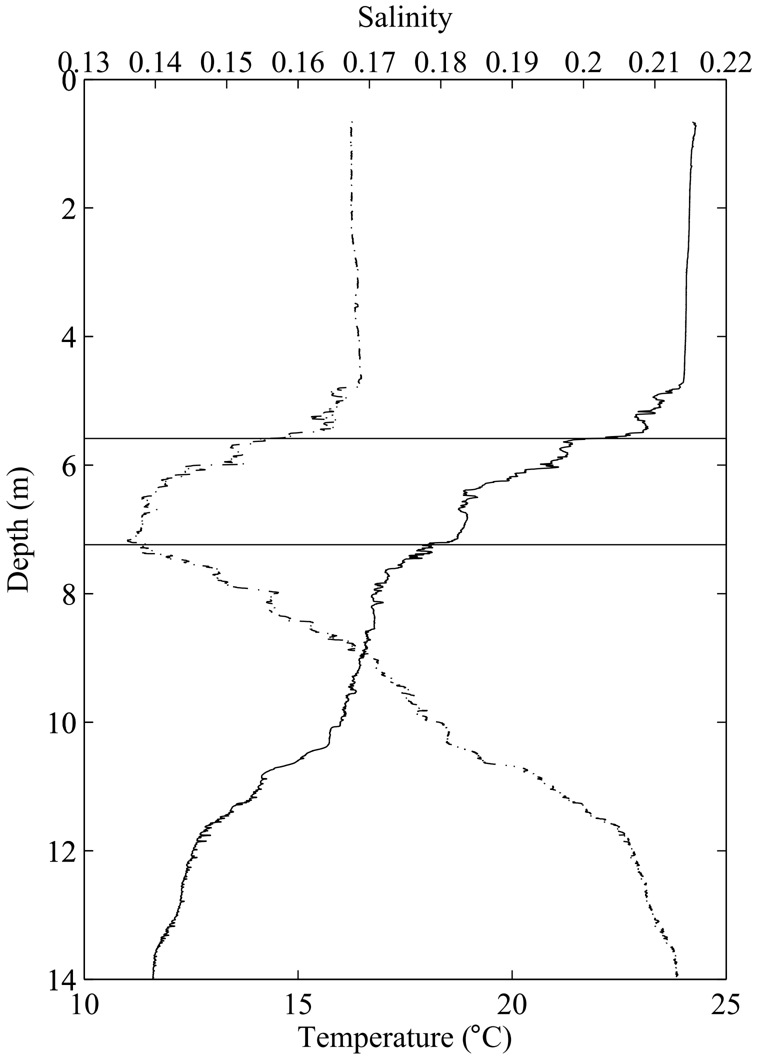

FIGURE 2.13: Profiles of salinity (dot-dashed) and temperature (solid) at p176 taken on day 202. The representative bounds of the intrusion in the northern basin, between the 18°C and 22°C isotherms, are indicated by the dashed lines.

estimates obtained from temperature gradient profiles are shown in figure 2.15. Within the intrusion region, defined by the 18°C and 22°C isotherms, the TKE dissipation varied between 6×10^{-9} m^2 s^{-3} and 7×10^{-7} m^2 s^{-3} with an average value in this region of 1.1×10^{-7} m^2 s^{-3}. Such variation may be expected as each profile records one event at a particular time (Imberger & Ivey, 1991). The average buoyancy frequency in the region of the intrusion was 0.046 s^{-1}, yielding an average vertical turbulent diffusivity, from (2.15), of 1.0×10^{-5} m^2 s^{-1}. The thickness of the inertia-buoyancy intrusion was calculated, from the equation for

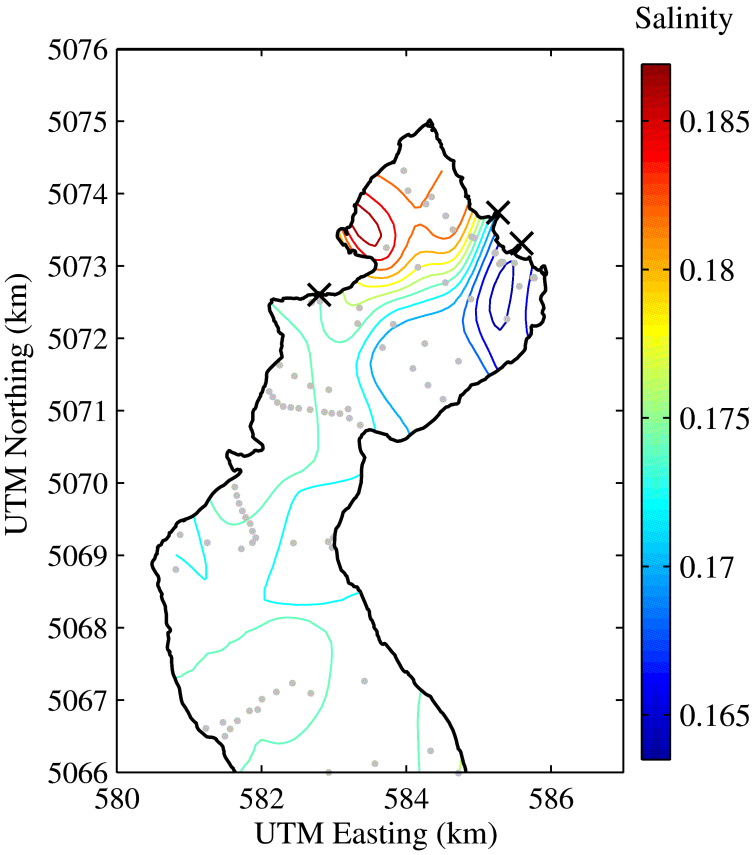

FIGURE 2.14: Horizontal cross-section of salinity at the isotherm of the Canale Italsider intrusion. The locations of the profiles are indicated by dots. Values were interpolated with a finite impulse response filter. Inflow locations are marked by ×. The axes give the Universal Transverse Mercartor (UTM) coordinates.

a 2D intrusion (2.8), to be 0.9 m. The 2D volume flux was calculated from the combined river inflow and entrained fluid volume flux, 74 m^3 s^{-1}, and the width of the lake, 2100 m. The horizontal length scale over which the intrusion was governed by an inertia-buoyancy force balance, calculated using (2.6) with the values given in table 2.4, was 3 km. The horizontal length scale for diffusion to reduce the concentration of the inflow tracer in the diffusive-buoyancy regime, calculated using (2.12) with the values given in table 2.5, was 900 m. These measurements yield a total length scale of 4 km (3.9 km) for the inflow intrusion to be integrated into the lake water, in good agreement with that observed from the salinity in figure 2.14. The estimated length scales of the consecutive stages of the Canale Italsider interflow, which are calculated above, are summarised in

Parameter	Value
Source volume flow rate per unit width	0.035 m^2 s^{-1}
Buoyancy frequency	0.046 s^{-1}
Turbulent diffusivity	1.0×10^{-5} m^2 s^{-1}

TABLE 2.4: Field measurements used in calculating the horizontal length scale of the inertia-buoyancy intrusion.

table 2.6.

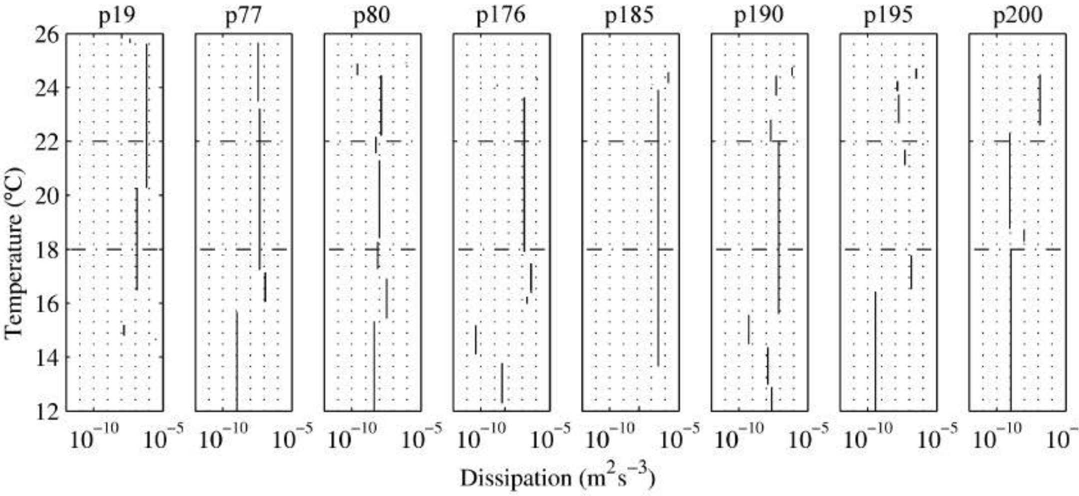

FIGURE 2.15: Profiles of dissipation plotted with temperature at stations p19, p77, p80, p176, p185, p190, 195, and p200. The representative bounds of the intrusion in the northern basin, the 18°C and 22°C isotherms, are indicated by the dashed lines.

2.5 Discussion

The amount of mixing and length scales observed for the stages of the Canale Italsider interflow will now be compared to the results of previous studies, and the implications for lake models will be highlighted.

2.5.1 Inflow mixing

Spigel *et al.* (2005) measured γ_p for two rivers flowing into Lake Taupo, New Zealand. They observed a value of γ_p of 1.9 in the plunge region of both rivers,

Parameter	Value
Background buoyancy frequency	0.046 s^{-1}
Intrusion thickness	0.9 m
Turbulent diffusivity	1.0×10^{-5} m^2 s^{-1}

TABLE 2.5: Values used to calculate the length scale over which the diffusive-buoyancy intrusion is diluted.

Length Scale	Estimate for Canale Italsider (m)
Off-shore extent of plunge curve	120
Horizontal length scale of underflow from the inlet	100
Horizontal length of inertia-buoyancy intrusion	3000
Horizontal length of diffusion-buoyancy intrusion	900

TABLE 2.6: Summary of the length scales of the consecutive stages of the Canale Italsider interflow.

which is much larger than the value of 0.06 predicted by the laboratory experiments of Britter & Simpson (1978). The larger γ_p was caused by the inflows being in the entraining jet regime for larger Fr_0. The values of Fr_0 reported by Spigel *et al.* (2005), 2.6 in the Tongariro River and 3.4 in the Tokaanu Tailrace, were underestimated, because these reported values were based on a length scale formed from the square root of the cross-sectional area rather than the water depth. To illustrate this, the river depth at the mouth of the Tokaanu Tailrace, whilst not reported specifically at the separation point, was 1.4 m which gives a much larger Fr_0 of 69. At this large value of Fr_0, the higher values of γ_p observed are as expected from a laterally entraining jet. In the series of experiments by Johnson *et al.* (1987), six runs were carried out in channels that immediately widened upon meeting the lake and in which $Fr_0 < 3$. Of these runs, five runs used channels with aspect ratio W/H of 0.5 and these had values of γ_p ranging from 2.1 to 3.5. In the other relevant experimental run, W/H was 2 and γ_p was 0.5. These entrainment rates are higher than those predicted by Britter & Simpson (1978) experimental results because W/H is of order unity rather than being much larger than unity. In channels with deep, narrow inflows, the relatively large lateral surface area of the inflow allows horizontal entrainment to be significant, shown by the trend of reduced γ_p with increased W/H in the results of Johnson *et al.* (1989). The vertical entrainment that occurs as the river water falls below the lake water, measured by Britter and Simpson's experiments (1978), is not dominant in channels with these small aspect ratios. In typical river inlet geometries, as in the Canale Italsider inlet to Lake Iseo, the aspect ratio W/H is much larger than unity, which means that the entrainment predominantly occurs as river water falls beneath the lake water and the experimental results of Britter & Simpson (1978) are applicable. The value of γ_p reported by Rueda & MacIntyre (2009) is 0.7 for an inlet with $Fr_0 = 2.8$. This value of γ_p, whilst smaller than values reported elsewhere, is not as small as the value predicted by the experiments of Britter & Simpson (1978). We suspect this is because Fr_0 is not small enough.

The results in the prior literature, along with those reported here, suggest that the linear relationship between Fr_0 and γ_p in (2.3) is not appropriate over the entire range $1 < Fr_0$. The experimental results of Britter & Simpson (1978), expressed in (2.14), provide a suitable estimate in the regime of Fr_0 slightly larger than unity. Improved parameterisation of γ_p, which is applicable to all plunging inflows that meet the geometric criteria, should allow for different regimes at small and large Fr_0. These two regimes correspond to the lateral falling and entraining jet mechanisms.

The dilution of conserved quantities calculated from field observations indicates a total mixing ratio of 1.5. The numerical entrainment calculated using the method described by Antenucci *et al.* (2005) agrees with the measured mixing ratio to within the level of variability present between estimations from different tracers. The calculations of mixing ratios in the plunge region and underflow show that the majority of entrainment into the Canale Italsider interflow occurs in the underflow, with a ratio γ_p/γ_u of 0.04. For a model to describe the Canale Italsider intrusion accurately, the underflow entrainment must be modelled accurately, but the plunge region mixing can be neglected. Further tracer-dilution field and laboratory experiments with higher spatial resolution could give separate estimates of the mixing in the plunge region and underflow to further validate these calculations.

The dominance of mixing in the underflow observed in Lake Iseo does not necessarily occur at inlets with other parameter values. When $Fr \gg 1$ or when the bathymetry at the inlet is stepped, the plunge region mixing ratio will be greater than observed in this study (Spigel *et al.*, 2005). When the neutral buoyancy depth in the ambient is reduced, the entrainment into the underflow will reduce because the underflow will not travel as far before lifting away from the lake-bed. All mixing processes that contribute substantially to dilution of a specific inflow must be represented accurately in a hydrodynamic model if it is to form a sound basis for pollutant transport or ecological analysis (Botelho & Imberger, 2007; Rueda *et al.*, 2007; Vilhena *et al.*, 2010).

Models of plunge region mixing are currently lacking and, according to Dallimore *et al.* (2004) and Rueda & MacIntyre (2010), it is a priority that these models be further improved and validated. The application, developed here, of Britter and Simpson's (1978) laboratory results to the plunge region gives a widely applicable improved plunge region mixing model, in the regime of Fr_0 slightly larger than unity, which can be incorporated into hydrodynamic models of lakes.

2.5.2 Inflow length scales

The length scale of the plunge region observed in the field study supported the lateral falling mechanism. This suggests that the proposed lateral falling mechanism governs how hypopycnal river inflows with sharply diverging riverbanks plunge in the limit of Fr_0 slightly larger than unity. These criteria for lateral falling are met in many river-lake systems in various climates, for at least part of the year (Imberger & Patterson, 1989). In any such system, the size of the plunge region can be modelled using (2.13) and the amount by which the river water is diluted using (2.14). When rivers enter coastal oceans or fjords in geometries similar to that considered in this study, it is reasonable to speculate that, in the absence of other dominating mechanisms such as tidally induced flows, the lift off of the buoyant inflow from the river bed will be governed by the same lateral falling dynamics as in the plunging region (Luketina & Imberger, 1987).

The intrusion depth calculated by the numerical model of Antenucci *et al.* (2005), that implies the length scale of the underflow, fell within the range of intrusion depths observed in this field study. The horizontal length scale of the intrusion was of the order of 4 km, supported by both the salinity measurements and calculations based on the intrusion dynamics. This length scale is important from a biological perspective, because it is the length scale over which the inflow potential energy transports nutrients; beyond this distance, horizontal dispersion is required to transport the nutrients into the lake.

2.6 Conclusions

In this chapter we discussed field observations of the inflow of the river Oglio into Lake Iseo. We have compared the observed length scales and mixing rates of the different phases of the inflow with existing models. Notably, we found that the offshore extent of the plunge region was predicted reasonably well by a model of the newly identified lateral falling mechanism. In this model $x_j \sim Fr_0$, which is significantly different from the model of laterally entraining model of plunging, in which $x_j \sim Fr_0^4$, where x_j is the offshore extent of the plunge region and Fr_0 is the densimetric Froude number of the river at the separation point from the riverbank. We also considered the mixing ratio for plunge regions in which entrainment is predominantly vertical rather than horizontal. We calculated the mixing ratio derived from laboratory measurements (Britter & Simpson, 1978), $\gamma_p = 0.06$, which broadly agreed with previous field measurements in such plunge regions (Elder & Wunderlich, 1972; Hebbert *et al.*, 1979).

The river water was observed to descend as an underflow down to the metalimnion, where it intruded at an isotherm of around $20°C$. The intrusion could be observed from tracers already existing in the river inflow, without adding any artificial tracers. The distance to where the salinity of the inflow could no longer be distinguished from the surrounding water was approximately 4 km. Vertical diffusion was calculated to dilute the intruding water with surrounding lake water over a length scale which agreed with this observed distance.

In section 3.3.5, parameter values typical of a lake will be applied to a theory developed in the next chapter to calculate the time for a basin to fill with water entrained into an underflow. At Iseo during the experiment, a typical volume flow per unit width into the lake was 0.035 $\mathrm{m}^2\ \mathrm{s}^{-1}$, the reduced gravity of the river in the lake was 0.021 $\mathrm{m\ s}^{-2}$, the depth of the lake basin was 250 m, and the average bottom slope to the bottom of the lake was 1°. The parameterisation of Fernandez & Imberger (2006) with this bottom slope and a bottom drag of 0.015, typical for the lake bed material, gave an entrainment coefficient of 5×10^{-3}.

In the rest of the thesis, we will consider an inflow into a basin of uniform, light fluid. This means that the underflow stage continues to the bottom of the basin. We shall focus exclusively on the underflow stage. We will consider inflows which deliver enough fluid to drive the evolution of the density stratification in the basin. We will first discuss different mathematical models for the evolution of the stratification in basins fed by gravity current and then report laboratory experiments of filling basins. Using laboratory experiments instead of field experiments allows the underflow behaviour to be isolated from the noise introduced by the many other processes which occur simultaneously in a field setting. Comparing the models and experiments will allow us to test whether the assumptions made by the different models are good approximations of the real underflow processes.

CHAPTER 3

MODELS OF GRAVITY CURRENT FED BASINS

We will now turn from a field investigation to develop mathematical models which we will compare, in chapter 5, with laboratory experiments. We will also turn to focus on how the inflow modifies the stratification in the lake basin, rather than only the dynamics of the inflow.

More specifically, this chapter considers theoretical and numerical models for the density stratification which develops in a two-dimensional (2D) basin fed with relatively dense fluid from a gravity current. In one case we will compare the numerical models with asymptotic limits. We will also compare the different ways that the stratification in the basin develops under the different assumptions made in the models.

The basin initially contains fluid of uniform density, unlike the lake examined in the previous chapter. An outflow with equal volume flux to the inflow leaves from the top of the basin at the opposite side from the inflow, maintaining a constant volume in the basin. We will consider four models which span a spectrum of varying degrees of mixing. Two simple end-member cases at each extreme of the spectrum (cases 1 and 4) are discussed to give complete coverage of cases, and give a context for the intermediate cases (cases 2 and 3). Section 3.1 considers the full mixing end-member (case 1), in which the inflow is continuously and completely mixed with the fluid throughout the basin. Section 3.2 considers the no mixing end-member (case 4), in which the inflow and the fluid initially in the basin do not mix, and reside in separate parts of the basin. Section 3.3 considers an inflow which is partially mixed with the fluid in the basin (case 2). The mixing occurs through turbulent entrainment, as outlined by Morton *et al.* (1956), in which ambient fluid is drawn into the gravity current and mixed locally with the fluid in the current. Finally, section 3.4 considers another partially mixed model (case 3) with less mixing than in case 2. Fluid from the uniform part of the basin is drawn into the gravity current, but the gravity current itself retains a stratified density profile.

Each case of mixing described above will be considered in both a basin which has constant horizontal area at all depths (which is simpler to describe mathematically) and a basin with a horizontal area which reduces linearly with depth (i.e. has a triangular vertical cross section, which is more typical (Håkanson, 1977) of a lake or reservoir). Sketches of the two basins are shown in figure 3.1. The geometry drawn in figure 3.1(a) is not particularly representative of a lake basin, but shows one way in which the constant horizontal area case could be constructed in a laboratory experiment.

3.1 Full mixing (case 1)

When mixing in a basin is dominant, it will fully homogenise the fluid in the basin. This could theoretically occur, for example, in a lake in strong wind conditions in which the turbulent kinetic energy in the ambient lake water is high enough to fully mix the lake water. In this idealised end-member case, fluid from an inflow at a different density from the fluid in the basin will instantaneously

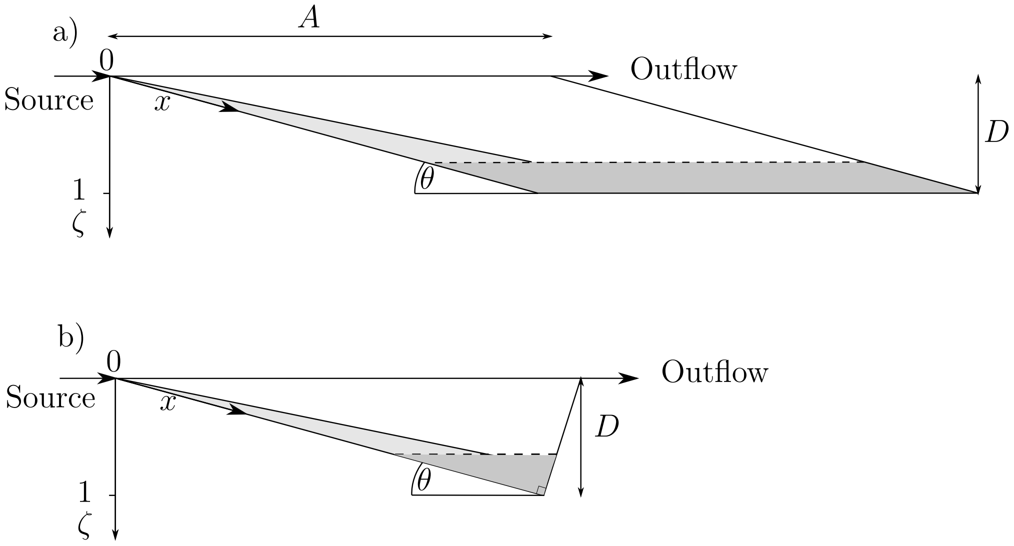

FIGURE 3.1: Schematic of a) the basin with the same width at all depths and b) the basin with triangular section. The gravity current is shown in light grey and the ponded region is shown in dark grey.

alter the density throughout the basin. For an inflow with constant flow rate and density, conservation of mass implies that the density of the basin fluid, $\rho(t)$, will evolve according to

$$\rho = (\rho_i - \rho_0)e^{-Q_s t/V} + \rho_0, \tag{3.1}$$

where ρ_0 is the density of the source, ρ_i the initial density of the basin fluid, Q_s the source flow rate, V the volume of the basin, and t the time since the inflow started. The density within the basin is always uniform and approaches the inflow density asymptotically with an exponential decay. The e-folding time, the time taken for the density to reduce by a factor of e, is V/Q_s. This behaviour will be the same for both the constant width basin and the triangular basin. We now consider the opposing end-member of no mixing.

3.2 No mixing (case 4)

In the idealised case with no mixing, the inflow fluid flows undiluted in a gravity current down the incline. When fluid in the gravity current reaches the bottom of the basin, it ponds. The height of the ponded region grows as more fluid reaches the bottom of the basin until the ponded region fills the basin, in a time $t_f = V/Q_s$. In the constant width basin, such as that shown in figure 3.1(a), the height of the top of the ponded region, h_{tp}, simply increases at a constant rate according to

$$h_{tp} = Q_s t_f / A, \tag{3.2}$$

where A is the width of the basin. In the triangular basin, the height of the ponded region evolves according to

$$h_{tp} = \sqrt{2 Q_s t \cos\theta \sin\theta}, \tag{3.3}$$

where θ is the angle relative to horizontal of the slope along which the gravity current falls. The density of the fluid above the ponded region remains at the density of the initial fluid in the basin, and the density of the fluid in the ponded region remains at the density of the inflowing fluid. The outflowing fluid has the density of the initial fluid until the basin fills with inflowing fluid, at which point the density instantaneously changes to the density of the inflow fluid.

3.3 Persistently entraining gravity current (case 2)

The behaviour of an inflow entering a basin of fluid is described more realistically by models which allow the inflowing fluid to partially mix with fluid in the basin. In this section we will use the entrainment model originally suggested by Morton *et al.* (1956) and applied to filling box models by Germeles (1975) and Worster & Huppert (1983). We will extend the numerical model to consider the density profile which is established in basins of varying cross-sectional area and compare numerically calculated profiles to asymptotic, analytical approximations.

3.3.1 Equations describing the evolution of a filling box stratification

The development of a steady, 2D, turbulent gravity current along an incline may be determined from the conservation of volume, momentum, and buoyancy along the slope. Under the Boussinesq assumption that density changes may be neglected in the fluid inertia (Boussinesq, 1903), these conservation laws are

$$\frac{d}{dx}(uh) = Eu \tag{3.4}$$

$$\rho_r \frac{d}{dx}\left(u^2 h\right) = \rho_r g' h \sin\theta \tag{3.5}$$

$$\frac{d}{dx}(uhg') = -uh\frac{d}{dx}g'_a, \tag{3.6}$$

where x is the distance downwards along the slope, u the velocity in the gravity current down the slope, h the thickness of the gravity current normal to the slope, E the entrainment coefficient, $g' = g(\rho_p - \rho_a)/\rho_r$ the reduced gravity of the fluid in the current, $g'_a = g(\rho_a - \rho_r)/\rho_r$ the reduced gravity of the ambient fluid, g the acceleration due to gravity, θ the angle the incline makes with horizontal, ρ_p the density in the gravity current, ρ_a the density of the ambient and ρ_r a constant reference density. The value of E in experiments in this work will be measured from the experiments, as discussed in section 5.1.2. This analysis is valid for any form of the density and velocity profiles within the gravity current, assuming that the profiles remain self-similar along the current (Turner, 1973). In this model we shall assume, as has been done commonly throughout the literature, that the density and velocity profiles have a “top hat” form (Morton *et al.*, 1956), i.e., they are a Heaviside step function falling from the mean value in the current to the ambient value at a distance h in a perpendicular direction from the slope.

In the momentum equation for the gravity current, (3.5), the bottom drag has been neglected. This simplification is an approximation to the flow on adequately steep inclines, such as were used in the laboratory experiments in chapter 5 and was found in the underflow region of Lake Iseo ($\sim 10^\circ$). For parameters typical of the laboratory experiments ($g' = 0.2$ m s^{-2}, $h = 0.01$ m, $\theta = 8.6^\circ$, $u = 0.1$ m s^{-1}, and $C_d = 0.006$), the drag term, $\rho_r C_d U^2$, is a factor of 5 smaller than the buoyancy term. There is some uncertainty in these values as they are difficult to measure, particularly C_d and h. Whilst drag does not dominate the turbulent flows discussed in chapter 5, it may make some contribution to the momentum balance. It would be worthwhile in future investigations to examine the impact of drag on the system. At much smaller angles of inclination, the drag term can be dominant in the momentum equation and should be included in the momentum equation (Lane-Serff, 1993).

The density stratification in the ambient is modified as the gravity current entrains fluid from the ambient and discharges its fluid at the bottom of the basin. For the constant width basin, shown in figure 3.1(a), the evolution of the ambient density is

$$\frac{\partial g'_a}{\partial t} = \frac{uh}{A}\frac{\partial g'_a}{\partial z}, \tag{3.7}$$

where z is the vertical distance in the basin below the virtual origin of the source (Worster & Huppert, 1983). To use this evolution equation for the ambient a number of simplifying assumptions about transport of buoyancy in the ambient must be made. The horizontal advection of buoyancy in the ambient is assumed to be negligible. This is valid because the density gradient in the stratified ambient is very nearly vertical and the reduction of the flow to one dimension is a good approximation. The motion of the ambient is assumed to be an upwards return flow in response to the downwards volume flux of the gravity current. Conservation of volume shows that the volume flux upwards in the ambient at any height must equal the volume flux downwards in the gravity current. Diffusion is assumed to transport a negligible amount of mass relative to advection. This is valid because the ambient motion is laminar and, at typical flow rates in the laboratory experiments, advective mass transport acts much faster than diffusive mass transport. In lakes, under some circumstances, such as when strong winds raise the turbulent kinetic energy of the ambient lake water, diffusion can play a significant role. For the triangular basin, shown in figure 3.1(a), the evolution of the ambient density profile is

$$\frac{\partial g'_a}{\partial t} = \frac{uh\sin\theta\cos\theta}{D-z}\frac{\partial g'_a}{\partial z}, \tag{3.8}$$

where D is the depth of the bottom of the basin below the virtual origin. The virtual origin will be discussed in section 3.5. The boundary condition for the density of fluid at the bottom of the ambient is set by the density of fluid that leaves the gravity current at the bottom of the basin to form the bottom layer of the ambient. Non-dimensionalising the variables with the scalings

$$\begin{aligned}
\zeta &= zD^{-1}, \\
\tau_c &= tE^{2/3}F_0^{1/3}\sin^{-2/3}\theta A^{-1}, \\
f &= g'uhF_0^{-1}, \\
q &= uh\sin^{2/3}\theta E^{-2/3}D^{-1}F_0^{-1/3}, \\
m &= u^2h\sin^{1/3}\theta E^{-1/3}D^{-1}F_0^{-2/3}, \\
\delta &= g_a'E^{2/3}D\sin^{-2/3}\theta F_0^{-2/3},
\end{aligned} \tag{3.9}$$

where F_0 is the source buoyancy flux per unit width, converts (3.4) - (3.7) into dimensionless form as

$$\frac{dq}{d\zeta} = \frac{m}{q}, \tag{3.10}$$

$$\frac{dm}{d\zeta} = \frac{fq}{m}, \tag{3.11}$$

$$\frac{df}{d\zeta} = -q\frac{d\delta}{d\zeta}, \tag{3.12}$$

$$\frac{\partial\delta}{\partial\tau_c} = q\frac{\partial\delta}{\partial\zeta}, \tag{3.13}$$

with boundary conditions that $\delta(\tau = 0, \zeta) = 0$, $f(0) = 1$, $q(0) = 0$ and $m(0) = 0$. In the case of the triangular basin, the dimensionless time is instead

$$\tau = tE^{2/3}{F_0}^{1/3}\sin^{1/3}\theta\cos\theta D^{-1} \tag{3.14}$$

and (3.13) is instead

$$\frac{\partial\delta}{\partial\tau} = \frac{q}{1-\zeta}\frac{\partial\delta}{\partial\zeta}. \tag{3.15}$$

3.3.2 First front of the ponded region

The location of the first front can be expressed analytically for both the constant width and triangular basin geometries. For a gravity current which starts at $\zeta = 0$ from a source of buoyancy with no volume flux, (3.10) and (3.11) give the flow rate in the current as it falls through the uniform density portion of the ambient as

$$q = \zeta. \tag{3.16}$$

Using this explicit expression for q and the the chain rule, (3.13) can be integrated to give the evolution equation for the depth of the first front

$$\zeta_f = e^{-\tau_c}. \tag{3.17}$$

For the triangular basin, the depth of the first front is given by

$$\zeta_f = -\mathcal{W}(-e^{-1-\tau}), \tag{3.18}$$

where $\mathcal{W}$ is the product-log function, also known as the Lambert-W function. The product-log function is described and the derivation of (3.18) is given in appendix A. The depth of the first front in the two geometries is plotted in figure 3.2. In the triangular geometry, the first front initially rises infinitely quickly as the width of the basin at the bottom vertex is 0; in the constant width geometry, however, the first front rises at finite speed throughout. In both cases, the first front takes an infinite time to reach the buoyancy source when the volume flux at the source is zero because the speed of the front asymptotically reduces to zero as it approaches the source (Caulfield & Woods, 2002).

There are, in fact, two reasonable options for how the time scales for the two basins may be compared. In figure 3.2, the abscissa for the two curves is plotted with $\tau_c = \tau$. Setting the time scales for the two basins equivalent in this way implies $A = D/(\sin\theta\cos\theta)$, i.e., the maximum width of the triangular basin is the same as the width of the constant width basin and volume of the constant width basin is twice that of the triangular basin. The abscissa in figure 3.3 is plotted with $\tau_c = 2\tau$. This option implies $A = D/(2\sin\theta\cos\theta)$, i.e., the basins have the same volume and the maximum width of the triangular basin is twice the width of the constant width basin. In this case, the curves for the rise of the first fronts in the two basins intersect at $\zeta_f = -\mathcal{W}(-2e^{-2})/2$. The basin which asymptotically approaches being full more quickly depends on which comparison is used. The front always starts rising more slowly in the constant width basin, however, because it is wider at the bottom.

The location of the first front is only affected by the volume of fluid transported by the gravity current upstream of the first front. In both the case 2 model and

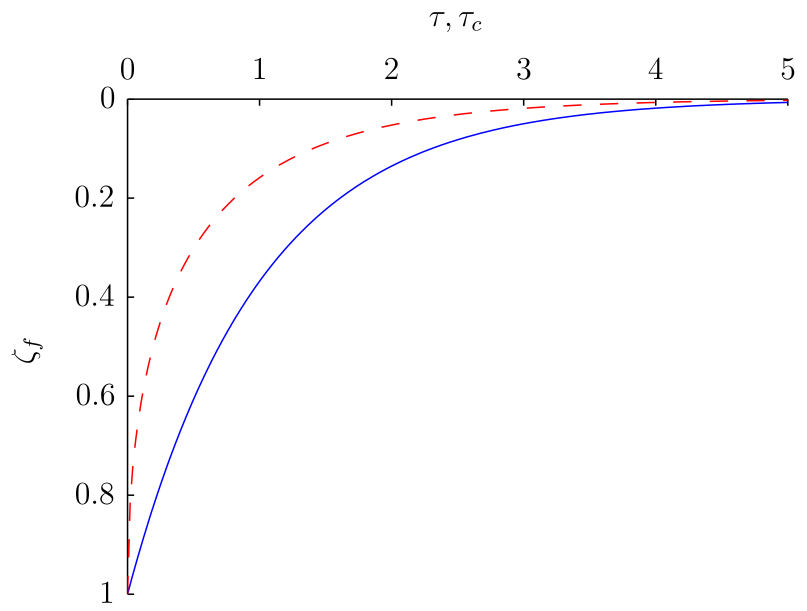

FIGURE 3.2: Depth, ζ_f, of the first front of the ponded region in a constant width basin as a function of dimensionless time, τ_c, (blue, solid line) and of the first front in a triangular basin as a function of dimensionless time τ (red, dashed line). The two basin have the same maximum width, but different shapes.

the case 3 model (to be discussed in section 3.4), the gravity current – whilst it is above the ponded region – transports the same amount of fluid. Therefore, the evolution of the first front location applies equally to both models.

3.3.3 Numerical scheme to calculate the evolving ambient stratification

The system of equations (3.10) - (3.13) was solved numerically, using an extension to the scheme described by Worster & Huppert (1983). Analytic solutions for the gravity current fluxes were used in the uniform part of the ambient: (3.16), $m = \zeta$ and $f = 1$. The gravity current fluxes through the stratified part of the ambient were calculated from (3.10) - (3.12), using a second order Runge-Kutta scheme.

The evolution of the ambient stratification was solved by using an Euler integration scheme, with a coordinate system that moves with isopycnal layers in the ambient. At each time step a layer of dense fluid is introduced at the bottom

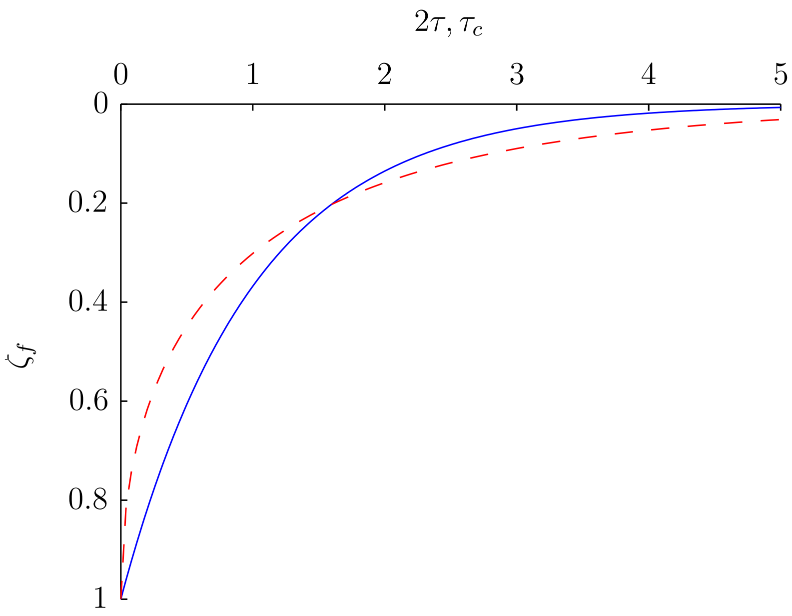

FIGURE 3.3: Depth, ζ_f, of the first front of the ponded region in a constant width basin as a function of dimensionless time, τ_c, (blue, solid line) and of the first front in a triangular basin as a function of dimensionless time τ (red, dashed line). The two basins have the same volume, but different shapes.

of the basin. The fluid in this layer is deposited by the gravity current in the previous time step and ponds at the bottom of the basin. The layers rise over the following time steps by displacements $\Delta\zeta_i$, calculated from either (3.13) or (3.15), depending on the basin geometry. In the triangular basin, the horizontal cross-sectional area at the bottom vertex is zero, which implies that the upwelling speed of the ambient fluid asymptotically approaches infinity as $\zeta \to 1$. This singularity was handled in the numerical scheme by using the analytical asymptotic expression expanded around $\zeta = 1$ for the thickness of the layer at the bottom vertex. This expression for the thickness of the bottom layer is $\Delta\zeta|_{\zeta=1} = -\sqrt{2q|_{\zeta=1}\Delta\tau}$, derived from integrating (3.15).

To check for errors in the implementation of the numerical scheme, the results for a constant width geometry were compared to those given by Worster & Huppert (1983). The displacement of the first front at $\tau = 11.88$ was reproduced to within 1% (better than the accuracy with which the results could be read from Worster and Huppert's figure 6), giving confidence that the code implementation was free of errors. The code listing used for the numerical scheme is available at `http://www.repository.cam.ac.uk/handle/1810/245309`, Cambridge University's electronic repository, and in appendix B.

3.3.4 Large time asymptotics for a triangular basin

We will now investigate the large time asymptotic behaviour of the pure buoyancy source filling box, which has not been done before for a variable area basin. To gain confidence in the numerical scheme, we will compare the numerical results with analytical expressions for the asymptotic behaviour in the limit of $\tau \to \infty$.

The fluxes along the gravity current, calculated by the numerical scheme at $\tau = 10$, are shown in figure 3.4. Substituting (3.15) into (3.12), making the assumption that $\partial\delta/\partial\tau = 2$ in the limit of $\tau \to \infty$, and integrating gives

$$f = (\zeta - 1)^2 \tag{3.19}$$

as the asymptotic limit for the buoyancy flux along the gravity current. The numerical result for f at $\tau = 10$ in figure 3.4 agree well with the asymptotic expression for f at large time and would be indistinguishable on this plot. An asymptotic solution for the fluxes in the gravity current in the large time limit may be calculated by substituting (3.19) into (3.11). The power series solutions to the nonlinear ordinary differential equations formed from (3.10) and (3.11) may be found by matching terms in powers of ζ, which yields

$$q = \zeta - \frac{\zeta^2}{4} - \frac{\zeta^3}{120} + \cdots \tag{3.20}$$

$$m = \zeta - \frac{3\zeta^2}{4} + \frac{11\zeta^3}{120} + \cdots . \tag{3.21}$$

These power series solutions match well with the numerical solution, shown in figures 3.5 and 3.6. The power series solutions are shown alongside the numerical solution at $\tau = 10$. As more terms of the power series are included, the series solutions get closer to the numerical result, although the power series for the momentum flux is not monotonic when two or three terms are used.

The asymptotic solution for the ambient density profile was found by substituting (3.20) into (3.15) and integrating. The constant of integration was determined by the constraint that the total mass increase in the basin is equal to the total mass delivered by the source. This integral constraint is $\int_0^1 \delta \, \mathrm{d}V = \int_0^\tau f \, \mathrm{d}\tau$,

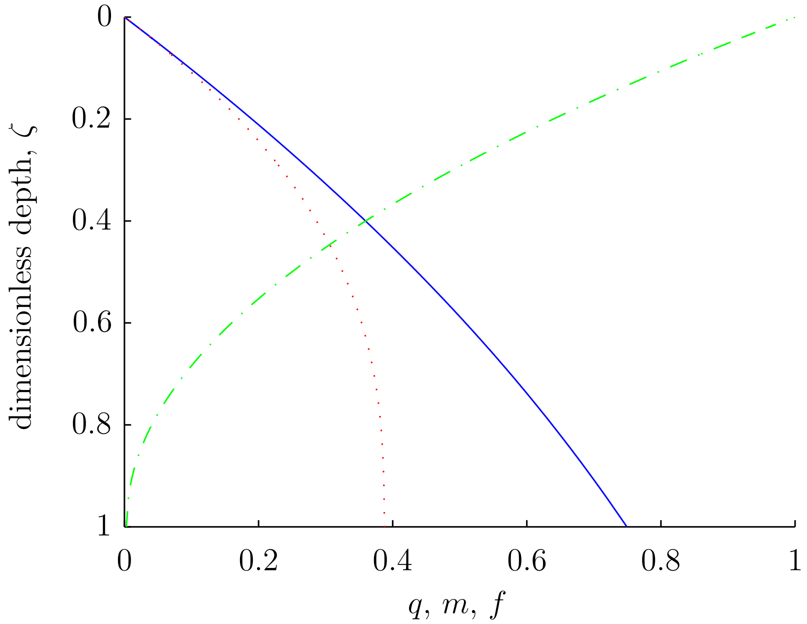

FIGURE 3.4: Numerically calculated fluxes along the length of the gravity current at $\tau = 10$. The volume flux, q, is shown by the solid, blue line; the momentum flux, m, is shown by the dotted, red line; and the buoyancy flux, f, is shown by the dot-dashed, green line.

where $\mathrm{d}V = (1-\zeta)\,\mathrm{d}\zeta$. Using only the first term of the power series for q gives

$$\delta = 2\ln\zeta - 2\zeta + 2\tau + 11/3. \tag{3.22}$$

Using two terms of the power series for q, we obtain

$$\delta = 2\ln\zeta + 6\ln(\zeta - 4) + 2\tau + 96\ln 2 - 54\ln 3 - 12. \tag{3.23}$$

The numerical and asymptotic solutions for δ are shown in figure 3.7. The numerical result agrees well with the asymptotic solution, even without using the second term for q. Surprisingly, when $\tau >> 1$ is not true, such as in figure 3.7 at $\tau = 0.5$, the asymptotic form matches reasonably well with the numerical result below the first front of the ponded region.

The accuracy of the numerics is further verified by the fact that mass is conserved with an anomaly of less than 0.2% with a time step of $\Delta\tau = 0.01$.

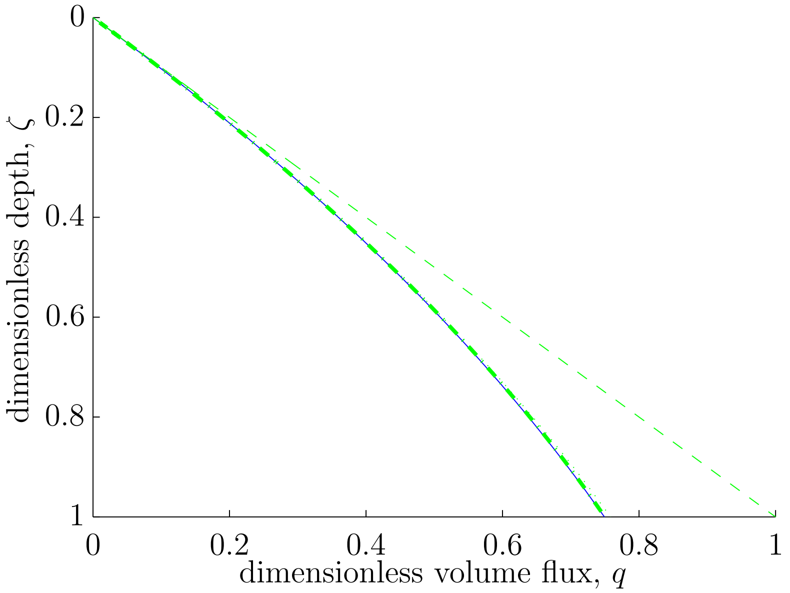

FIGURE 3.5: The volume flux profile along the gravity current in the limit as $\tau \to \infty$ calculated by: the numerical scheme at $\tau = 10$ (solid blue line); the first term in the asymptotic solution (dashed green); the first two terms in the asymptotic solution (dot-dashed green); and the first three terms in the asymptotic solution (dotted green).

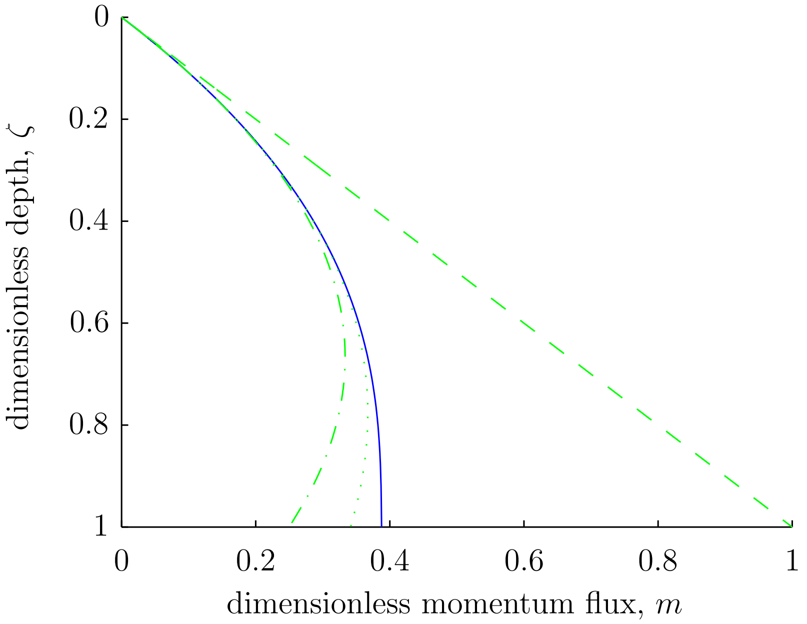

FIGURE 3.6: The momentum flux profile along the gravity current in the limit as $\tau \to \infty$ calculated by: the numerical scheme at $\tau = 10$ (solid blue); the first term in the asymptotic solution (dashed green); the first two terms in the asymptotic solution (dot-dashed green); and the first three terms in the asymptotic solution (dotted green).

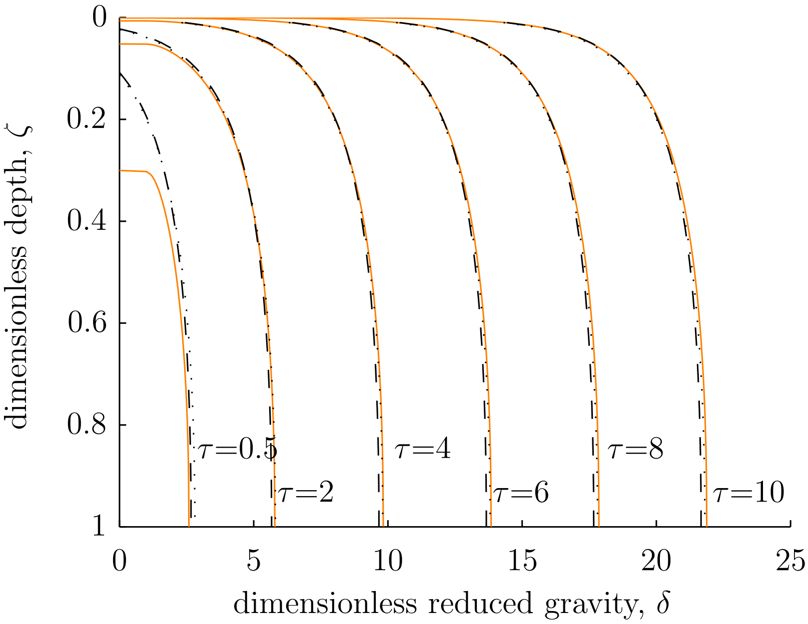

FIGURE 3.7: The ambient density profile at $\tau = 0.5, 2, 4, 6, 8$ and 10 from: the numerical scheme (solid orange); the asymptotic solution using the first term in q (black dashed); and the asymptotic solution using the first two terms in q (black dotted), almost indistinguishable from the dashed line.

3.3.5 Numerical results

The evolution of the ambient density profile in the constant width basin is shown in figure 3.8. The density of fluid deposited by the plume at the bottom of the basin continuously increases over the course of the filling process. This is because the average density of the ambient through which the gravity current falls increases with time. The current, which entrains fluid from this ambient, therefore gets denser over the course of the filling process. This means that the fluid at the bottom of the current is always the densest fluid in the system at that instant, and the fluid in the current is thus always transported to the bottom of the basin before upwelling in the ambient (Baines & Turner, 1969).

The density profile is discontinuous at the top of the ponded region, with δ jumping from 0 to 1. This discontinuity arises because the fluid first deposited by the gravity current into the ambient, thereafter remaining at the top of the ponded region, has a density of 1. The fluid initially in the ambient, thereafter remaining directly above the top of the ponded region, has a density of 0. Fluid with a density less than 1 is never deposited into the ambient. The density gradient, $\partial\delta/\partial\zeta$, within the ponded region increases as ζ decreases towards the top of the ponded region. This is because fluid is entrained from the ponded region into the plume, bringing the isopycnals closer together as the fluid is advected up the basin.

The evolution of the ambient density profile in the triangular basin is shown in figure 3.9. As in the constant width basin, fluid in the current is always transported to the bottom of the ambient before upwelling in the ambient. Again, like in the constant width basin, the density profile is discontinuous at the top of the ponded region because fluid deposited at first by the gravity current has a density of 1, whereas the fluid initially in the basin has a density of 0. Unlike the constant width basin, which has a discontinuous density gradient at the top of the ponded region, the density gradient in the triangular basin is continuous, asymptotically tending towards infinity at the top of the ponded region. This asymptotically infinite density gradient is caused because fluid entering the ambient at the bottom vertex of the basin enters at a finite volume flow rate into an infinitesimally narrow basin and thus rises at a velocity which rises at an asymptotically infinite velocity at the vertex. The density gradient near the top of the ponded region in the triangular basin is therefore larger than in the constant width basin. The

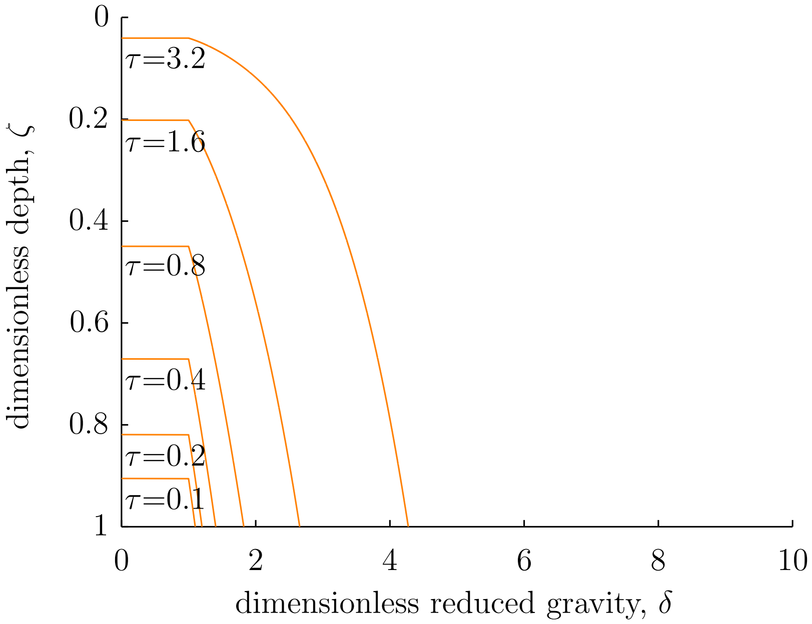

FIGURE 3.8: The time evolution of the ambient density profile in a basin of constant width.

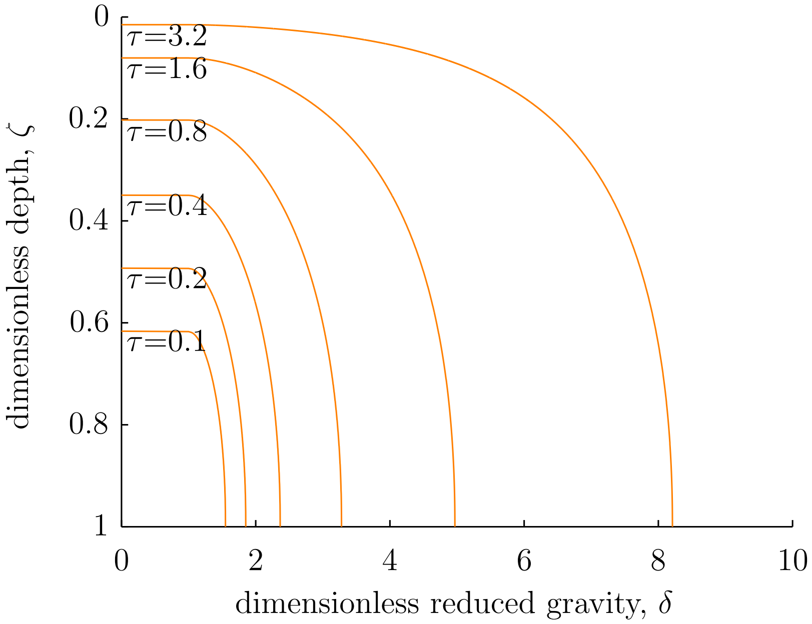

FIGURE 3.9: The time evolution of the ambient density profile in a basin of triangular section.

density gradient in the triangular basin is further increased by layers of fluid spreading horizontally as they rise up to the wider part of the triangular basin. By conservation of mass, the layers are squeezed together vertically, bringing the isopycnals closer together and increasing the density gradient as fluid advects upwards.

To gain a sense of scale for the filling process, we can consider examples with dimensional values typical for a laboratory experiment and for a lake. The triangular basin fills 2/3 of its depth at dimensionless time $\tau_{2/3} = \ln 3 - 2/3 = 0.432$. For scales typical of the laboratory tank in chapter 4 ($F_0 = 10^{-4}$ m^3 s^{-3}, $\theta = 8.6°$, $D = 0.2$ m and $E = 0.012$), the dimensional time is $t_{2/3} = 68$ s. For scales typical of a lake (given in section 2.6 as $F_0 = 7.35 \times 10^{-4}$ m^3 s^{-3}, $\theta = 1°$, $E = 5 \times 10^{-3}$ and $D = 250$ m), $t_{2/3} = 1.8$ days.

3.4 Peeling gravity current (case 3)

In the model considered in case 2, the gravity current is assumed to have a uniform density profile, with a single value of density at each depth in the basin, z. We now consider a model with less mixing, where fluid in the gravity current is linearly stratified rather than homogeneous. It will be shown that the assumption about the internal density profile in the current has important implications for the transport of fluid from the current and for the stratification which develops in the basin.

3.4.1 Efflux from a stratified gravity current beneath a stratified ambient

When a gravity current is idealised as having a uniform density profile, all the fluid in the current at a given z has the same depth of neutral buoyancy in the ambient stratification. It is more realistic to assume that gravity currents contain fluid ranging from the peak value in the current to the local density in the ambient, as shown schematically in figure 3.10. Typical time-averaged density and velocity profiles for currents along a smooth surface were observed by Ellison & Turner (1959) and their observations are shown in figure 3.11.

When a stratified gravity current falls through an ambient of uniform density,

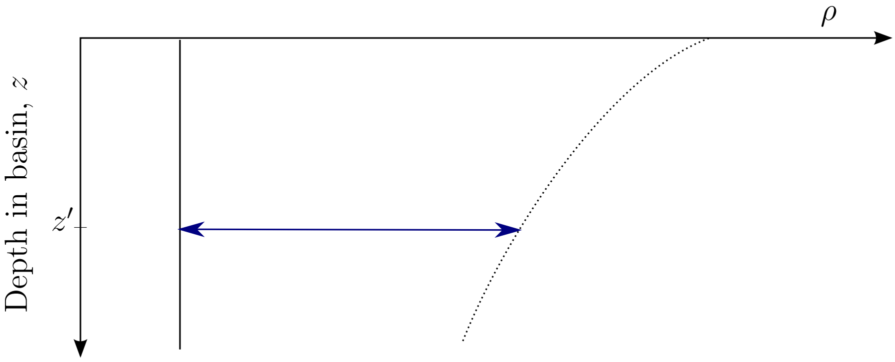

Figure 3.10: Schematic of the density of the ambient and gravity current across the depth of a basin. The solid line shows the uniform ambient density and the dotted curve shows the peak density in the gravity current. At any depth in the basin, z', a stratified current can contain fluid with density ranging between these curves, indicated by the blue arrow. In a uniform ambient, all fluid in the gravity current is denser than the ambient fluid. Gravity current fluid will therefore all fall to the bottom of the basin, whether the current has a uniform or stratified density profile.

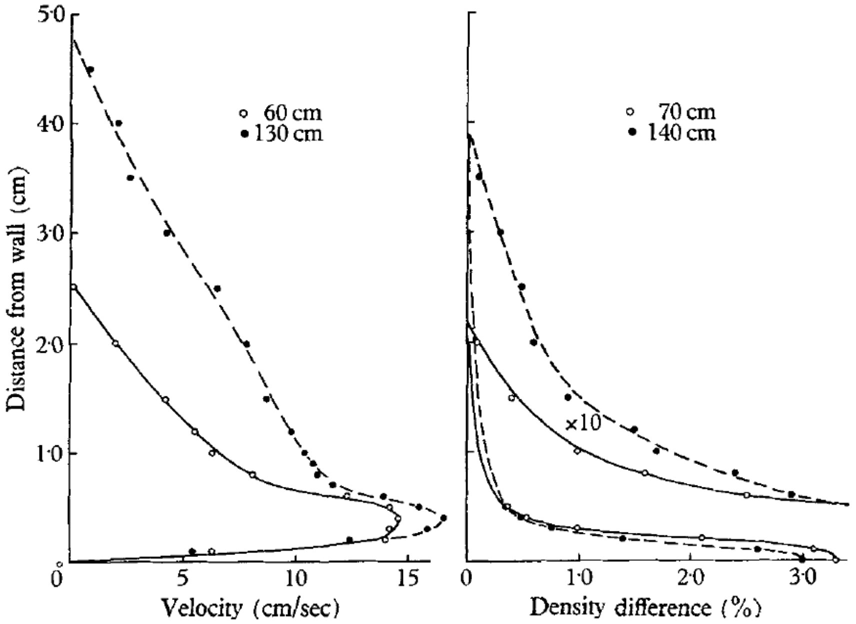

Figure 3.11: Typical time averaged profiles of (a) velocity and (b) density in a gravity current inclined at 14° beneath a uniform ambient measured by Ellison & Turner (1959).

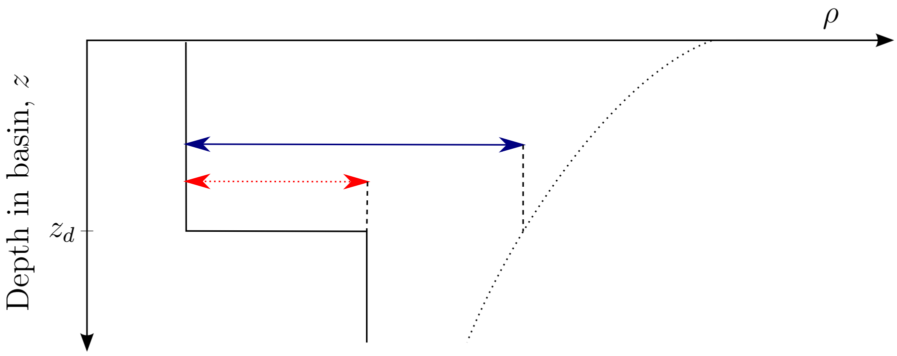

Figure 3.12: Schematic plot of density of the ambient and gravity current across the depth of a basin. The solid curve shows the two layer ambient density and the dotted curve shows the peak density in the gravity current. At the depth of the discontinuity in the ambient, z_d, a stratified current can contain fluid with densities spanned by the blue arrow. Fluid within the range of the dotted red arrow will be neutrally buoyant in the ambient at this depth.

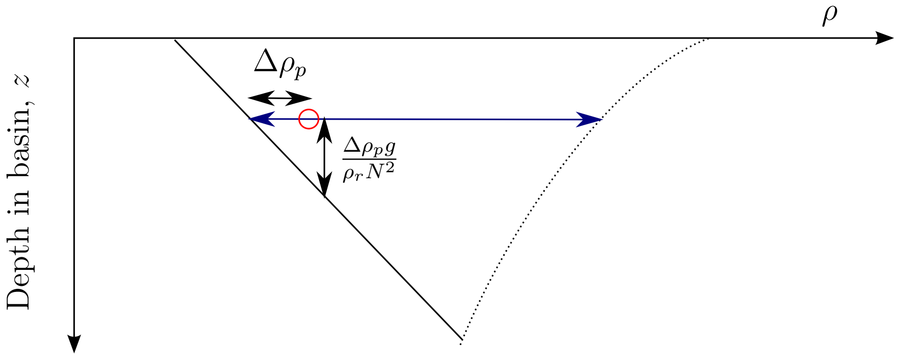

Figure 3.13: Schematic plot of density of the ambient and gravity current across the depth of a basin. The solid line shows the linearly stratified ambient density and the dotted curve shows the peak density in the gravity current. The vertical black arrow shows the depth to which a parcel of fluid in the current, with density and depth indicated by the red circle, must be displaced to become neutrally buoyant in the ambient.

as plotted in figure 3.10, the current behaves similarly to a gravity current with a uniform density profile. If a parcel of fluid from the ambient mixes with an infinitesimal amount of denser fluid from within the current, the parcel becomes denser than the ambient fluid and falls to the bottom of the ambient. The assumed profile within the current makes no difference to this general pattern of motion.

Now, compare the behaviour of a gravity current with a uniform density profile to that of a gravity current with a continuous, stratified density profile when they fall through a two layer ambient (shown in figure 3.12). Also, assume that the peak density in both gravity currents is higher than the density of the lower layer of the ambient, so that the currents penetrate into the lower layer and continue falling through it. A gravity current with a uniform density profile transports all of its fluid to the bottom of the lower layer, because all of the fluid in the current is denser than the lower layer of the ambient. In a gravity current that has a stratified density profile continuous with the surrounding ambient, the lightest portion of the current with density less than the lower layer, indicated by the red arrow in figure 3.12, is neutrally buoyant at the discontinuity depth, z_d. This fluid will peel away from the current to intrude into the ambient at z_d, as seen in the experiments of Wells & Wettlaufer (2007), and discussed by Monaghan (2007). Even when fluid from the lower layer mixes with the intrusion, the intrusion will remain neutrally buoyant at the top of the lower layer.

In an ambient with a continuous stratification, laboratory experiments have shown that fluid from an underflowing current can efflux fluid into the ambient across a range of intermediate depths, well above the average neutral buoyancy depth of the fluid in the gravity current (Baines, 2005). Experiments conducted in the present study also exhibited intermediate depth intrusions into the stratified part of an ambient, and these will be discussed in chapter 5. There are, in principle, at least two mechanisms by which these intermediate depth intrusions can occur. In the first mechanism, a parcel of fluid from the ambient engulfs a small amount of fluid from the density current, through Holmboe instability for example, and becomes fully mixed. This parcel can then have an arbitrarily small density anomaly, $\Delta\rho_p$, relative to the ambient at that depth. The density anomaly depends on the volume and density of the engulfed current fluid. If the parcel does not entrain any further fluid, it will be neutrally buoyant at a depth $\Delta\rho_p g/(\rho_r N^2)$ below its initial depth, indicated in figure 3.13. In this expression, N

is the buoyancy frequency of the ambient. If the parcel is advected by this depth, it can come to rest there, resulting in the efflux of the engulfed current fluid into the ambient. This mechanism was proposed by Baines (2005). In the second mechanism, the ambient becomes layered through the spontaneous sharpening of density interfaces. Intrusions into the ambient can then occur by the mechanism described above for the two layer ambient (Ivey *et al.*, 2008; Oglethorpe *et al.*, 2013).

The results of the filling box model in section 3.3 featured both discontinuities in the ambient density profile and a continuously stratified region, shown for example in figure 3.9. The uniform density profile assumed in the gravity current model excluded the possibility of intermediate depth efflux from the gravity current. To explore how the ambient stratification evolves when intermediate depth efflux occurs, we now consider a model that uses a stratified gravity current.

3.4.2 Description of the peeling model

To demonstrate the potential impact of a stratified profile within the current on the evolution of the ambient, we modified the model used in case 2. Both the model of the gravity current and the motion in the ponded region were modified.

The overall scheme of the model was as follows. When the density current was travelling beneath a uniform ambient, all fluid entrained into the current became denser than the uniform part of the ambient. All the fluid entrained into the stratified current thus fell through the uniform part of the ambient. The entrainment which occurred in the uniform ambient was modelled with the same entrainment law used in section 3.3. In departure from the case 2 model, the current was assumed to have a stratified density profile. When the current reached the part of the basin with a stratified ambient (i.e., the ponded region), the peeling mechanism became possible. An extreme assumption was made in the model about the motion in the stratified ponded region. All the fluid in the current was modelled as moving – without any further change in density – to its neutrally buoyant height within the ambient. The absence of mixing is clearly a lower bound on the amount of mixing in the ponded region. Within the ponded region, the motion was a purely kinematic process, equivalent to an adiabatic reordering of fluid in the ponded region to a stable stratification. This approximation is at least somewhat justified, because the gravity current has a

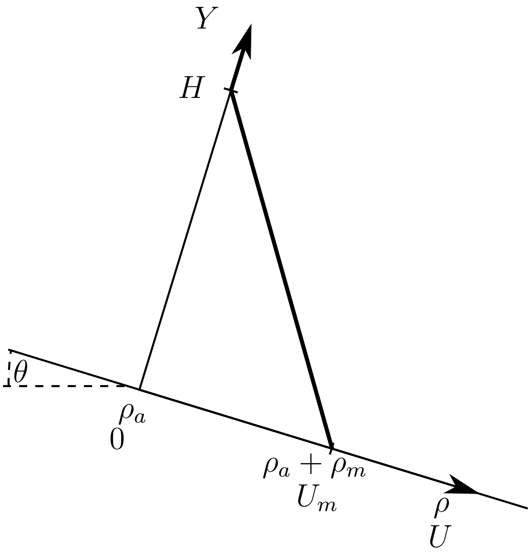

FIGURE 3.14: Density and velocity profile of the gravity current assumed in the case 3 model.

much reduced buoyancy flux in the ponded region and thus the driving force for shear is reduced.

The gravity current was assumed to have simple linear profiles of velocity and density, which are the first two terms of the Taylor series approximation to the actual profiles, rather than top hat profiles considered in case 2. These simple kinds of profiles have been used in other studies (Cooper & Hunt, 2010). To simplify the analysis, it was assumed that the density and velocity profiles have the same thickness. More terms in the series expansions and different thicknesses for the velocity and density profiles could be included in the analysis in a reasonably straightforward manner, but will not be considered here. The simple profiles used are sufficient, however, to demonstrate the impact of fluid peeling away from a stratified current. The profiles of velocity and density at a depth z in the basin are, respectively,

$$U = \begin{cases} U_m(H-Y)/H, & Y < H \\ 0, & Y > H \end{cases} \tag{3.24}$$

$$\rho = \begin{cases} \rho_a + \rho_m(H-Y)/H, & Y < H \\ 0, & Y > H \end{cases} \tag{3.25}$$

where U_m is the maximum velocity in the profile, H the thickness of the current,

Y the perpendicular distance from the boundary, ρ_a the density of the ambient at the depth z, and ρ_m the maximum density difference in the profile relative to the ambient. These profiles are plotted in figure 3.14. Based on these linear profiles, the fluxes in the gravity current of volume, momentum and buoyancy are, respectively,

$$Q = \int_0^H U \; \mathrm{d}Y = \frac{U_m H}{2} \tag{3.26}$$

$$M = \rho_r \int_0^H U^2 \; \mathrm{d}Y = \frac{\rho_r U_m^2 H}{3} \tag{3.27}$$

$$F = \int_0^H \frac{g}{\rho_r}(\rho - \rho_a) U \; \mathrm{d}Y = \frac{G'_m U_m H}{3}, \tag{3.28}$$

where $G'_m = g\rho_m/\rho_r$ is the maximum reduced gravity in the current relative to the local ambient. Redefining the dimensionless parameters in terms of the profile peak values as

$$f = \frac{1}{F_0}\frac{G'_m U_m H}{3}, \tag{3.29}$$

$$q = \left(\frac{16\sin^2\theta}{9F_0 E_{av}^2 D^3}\right)^{1/3} \frac{U_m H}{2}, \tag{3.30}$$

$$m = \left(\frac{2^2\sin\theta}{3F_0^2 E_{av} D^3}\right)^{1/3} \frac{U_m^2 H}{3}, \tag{3.31}$$

$$\delta = \left(\frac{9E_{av}^2 D^3}{16F_0^2\sin^2\theta}\right)^{1/3} G'_a, \tag{3.32}$$

$$\tau = \left(\frac{9F_0 E_{av}^2}{16A^3\sin^2\theta}\right)^{1/3} t, \tag{3.33}$$

where $G'_a = g(\rho_a - \rho_r)/\rho_r$, leads to the same system of dimensionless equations, (3.10) - (3.12), for the current in the uniform ambient and first front evolution equation, (3.17), as in case 2. Here we follow a convention that, for a gravity current with a non-uniform velocity profile, the entrainment coefficient, E_{av}, is the ratio of the entrainment velocity to the average velocity in the current, $U_m/2$.

As no mixing happens within the ponded region, the depth of an isopycnal with density δ_i in the ponded region can be derived by summing the volume of fluid which is delivered to this region with density exceeding δ_i. These depths give the stratification. To derive the evolving stratification, expressions for the following quantities are required. The peak density in the current, in dimensionless terms, is $\delta_m = 3f/(2q) = 3/(2\zeta)$. The depth in the gravity current profile to fluid with density δ_i is

$$y_i = h(1 - \delta_i/\delta_m), \tag{3.34}$$

where h is the dimensionless thickness of the current. For the system of equations (3.10) - (3.12), $h = \zeta$. The volume flow in the current of fluid with density greater than δ_i is

$$q_i(\delta_i, \zeta) = \int_0^{y_i} u \ \mathrm{d}y, \tag{3.35}$$

where $u = 2(1 - y/h)$. Fluid of density δ_i only starts to enter the ponded region once the ponded region has reached the height at which $\delta_m(\zeta) = \delta_i$. For fluid with $\delta_i < 3/2$, this occurs from $\tau = 0$. For fluid with $\delta_i > 3/2$, the fluid starts to pond when $\zeta_f = 3/(2\delta_i)$. Thus, using $\zeta_f(\tau)$ from the first front evolution equation, (3.17), the time at which fluid with density δ_i first reaches the ponded region is

$$\tau_i = \begin{cases} 0, & \delta_i < 3/2 \\ \ln(2\delta_i/3), & \delta_i > 3/2 \end{cases}. \tag{3.36}$$

Summing the volume of fluid which arrives to the ponded region with each density gives the depth of the isopycnals as

$$\begin{aligned} \zeta_i(\delta_i, \tau) &= 1 - \int_{\tau_i}^{\tau} q_i \ \mathrm{d}\tau & (3.37) \\ &= \begin{cases} 1 - \displaystyle\int_0^{\tau} 2 \int_0^{h(1-2\delta_i\zeta_f/3)} 1 - \frac{y}{h} \ \mathrm{d}y \ \mathrm{d}\tau, & \delta_i < 3/2 \\ 1 - \displaystyle\int_{\ln(2\delta_i/3)}^{\tau} 2 \int_0^{h(1-2\delta_i\zeta_f/3)} 1 - \frac{y}{h} \ \mathrm{d}y \ \mathrm{d}\tau, & \delta_i > 3/2 \end{cases} & (3.38) \\ &= \begin{cases} e^{-\tau} - \dfrac{4\delta_i^2 e^{-3\tau}}{27} + \dfrac{4\delta_i^2}{27}, & \delta_i < 3/2 \\ 1 + e^{-\tau} - \delta_i^{-1} - \dfrac{4\delta_i^2 e^{-3\tau}}{27}, & \delta_i > 3/2 \end{cases}. & (3.39) \end{aligned}$$

The ambient density profiles in the basin are plotted for five different times in figure 3.15.

When this approach is applied to a triangular basin, the quantities used to derive the stratification change as follows. The top of the ponded region, $\zeta_f(\tau)$, rises according to (3.18), replacing (3.17). The dimensionless time, previously (3.33), becomes

$$\tau = \left(\frac{9F_0E^2 \sin\theta \cos^3\theta}{16D^3} \right)^{1/3} t. \tag{3.40}$$

The time at which fluid with density δ_i first reaches the ponded region is

$$\tau_i = \begin{cases} 0, & \delta < 3/2 \\ 3/(2\delta_i) + \ln(2\delta_i/3) - 1, & \delta > 3/2 \end{cases}. \tag{3.41}$$

The fluid accumulated in the ponded region of the basin is now in a triangular geometry with dimensionless volume $(1-\zeta)^2/2$. The depth of the isopycnals in the triangular basin is

$$\zeta_i(\delta_i, \tau) = 1 - \sqrt{2 \int_{\tau_i}^{\tau} q_i \, \mathrm{d}\tau} \tag{3.42}$$

$$= \begin{cases} 1 - \sqrt{2 \int_0^{\tau} 2 \int_0^{h(1-2\delta_i\zeta_f/3)} 1 - \frac{y}{h} \, \mathrm{d}y \, \mathrm{d}\tau}, & \delta_i < 3/2 \\ 1 - \sqrt{2 \int_{\frac{3}{2\delta_i} - \ln(\frac{3}{2\delta_i}) - 1}^{\tau} 2 \int_0^{h(1-2\delta_i\zeta_f/3)} 1 - \frac{y}{h} \, \mathrm{d}y \, \mathrm{d}\tau}, & \delta_i > 3/2 \end{cases} \tag{3.43}$$

$$= \begin{cases} 1 - \left\{ \left[\mathcal{W}\left(-e^{-\tau-1}\right) + 1\right]^2 - \frac{2}{27}\delta_i^2 \left[3\mathcal{W}\left((-e^{-\tau-1})^4\right) + \right.\right. \\ \qquad \left.\left. 4\mathcal{W}\left((-e^{-\tau-1})^3\right) + 1\right] \right\}^{1/2}, \delta_i < 3/2 \\ 1 - \left\{ \frac{2}{27}\delta_i^2 \left[3C^4 + 4C^3 - 3\mathcal{W}\left((-e^{\tau-1})^4\right) - 4\mathcal{W}\left((-e^{\tau-1})^3\right)\right] \right. \\ \qquad \left. - C^2 - 2C + \mathcal{W}\left((-e^{\tau-1})^2\right) + 2\mathcal{W}\left(-e^{\tau-1}\right) \right\}^{1/2}, \delta_i > 3/2 \end{cases} . \tag{3.44}$$

where $C = \mathcal{W}\left(\frac{-3e^{\frac{-3}{2\delta_i}}}{2\delta_i}\right)$. The ambient density profiles in the basin are plotted for five different times in figure 3.16.

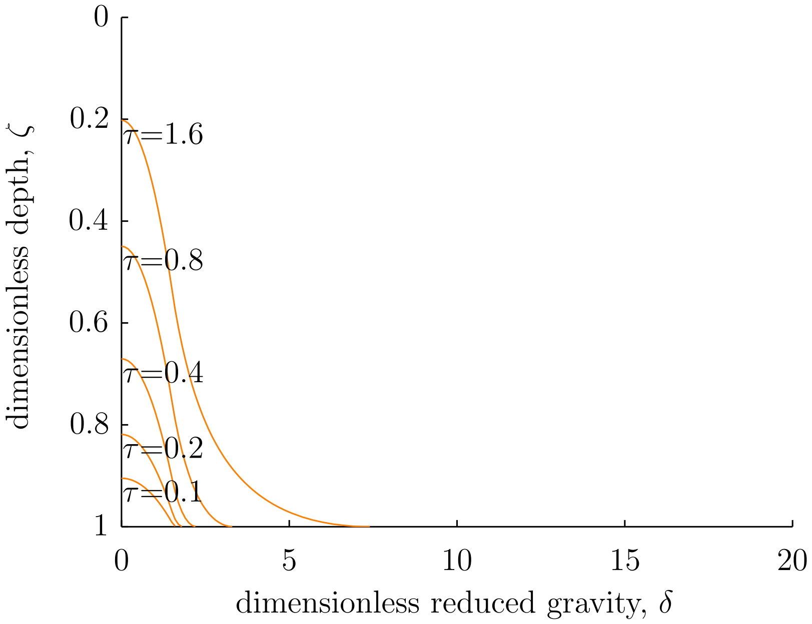

FIGURE 3.15: The time evolution, according to the peeling model, of the ambient density profile in a basin of constant width.

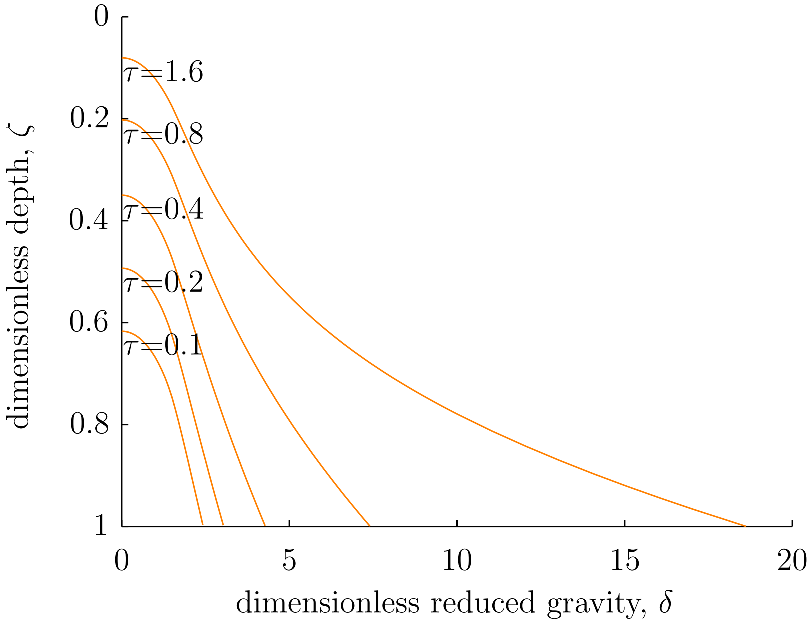

FIGURE 3.16: The time evolution, according to the peeling model, of the ambient density profile in a triangular basin.

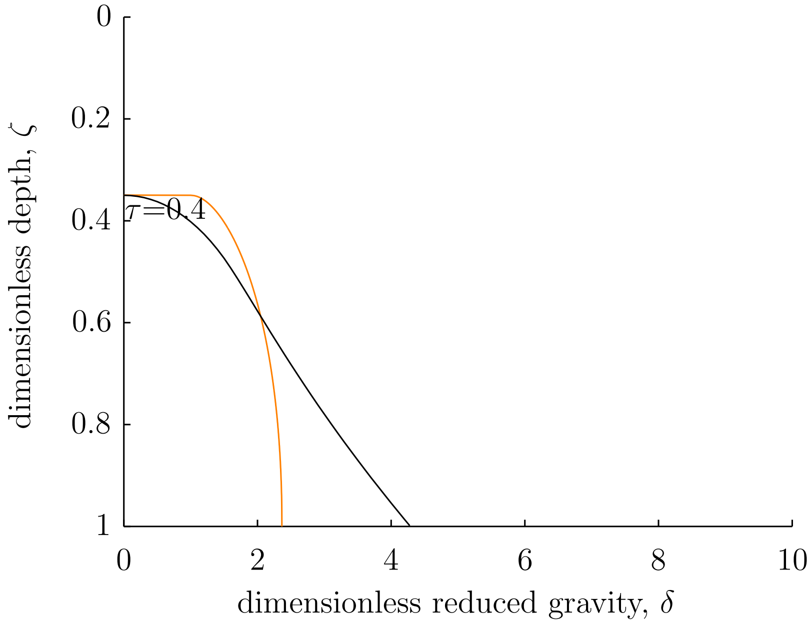

FIGURE 3.17: Comparison of the stratification in a triangular basin generated by a model of a persistently entraining gravity current (orange) and by a model of a peeling gravity current (black).

3.4.3 Numerical results for a peeling gravity current model

The density profile calculated by the case 2 and case 3 models are plotted at a series of times separately in figures 3.15 and 3.16 and, for easier visual comparison, at $\tau = 0.4$ on the same axis in figure 3.17. The density profiles at the top of the ponded region are continuous throughout the duration of the filling process, unlike the profiles in the case 2 model. The continuous ambient profile occurs because there is no discontinuity with the surrounding ambient fluid in the density profile of the gravity current, unlike the top hat gravity current profiles in case 2. The lightest fluid in the current peels away from the current and is adiabatically arranged at top of the ponded region, making the ambient density profile continuous. This is in contrast to case 2, in which the uniform density profile of the current is not continuous with the neighbouring ambient fluid.

The rise of the first front with respect to time has the same functional form as in case 2. This is expected because above the ponded region, the integrated fluxes are subject to the same dimensionless governing equations. For the time scale in the two cases to be the same, the entrainment coefficients – which are defined in different ways for currents with either uniform or linear velocity profiles – must be redefined to give the same entrained volume flux. The current with a uniform density, described by (3.4) - (3.6), has the volume conservation equation

$$\begin{aligned} \frac{d(Q_u)}{dx} &= Eu && (3.45) \\ &= EM_u/Q_u, && (3.46) \end{aligned}$$

where M_u is the momentum flux and Q_u the volume flux of the uniform profile current; the linear profile gravity current, described by (3.24), has the volume conservation equation

$$\frac{dQ}{dx} = \frac{3E_{av}M}{4Q}. \tag{3.47}$$

The equivalent entrainment coefficient, defined as $E_{eq} = 3E_{av}/4$, shall be used in the peeling model to make the current with the linear profile entrain the same volume in the uniform ambient as the current with the uniform profile.

The density range of the ponded fluid in the peeling model is larger than the range in the persistently entraining model, because the amount of mixing within the gravity current is lower in the peeling model. In the peeling model, entrained fluid is not fully homogenised within the gravity current, but remains stratified. Furthermore, no mixing occurs in the ponded region of the peeling gravity current model, unlike in the persistently entraining gravity current.

3.5 Limits on the validity of the models with gravity currents

There are a number of limitations on when the gravity current models of the filling of a basin are representative of a real inflow to a lake basin. These apply to both cases 2 and 3.

The gravity current model has a source of pure buoyancy, with an infinitesimally small volume flux at the source. In reality, a river flowing into a lake is a source of both buoyancy and volume flux. This difference in the nature of the source driving the system may be accounted for by the use of a virtual origin correction (Hunt & Kaye, 2001). The coordinate system is set such that the buoyancy source is located at the virtual origin, $\zeta = 0$. The actual source, which has a volume flux, is offset by a depth ζ_v below the virtual origin. The offset is set so that currents from either the pure buoyancy source at the virtual origin or the volume and buoyancy source at the actual origin develop identically in the domain below ζ_v. With this correction applied, the response of a basin to a virtual source in the model is the same as the response to an actual source supplying the same buoyancy in a lake, but only until the ponded region reaches the depth of the actual source, ζ_v. In the model the source buoyancy flux is constant. At large times, the density in the basin increases without limit, as discussed in section 3.3.4. In a lake, an inflow does not supply a constant buoyancy flux, but can be approximated as supplying fluid at constant density. At large times, the density in the basin approaches the source density and the buoyancy flux of the inflow decreases towards 0. This behaviour is somewhat similar to the full mixing model considered in case 1 (section 3.1). The models with gravity currents are therefore only valid for times before the ponded region has reached the depth of the actual source, ζ_v. In the constant width basin this occurs at $\tau = -\ln \zeta_v$; in the triangular basin this occurs at $\tau = \zeta_v - \ln \zeta_v - 1$.

The system of equations (3.10) - (3.12) and (3.15) do not describe the physical system well near the bottom vertex of the triangular basin. When the head of the gravity current reaches the end wall, it is suddenly decelerated. This crashing of the current causes additional mixing as kinetic energy is dissipated, as will be discussed in section 4.1.4. The qualitative effect of this additional mixing is to average the density of the ambient fluid over a small region close to the bottom vertex before the fluid upwells. The proportion of the basin volume which is near to the bottom vertex is small, because the width there reduces to 0. We will therefore look at models which leave out the additional mixing processes that occur at the vertex. Whilst these mixing processes could be parameterised in some way, for the purposes of the current discussion, a model with fewer parameters is desirable.

A further limitation of the model description of the ambient stratification is that the volume filled by the gravity current is not accounted for in the model. In reality, the gravity current is contained within a finite volume along the sloping boundary. Within the thickness of the gravity current from the lower boundary, the density will not be that of the ambient fluid but that of the gravity current. This volume is not represented in the model. The thickness of the gravity current is small relative to the basin depth, so a reasonable approximation can be made by neglecting it.

A limitation specific to the peeling model is that turbulent mixing in the ponded region is neglected in the model. The mixing that occurs here in reality will reduce the density gradient in the ponded region. The densest fluid entering the ponded region has furthest to descend to its neutral buoyancy height at the bottom of the ponded region. This fluid will thus have its density reduced most by the neglected mixing.

In chapter 5, results of laboratory experiments in a basin fed by a gravity current will be discussed in detail. The limitation of these models will be discussed further in light of the observations. Extensions to the peeling model will be suggested in chapter 6.

3.6 Generalised basins with power law shapes

The two basin geometries discussed in this chapter are special cases of a more general basin shape described by a power law, where

$$A = \frac{D}{\sin\theta\cos\theta}\left(1 - \frac{z}{D}\right)^{a}, \tag{3.48}$$

is the width of the basin and a is the basin shape parameter. Power law functions have been used in previous literature to make approximations to lake basin geometries (Håkanson, 1977; Hayashi & van der Kamp, 2000). The triangular case is described by the special case $a = 1$, and the constant width case is the limit as $a \to 0$. For the general basin shape, (3.13) generalises to become

$$\frac{\partial\delta}{\partial\tau} = \frac{q}{(1-\zeta)^{a}}\frac{\partial\delta}{\partial\zeta}. \tag{3.49}$$

Considering a gravity current that falls along a slope of constant inclination, the system of conservation equations for the gravity current, (3.10) - (3.12), remains unchanged. In the general basin shape, the evolution equation for the first front of the ponded region is

$$\tau = \frac{-(1-\zeta_f)^{a}}{(\zeta_f - 1)^{a}} B_{1/2}(-a, a+1), \tag{3.50}$$

where $B_{c1}(c_2, c_3)$ is the incomplete beta function. This expression was derived using the computer algebra system Mathematica™. For $a = n$ and $a = 1/n$ where $n \in \mathbb{N}$, (3.50) simplifies to summations of logarithms, polynomials and trigonometric functions. For example, by integrating (3.49) in the case of $a = 1/2$, we derive that

$$\tau = 2\left[\tanh^{-1}(\sqrt{1-\zeta_f}) - \sqrt{1-\zeta_f}\right]. \tag{3.51}$$

To express the large time asymptotic solution for the density profile, δ, found from the power series for q truncated after two terms in analytical form requires Gauss hypergeometric functions. This is the general expression for (3.23) in the triangular case. The expressions for the behaviour of the generalised cases can be complicated functions, which are difficult to interpret. They are useful, however, as they give closed form solutions which can be manipulated algebraically and can be used to validate numerical models.

3.7 Comparison of different basin mixing models

In this chapter, we have discussed four different models of the mixing which occurs in a basin fed by dense fluid from a gravity current. The models progressively ranged from case 1, in which inflow fluid mixed completely with fluid in the basin, to case 4, in which inflow fluid did not mix at all with the fluid in the basin.

The average density of the basin fluid reaches the source density fastest, in time V/Q_s, when there is no mixing and the ambient fluid is gradually displaced by undiluted source fluid which ponds at the bottom of the basin, case 4. The average density of the basin fluid takes the longest time to reach the source density when the fluid in the basin is fully mixed, case 1. The density in the basin asymptotically approaches the source density with an e-folding time of V/Q_s. In cases 2 and 3, the models are only valid until the first front reaches the height of the physical source beneath the virtual origin. At this time no fluid in the basin has a density as great as the physical source.

Two partial mixing cases were considered: case 2, where the gravity current has a uniform density profile and fluid is persistently entrained until the gravity current has reached the bottom of the basin; and case 3 where the gravity current has a linear density profile and fluid peels away in the stratified part of the ambient to its neutral buoyancy depth. In case 2, a front, at which the density is discontinuous, rises to the source height. In case 3, a front, at which the density is continuous, rises to the source in exactly the same time as case 2. The reduced mixing in case 3 means that the fluid in the ponded region spans a larger range of densities. For example, at $\tau = 0.4$, the peak density in the peeling gravity current model is approximately 1.8 times larger than the peak density of the persistently entraining model. The stratification of the gravity current in case 3 is required to allow efflux from the gravity current to occur at intermediate depths within the stratified part of the ambient.

Having considered the implications of the different assumptions made in these models, we turn, in the following two chapters, to a series of laboratory experiments. By visualising the flow and measuring the stratification in basins being filled by fluid from a gravity current, we will see when these different assumptions are valid. In particular, we will assess whether efflux from the gravity current into a stratified ambient is important in the evolution of the basin stratification.

CHAPTER 4

LABORATORY APPARATUS AND TECHNIQUES

This chapter will describe the apparatus and techniques used to observe the stratification in basins fed by gravity currents under controlled, laboratory conditions. We justify the choice of basin geometry, describe the design developed to minimise unwanted effects in the apparatus and, to finish, discuss the signal processing developed to measure the quantities of interest. This information will allow other investigators to reproduce these experiments and avoid the problems which were encountered during this investigation. The scientific results from these experiments will be discussed later in chapter 5.

4.1 Design of apparatus

Broadly speaking, the experiments incorporated the methods used by Fernandez & Imberger (2008), Baines (2001) and Wells & Wettlaufer (2007). Salt water was delivered to an inclined, perspex tank containing lighter, salt-free water. The evolving density profile in the basin was measured using a conductivity probe which repeatedly descended on a traverse through the water column. The dense inflow fluid was, in some instances, dyed with either food colouring, milk or methyl blue so that the dense fluid could be observed visually. In this section, the specific design of the components of the apparatus will be discussed. A photograph of the apparatus is shown in figure 4.1 and a schematic in figure 4.2. Throughout the design of the experiment, measures were taken to minimise sources of mixing other than of the entrainment into the continuous-flux, quasi-steady gravity current.

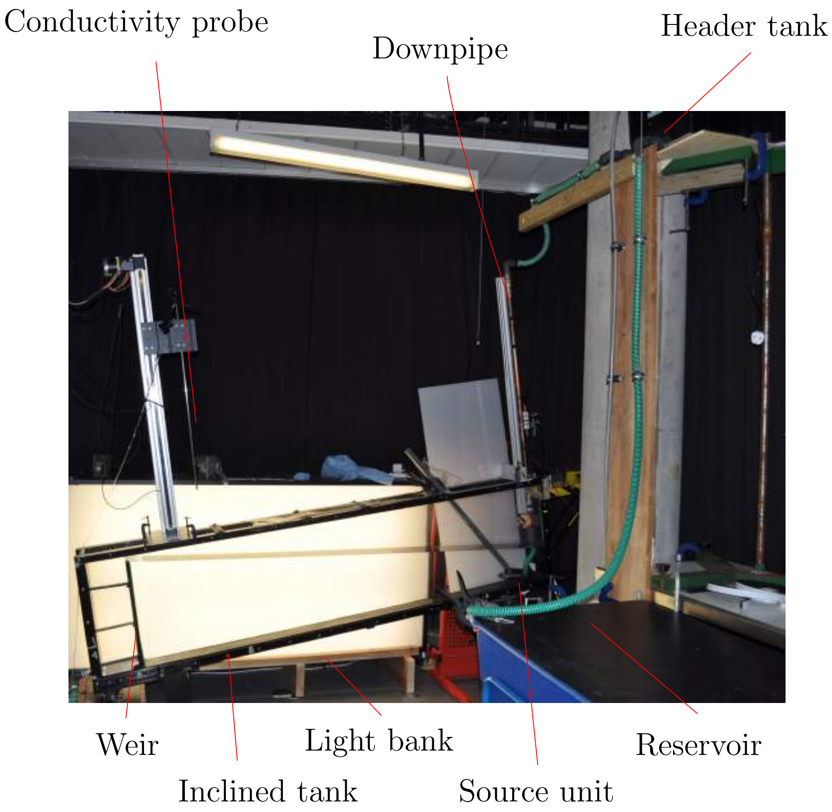

FIGURE 4.1: Photograph of experimental apparatus.

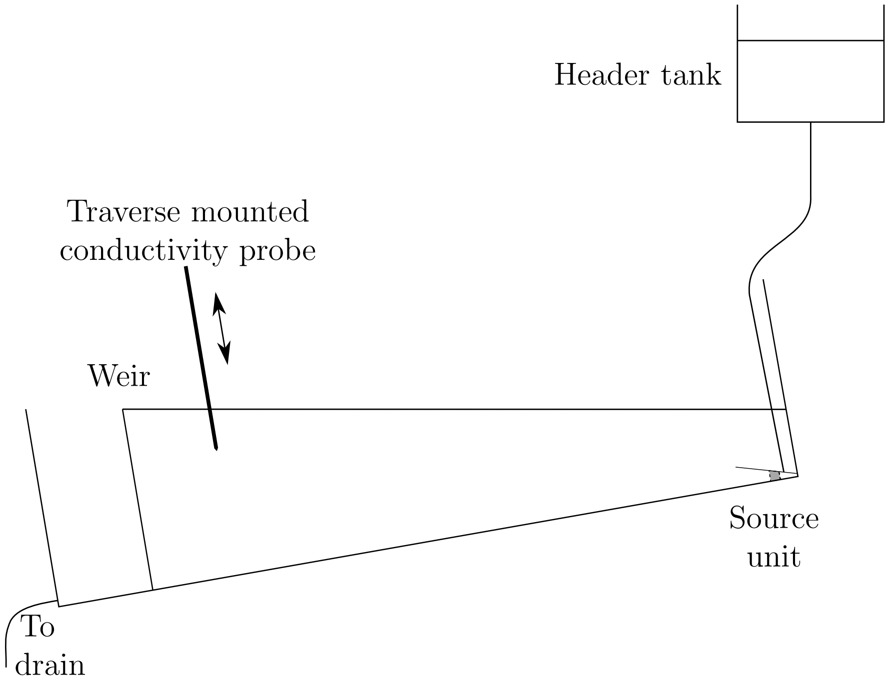

FIGURE 4.2: Schematic diagram of experimental apparatus.

4.1.1 The basin

The theoretical basin geometry chosen for comparison with experiments was the triangular geometry, drawn in figure 3.1(b) and discussed in the previous chapter. This basin shape is typical of a lake or reservoir (Håkanson, 1977). The geometry was attractive because it was easily constructed by tilting a cuboid tank about its lower corner, as shown in figure 4.2. Further, this 2D basin geometry can be described with two parameters alone: the bottom slope and the height of the source above the bottom of the tank. A basin of constant horizontal cross-sectional area at all depths has a third dimensionless parameter to describe the horizontal cross-sectional area, which was avoided in the triangular basin. The disadvantage of a triangular basin is that the solutions of the filling box model are based on product-log functions rather than exponential functions, making the data processing and analysis more cumbersome.

The tank used for the working section of the experiment was 15 cm in width, 50 cm in height and 235 cm in length. The angle of inclination, set to 8.6° throughout these experiments, was measured with a digital inclinometer at three points along the base. These measurements showed the tank to have a constant inclination to within 0.1°. The width was judged large enough to ensure that the turbulence at the gravity current interface, which had an integral length scale of $\sim$1 cm, was fully three dimensional and would not be constrained by the width of the tank. The tank width was also large enough that frictional effects of the perspex walls would be negligible relative to friction at the base. The width was small enough to keep the volume of water manageable with the available pumps and reservoir tanks. A long tank was used so that the volume entrained by the gravity current was increased relative to that from other mixing processes.

4.1.2 Supply of dense fluid

A large reservoir of dense fluid was prepared in advance of each set of experimental runs. When the dye concentration in the inflow fluid needed to be controlled, the dye was mixed with this reservoir prior to the experiment. Water was pumped to recirculate through a constant-level header tank 1.5 m above the working section tank. A pump with a metal casing and impeller capable of a large flow rate of 0.5 $\mathrm{l\ s^{-1}}$ was found to heat the water at approximately 200 W, which would have had a significant influence on the density of the inflowing water. By using a P-16 Charles Austin pump, which had a plastic casing and impeller and a lower, variable flow rate, the heat supplied to the water was reduced to a negligible level, around 15 W.

The header tank, shown in figure 4.3, provided a pressure head adequate to deliver a large enough flow of water, whilst not varying by more than 1%. Direct pumping into the working section was found to give too variable a flow rate. The piping from the header tank to the manifold was restrained to prevent movement, ensuring that variations in the pressure drop between the header tank and the source manifold were insignificant. The maximum source flow rate was sized to ensure that the source Reynolds number was large enough to produce a turbulent gravity current. The source Reynolds number is defined as $Re_s = Q_s/\nu$, where Q_s is the volume flow rate per unit width supplied at the source and ν is the kinematic viscosity, and gives a measure of the relative importance of inertial and viscous forces. In preliminary experiments, very little entrainment occurred because the small flow rate produced a current which was significantly damped by viscosity. In the experiments reported in chapter 5, higher flow rates were also used, with Re_s varied between 110 and 1500.

Two valves were built into the down pipe: a ball valve to allow the flow to be

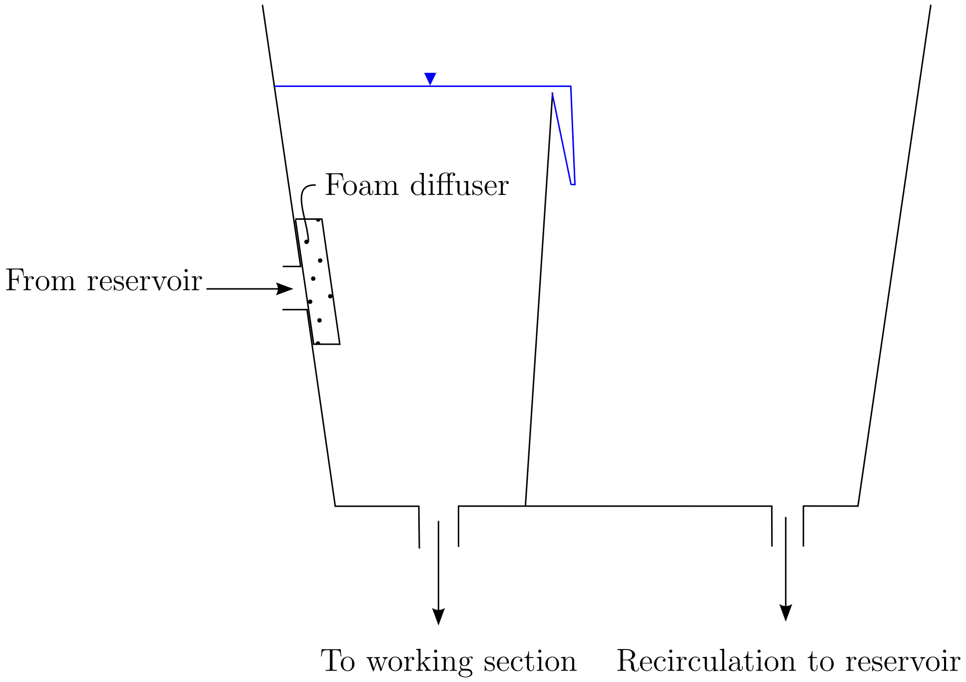

FIGURE 4.3: Schematic of recirculating header tank. Water overflows the weir, maintaining a constant pressure supply to the working section.

switched on rapidly, and a gate valve to allow the flow rate to be set at different values between runs. A needle valve would have delivered greater accuracy and repeatability in setting the flow rate and would have been preferable, but was unavailable. A diaphragm valve was used in preliminary experiments. The diaphragm was found to gradually relax over the course of 10 minutes after being opened, leading to an unacceptable 20% variation in source flow.

Source unit

Delivering dense fluid as a gravity current evenly across the width of the tank without elevating the mixing of ambient fluid in the neighbourhood of the source unit has been found to be challenging by many researchers (Cenedese & Adduce, 2008; Baines, 2001). This may be a reason why continuous flux gravity currents have received little research attention relative to finite volume gravity currents. A major problem is that the thickness of a gravity current flowing down a slope is set by the flow rate, reduced gravity of the current and the angle of the slope. This quasi-steady state of flow is the normal Richardson number condition for the slope (Ellison & Turner, 1959). If the source unit delivers fluid at a different thickness to that set freely by the current, this introduces an additional length scale to the system, potentially changing the behaviour of the system. In practice, it was found that if the height of the outlet was too large, the lighter, ambient fluid flowed above the gravity current in the opposite direction into the manifold. The back flowing ambient fluid was mixed into the source fluid in the energetic circulation within the manifold, changing the density and volume supplied by the source unit to the working section. If the height of the outlet was too small, the source fluid was delivered to the slope with too much kinetic energy, which was then turbulently dissipated. This could lead to substantially elevated mixing at the source, potentially in the form of a hydraulic jump.

To allow the gravity current to adopt its normal Richardson number thickness with minimal excess mixing at the source, an angled plate was used at the source to form an expanding region. The inlet design is shown in figure 4.4. The inflow was able to separate from the upper plate at the natural thickness for the current. We believe this configuration is novel, although the circular bottomed weir described by Baines (2001) may reduce mixing at the source because it has a similar expanding region. This transition from a one layer to a two layer flow is the same configuration as the 2D plunge point described in section 2.1.1. Little mixing occurs at such a transition, entraining a volume flux of around 6% of the source volume flow rate (Britter & Simpson, 1978), with other researchers (Elder & Wunderlich, 1972) reporting even lower values. The flow from the source unit was visualised with dye, shown in figure 4.5, demonstrating that no heightened mixing was apparent in the vicinity of the source.

A strip of foam, approximately 2 cm by 2 cm by 20 cm, was placed at the thin end of the expanding section of the manifold, just downstream of the downpipe. The foam prevented pressure variations due to the vigorous circulating, turbulent motions at the mouth of the downpipe from causing uneven delivery of source fluid across the width of the working section. The evenness of the flow across the width of the tank was verified by viewing the dyed current from above, as shown by the photograph in figure 4.6.

We believe that this method of fluid delivery has advantages over some of the methods used by other researchers. Others (Wettlaufer, J. private communication) delivered the fluid from a depression spanning the width of the slope, allowing the source fluid to brim over a weir with the thickness selected by the

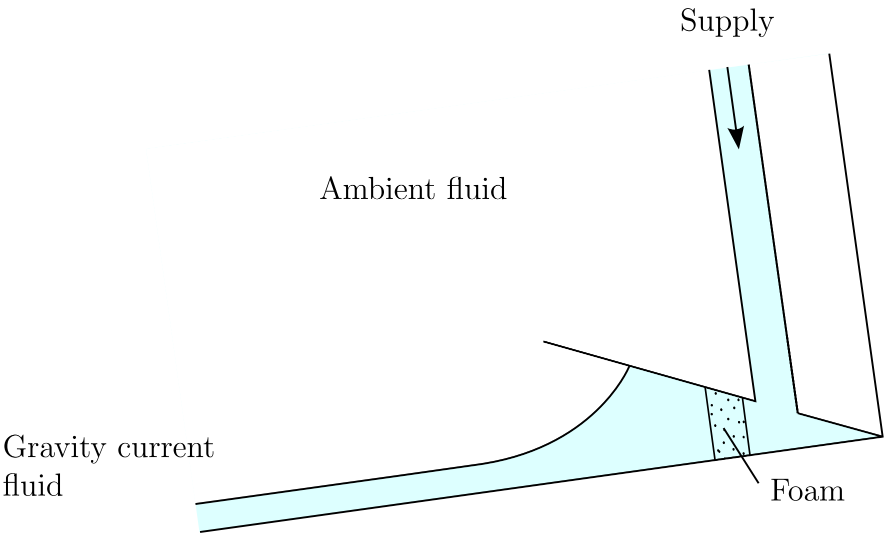

Figure 4.4: A schematic of the angled plate design for the source unit. The source fluid is coloured blue.

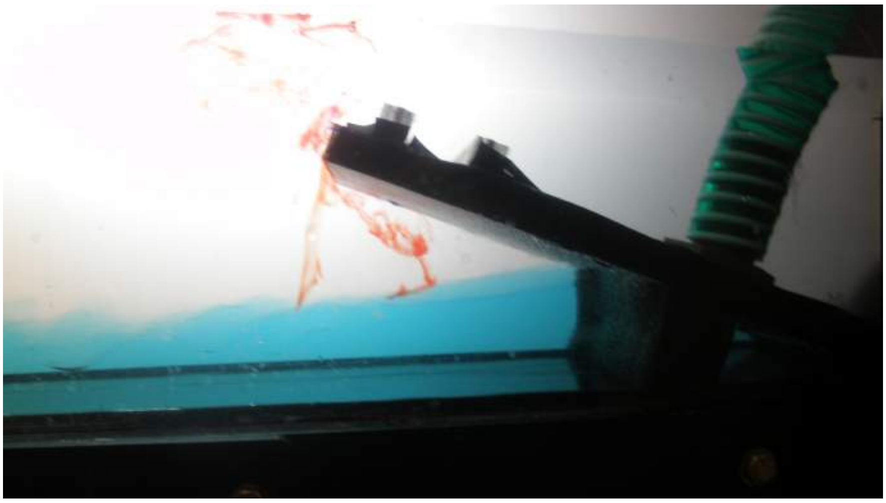

Figure 4.5: Photograph of red dye pipetted into the ambient fluid at the upper, downstream edge of the source unit. There is relatively little shear or turbulence in the ambient fluid above the gravity current. Strong shear and dilution is visible at the turbulent interface of the current. The deformation of the fluid filament observed above the source unit was caused by removing the pipette.

Figure 4.6: Photograph of the front of the gravity current, dyed red, from above as it flows along the base of the tank from left to right. The flow is evenly distributed across the width of the tank. The lobe and cleft structure can be seen at the head at a scale of approximately 1 – 4 cm. A thin layer retarded by wall friction can also be seen.

system, or (Wåhlin *et al.*, 2008) used a constant depth outflow unit containing flow straighteners. It would be interesting in future work to make a careful comparison of the mixing generated by different source units so that delivery of gravity currents in the laboratory could be improved and so that the transition to developed flow in gravity currents could be better understood.

To prime the source before each experiment, the ball valve was closed and the pipe work was filled with source fluid from the reservoir. The tank working section and manifold were filled with ambient fluid until the weir brimmed full. Bubbles were removed from the manifold with a syringe. The experiment was then initiated by opening the ball valve. Time in the experiments was measured from $t = 0$ at the instant that the gravity current released by the source first met the end wall.

4.1.3 Measuring the source flow rate

The source flow was measured by collecting the water overflowing the weir into the part of the tank behind the weir. Because this volume had a uniform cross-sectional area at all heights, the volume flow rate could be measured from the rate of rise of the free surface. A valve at the end of the tank was opened to periodically drain this section and then reseal it. This method gave a flow rate measurement with an accuracy of better than 1.5% and a variability between repeat measurements typically of 0.5%.

An alternative measurement approach was trialled with an Omega FDT-21 transit-time acoustic flow meter installed on the copper downpipe. These measurements were less accurate and reliable than the measurements derived from the rise of the free surface.

4.1.4 End wall and weir

The end wall of the working section, formed by the weir at the bottom of the slope, was designed to minimise two sources of unwanted mixing: the mixing at the head of the gravity current which initially ran down the slope, and the mixing caused by the collision of the head against the weir at the bottom of the slope. Both these mixing processes combine to form mixed fluid at the beginning of the filling process. These unwanted mixing processes add uncertainty, reducing the ability of the apparatus to focus on the measurement of interest in this study – the turbulent entrainment into the continuous-flux, quasi-steady gravity current considered in the case 2 and 3 models in chapter 3. The mixing in the head and in the crashing against the boundary can occur in lakes, but as they complicate the present study we wish to minimise them in the experiment.

The mixing at the head of the gravity current is very different from the quasi-steady gravity current far behind it. There is much more entrainment into the head than into the steady gravity current behind it. The majority of mixing at the head of the gravity current is done by eddies generated at the leading front of the current which are then left behind in the wake of the head. The fluid at the very front of the gravity current is not stably stratified, and therefore mixing occurs there much more readily than in the continuous-flux, quasi-steady gravity current far behind the head. The photograph in figure 4.7 of the head of a turbulent gravity current, visualised with diluted milk, shows the eddy structures formed at the head. Methods to exclude the fluid in the gravity current head from the experiments were explored, so that a larger proportion of the mixed fluid in the experiment would be generated in the continuous-flux, quasi-steady gravity current, the focus of this investigation.

Descending partition to separate the head from the filling basin

In an attempt to exclude the mixed fluid in the head, a vertically sliding partition 20 cm from the end of the tank was trialled. The partition was pushed downwards by hand after the head of the gravity current had passed, as shown in the schematic in figure 4.8, to isolate the head of the gravity current away from the filling basin. The behaviour of the gravity current at the end wall with and without the descending partition was observed with photometry methods, using routines in the DigiFlow software package (Dalziel, 2008). These two cases were compared to determine which apparatus caused less mixing. The false colour image in figure 4.9(a), taken from the series of images, shows the mixed fluid generated by the head after it had crashed against the end wall in the absence of a descending partition and figure 4.9(b) shows the mixed fluid generated after the partition was brought down. A vortex formed by the motion of the descending partition generated a substantial volume of mixed fluid. Comparing the volume generated in these two cases is difficult because the start times at which mixed fluid begins to accumulate are not directly comparable. Judging from the approximate comparison that was possible, the two methods generated similar amounts

FIGURE 4.7: Photograph of the head of a turbulent gravity current as it flows from right to left.

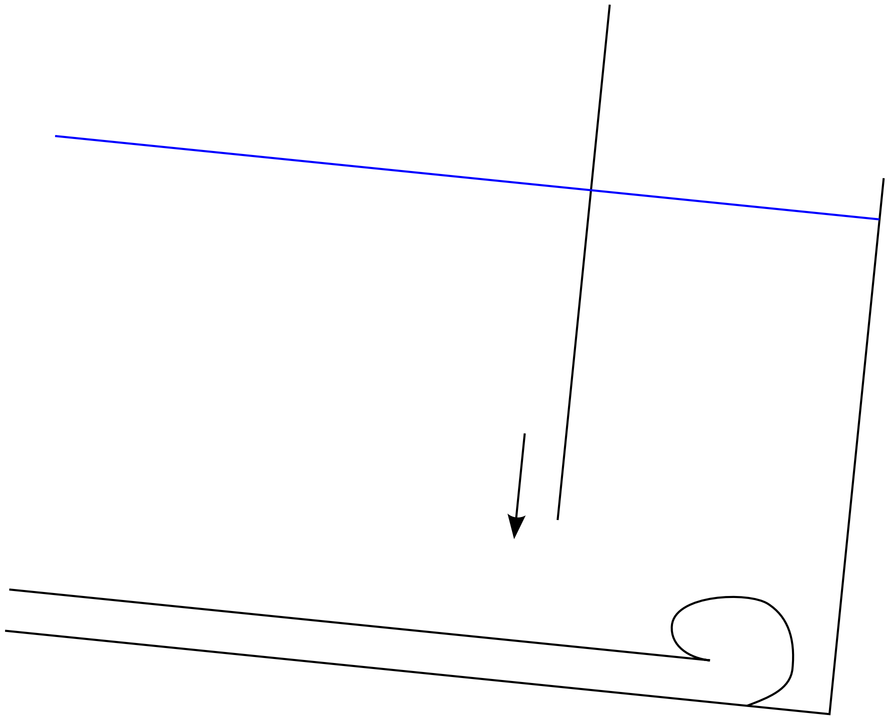

FIGURE 4.8: Schematic of descending partition used to isolate the head of the gravity current away from the filling basin.

of mixed fluid. To bring the partition down in a repeatable manner between different experimental runs was impractical, leading us to use the simple method of allowing the gravity current to crash with the back wall and overturn. The head of the gravity current only generates mixing for a short time in the experiment, so it is reasonable to assume that the volume entrained is insignificant compared to the volume entrained into the continuous-flux, quasi-steady gravity current over the full duration of the experiment.

Modifications to reduce mixing from crashing against the end wall

Methods of reducing the amount of mixing generated in the crashing and subsequent overturning of the gravity current as it collided with the end wall were examined. Some previous authors have discussed the overturning which occurs when a gravity current travelling along a horizontal surface collides with a vertical wall. Rottman *et al.* (1985) observed in experiments that a gravity current travelling along a horizontal surface would rise to twice the height of the current

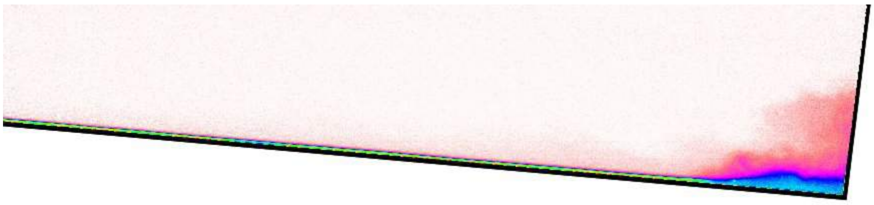

(a) – Gravity current as it crashes against the end wall.

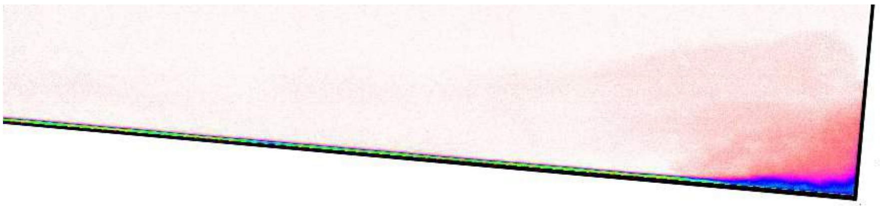

(b) – Gravity current after the partition was pushed down to form the end wall and cut off the head of the gravity current.

FIGURE 4.9: False colour images of preliminary experiments comparing the amount of mixed fluid generated at the end wall. The frames are at the time when the current interacting with the back wall had first reached its maximum height. The attenuation of light by the dyed gravity current fluid is shown in the false colour scale.

when it collided with a vertical wall, in line with their hydraulic theory. They also observed dilute wisps of current fluid rising to three times the current height; the trajectory and concentration of these wisps were not predicted by the hydraulic theory.

Kaye & Hunt (2007) studied overturning at the wall of a cylindrical basin fed by a plume. In their experiments, dense fluid fell from a point source as a plume at the centre of the cylinder, spread out over the floor of the basin as a radial gravity current, and collided with the basin wall. When the radius of the cylinder was similar to the height of the source, the gravity current was still driven by its momentum when it collided with the wall. The overturning height was roughly half the depth of the source height, and the overturning current engulfed ambient fluid. In experiments where the radius of the cylinder was larger than the height of the source, the gravity current became buoyancy driven when it collided with the wall. The overturning height reduced as the cylinder radius increased and the overturning did not engulf as much fluid, but overturned through a slumping mechanism which generated waves but less mixing after hitting the wall.

In the case of gravity currents down inclined slopes in this investigation, the gravity current was assumed to be in the normal Richardson number condition by the time it reached the wall, in which the flow has developed to flow at constant Richardson number. Thus, the flow was buoyancy driven and the overturn at the wall may be expected to occur by the slumping mechanism observed by Kaye & Hunt (2007), leading to less mixing than the crashing mechanism. There are no studies, to our knowledge, that consider a gravity current travelling down an inclined surface and colliding with a wall.

To try to reduce the mixing occurring in the collision with the back wall, porous foam and floors with reduced slope were added in various configurations in the neighbourhood of the end wall. Photographs of the collisions of the current with the back wall in each of these cases are shown in figure 4.10. Qualitative observations of these collisions suggested that none of the modifications gave a clear reduction in the volume of mixed fluid generated. Reducing the kinetic energy of the current as it was decelerated at the bottom of the basin by these different methods inevitably generated mixed fluid. Each of the modifications introduced extra length scales to the experiment and complicated the processes occurring. For these two reasons the unmodified original case of a fixed weir, orthogonal to the tank floor, was used in the experiments.

Another important part of setting up the weir was preventing leaks. The weir was sealed against the wall and base of the tank with electrical tape to prevent leakage. Owing to deformation of the tank when it was filled with water (on a scale of up to 5 mm), some leakage did occur. This leakage was shown to be negligible (around 1 mL s^{-1}). In future experiments, external bracing of the tank around the weir would reduce the deformation and would be a better way of preventing leakage.

4.1.5 Conductivity probe

The main quantitative observations in the experiments, the density profiles, were measured by a traversing conductivity probe. The probe measured the density of the ambient fluid in the tank as it filled with fluid from the gravity current. Photometry techniques that were trialled as an alternative, were found to give less accurate measures of the density profile. Photometry was also found to leave a region very close to the tank base (approximately 1 cm) inaccessible to measurements. In the presence of dense fluid with varying refractive index, the paths of rays reaching the camera from close to the tank base were altered. The

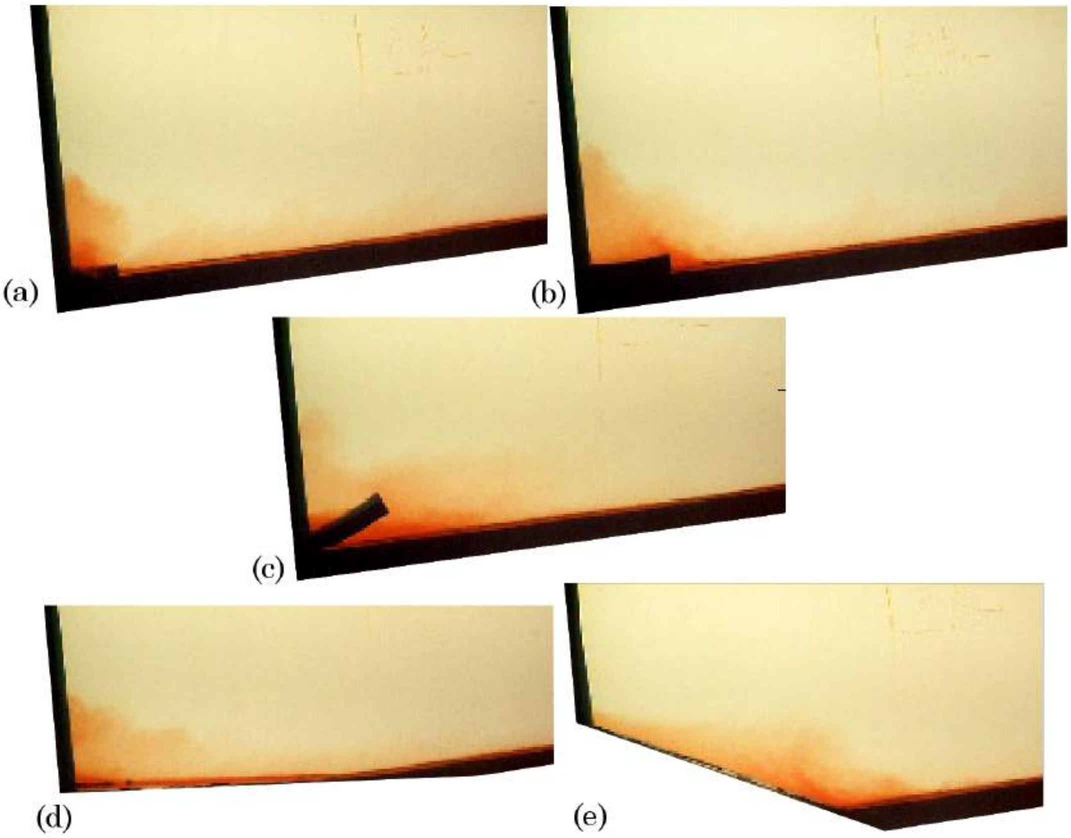

FIGURE 4.10: Photograph of the head of a turbulent gravity current colliding with end wall. The different modifications shown were trialled to reduce the amount of mixed fluid generated in the collision. In (a) a small horizontal false bottom 5 cm long was located at the base of the weir. In (b) foam filling the width of the tank and 3 cm by 15 cm in cross-section was laid along the bottom of the tank at the base of the weir. In (c) foam was inclined so that the gravity current ran into the underside of the foam. In (d) a horizontal false bottom 30 cm long was located at the base of the weir. In (e) an inclined false bottom was placed so that the gravity current ran up the incline. None of these configurations substantially reduced the volume of mixed fluid generated in the crash against the end wall.

light was refracted so that it came from the light bank behind the tank rather than from the dark tank base, substantially changing the intensity measured by the camera. This meant the light intensity to dye concentration relationship needed for the photometry could not be used close to the tank base. Refractive index matching, which could have prevented the deflection, was not feasible with the large volumes of fluid used in this experiment.

The conductivity probe used was of an aspirating design, similar to that described by Holford & Linden (1999) and by Tavoularis (2005). The resistance between the electrodes was dominated by the resistance of the fluid passing through the small aperture – 0.2 mm in diameter – at the tip of the probe. Leads from the electrodes were attached to a Wheatstone bridge circuit, which in turn led to a UEI PowerDAQ PD2-MF analogue to digital data acquisition card in a PC. The card was driven and the data were logged via scripts in the DigiFlow software package. An oscilloscope was used to check that the voltage from the bridge circuit was amplified as much as possible without clipping the signal. The electronics within the bridge had a response frequency of around 100 Hz, which was the limit on the frequency of data logging. The fluid was drawn through the aperture at a flow rate of approximately 10 mL min^{-1}, giving a fluid speed of 5 m s^{-1} through the tip.

The probe was mounted on a sturdy plastic plate attached to the belt traverse. The mounting was designed to minimise vibration of the probe, which was reduced to below 1 mm at the probe tip. A stepper motor was used to control the position of a linear belt. The belt was steel reinforced to prevent any stretching and toothed to prevent any slippage. These specifications meant that the profiler's position could be reliably controlled, to within 0.2 mm, by counting the steps moved by the stepper motor. The stepper motor was driven by a digital signal from the data acquisition card controlled from scripts in the DigiFlow software package (Dalziel, 2008).

The speed of fluid being drawn through the probe tip was faster than the speed of descent of the probe, keeping the probe supplied with fluid from the depth of the probe tip. The effect of the speed of descent of the probe on the density measured was tested with a stably stratified fluid composed of three homogeneous layers separated by sharp density interfaces. The traverse was moved at speeds ranging from 10 mm s^{-1} to 100 mm s^{-1}, the maximum speed achievable with the

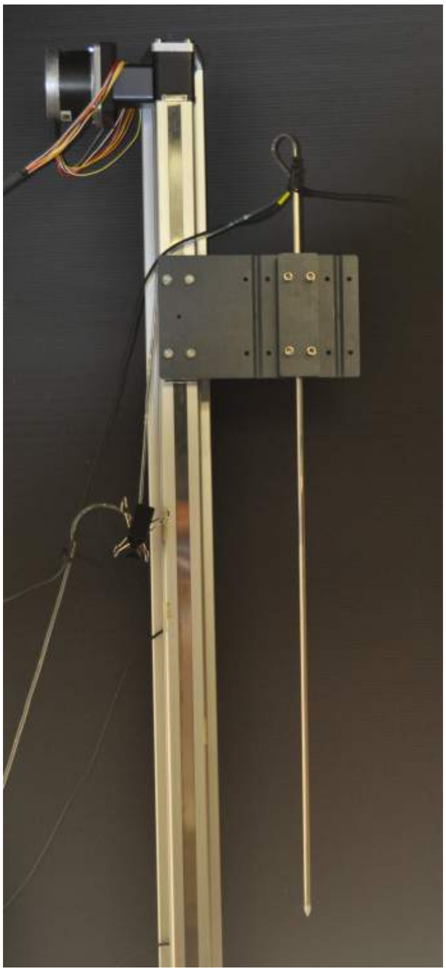

Figure 4.11: Photograph of the traversing conductivity probe.

traverse. The depths of the density interface measured by the probe moving at these different speeds were within 2 mm of each other, with no clear trend in depth with speed. When the traverse moved at a speed below 20 mm s^{-1}, the probe tip vibrated more strongly, increasing the magnitude of high frequency noise in the conductivity signal. A speed of 50 mm s^{-1} was used in the experiments to reduce noise in the signal, achieve a fast probe movement, and reduce the sample spacing to 0.5 mm.

The conductivity probe voltage measurements were calibrated against calibration solutions of known density. The fitted calibration curves are shown in figure 4.12. The salinity of the calibration solutions were measured with an Anton Paar densitometer (model DMA5000) to an accuracy of 5×10^{-6} kg L^{-1}. Quadratic calibration curves for density as a function of voltage were made from calibrations on three occasions during the series of experiments and used for the experiments which followed each calibration. The standard deviation of the calibration measurements from the quadratic curve fitted to all the data taken was 8×10^{-4} kg L^{-1}. This deviation was caused mainly by the difference in temperature between the different calibration measurements. During the experiments the source water was kept at the same temperature as the fluid in the working section, within 1°C, to ensure that temperature variations did not significantly affect the density measurements.

The typical accuracy of density measurement from the conductivity probe can also be found by comparing the mass delivered by the source to the mass in the tank implied by the probe measurements. This could not be done in experiments with high flow rates, as the time taken for the source fluid to reach the conductivity probe was too large relative to the time taken to fill the tank. In these cases a significant proportion of the mass delivered to the tank had not reached the profiler before the measurements stopped. In experiments in which this source of error was small, i.e., in experiments in the range $Re_s < 400$, the mass calculated from the conductivity measurements was, on average, within 5% of the mass delivered by the source. The mass conservation calculation will be discussed in the next section.

These two accuracy estimates for the conductivity probe measurements of the density are of approximately similar magnitude.

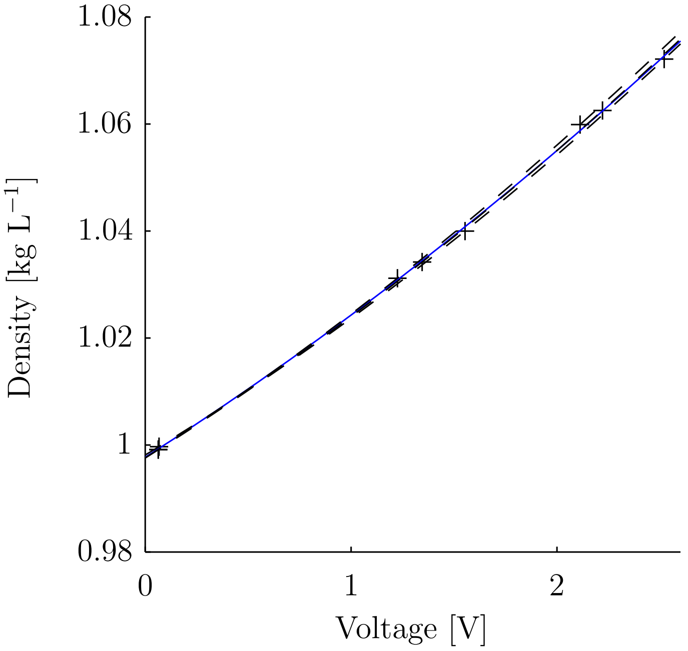

FIGURE 4.12: Calibration measurements for the conductivity probe. Nine individual measurements are shown by crosses. Three different calibration curves used are shown with dashed lines. The least squares fit to all the measurements is shown by the solid blue line.

4.1.6 Mass conservation within measurements

The buoyancy added to the basin by the source was conserved during the experiments. The accuracy of the measurements can be assessed by how well mass was conserved. The buoyancy per unit width within the basin integrated over the profiles, for a range of experiments, is shown in the plots in figure 4.13. The buoyancy within the basin was calculated from

$$B(T) = \int_{H_b}^{H_s} g'_a H/(\sin\theta\cos\theta)dH \tag{4.1}$$

where H is the height above the bottom of the basin, H_s the height of the source unit, H_b the bottom of the profiler, g'_a the reduced gravity measured by the profiler, and θ the angle of the slope. In these runs the deviation in the measured buoyancy was between 0.0042 m^{3}s^{-3} above and 0.0010 m^{3}s^{-3} below the buoyancy supplied by the source since $t = 0$. The measurements tended to have a higher mass excess in higher source flow rate runs.

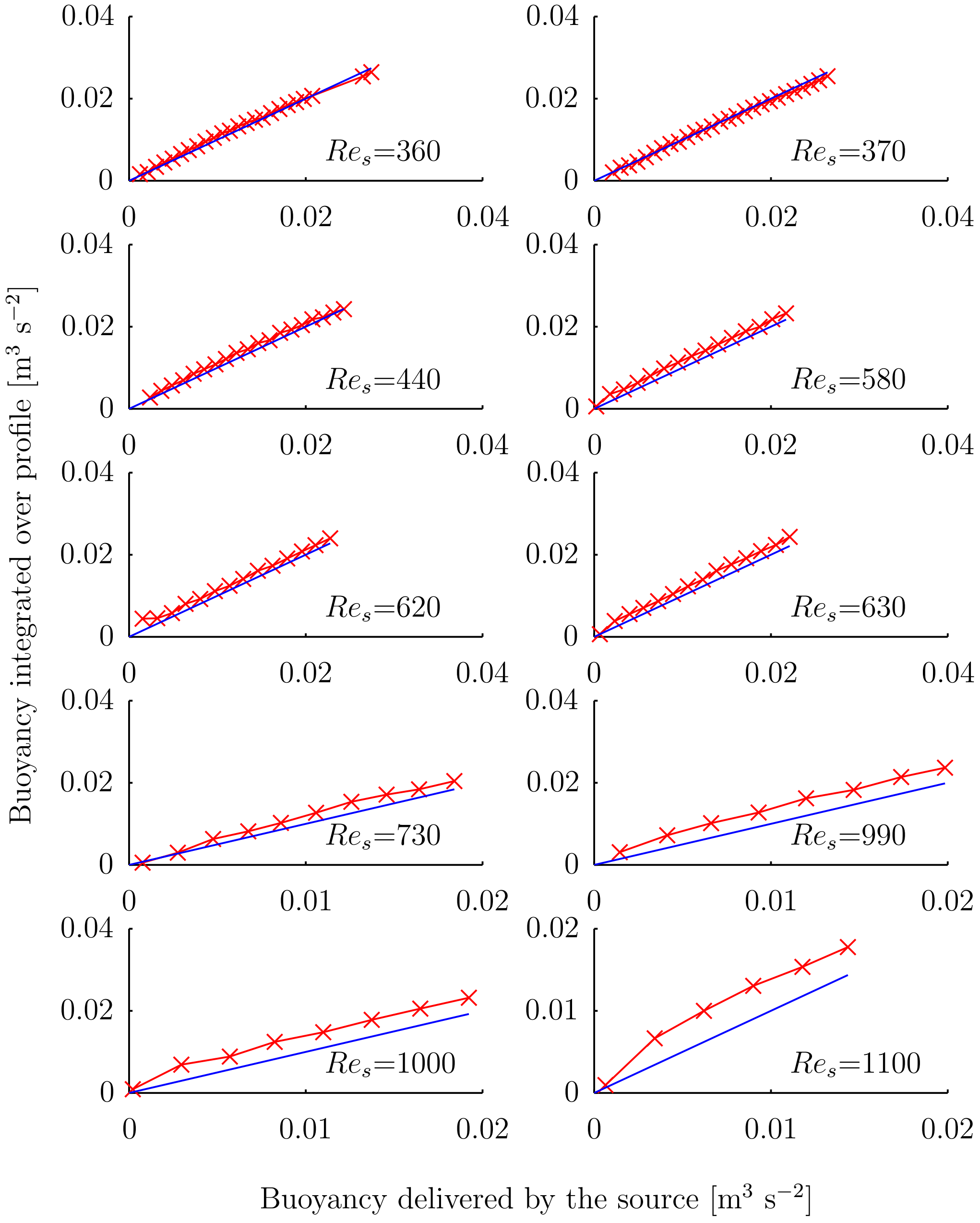

FIGURE 4.13: Plots of total buoyancy measured within the basin by the conductivity probe against the buoyancy delivered by the source since $t = 0$. The blue line is the ideal mass conserving case.

The deviation from mass conservation in the measurements was contributed to by the following sources. First, the start of the filling process, at $t = 0$, was taken as the time at which the gravity current reached the end wall at the bottom of the basin. This was the time that fluid started to pond at the bottom of the ambient. The buoyancy source was started approximately 30 s before this, and the gravity current took this amount of time to run down the slope to the end wall. The buoyancy which entered the basin over the time before $t = 0$ was not accounted for in the models of the ambient stratification. This effect was stronger in the high Re_s experiments, where the time scale of filling was small, and thus the gravity current travel time of approximately 30 s was more significant. At $Re_s = 1100$, this introduced an unaccounted buoyancy excess of approximately 0.008 $\mathrm{m}^3\mathrm{s}^{-3}$, and at $Re_s = 360$ this introduced an unaccounted buoyancy excess of approximately 0.003 $\mathrm{m}^3\mathrm{s}^{-2}$. This unaccounted mass flux is of a similar magnitude to the observed mass discrepancy, although slightly larger.

Secondly, the dense fluid introduced from the source took time to reach the conductivity probe. The model assumed that fluid entered the ambient stratification immediately from the source. This was why $t = 0$ was set by the time that the gravity current met the end wall and started to pond in the ambient, rather than when the source flux was started.

Thirdly, the density in the bottom 5 cm of the basin was not measured by the profiler. The density in this region was therefore unknown. This volume was less than 3% of the basin volume, so it was a minor deficit in the measured density.

Finally, the initial ambient density was calculated from the minimum of the unfiltered density signal. Noise in the conductivity measurements was included in this value, slightly increasing the g'_a measurements. Despite these sources of uncertainty, mass was conserved adequately in the measurements for them to be used to distinguish between the models described in chapter 3.

4.2 Routines for density profile analysis

4.2.1 Locating the top of the ponded region

To identify the height of the top of the ponded region, a processing routine was developed to pick out this height from the density profile. A typical profile of the reduced gravity, g'_p, of the fluid in the basin is shown in figure 4.14, where

$g'_p = g(\rho_a - \rho_0)/\rho_r$ and $\rho_r = 1.0$ kg L^{-1}. Different routines to achieve this were considered, three of which are described here.

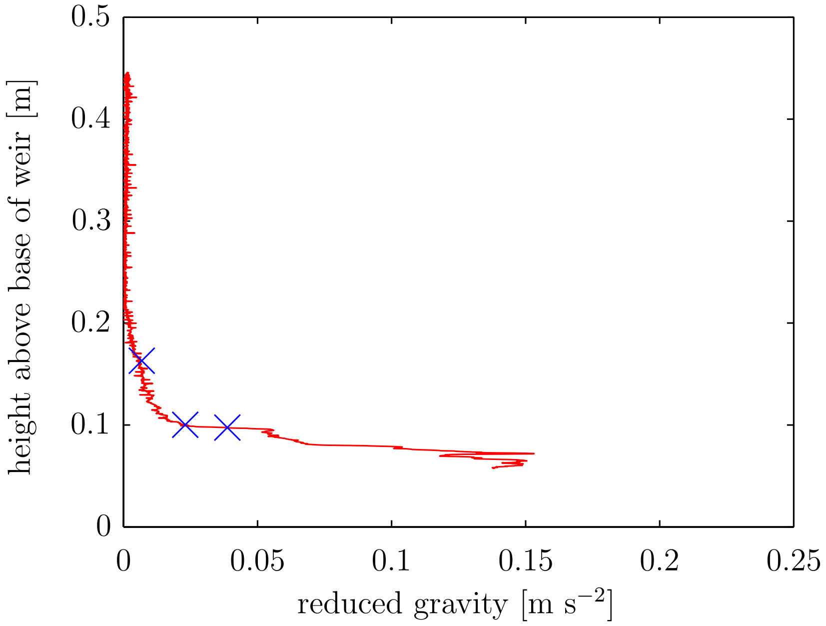

FIGURE 4.14: A profile of g'_p measured by the traversing conductivity probe. The top of the ponded region is shown by three blue crosses, as identified by the single point threshold routine with for three values of ψ: 0.05, 0.13 and 0.2.

The simplest method considered we will call the *single point above threshold* routine. A threshold value was used, set to a proportion, ψ, of the source reduced gravity, g'_0. The first sample at which g'_p was above the threshold $\psi g'_0$, searching from the top, was identified as the top of the ponded region. The points identified, reasonably successfully, for 3 different values of ψ are shown in figure 4.14. A profile which this routine struggled with is shown in figure 4.15. This routine was inadequate because at small ψ the noise in density measurement caused the top of the ponded region to be incorrectly identified far above the ponded region. At large ψ, the top of the ponded region was incorrectly identified too low, within the ponded region.

The problem with this method is that a single sample with g'_p greater than the threshold can set the height of the interface. To avoid this problem, a *proportion above threshold* routine was developed. This routine required that a proportion, greater than a parameter ϕ, of the samples within the ponded region must have g'_p

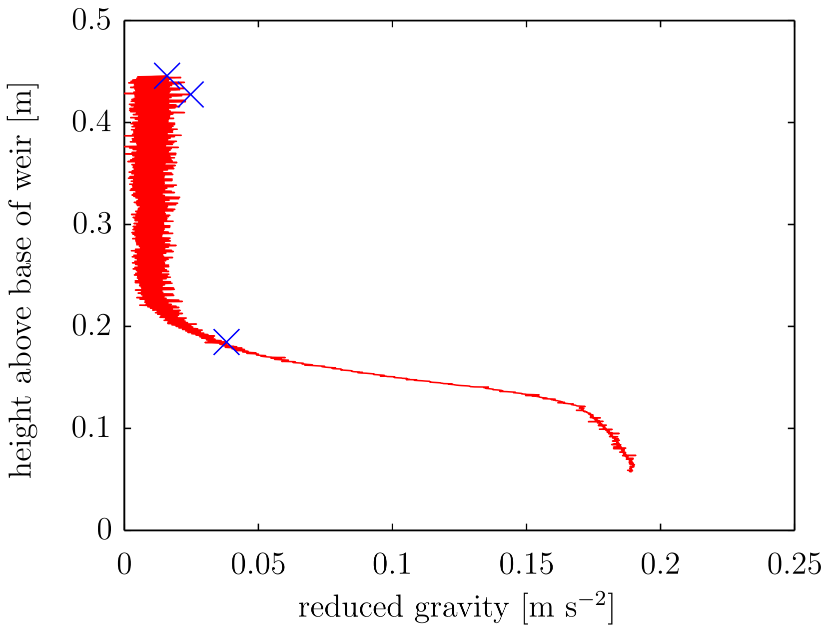

FIGURE 4.15: A profile of g'_p demonstrating how noise makes the *single point above threshold* routine fail. The identified heights are shown for three values of ψ: 0.05, 0.13 and 0.2.

greater than the threshold $\psi g'_0$. The top of the ponded region was identified as the sample at the greatest height that both met the criteria set by ϕ and itself had g'_p above $\psi g'_0$. This routine ignores individual, anomalous samples which cross the threshold density, but which are a large height above the majority of the samples which cross the threshold. An example illustrating the routine is shown in figure 4.16. The top of the ponded region, identified by the routine for the same profile as in figure 4.15, is indicated in figure 4.17. Comparing these figures shows the improvement in accuracy achieved by the *proportion above threshold* routine when the g'_p signal is noisy. A value of $\phi = 0.95$ was used in the data analysis as this reduced the impact of noise in the g'_p signal whilst not requiring that all g'_p samples in the ponded region were above $\psi g'_0$. If a profile contained no points which met the criteria for the top of the ponded region, the profile was omitted from the analysis on the grounds that it was too noisy. Such profiles were rare. The time taken for the profiler to descend to the top of the ponded region was included when calculating the time at which the height measurement was made.

An alternative method of identifying the ponding height, used by Ellison &

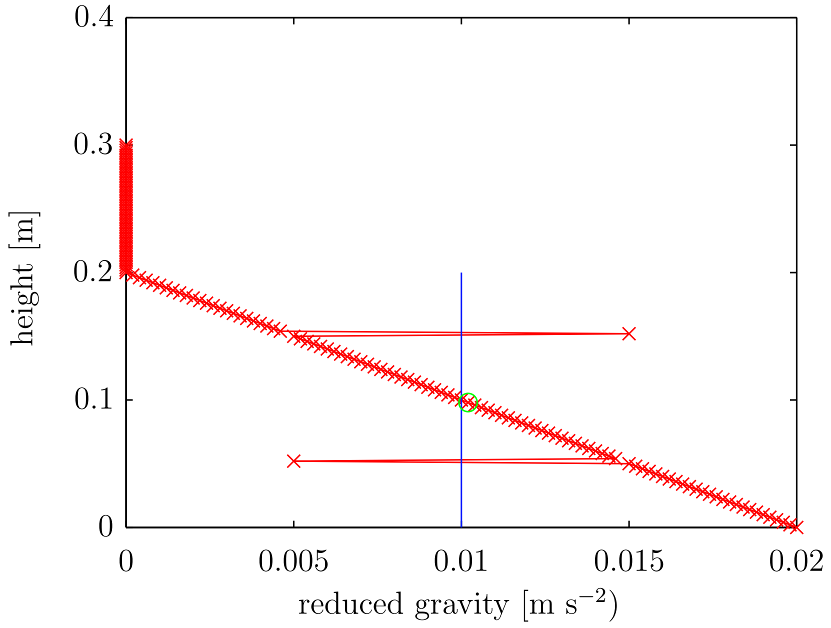

FIGURE 4.16: An example of a g'_p profile showing the *proportion above threshold* routine. The value of the g'_p threshold is shown by the blue vertical line. The height at which the underlying, monotonic signal crosses the threshold (0.1 m) is found by the routine. The anomalous data at 0.15 m would mislead the *single point above threshold* routine.

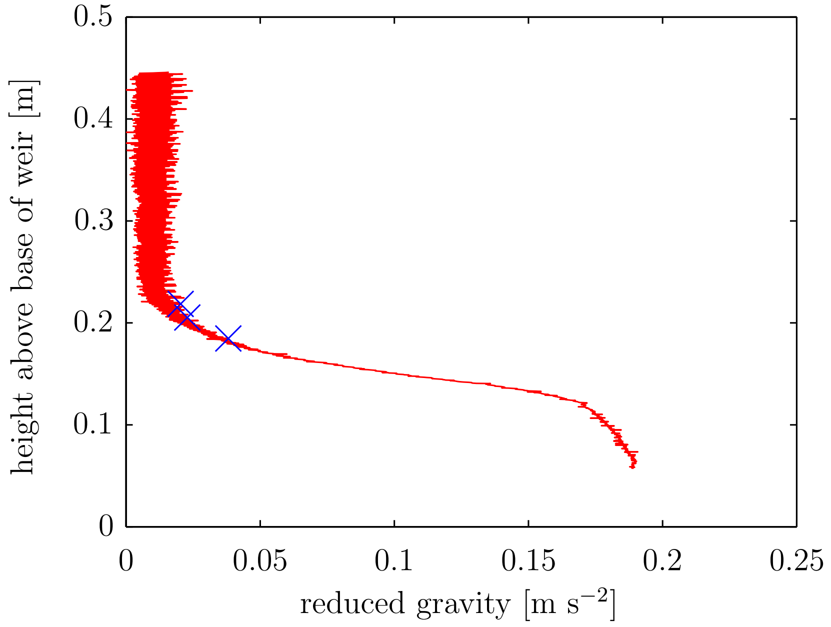

FIGURE 4.17: A profile of g'_p, the same as in figure 4.15, demonstrating how noise does not make the *proportion above threshold* routine fail. The identified heights are shown with $\phi = 0.95$ for three values of ψ: 0.05, 0.13 and 0.2.

Turner (1959), took the intersection of the $g'_p = 0$ line with the tangent at the inflection point of the density profile. In some of the test profiles, this method gave similar results to the other routines with $\psi = 0.1$ and $\phi = 0.95$. It could not be applied when the profile had more than one inflection point, and therefore it was not used.

For the analysis in the rest of this thesis, the proportion above threshold routine was used.

4.2.2 Thickness of the homogeneous layer within the ponded region

Within the ponded region, two layers were observed with markedly distinct density gradients, as will be later discussed in section 5.3.1. The upper layer was more strongly stratified and the lower layer was relatively homogeneous in density. To examine trends in the thickness of the two layers, an algorithmic method of identifying the interface between them was developed. One of the density profiles analysed, clearly showing the two layers within the ponded region, is plotted in figure 4.18(a) and again in figure 4.21. Two approaches to identifying the layer thickness were developed: the extreme-curvature algorithm and the two line segment least-squares algorithm. We will now describe these two approaches and give reasons for preferring the extreme-curvature method.

Extreme-curvature algorithm

The extreme-curvature algorithm is based on the idea that the interface between the relatively homogeneous layer and the relatively stratified layer is the point with the highest magnitude curvature of the whole profile. The curvature is expressed in terms of the second derivative as

$$\kappa = \frac{d^2\rho}{dZ^2} \Bigg/ \left[1 + \left(\frac{d\rho}{dZ}\right)^2\right]^{3/2} \tag{4.2}$$

$$\approx \frac{d^2\rho}{dZ^2}, \tag{4.3}$$

where ρ is the density and Z the vertical height above the base at the position of the profiler. The term $d\rho/dZ$ is small enough that the approximate form, (4.3), is

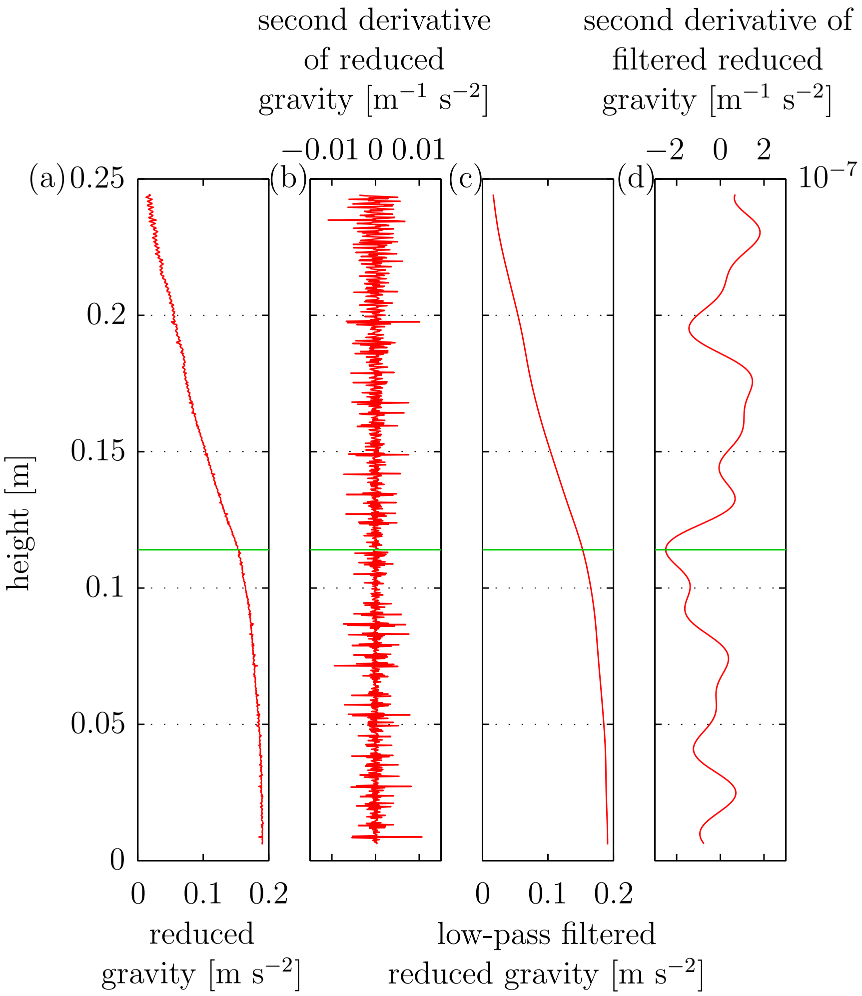

FIGURE 4.18: Plots of the density profile from the $Re_s = 370$ run at different stages in the analysis process. Height is measured vertically from the bottom of the profiler. (a) shows the unfiltered density profile read from the analogue-to-digital card on the PC. (b) shows the second derivative of this unfiltered density. (c) shows the density profile after having a low-pass filter with a wavelength of 1 cm applied to it. (d) shows the second derivative of this filtered density. The green horizontal line shows the height of the minimum value of the second derivative.

adequate for this analysis. With the sign conventions adopted here, the extremum in curvature at the interface is the most negative value of the second derivative of the profile.

The second derivative of the measured data, shown in figure 4.18(b), cannot be used directly because the signal to noise ratio is too small. The high frequency noise must be removed to reveal the curvature of the underlying large scale density profile. A low-pass filter was found to make the second derivative of the underlying profile clearer than other filters tested (median and moving average filters). The filtered density profile and its second derivative are plotted in figures 4.18(c) and 4.18(d) respectively. The global minimum in the curvature was used to identify the interface between the two regions of distinct density gradient.

In some density profiles, particularly those from experiments with high Re_s, it was difficult to identify the height of the interface, either using an algorithm or by visual inspection. Processing these profiles to find the point of extreme curvature generated anomalous interface heights. The relatively homogeneous layer was a weaker feature in these high Re_s profiles, and may not have been present at all. The extreme-curvature algorithm was modified in the two following ways to deal with difficult features so that a single approach could be consistently applied to all the profiles. First, the profiles were averaged over three consecutive traverses so that the turbulent perturbations were averaged out, leaving a stronger signal of the mean stratification. Second, the measured profiles were padded with repeated values at the beginning and end of the sequence. This prevented the frequency spectrum having maxima at the last sample, where the sequence was reflected by the low-pass filter used.

In cases where the algorithm identified the height of the lower layer at anomalous values, the actual thickness of the lower layer could be identified from local minima in the second derivative of the density other than the global minimum. Such a situation is shown in figure 4.19 for the profile at $Re_s = 990$ using the unmodified extreme curvature algorithm. By ignoring local minima which give rise to erroneous interface heights, the actual thickness of the interface height could be found automatically. Finding which data points were erroneous is difficult to do without presupposing the form of the trend, so this approach was not pursued further.

The main parameter which can be altered in implementing this algorithm is selecting the cut-off frequency of the low-pass filter. In principal, a low value allows the height of the interface to be located with more precision. However, if the wavelength is too small, features other than the homogeneous lower layer can have more extreme second derivatives and cause anomalous results. The results calculated with two different cut-off wavelengths are shown in figure 4.20. With a cut-off wavelength of 1 cm, the interface was automatically identified in all

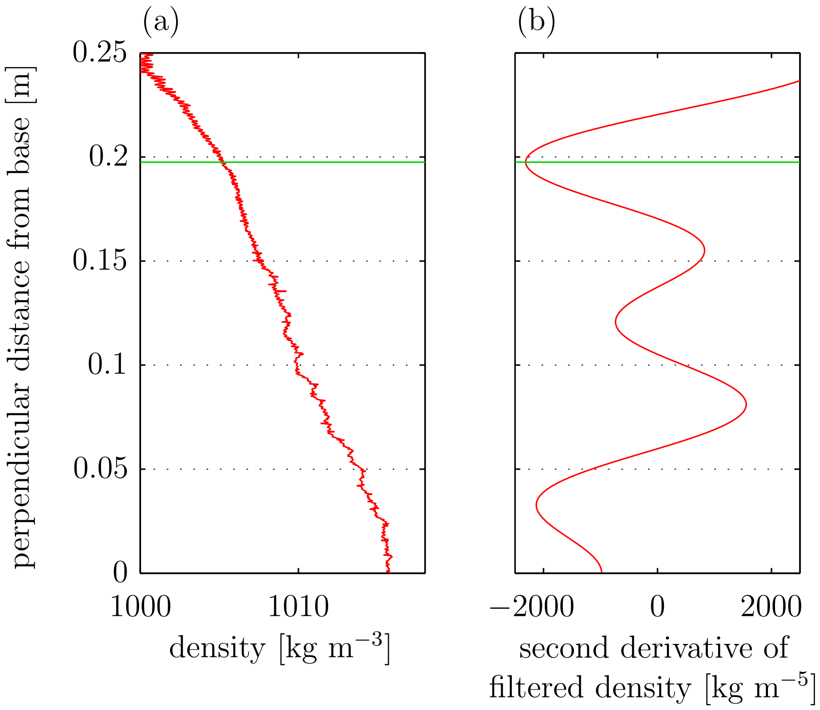

FIGURE 4.19: Plot of the density profile in the Re_s = 990 run. In this instance, the extreme curvature algorithm fails to identify the interface between the stratified and homogeneous layers because the filtered signal contains another point with higher curvature.

but three cases (Re_s =440, 630 and 730). With a cut-off wavelength of 5 cm, the interface was automatically identified in all but one case (Re_s = 1500). The trend in the thickness of the homogeneous layer was the same as when using a 1 cm cut-off wavelength to within the scatter in the data. The thickness was consistently around 2 cm smaller when the 5 cm cut-off was used. This systematic difference in the layer thickness is acceptable, as the change in gradient between the two layers happens over a height of around 2 cm. It is therefore not possible to identify the thickness more precisely.

Two line segment least-squares algorithm

The two line segment least-squares algorithm uses a different approach to identify the thickness of the lower layer. It therefore serves as a good check on the extreme-curvature algorithm. The general approach is to use an optimisation routine to find a curve, with the form of two joined line segments, which minimises the residual sum of squares relative to the measured profile.

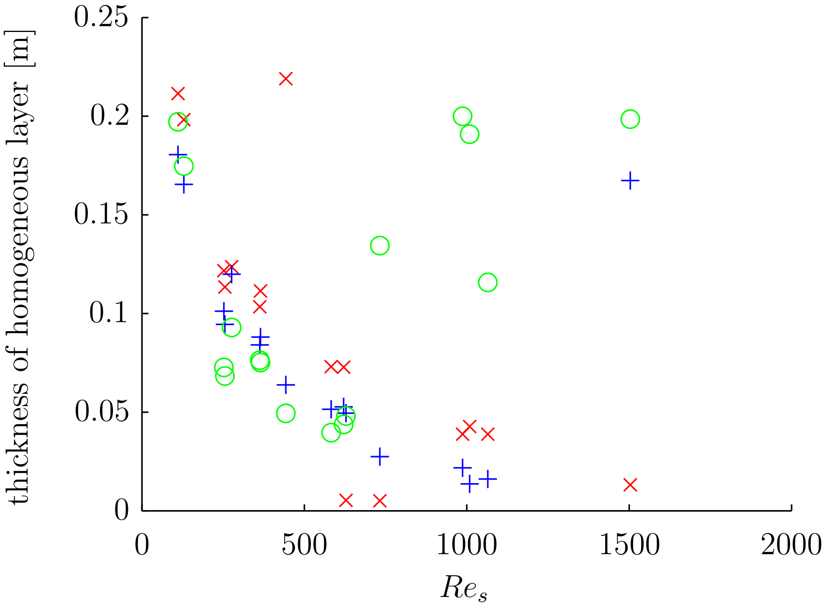

FIGURE 4.20: Plots of the thickness of the lower layer found by different algorithms. The extreme curvature algorithm with a cut-off wavelength of 5 cm is shown by blue plus symbols and with a cut-off wavelength of 1 cm by red cross symbols. The two line least-squares algorithm is shown by green circle symbols.

In the first step to finding this curve, the values of density and height at the top and bottom of the ponded region (ρ_t, ρ_b, Z_t and $Z_b = 0$ respectively) were taken from the profile. The top of the ponded region was found by the algorithm described in section 4.2.1. The density and height at which the line segments join, ρ_j and Z_j, are left as free parameters defining the curve

$$\rho_{opt} = \begin{cases} \rho_t + \left(\dfrac{\rho_j - \rho_t}{Z_j - Z_t}\right)(Z_t - Z), & Z > Z_j \\ \rho_b - \left(\dfrac{\rho_b - \rho_j}{Z_j}\right) Z, & Z < Z_j. \end{cases} \tag{4.4}$$

These free parameters were used as control parameters by the optimisation routine to minimise the residual sum of squares. The least squares optimisation routine used was a hybrid of the steepest descent method and the Gauss-Newton method implemented in matlab™ (Marquardt, 1963). A density profile from an experiment and the least-square optimal two-segment curve are plotted together in figure 4.21. This algorithm can, when there is a clear change of gradient, successfully locate the change in gradient to ∼3 cm, a reasonable approximation.

However, this least squares algorithm has some drawbacks. The error which forms the objective function of the minimisation comes equally from the whole profile, rather than depending only on the profile in the neighbourhood of the feature of interest – the interface where the gradient changes. This means that parts of the profile far from the interface can have more influence over the interface's location than the part of the profile containing the interface. This can introduce error into the algorithm's identification of the interface's height. Furthermore, the algorithm assumes the profile has the form of two straight lines. When this form is a poor approximation, the algorithm can converge on spurious solutions; this is particularly true when the profile is close to a single straight line, in which case the location of the joining point is under-constrained and can converge to any height. This occurred particularly when the lower layer was small enough that the solution was close to a single straight line. This was the cause of anomalously high interfaces in the data, shown in figure 4.20, at large Re_s.

The thicknesses of the lower layers found by the two algorithms are shown in figure 4.20. The trend in the homogeneous lower layer found by the least-squares algorithm is similar to that found by the extreme curvature algorithm at values of $Re_s < 700$. This provides confidence that both algorithms are successfully identifying the interface between the two layers in the density profiles. At $Re_s > 700$ the least-squares algorithm is unreliable and places the joining point too high up the profile. The thicknesses identified by the least squares algorithm at these values of Re_s are artefacts of the analysis method and are erroneous. If the least square algorithm were needed to perform more robustly at high Re_s, a weighted least squares error could be used, but this is not needed for the present analysis. The least squares algorithm generates more anomalous data points and will therefore not be used in the analysis, other than to provide supporting evidence for the trend over $Re_s < 700$.

For the analysis in the rest of this thesis, the extreme curvature algorithm was used.

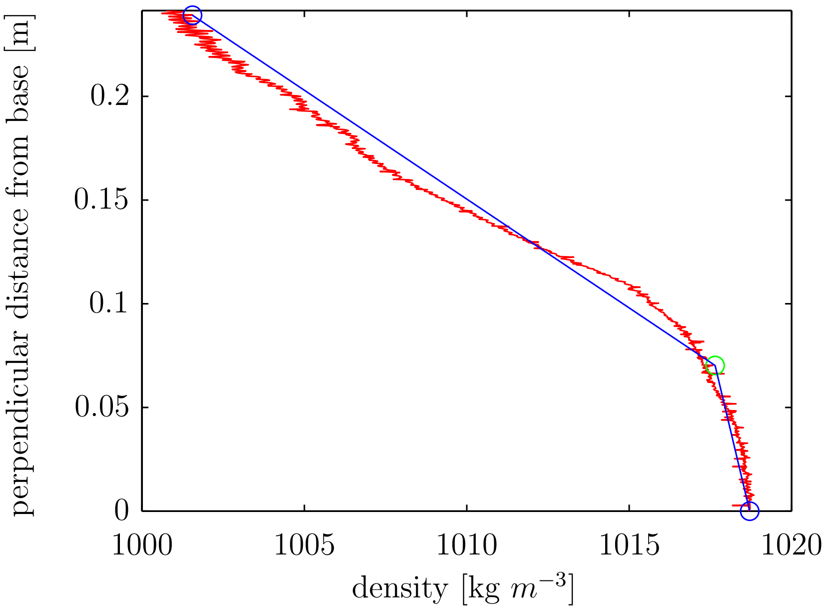

FIGURE 4.21: Plots of the density profile from the $Re_s = 370$ run (in red) and the two-segment least-squares best fit curve (in blue). The fixed points are shown by blue circles and the joining point of the segments, which was free to move under the optimisation routine, by a green circle.

4.3 Summary

In this chapter we have described the apparatus and methods which will be used for the experiments in chapter 5. In section 4.1, the designs of different components were discussed, giving the reasoning for choosing between alternative options. In section 4.2.2, the routines used to process the raw data from the experiments were discussed. We now turn to examine the observations and measurements made with this apparatus. We will also discuss which of the models described in chapter 3 make the best approximation to the observed behaviour of a filling basin fed by a gravity current. We will show that, in these experiments, efflux from a gravity current in a stratified ambient does occur.

Chapter 5

Laboratory Experiment Results

This chapter will discuss the qualitative and quantitative observations from tank experiments analogous to the filling of a lake basin by a dense river which forms an underflow within the lake. We will begin by calculating the entrainment coefficient as a function of the Reynolds number from the accumulation of dense fluid in a ponded region at the bottom of the basin. We will then examine the flow within the ponded region, initially qualitatively with dye pulse measurements and then with measurements of the evolving density profile. The predictions of the persistently entraining model and the peeling model described in chapter 3 will be compared with the experimental data to understand when the theoretical assumptions in those models can be applied.

5.1 Evolution of the front of the ponded region

As dense fluid accumulates in the ponded region at the bottom of the basin, the first front of the ponded region rises through the basin. Once the ponded region is initially established, the location of the first front is only affected by the behaviour of the gravity current upstream of the first front; the location of the first front is not affected by how the fluid is rearranged within the ponded region. Observations of the first front therefore relate both to the persistently entraining and the peeling models (case 2 and case 3) discussed in chapter 3. Comparing experimental observations to the theoretical prediction for the rise of the first front in (3.18) will show when the model for entrainment into a gravity current from a uniform density ambient (Ellison & Turner, 1959) is a good approximation.

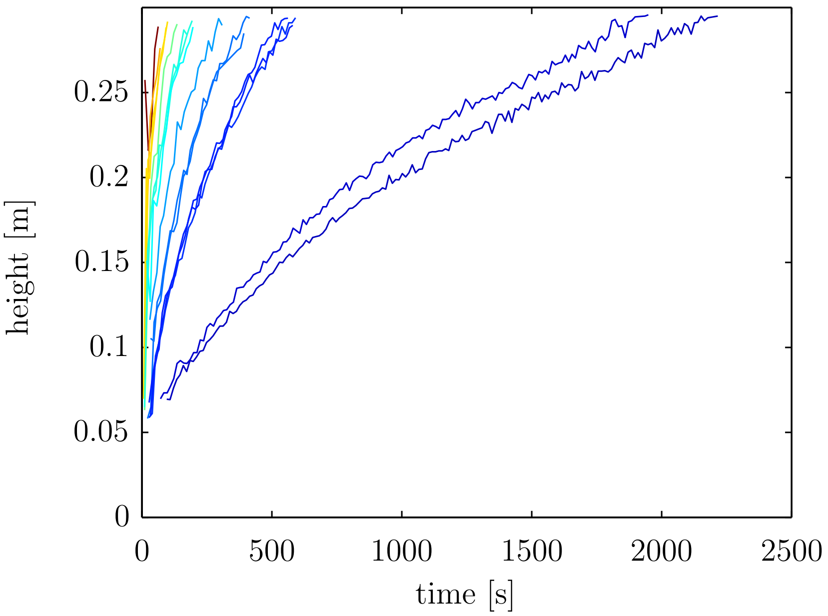

FIGURE 5.1: The evolution of the front height for a series of experiments with different source flow rates. The colour scale shows the Re_s for the experiment, ranging from blue at 110 to red at 1500.

A series of experiments was conducted with 16 different source flow rates. The source flow rates varied over a range of source Reynolds numbers, $Re_s = Q_s/\nu$, from 110 to 1500, where Q_s is the volume flow rate per unit width supplied at the source and ν is the kinematic viscosity. The kinematic viscosity of water at 20°C is 1.01×10^{-6} m^2 s^{-1}. In all experiments the inclination of the tank was

8.6°, the source height was 29 cm above the bottom of the tank, and the reduced gravity of the source fluid was 0.20 m s^{-2}, to within 0.01 m s^{-2}. The evolution of the first front location for each experiment in the series, processed from the conductivity probe data as described in section 4.2.1, are shown in figure 5.1. The curves show that, in all experiments, from $t = 0$ the dense fluid ponds over a small height at the bottom of the basin. The top of the ponded region rises as more dense fluid is supplied to the basin, until it reaches the source height and the experiment ends. In each experiment, the curves show that the top of the ponded region rose most quickly at first and then slowed. This is predicted by (3.18) from the theory for an entraining gravity current filling a triangular basin. At higher source flow rates, the top of the ponded region rose quicker. The curves rise monotonically, apart from some small amplitude oscillations from waves on the top of the ponded region causing the interface to rise and fall a small amount at the location of the profiler. This noise was significantly larger in the first data point taken in the highest flow rate experiment than in other cases. In this worst case the front descended 0.04 m in one time step. This is the first segment of the red line shown in figure 5.2. The profile used in this data point was taken whilst the gravity current was rebounding from crashing against the back wall. This was removed from the data set used in later analysis, because it was a significantly anomalous point which would complicate later data processing.

To compare these curves with the prediction from the theory for an entraining gravity current filling a triangular basin given in (3.18), the time and height scales need to be non-dimensionalised. The scaling of depth to form ζ in (3.9) is based on the height of the virtual origin above the bottom of the basin. The virtual origin was assumed, as an initial approximation, to be at the physical source, making the depth scale D_s equal to the depth of the tank. The non-dimensional time in (3.14) is based on values measured for the experimental run and the entrainment coefficient, E. As an initial approximation, a value of $E = 0.012$ was taken from Ellison & Turner (1959) in their figure 8 for the inclination used in the experiment. The non-dimensionalised data are shown in figure 5.2. The experimental data do not successfully collapse to the theoretical curve under this non-dimensionalisation, although the range of filling times for the different runs in dimensionless units is less than the range of dimensional filling times. The deviation of the data from the theoretical prediction using a constant value for

E is broadly correlated with the flow rate. Flows with a low source flow rate fill slower than the model; flows with a high source flow rate fill faster than the model.

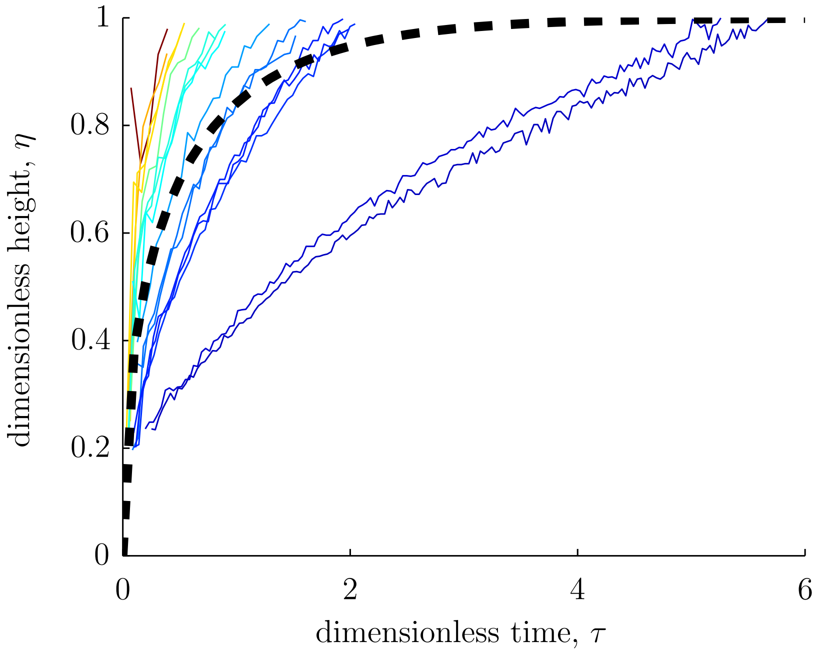

FIGURE 5.2: The evolution of the front height, plotted in dimensionless quantities using a constant value of $E = 0.012$. The theoretical prediction is plotted with the dashed line. The colour scales with Re_s for the experiment, from blue at 110 to red at 1500.

5.1.1 Visualising the upper boundary of the gravity current

Visually inspecting dyed gravity currents in these different runs suggested there was large variation in the intensity and character of the turbulent entrainment occurring in runs with different source flow rates. The difference in the character of the entrainment was seen more clearly in another set of runs by adding an opaque dye to the source fluid. Of the available dyes, skimmed milk was found to have the smallest attenuation length for visible light (Simpson, 1987). The milk was diluted to 1 part in 10 with water to reduce fouling the apparatus with fat. At this concentration, a black piece of plastic immersed in the liquid became obscured after a distance of about 0.5 mm. The salt solution used to form the gravity currents had a density of 1.016 kg L^{-1}. This dye allowed structures formed by the boundary of the dense current, such as waves, eddies or filaments, to be seen. Photographs of currents at three different flow rates spanning the range of Re_s achieved in the experiments are shown in figures 5.3 to 5.5.

For the flow in figure 5.3, the flow rate was set to give $Re_s = 100$. The boundary of the current formed a smooth flat sheet with no visible perturbations. The flow was laminar with no visible turbulence at the interface of the current.

For the flow in figure 5.4, the flow rate was set to give $Re_s = 300$. The boundary of the current was smooth with regularly periodic perturbations across the whole surface. The perturbations were V shaped, had a wavelength of approximately 2 cm and moved downstream. We presume that these were roll waves which, after being initiated, spread laterally to form the V shaped waves (Balmforth & Mandre, 2004). On occasion, localised mixing events were seen on the surface dilute filaments of dye were brought into the upper ambient fluid.

For the flow shown in figure 5.5, the flow rate was set to give $Re_s = 900$. The boundary of the current was a diffuse, disordered field of unsteady, turbulent eddies. Filaments of dye, which were much more convoluted and diluted than the wave-like structures seen at $Re_s = 300$, were seen throughout the current. The flow was in a developed turbulent state with no visible laminar part, not even at the source. It is not possible to say from this visualisation, however, that the turbulence was fully developed. This transition in the turbulent activity at the upper interface of the gravity current is similar to that seen in rotating gravity currents by Cenedese & Adduce (2008). In the present experiments, the laminar flow persisted to larger Re_s than in Cenedese and Adduce's experiments. In the present experiments, the flow was observed in one state (either laminar, wave-like or turbulent) along the length of the current, whereas in Cenedese and Adduce's experiments the currents transitioned from a laminar to a wave-like to a turbulent flow over a distance of around a metre.

The observed change in the character of the turbulence and the visible engulfment of ambient fluid suggests deviation from the theoretical prediction seen in figure 5.2 was because E increased as Re_s increased. At higher Re_s, the current is stabilised less by viscosity, allowing E to increase. E is therefore not a function of θ alone as implied by the results of Ellison & Turner (1959). In the following section, we will see whether E being a function of Re_s improves how well the filling box process is described by the entraining gravity current model.

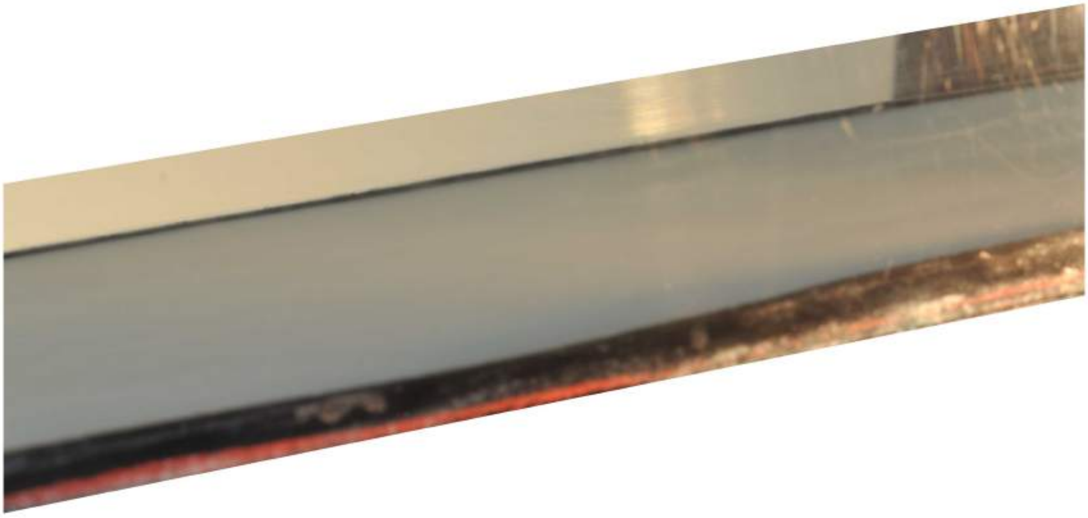

Figure 5.3: Photograph of the visualisation of the current boundary with milk, taken from above looking across the current. The current had $Re_s = 100$. The white current is flowing from right to left. At this Re_s, the current forms a smooth sheet. The black base of the tank is obscured by the current.

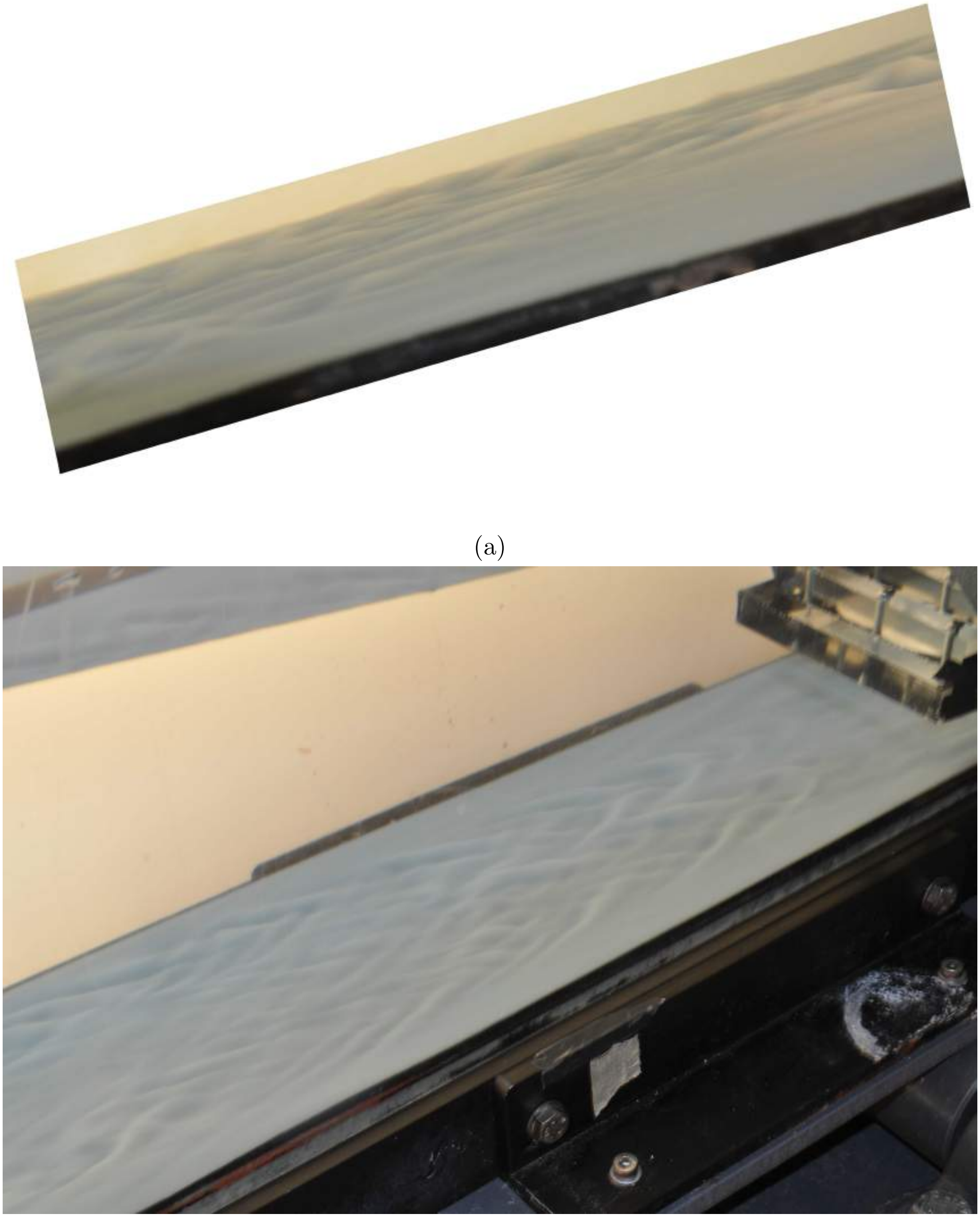

(a)

(b)

FIGURE 5.4: Visualisation of the current boundary with milk, as in figure 5.3, when $Re_s = 300$. The white current is flowing from right to left. In (a), the photograph is looking across the current at a shallow angle, and, in (b), the photograph is taken from over the current. The angled plate of the source unit is visible in the top right corner.

(a)

(b)

Figure 5.5: Visualisation of the current boundary with milk, as in figure 5.3, when $Re_s = 900$. The white current is flowing from right to left. Both photographs are looking from above, across the current.

5.1.2 Finding the variation in entrainment, E

To find the variation in E, the experimental data for the front height were fitted with the functional form for a triangular basin being fed by an entraining gravity current, (3.18). The residual sum of squares was minimised to fit the curves. The free parameters in the curve fit for each run gave a value for E, giving the variation in E with Re_s over the different runs.

The height of the front above the bottom of the tank is given in the filling basin model as

$$H = (1 + \mathcal{W}(-e^{-1-T/T_s}))D_s, \tag{5.1}$$

where T_s is the decay time scale and D_s is the depth of the tank beneath the virtual origin. The dimensionless variables τ and ζ_f in (3.18) are given by T/T_s and $(D_s - H)/D_s$ respectively. From the values of T_s and D_s fitted for an experimental run, the dimensionalisations (3.14) and (3.9) give

$$E = \frac{D_s^{3/2}}{F_0^{1/2} T_s^{3/2} \sin^{1/2}(\theta) \cos^{3/2}(\theta)}. \tag{5.2}$$

The curve fit was carried out using a nonlinear least squares optimisation routine implemented in the matlab software package (Moler, 2004). The routine is a hybrid of the steepest-descent and Gauss-Newton methods (Marquardt, 1963).

The curve fitting was carried out using two alternative sets of parameters in the optimisation, and the results of the two approaches were compared. The first optimisation used two free parameters, the time scale, T_s and the height scale D_s; the second optimisation constrained the rate of rise of the interface at the source to match the volume flux provided at the source and used only one free parameter, D_s.

In the first optimisation, both T_s and D_s in equation (5.1) were used as control variables in the optimisation routine. The experimental data for the top of the ponded region, $H(T)$, were found using the *proportion above threshold* routine described in section 4.2.1, with the threshold reduced gravity set to 10% of the source reduced gravity and proportion above threshold parameter of $\phi = 0.95$. The product-log curves found for each of the experiments are plotted in figure 5.6, along with the experimental data. The trend in the data is well captured by this functional form in most cases. The earliest few data points in some of the experimental runs, such as the Re_s = 620, 990 and 1000 cases, are anomalous. In the Re_s = 620 and 1000 cases the first two or three data points do not rise monotonically with time. These anomalous points lie far from the fitted curves. These anomalous data points come from waves on the interface caused by the crashing of the gravity current when it first hits the back wall at the bottom of the slope. These anomalies were included in the data set as it made negligible difference to value of E found by the least squares method; selecting a criteria for discarding the anomalous points would have added unnecessary complexity to the analysis. A similar anomalous point occurred in the Re_s = 1500 case, shown in figure 5.2, but was excluded in the least squares analysis; the small number of data points taken in that experimental run meant that the anomalous point had a large influence on the values of T_s and D_s found by the optimisation routine.

The entrainment rates found from these fitted curves are plotted in figure 5.7. The trend in E exhibits distinct regimes, supported by the regimes of the gravity current boundary observed with the opaque dye visualisations. The entrainment rate is very small (less than 5×10^{-5}) for $Re_s < 200$. For $Re_s > 200$, the E values calculated by the two parameter least squares are larger. The E values are very scattered, but the data give some support to a trend of E gradually increasing as Re_s increases. The linear trend found by a least squares fit to the data with $Re > 200$ is given in figure 5.7. Many of the data points which are distant from the trend line (Re_s =620, 990 and 1000) have anomalous, non-monotonic data points in their first front height data series.

The source flow rate implied by these fitted curves can be found from the rate of volume increase in the ponded region when the upper interface of the ponded region reaches the source height. Figure 5.8 shows the flow rates calculated for the fits compared against the actual source flow rates. The source flow rate implied by these least square fits differ, in some cases substantially, from the actual source flow rates in the experimental runs. The error in the calculated flow rates compared to the actual flow rate ranged from 4% to 220%. Many of the calculated source flow rates fall close to the line of expected flow rates, but some, particularly those with anomalous data points mentioned above, have large errors. By having two free parameters, the curves can achieve small least squares error, but be inconsistent with conditions in the experiment, such as the source flow rate.

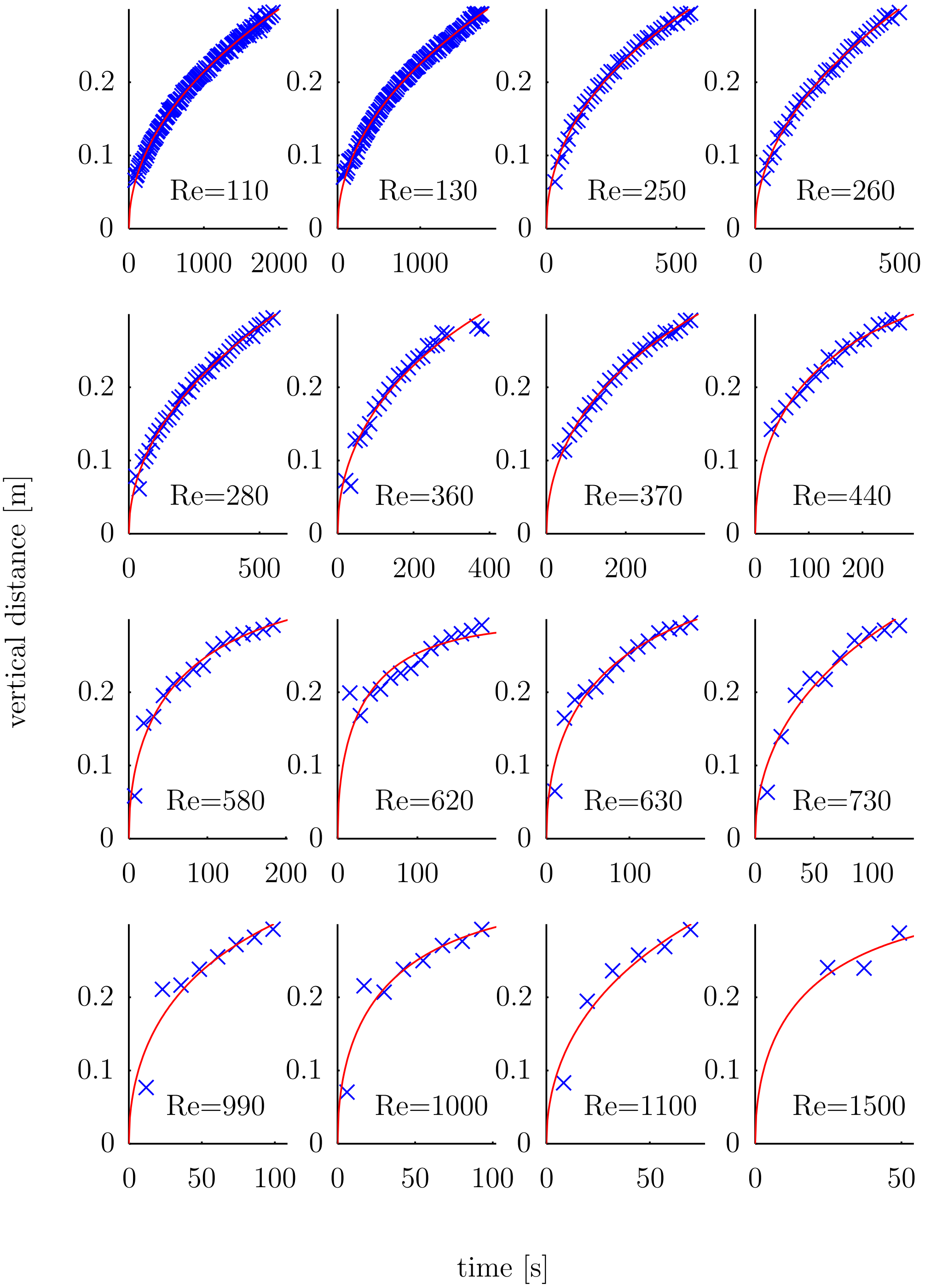

FIGURE 5.6: Optimised curve fits to the front height using T_s and D_s as free parameters. The source Reynolds number is given for each plot.

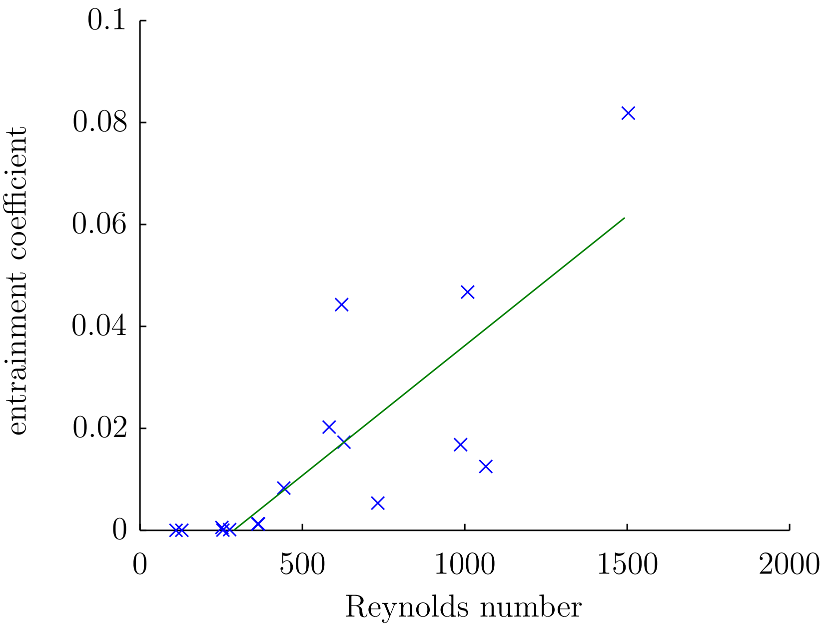

FIGURE 5.7: The entrainment coefficient calculated from the least squares optimisation using T_s and D_s as free parameters.

The calculation of E from the time series of the ponding region height can be improved by adding the known source flow rate as a constraint on the least squares optimisation routine. When the top of the ponded region reaches the source height, there is no entrainment into the gravity current and the only contribution to the increase in volume of the ponded region comes from the source flow rate, Q_s. Accounting for the width of the tank at the source height gives the rise speed as

$$\frac{dH}{dT} = \frac{Q_s \sin\theta \cos\theta}{H_p}, \tag{5.3}$$

where H_p is the height of the physical source above the bottom vertex of the tank. From (3.15), the rise speed of the front when it reaches H_p is

$$\begin{aligned} \frac{dH}{dT} &= \frac{D_s}{T_s}\frac{\zeta}{1-\zeta} & (5.4)\\ &= \frac{D_s}{T_s}\frac{D_s - H_p}{H_p}. & (5.5) \end{aligned}$$

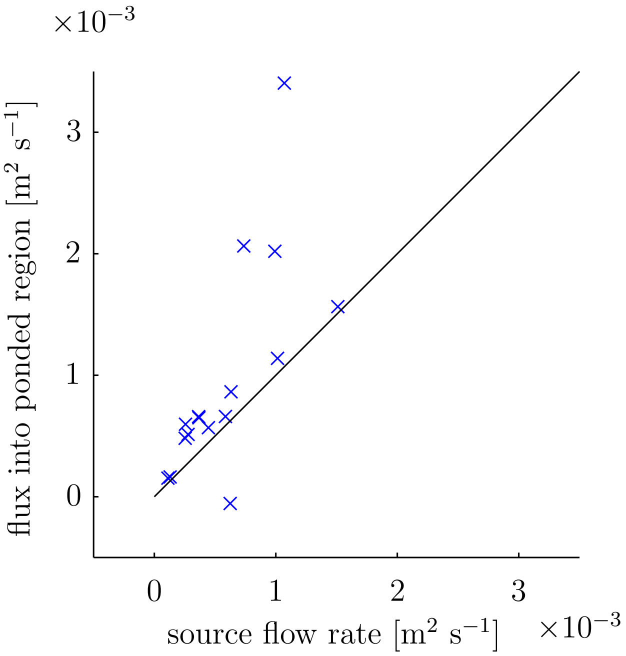

FIGURE 5.8: The source flow rate calculated from the flux into the ponded region compared with the flow rate delivered to the source in the experimental runs. The line shows where the points would lie if the two flow rates matched.

Equating these expressions for dH/dT allows the parameter T_s to be expressed as

$$T_s = \frac{D_s(D_s - H_p)}{Q_s \sin\theta \cos\theta} \tag{5.6}$$

in terms of known quantities and the optimisation control parameter D_s. Substituting (5.6) for T_s in (5.1) reduces the number of control parameters in the optimisation to one, D_s alone.

The optimisation can be carried out with T_s as the single control parameter instead. It is better to use D_s as the control parameter than T_s, because the source flow rate is known at the explicit height H_p rather than the time, T_p implied from the curve (5.1), for the first front to reach H_p. In practice, using T_s was found to give larger residual errors in the least square error solution and less clear trends in derived parameters, such as E.

The fits from the least squares method using the single control parameter are shown in figure 5.9. The fitted curves do not follow the data quite as closely as in the optimisation using two parameters. Reducing the number of free param-

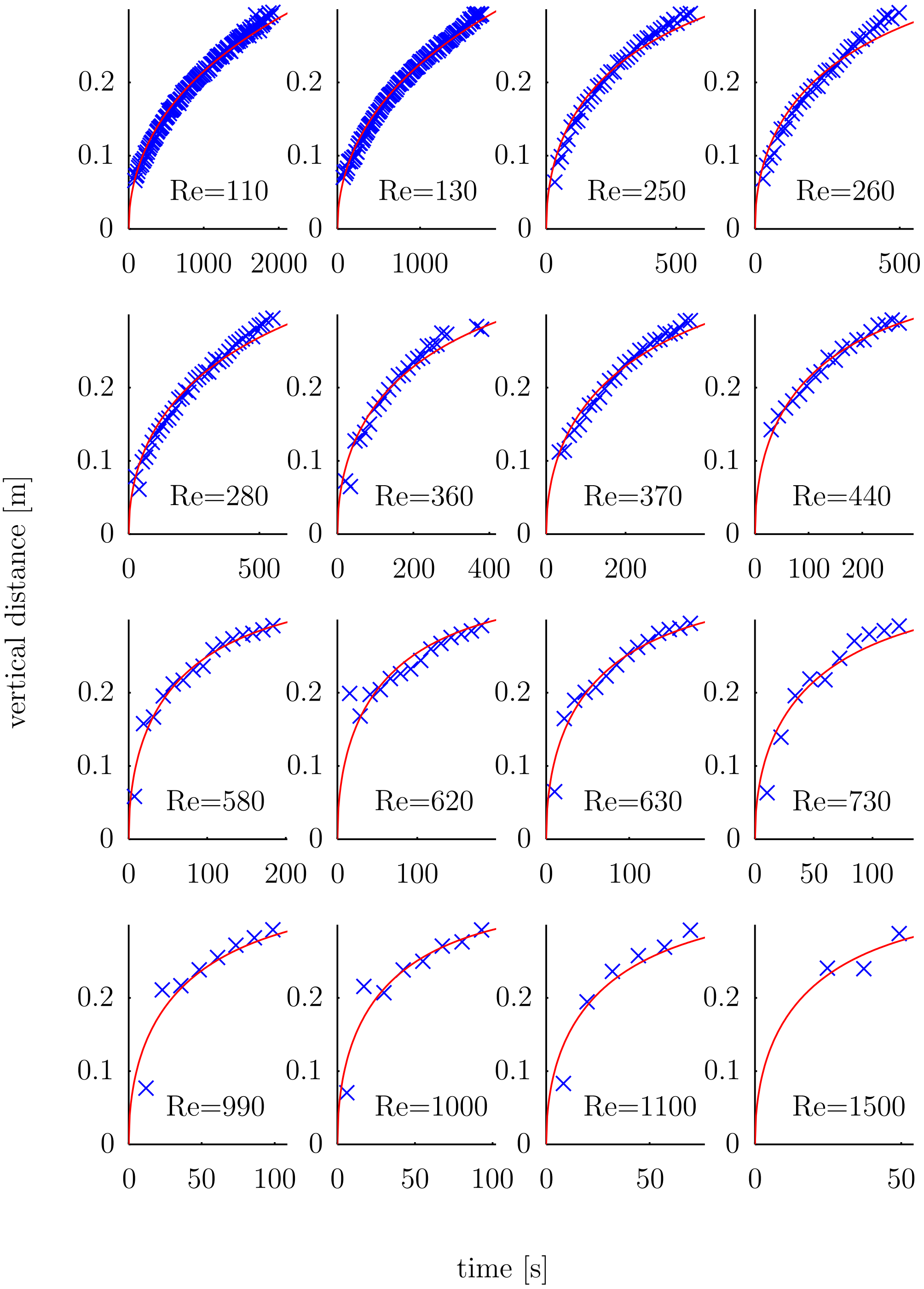

FIGURE 5.9: Optimised fits using the time as the fitting parameter.

eters by adding constraints to the optimisation routine was expected to increase the residual error. The single parameter best-fit curves are now, by construction, consistent with the source flow rates, and the trends with rising Re_s in the quantities derived from the best-fit curves are much clearer. The single parameter least square curves are also less affected by noise in the data (such as the anomalous first data point in the $Re = 620$ run). This means that a criteria for discarding anomalous points is not required.

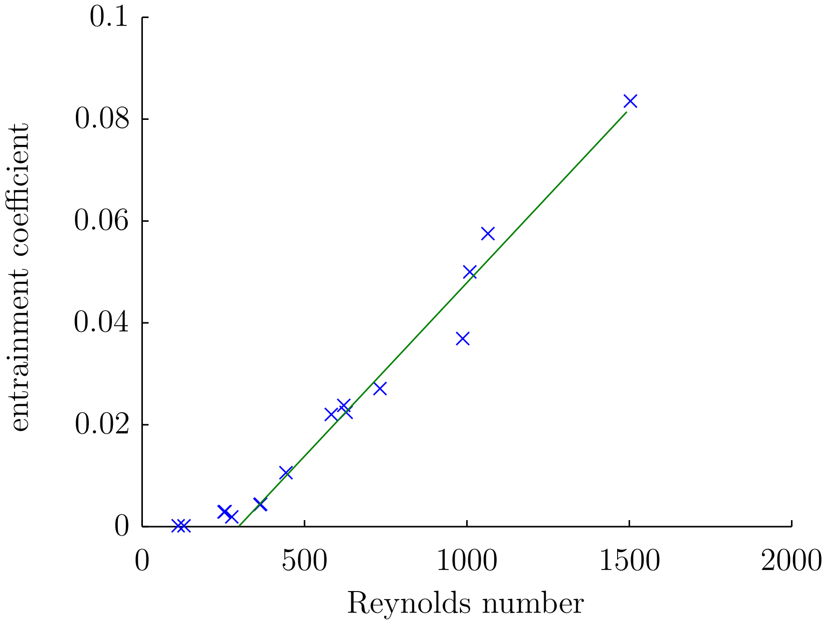

FIGURE 5.10: The entrainment coefficient calculated from the least squares optimisation using D_s as the only free parameter.

The values of E derived from the single control parameter optimisation are shown in figure 5.10. The one parameter fit gives a trend in E with much less scatter than the two parameter fit, shown in figure 5.7. The relationship between E and Re_s is similar. There is, as before, much less entrainment ($E < 2 \times 10^{-4}$) at $Re_s < 200$ than at higher Re_s. The trend for $Re_s > 300$ is well approximated by a linear trend with equation

$$E = 6.8 \times 10^{-5} Re_s - 0.020. \tag{5.7}$$

The values of E for $200 < Re_s < 300$ do not fit the linear trend very well. This is supported by the gravity current boundary visualisation in figure 5.4 which suggested that the turbulence was in a transitional regime around this value of Re_s. This parameterisation for E may be combined with (5.2) and (5.6) to give an expression for the depth of the physical source below the virtual origin

$$\begin{aligned} D_p &= D_s - H_p && (5.8)\\ &= \frac{Q_s \sin^{2/3}\theta}{E^{2/3}F_0^{1/3}} && (5.9)\\ &= \frac{Q_s \sin^{2/3}\theta}{(6.8\times 10^{-5}Re_s - 0.020)^{2/3}F_0^{1/3}}. && (5.10)\end{aligned}$$

This length scale is plotted in figure 5.11 for data with $Re_s > 300$ where (5.7) is valid. An expression for D_p is required to compare the theoretical models, which refer to the virtual origin, with the experimental observations, which refer to the physical origin. The simplification that $D_p = 0$ is no longer required. The empirical trend shows that as Re_s reduces, the depth of the physical source below the virtual origin increases. This is because as E decreases it takes a larger distance for the current to entrain the volume of fluid required at the physical source.

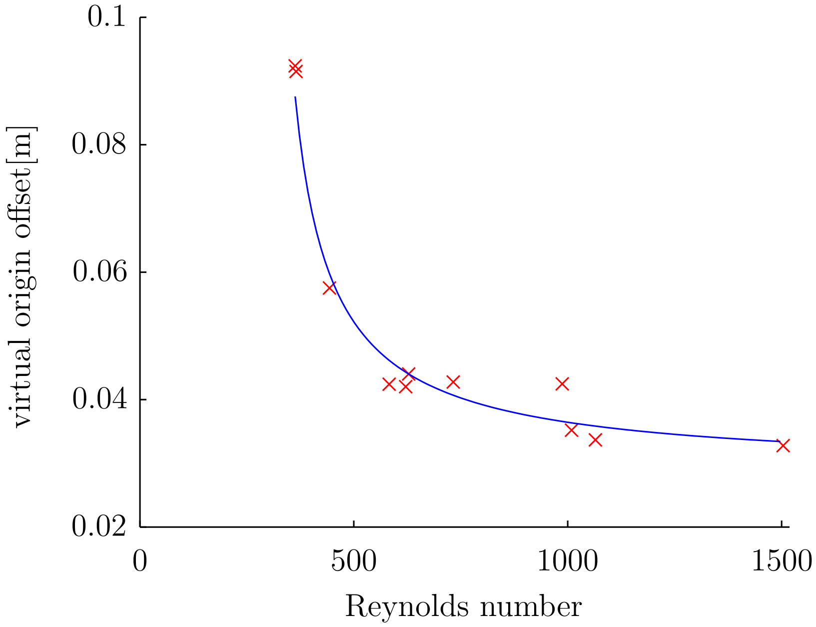

FIGURE 5.11: The distance of the physical source beneath the virtual origin found from the least squares optimisation using D_s as the only free parameter.

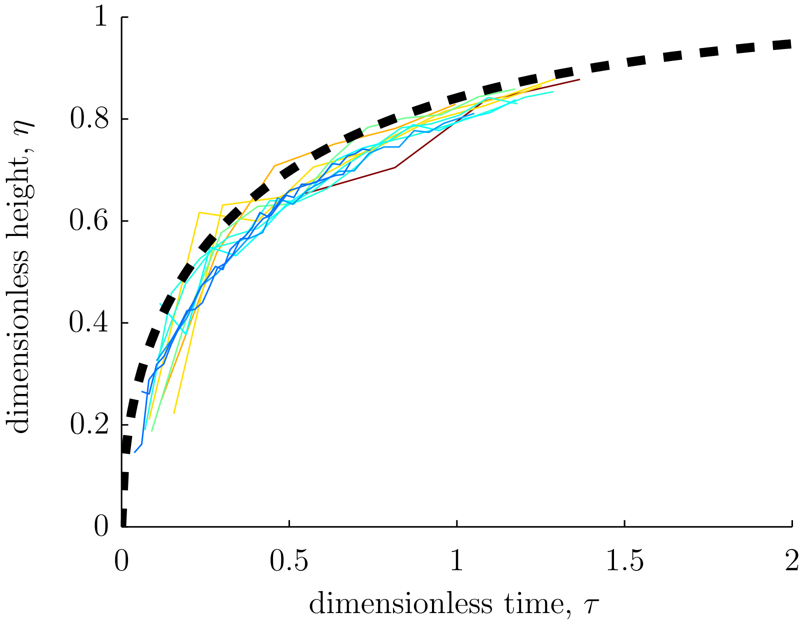

FIGURE 5.12: The evolution of the front height, plotted in dimensionless quantities using a variable value of E given by (5.7). The theoretical prediction is plotted with the dashed line. The colour scales with Re_s for the experiment, from blue at 110 to red at 1500.

With the trends observed from the experiment for E and D_s, (5.7) and (5.10), the plot of dimensionless experimental data shown in figure 5.2 can now be modified to include the variation of E with the Re_s of the current. The resulting collapse of the experimental data is shown in figure 5.12.

Using the empirically observed linear relationship for $E(Re_s)$, we successfully collapsed the observed first front heights onto the theoretical curve. The trend in the deviation of the data from the theoretical curve with Re_s, which was apparent in figure 5.2, is not present when this linear variation in E is used. The length scale and time scale of the data match the theory, which was enforced in some sense by using the least squares fitting to find E. None-the-less, the linear relationship for $E(Re_s)$ was a good approximation to the observed variation of E with Re_s. More significantly, the form of the first front curves match well onto the theoretically predicted curve. This is in no way set by the least squares optimisation. The close match of the data to the form of the theoretical curve demonstrates that the entraining gravity current, with a constant value of E set by Re_s, is a good model of the mixing occurring in the flow.

To check that the observed variation in E with Re_s was not caused by an implicit variation of Ri with Re_s, the values of Ri in the experiments were estimated. The velocity of the fluid in the gravity current was estimated from the speed, U_h, of the head of the gravity current. The speed of the head was shown by Britter & Linden (1980) to move at 60% of the speed of the following fluid in the tail of the current, giving the Richardson number for the current as $Ri = 0.6^3 F_0 / U_h^3$. The values of Ri in the experiments are shown in figure 5.13. The values of Ri observed here fall within the spread of those measured by Britter & Linden (1980) at the nearest inclinations they used, 5° and 10°. At these inclinations, they observed that Ri varied between 0.050 and 0.22. Figure 5.13 shows that over the range $250 < Re_s < 1100$ the value of Ri is constant, to within the scatter of the data. The error in the measured Ri, indicated by the error bars, was contributed mainly from the error in measuring the speed of the head. Over this range Re increases by a factor of 4.4 and E increases by a factor of 30, with a clear correlation as shown in figure 5.10. This suggests that over this range of Re_s, E depends strongly on Re_s and is independent of Ri. Outside the range $250 < Re_s < 1100$ there is some indication that Ri decreases with increasing source flow rate, but there is not a clear enough signal in the data relative to the noise for this to be certain.

Many previous studies have mentioned that the Reynolds number has influenced the entrainment into gravity currents (Ellison & Turner, 1959; Baines, 2001), but they have not quantified the impact on E in detail. Baines observed that at approximately $Re_s > 700$ the gravity current in his experiments became turbulent, in reasonable agreement with the present qualitative and quantitative observations. Experiments in rotating gravity currents (Cenedese & Adduce, 2008) have examined the impact of Reynolds number on entrainment quantitatively. Their experiments found a linear relationship for $E(Re_s)$ in the range $40 < Re_s < 100$ and a slightly sublinear relationship at higher Re_s. This relationship is similar to the present results, to within the accuracy of the measurements. It is interesting that $E(Re_s)$ in the non-rotating case, measured for the first time in this study, is so similar to the rotating case. This similarity is presumably because the length scales at which entrainment occurs in the rotating case are much smaller than the Rossby radius, the length at which the effects of rotation become significant.

The values of entrainment from the present experiments are plotted in fig-

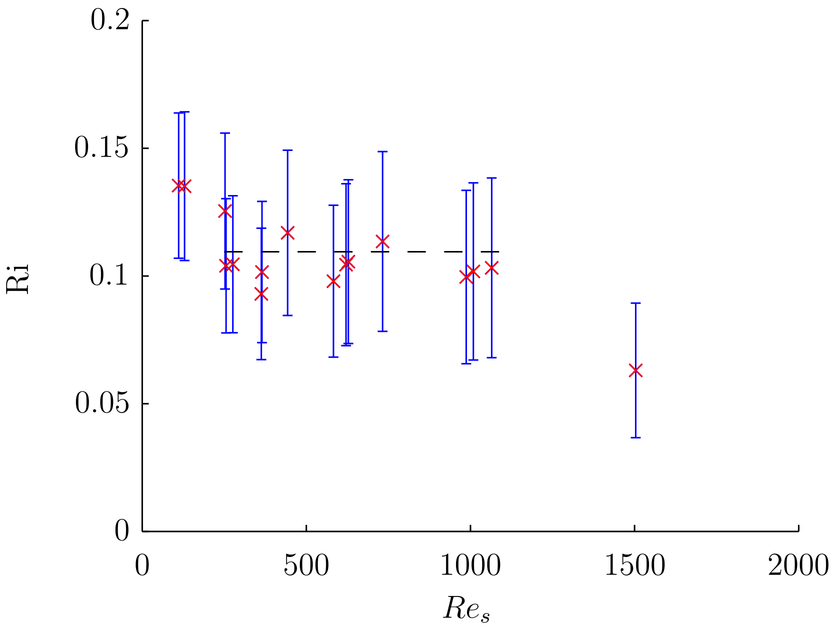

FIGURE 5.13: The indicative Richardson number of the gravity current in experiments at different source Reynolds numbers. The dashed line shows the mean of the values in the range $250 < Re_s < 1100$.

ure 5.14, alongside previously published measurements and the parameterisation given by Cenedese & Adduce (2010) and Turner (1986), discussed in section 1.5. The values of E in the present study were within the range of previously observations. However, at the lower values of Re_s used, approximately $Re_s < 440$, the entrainment rate is substantially lower than other observations at similar values of Fr. This is presumably because none of the previous studies examined laminar gravity currents at these values of Fr. The field measurements of Fernandez & Imberger (2006) in a limnological setting have higher entrainment coefficients than the oceanographic observations at these values of Fr. This suggests the greater bottom roughness typical of lakes increases the entrainment. These data are useful as they give more data in the sparsely populated parameter regimes highlighted by Cenedese & Adduce (2010).

The linear rise in E by over a factor of 3 as Re_s changes from 500 to 1000, typical at laboratory scales, should be considered when interpreting results of laboratory experiments. To assume that changes in Re do not affect E is often mistaken.

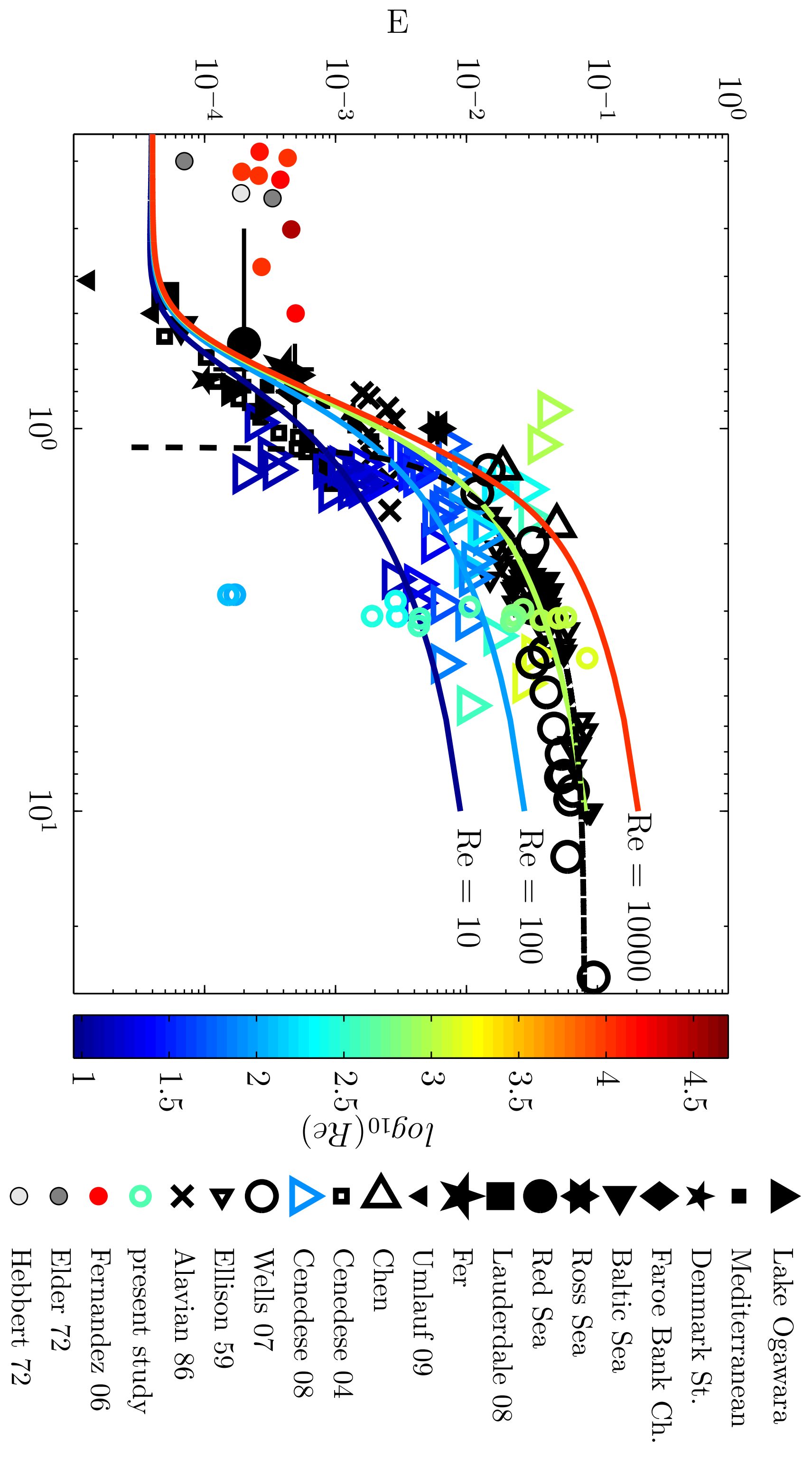

Figure 5.14: Observed entrainment coefficient measurements. Data (black symbols) and parameterisations (solid lines) from Cenedese & Adduce (2010). Dashed line shows the parameterisation from Turner (1986). Data is included from the present study (coloured open circles) and limnological observations (small filled circles) (Fernandez & Imberger, 2006). Colour scale indicates Reynolds number, where available.

5.1.3 Limits of the parameterisation for E in the filling box

The linear trend in $E(Re_s)$ is not valid for approximately $Re_s < 300$. The value of E given by (5.7) becomes negative, which is not physically meaningful. The data in figure 5.10 suggest that $E \to 0$ as $Re_s \to 0$, following a different trend from the higher values of Re_s. It would be interesting to take measurements of E with a more sensitive apparatus (Baines, 1983) to look at the transition in E at these low values of Re_s, where the transition to a turbulent gravity current occurs.

The linear trend in $E(Re_s)$ must also have an upper limit, as the entrainment coefficient cannot linearly increase without limit. The value found at $Re_s = 1500$, the largest flow rate used in the apparatus, suggests that the linear trend extends to at least this value of Re_s. However, the filling process was so fast that only 3 data points for the ponded region thickness could be taken. These few data points are not enough to assert that the form of the first front filling curve followed the functional form for an entraining gravity current. The greatest value measured reliably was $Re_s = 1100$, so we will confine our conclusions to the trends at $Re_s < 1100$. Also, the gravity current was most energetic at this high flow rate and the mixing generated by the current crashing against the back wall was becoming significant, potentially increasing the value measured for E above the actual value. Further experiments in larger tanks are required to see if E at $Re_s > 1100$ continue to increase to higher values and find the value of Re_s at which E stops increasing.

The entrainment rates measured here are larger than those of other laboratory experiments. Ellison & Turner (1959) found entrainment rates on a slope of 12° ranging from 0.015 to 0.02. It is not clear what the Reynolds number was in Ellison and Turner's experiments, but they were in a similar range to that considered here. Atmospheric observations (Princevac *et al.*, 2005) at very high Reynolds numbers of 10^7 found much higher entrainment rates, approximately 0.07, at Richardson numbers similar to the present laboratory experiments.

The higher values for E found here relative to other laboratory experiments may be because the first front of the ponded region was identified by a very low concentration threshold, 10% of the source concentration. If the concentration used to define the first front were increased, the first front would be identified at a lower height and the entrainment parameter would be reduced. When partial entrainment occurs within the gravity current, unlike the complete homogenisation assumed by the top hat model, the volume of entrained fluid depends on the concentration threshold used to define fluid as having been entrained.

The value of E in the present work is an upper bound, because mixing at the head of the gravity current and in the overturning at the back wall was included in the measurement of entrainment. This did not occur in the Ellison & Turner (1959) study.

5.2 Qualitative observations within the ponded region

In this section we will discuss the flow within the ponded region. To visualise how the source fluid is transported through the basin, pulses of different coloured dyes were introduced to the continuously inflowing gravity current. The dye was added through a long needle into the vigorously circulating pure source fluid at the back of the inlet unit. The dye was pre-diluted with fluid of the source density to ensure that it did not appreciably change the density of the inflow fluid that it was injected into. The photographs were processed to make the coloured dye more clearly visible. The intensity of the red, green and blue channels of each image were divided by the intensity of the respective channel in an initial image with no dye present. A video showing the dye pulse visualisation of the entire filling process is available at `http://www.repository.cam.ac.uk/handle/1810/245309`, and photographs from this video at five second intervals are given in figure 5.15. The photographs in figure 5.16, at two second intervals, show the gravity current falling through the ambient with more temporal resolution. In this run, the source flow rate was 0.094 L s^{-1}, the source reduced gravity was 0.6 m s^{-2}. The Reynolds number at the source was 600.

The first images of the sequence, figures 5.15(a) to 5.15(c), show the blue dye in the starting gravity current as it first travelled down the slope. The head of the gravity current is clearly visible in figure 5.15(b). In figure 5.15(c) the head had just reached the end wall. The head crashed against the back wall, shown in figure

5.15(d). Waves were reflected back away from the wall, seen in figures 5.15(e) to 5.15(f), whilst the first front continued to rise as more fluid was delivered to the ponded region by the gravity current.

Between figures 5.15(i) and 5.15(j) a pulse of the red dye was injected into the source fluid. The red dye can be seen descending in the gravity current in figure 5.15(j). There was no head feature to the gravity current because this dye was added to a continuous-flux gravity current, unlike in figure 5.15(b). In figure 5.15(k) some of red dye in the gravity current had almost reached the end wall. The lower part of the gravity current, closest to the inclined base, had a lower intensity of dye because the current had been refreshed with undyed source fluid. Red dye remained in the outer layers of the gravity current, which peeled away from the current. This efflux from the gravity current can be seen, in figures 5.15(k) to 5.15(o), entering the ambient directly at a range of depths within the stratified ponded region. Some blue fluid can be seen within the gravity current beneath the red dye. This fluid had been entrained into the gravity current from within the ponded region. Between figures 5.15(o) and 5.15(p), a pulse of green dye was injected into the source fluid. The green fluid peeled away from the outer layer of the gravity current, as the red dye did before it, to directly enter the ambient at a range of heights within the ponded region. In figure 5.15(t), the top of the ponded region reached the source unit, and the experiment was ended.

The movement of the dye shows that all the source fluid descends to the ponded region. No dye was visible above the ponded region. This shows that no fluid from the gravity current was able to intrude into the uniform density part of the ambient.

The observed peeling from the gravity current was inconsistent with a persistently entraining gravity current model, discussed in section 3.3, because the fluid in the gravity current did not all descend to the bottom of the ponded region. The observed efflux from the current at intermediate depths within the ponded region was partially consistent with the peeling model, described in 3.4. Fluid from the gravity current moved directly from the gravity current to its neutral buoyancy depth within the ponded region. However, the dye showed that further mixing of fluid occurred within the ponded region, contrary to the assumption of no mixing in the ponded region made in the peeling model. Mixing occurred as dyed fluid previously in the ambient was entrained into the gravity current, shown for example by the blue dye in the gravity current in figure 5.15(l). Also, continued turbulent activity could be seen in the eddies at the front of the red-dyed current as it moved through the ponded region. This indicates that further mixing did occur within the ponded region. The density distribution in the gravity current when it reached the ponded region was therefore not preserved as the fluid moved to its neutral buoyancy depth, but was altered by the further mixing. This means that the assumption of the peeling model, that fluid from the gravity current moves to its neutral buoyancy depth in the ponded region without further mixing, was only approximately correct. The peeling model may nonetheless prove to be a useful approximation to give a lower bound on the amount of mixing that occurs in the gravity current. This will be judged by comparison with the measured density profiles, which we will discuss in section 5.3.

The same visualisation was repeated at higher and lower Re_s, and a similar peeling phenomenon was observed. The details of the peeling were slightly different, as we will now discuss.

An experiment in which the source had $Re_s = 930$ is shown in figure 5.17. In a similar way to that described above, red dye was injected into the starting gravity current. Later, blue and then green dye were injected into the source fluid. These diluted dyes can be seen weakly in figure 5.17(a) in the the ponded part of the ambient. At 6 s before the first photograph was taken a pulse of red dye was injected. This pulse of more concentrated dye can be seen flowing down the slope. This pulse of dye was all transported to the ponded region. Part of this dye pulse falls to the bottom of the basin and part peels away at intermediate depths into the ponded region. Between figures 5.17(b) and 5.17(c) a pulse of blue dye was injected which repeats the path of the red dye before it. The clouds of dye can be seen to be more diffuse in this set of images than in the previous set, due to the increased turbulence in the current at the higher Reynolds number.

When the source flow rate was small enough for the gravity current to be laminar, the flow was somewhat different. Such a case, in which $Re_s = 100$, is shown in figure 5.18. The photographs, taken at 35 s intervals, show the green dye as it was moved from the gravity current into the ponded region. In the same way as before, red dye was injected into the starting gravity current. Later, blue dye and, shortly before the image in figure 5.18(a), green dye were injected into the source of the continuous-flux gravity current. The majority of the red dye,

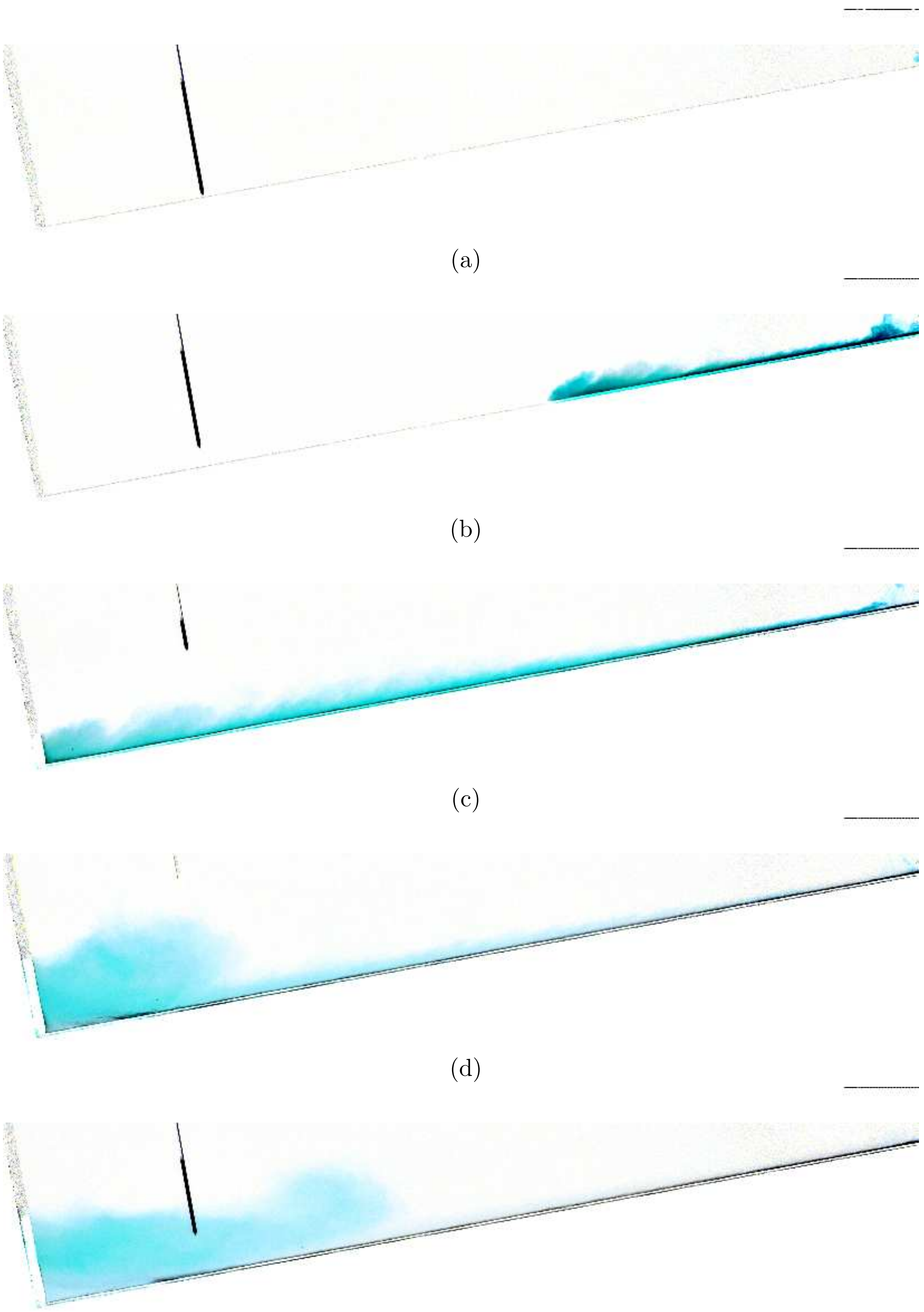

(a)

(b)

(c)

(d)

(e)

FIGURE 5.15: See overleaf for caption.

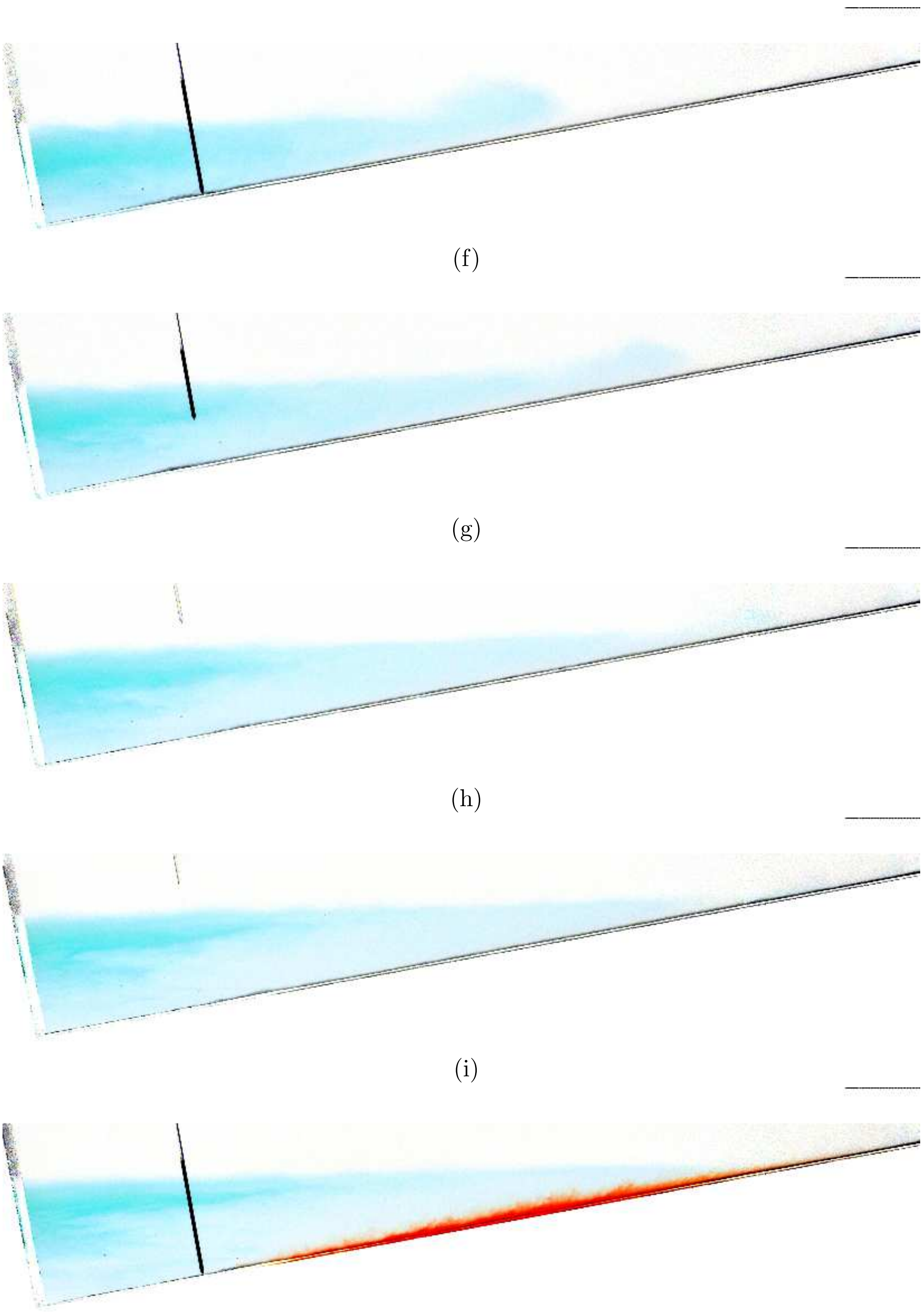

(f)

(g)

(h)

(i)

(j)

Figure 5.15: See overleaf for caption.

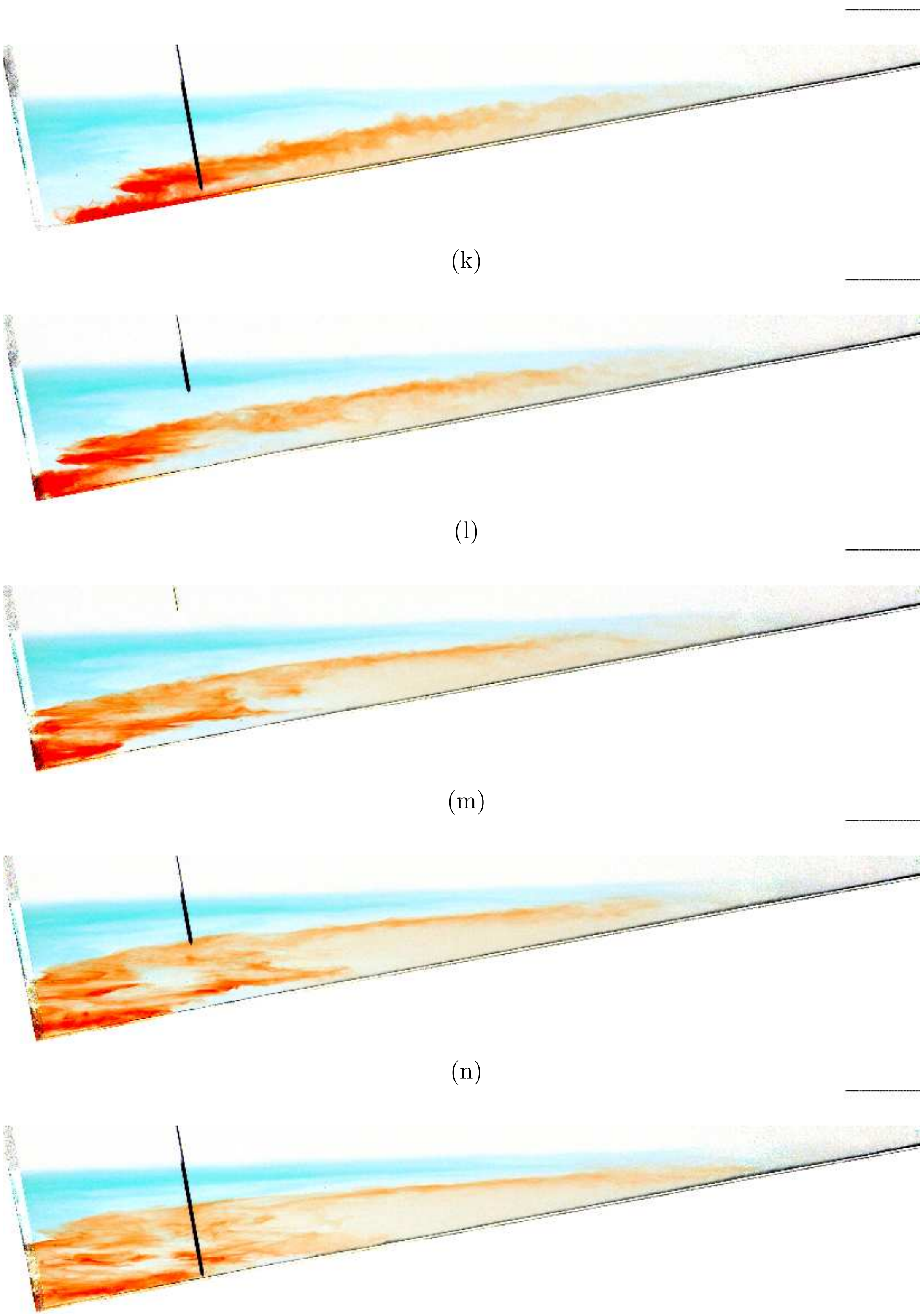

(k)

(l)

(m)

(n)

(o)

Figure 5.15: See overleaf for caption.

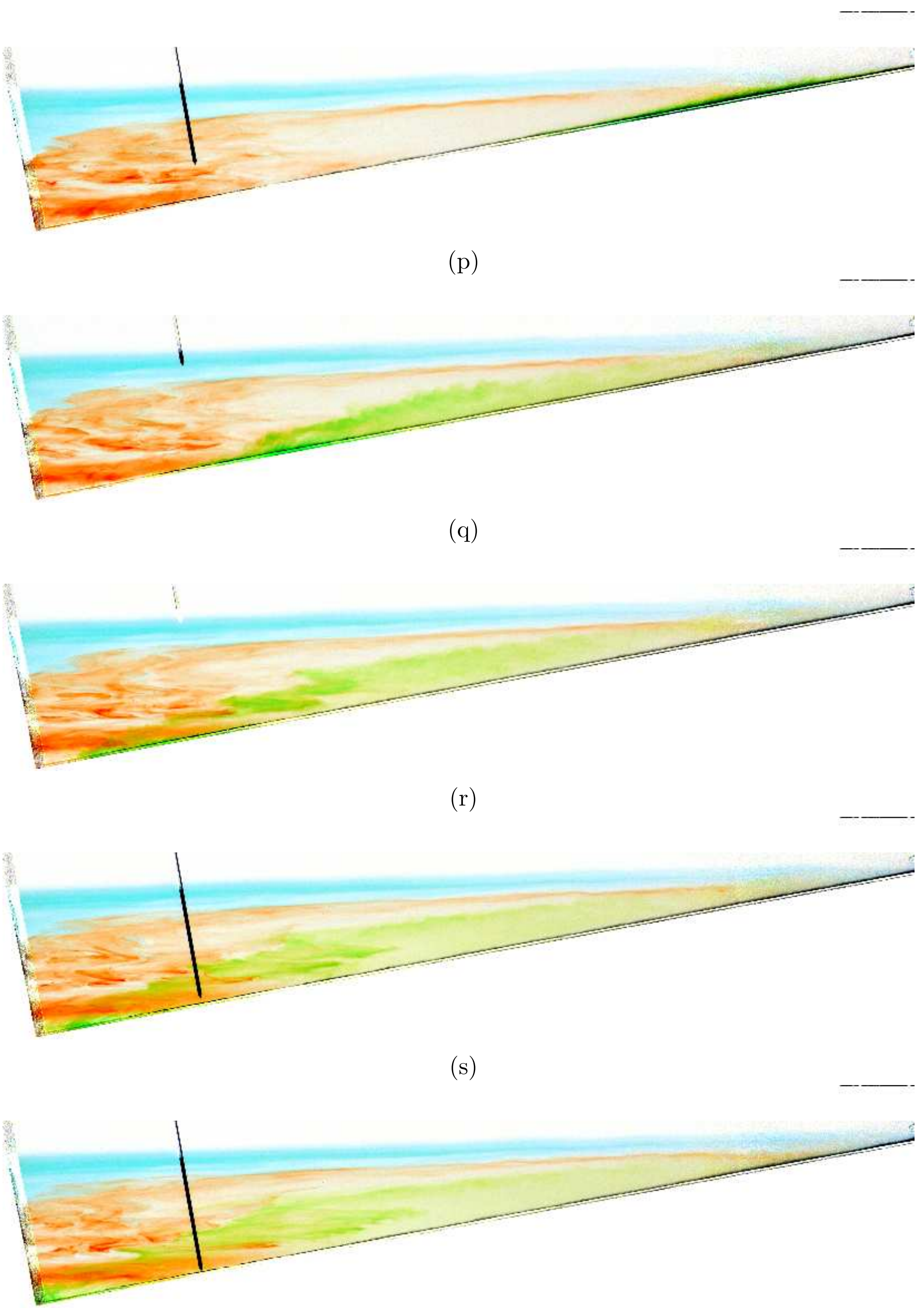
(p)

(q)

(r)

(s)

(t)

Figure 5.15: Images, at 10 second intervals, of consecutive pulses of different coloured dye, added to a continuous-flux gravity current at $Re_s = 600$ over the duration of the basin filling.

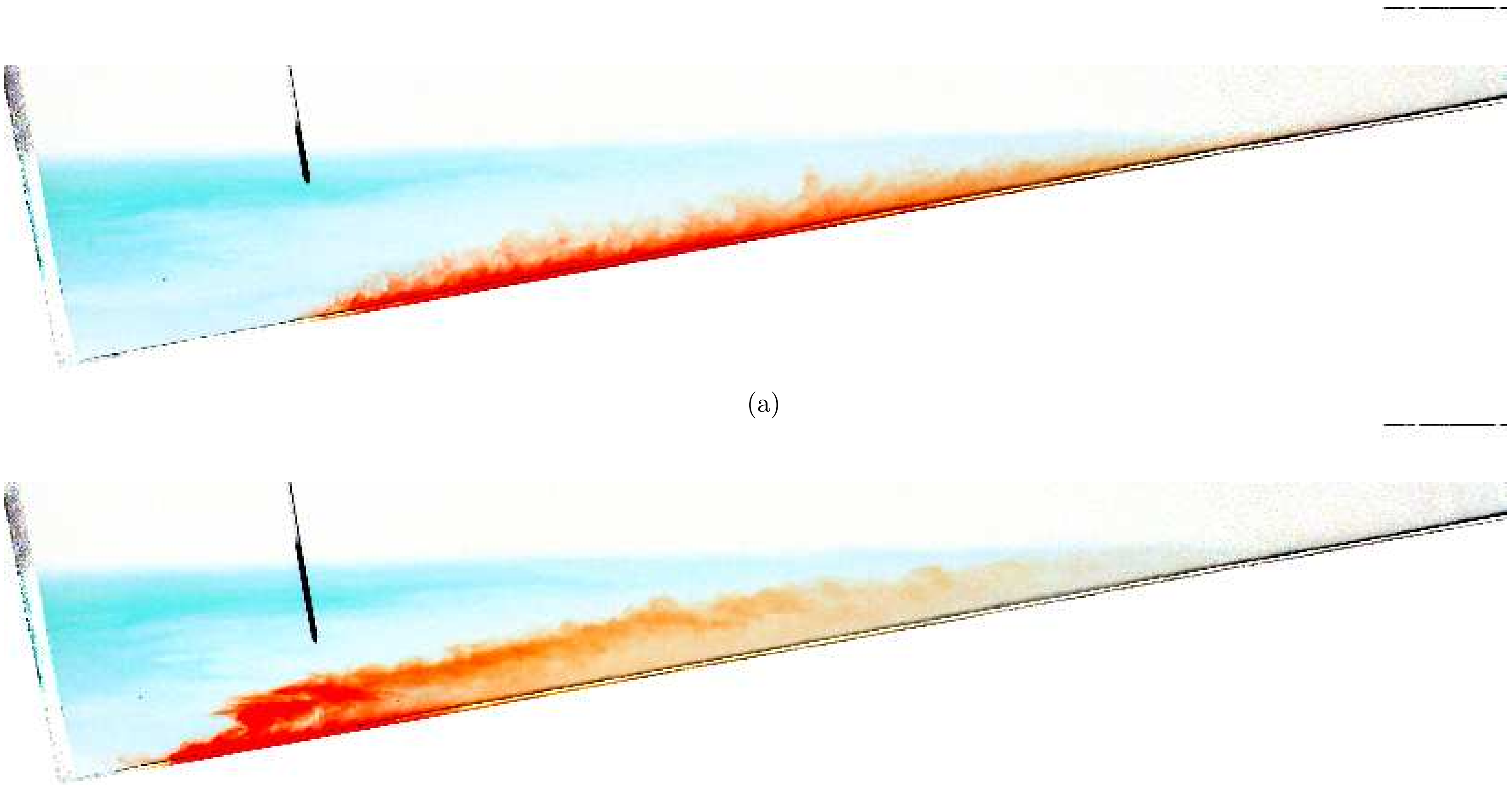

(a)

(b)

Figure 5.16: See overleaf for caption.

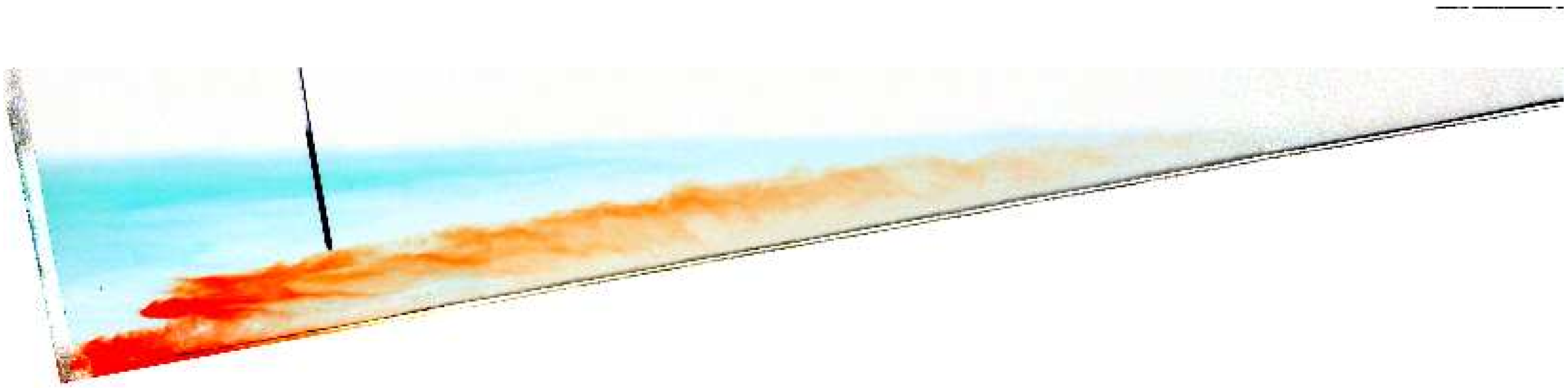

(c)

Figure 5.16: Images, at 2 second intervals, of a pulse of red dye in a continuous-flux gravity current at $Re_s = 600$. The red dye shows fluid at the top of the gravity current peels away from the current to enter the ambient fluid at all depths within the ponded region.

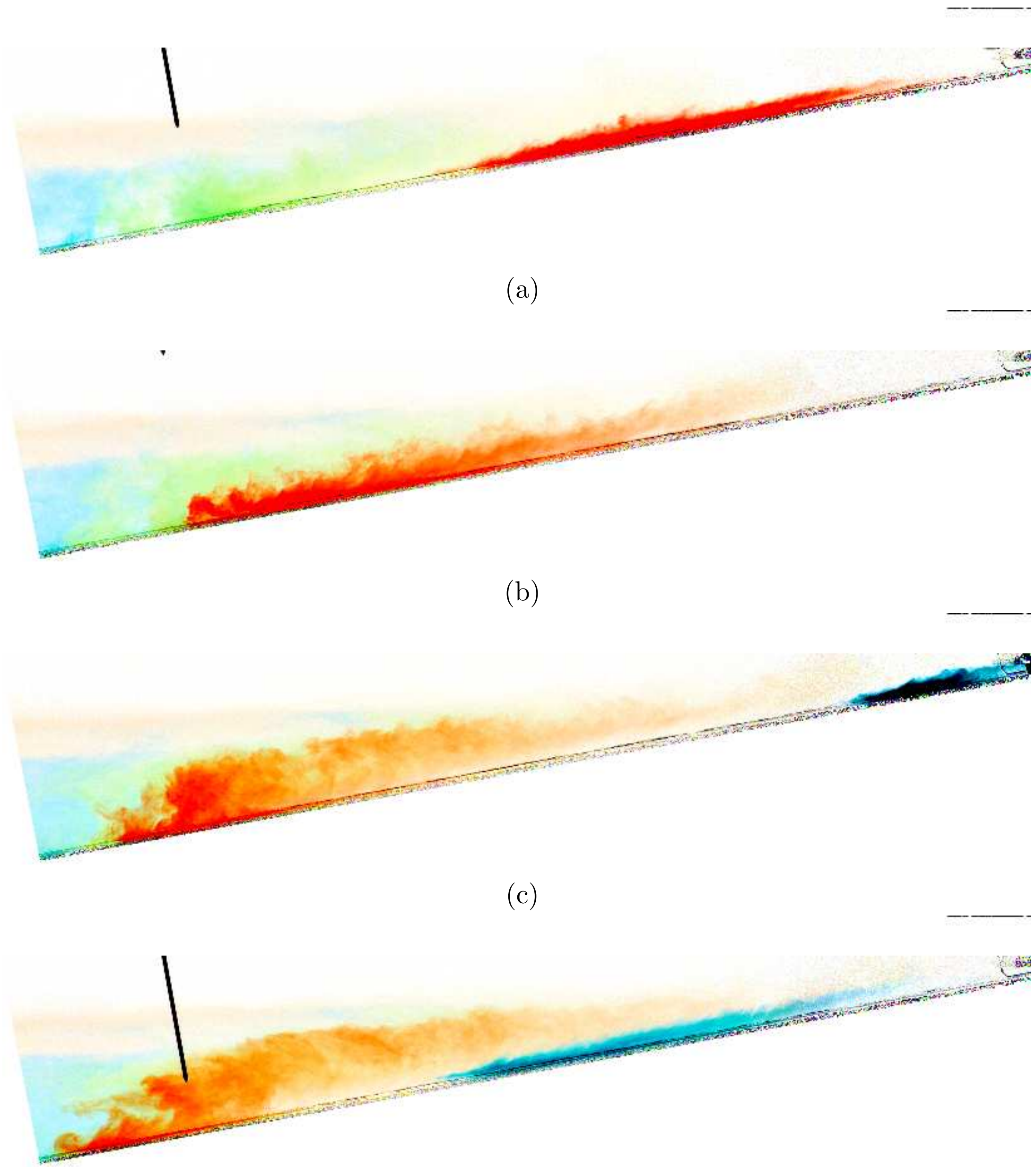

(a)

(b)

(c)

(d)

FIGURE 5.17: Images, at 5 second intervals, showing the evolution of a pulse of red dye injected into a continuous-flux gravity current at $Re_s = 930$.

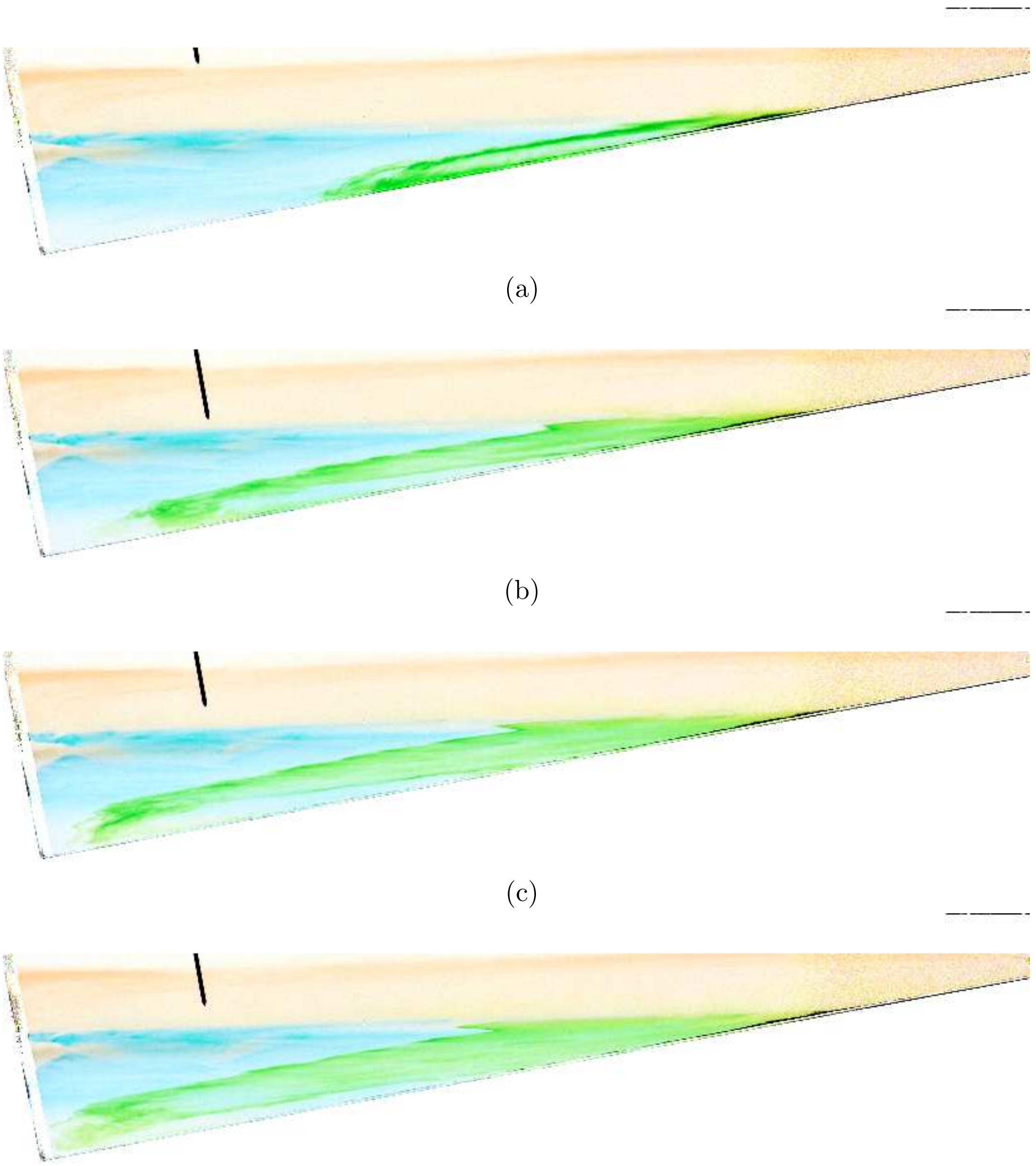

(a)

(b)

(c)

(d)

FIGURE 5.18: Images, at 35 second intervals, showing the evolution of a pulse of green dye injected into a continuous-flux gravity current at $Re_s = 100$.

which was in the head of the gravity current, forms a more diluted layer at the top of the gravity current. This is because the head of the gravity current entrained substantially more light ambient fluid than the continuous-flux, laminar gravity current behind it. Fluid which travelled in the head thus formed a dilute layer at the top of the ponded region. Some fluid dyed red, at the far left of the images, remained denser and was deposited lower in the ponded region. When the green pulse of dye entered the ponded region, some of the dye pulse was transported to the bottom of the ponded region and some peeled away at a range of depths within the ponded region, as in the higher Re_s runs. The motion within the ponded region was slower and much more laminar than in the higher Re_s runs. No eddies can be seen at the front of the dyed fluid and the internal waves in the ponded region were less energetic, unlike at higher Re_s. Fluid deposited later into the ponded region mainly remained closer to where the gravity current entered the ponded region.

The speed of fluid in the continuous-flux currents was measured very approximately from the movement of the dye pulses along the slope. This showed that, at $Re_s = 600$, fluid in the continuous-flux current moved faster than the head, by approximately 50 to 125%. As the fluid in the continuous-flux approached the end wall, it gradually slowed to much slower than the first front. The laminar currents, at low Re_s, descended significantly more slowly than the turbulent currents.

The dye pulse visualisation also showed features of the motion of the ambient fluid within the ponded region. Zigzagging streaks were visible in the pattern of the dye in the ponded fluid, such as in figures 5.15(s) and 5.15(t) towards the deepest end of the basin. These zigzag patterns look similar to the patterns formed by columnar mode internal waves in a stratified fluid (Imberger & Fandry, 1975). These internal waves may be present in the ponded region, driven by the exchange of fluid between the gravity current and the ambient ponded fluid (Wong *et al.*, 2001; Baines, 2001). The stratification in the ponded region reduces vertical motion in the fluid and gives rise to the large horizontal displacements made apparent by the zigzagging streaks of dye.

Significantly, the dye pulse visualisation showed that efflux from a gravity current was a robust feature of the experiments at different Re_s. We shall now discuss the density profiles measured during the experiment.

5.3 Measured density profiles within the ponded region

In this section, we will compare the predictions of the two entrainment models, described in sections 3.3 and 3.4, with the observed density profiles. The density profiles were measured with a continually descending traverse, as discussed in chapter 4.

To compare the experimental profiles, the time, depth and density measurements must be non-dimensionalised using the same scalings used in the theory, (3.9) and (3.14). This requires that the entrainment coefficient, E, the depth of the tank below the virtual origin, D_s, the angle of inclination of the slope, θ, and the source buoyancy flux, F_0 be specified for each experimental run. Of these, θ and F_0 can be measured straightforwardly from the apparatus, as described in section 4.1. As discussed in section 5.1.2, E and D_s vary with Re_s. The values used for the scalings were taken from the empirical, linearised relationship for E, (5.7), and the expression for D_s found from the source volume flux, (5.10).

The plots in figures 5.19 to 5.21 show the evolution of the experimental and modelled profiles in runs at 3 different Re_s, spanning the range of experiments with turbulent gravity currents. Plots are shown in figure 5.22 comparing the final observed profiles with the model for all the runs carried out in the range of Re_s $300 < Re_s \leq 1100$, in which the gravity current was turbulent. In this figure, only the last profile before the ponded region reached the source unit is shown for each run. The density profiles do not extend down to the bottom of the tank because the profiler was offset 0.3 m upslope from the end of the tank, preventing measurements from being taken at the very bottom of the tank. Only 1/30 of the volume of the tank below the source unit is in this unmeasured region, because the horizontal cross-sectional area of the tank reduces to zero at the bottom of the tank. Density profiles plotted against the cumulative volume from the bottom of the tank, given in figure 5.23, show the proportion of volume that was not profiled was small, to the point of being barely visible in these plots. We shall now discuss the evolution of the density profiles in the high, intermediate and low Re_s cases shown in these plots.

The observed profiles in figure 5.19 show a high Re_s run, $Re_s = 990$. From $\tau = 0$, source fluid ponds at the bottom of the basin. As time progresses, the

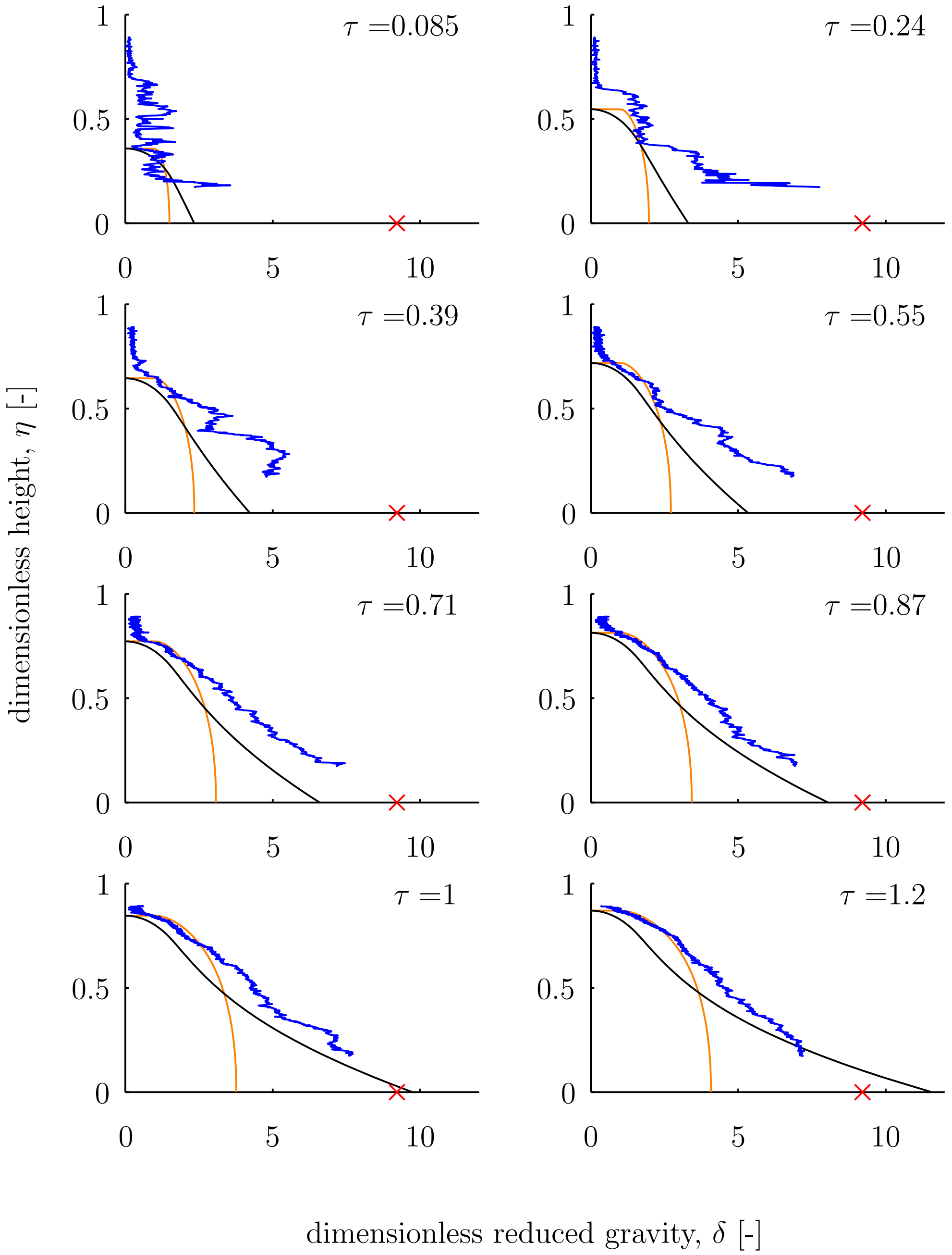

FIGURE 5.19: A time series of experimental profiles (blue line) plotted with the result of the persistently entraining model (orange line) and the peeling model (black line). The source flow gave $Re_s = 990$. The source density is indicated, in dimensionless units, by the red cross.

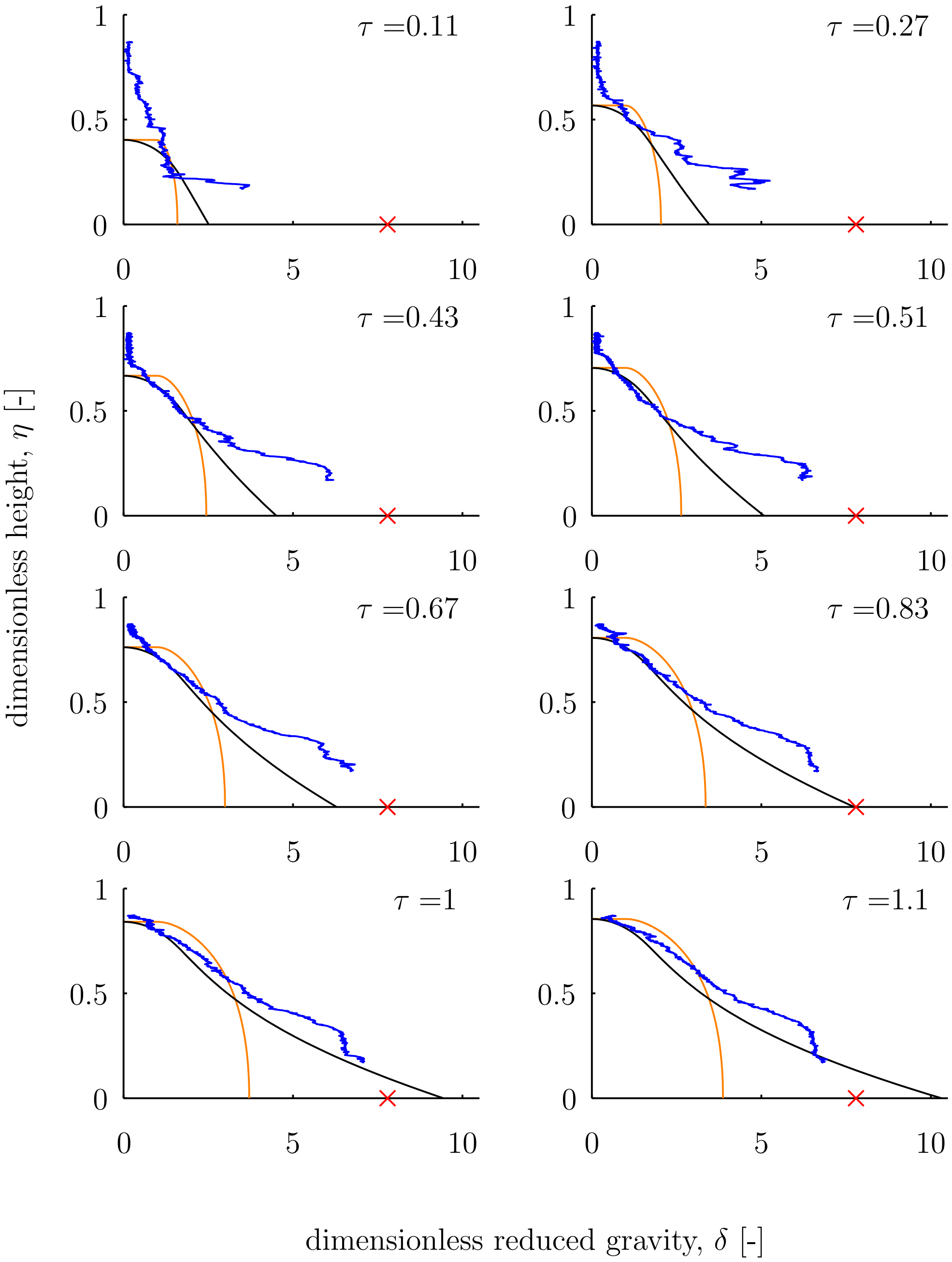

FIGURE 5.20: A time series of experimental profiles (blue line) plotted with the result of the persistently entraining model (orange line) and the peeling model (black line). The source flow gave $Re_s = 630$. The source density is indicated, in dimensionless units, by the red cross.

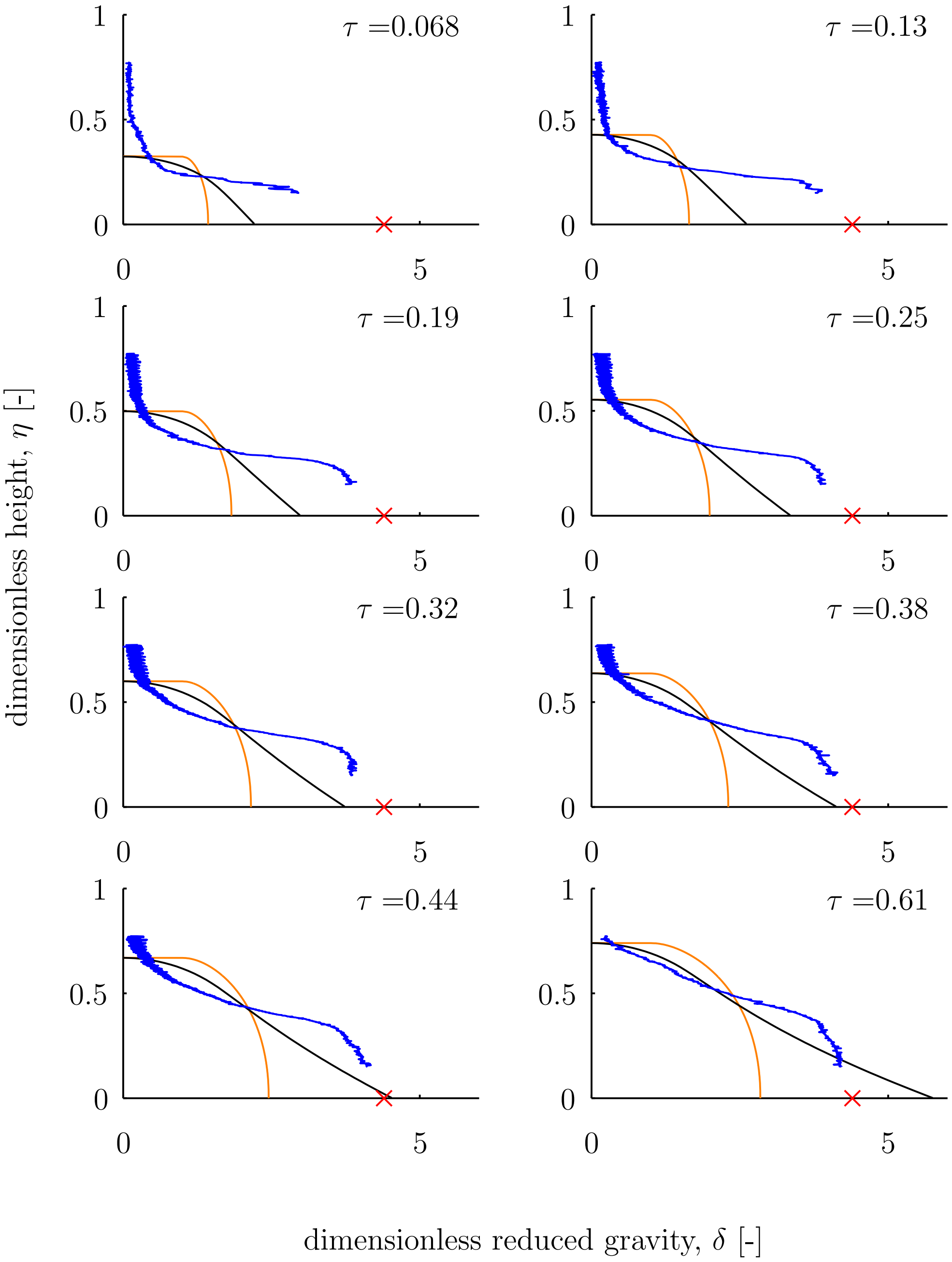

FIGURE 5.21: A time series of experimental profiles (blue line) plotted with the result of the persistently entraining model (orange line) and the peeling model (black line). The source flow gave $Re_s = 370$. The source density is indicated, in dimensionless units, by the red cross.

ponded region increases in thickness, reaching the height of the physical source, indicated by the top of the measured profile, at $\tau = 1.2$. The peak density in the ponded region also, on average, increases with time.

The large height to which the diluted source fluid reaches in the first traverse, at $\tau = 0.085$, is an artefact of the fact that the conductivity probe only measures the density at one point. A crest in the waves reflecting from the back wall passed through the location of the probe as this profile was being taken. The dilute source fluid shown reaching $\eta = 0.7$ did not fill the whole cross-sectional area. At the next profile, $\tau = 0.24$, the dense fluid fell to a lower depth, $\eta = 0.6$, with the isopycnals more horizontal. Because the horizontal cross-sectional area reduces at the bottom of the tank, the volume of the tank below the height $\eta = 0.65$ was only half the volume of the tank. The stratification established at $\tau = 0.24$ had homogeneous layers separated by large jumps in the density, rather than the continuous stratification shown in the models. This stratification was set up by the crashing of the gravity current against the back wall.

The peak density of the observed profiles at early times was larger than the prediction of either model. This was true in the early stages of runs at all values of Re_s. At $Re_s = 990$, the reduced gravity at the bottom of the profile was at 39% of the source reduced gravity in the first profile at $\tau = 0.085$, whereas the peeling model predicted 25% at the same dimensionless time and height. At the last profile, the fluid at the bottom of the profile was measured as 78% of the source density, whereas the peeling model predicted 85%. The fluid transported in the gravity current at the beginning of the experiment had a greater density than was assumed in the linear density profile used in the model. This fluid behind the head of the real gravity current was denser than in the model of the continuous-flux gravity current. The wake of the head could have prevented the current immediately behind the head from entraining ambient fluid, leading to the higher density. The density of fluid transported in the initial transient structures in the gravity current head were not accounted for in the model. Future work could use the observed stratification set up by the initial transient processes as the initial conditions for the numerical scheme to further evolve, but this was not pursued in the present work.

In the early traverses, the density profiles consist of layers of reasonably homogeneous density fluid, separated by interfaces with jumps in density. These layers

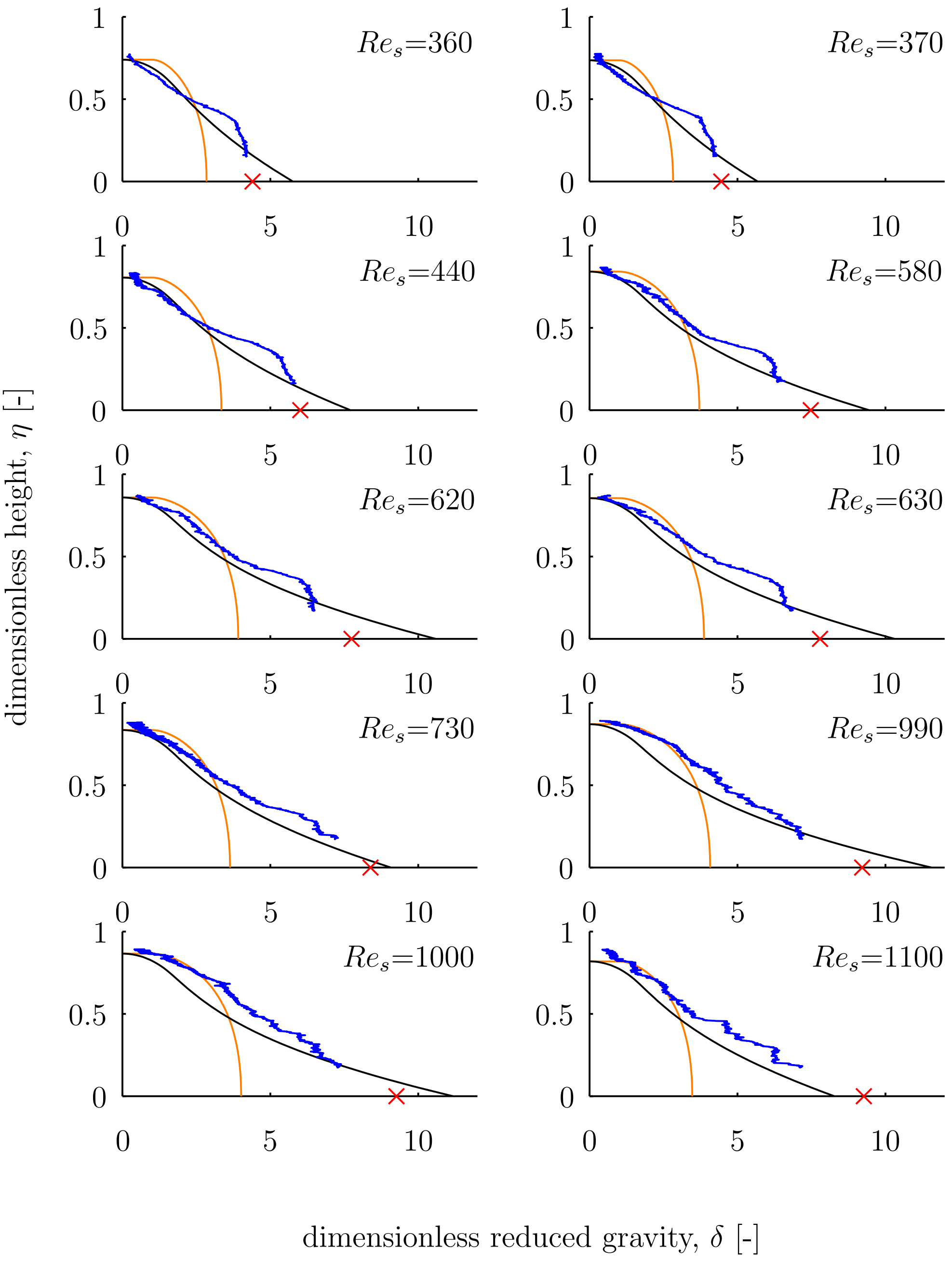

FIGURE 5.22: Density profile at the point when the ponded region reached the physical source. The measured profile is shown by the blue line, the persistently entraining model by the orange line and the peeling model by the black line. All runs in the range $350 < Re_s \leq 1100$ are shown. The source density is indicated, in dimensionless units, by the red cross.

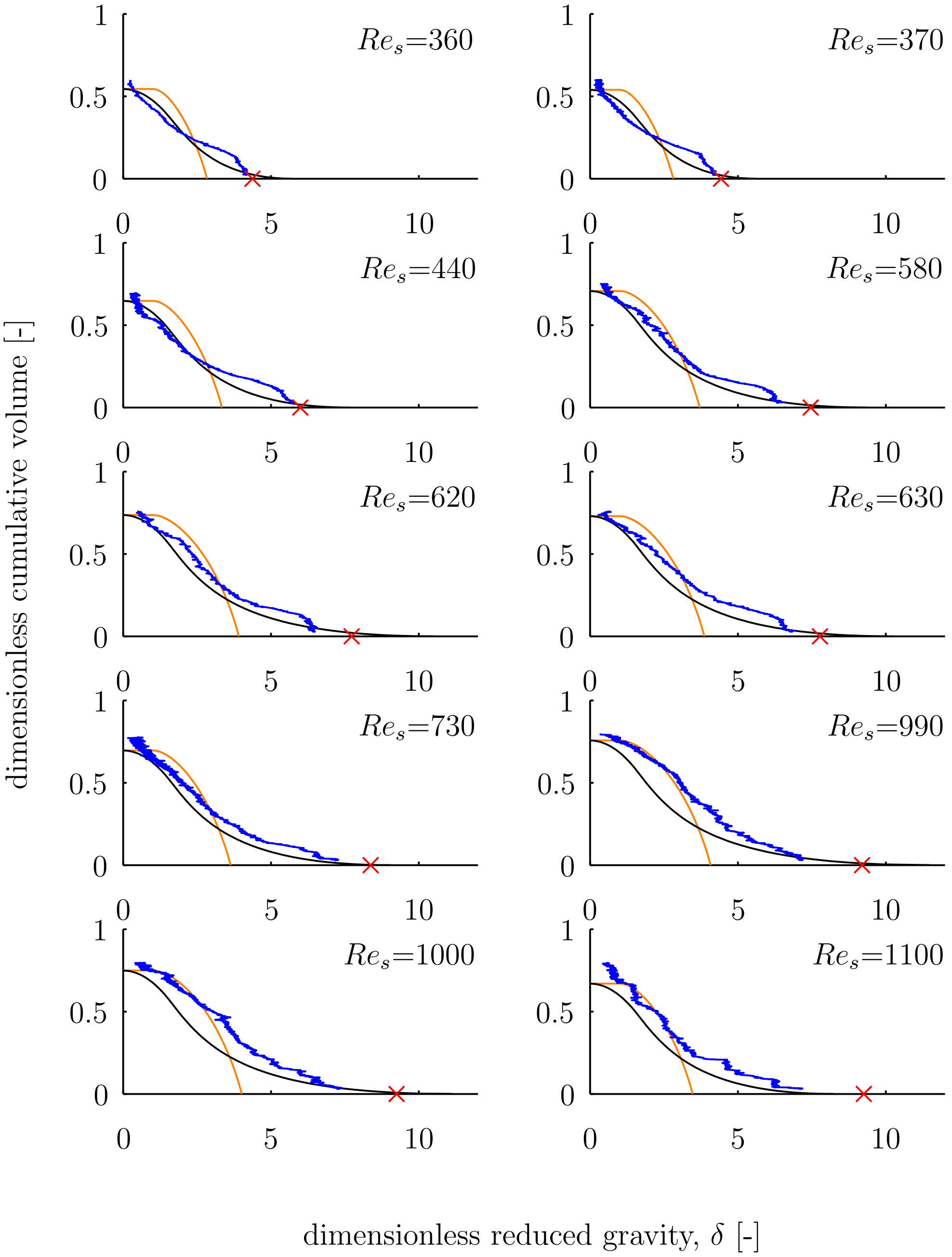

FIGURE 5.23: The profiles plotted against the cumulative volume in the tank. The high density fluid at the bottom of the tank has only a small volume, despite spanning a relatively larger proportion of the depth where the horizontal cross-sectional area is small in figure 5.22. The source density is indicated, in dimensionless units, by the red cross.

are presumably established by the turbulent mixing associated with the crashing of the gravity current against the back wall. As time continues, the uniform layers blur. By the profile taken at $\tau = 0.71$, the stratification is no longer layered, but has become continuous. The stratification remains continuous for the rest of the filling process. Fluid from the gravity current is more likely to peel away at large discontinuities in the ambient stratification, where the neutral buoyancy height for a larger range of fluid densities is situated. The peeling mechanism was therefore expected to lead to a continuous density gradient, as observed.

For the high Re_s runs, the density of the observed data is greater than the density given by the peeling model for almost all of the profiles taken. This underprediction of density by the peeling model is because of the slight excess of mass in the measurements, discussed in section 4.1.6.

At the intermediate Re_s, the profiles are similar in most respects to the $Re_s =$ 990 case. In figure 5.20, $Re_s = 630$, dense fluid is seen to pond at the bottom of the basin in the first profile. Over time, the top of the ponding region rises to the source and the density of fluid within the ponding region increases.

The major difference, compared to the $Re_s = 990$ case, is that a noticeable region of relatively homogeneous fluid accumulates at the bottom of the ponded region. The fluid in this homogeneous layer has a density close to the source fluid. The concentration of source fluid in the layer changes very little over the course of the experiment, changing from 79% of the source density when it is first observed at $\tau = 0.43$ to 88% at $\tau = 1.1$ in the final profile.

That this fluid is near source density implies that it is transported by a relatively undiluted sublayer within the gravity current. This undiluted layer flows in a somewhat laminar condition close to the solid boundary. At lower Re_s, such as this, the turbulence close to the wall is not strong enough to mix the densest fluid from close to the wall into the rest of the gravity current. Such an undiluted sublayer is not represented in the assumed gravity current profiles in the peeling model and therefore does not feature in the resulting density profiles for the ambient. Above this homogeneous layer within the ponded region, the density reduces, matching reasonably well with the density profile predicted by the peeling model. The volume of fluid in this homogeneous part of the ponded region is very small in the $Re_s = 630$ run. The homogeneous region accounts for less than 10% of the basin, as shown when the profile is plotted with respect to the accumulated volume in the basin rather than height in figure 5.23.

A low Re_s run is shown in figure 5.21, with $Re_s = 370$. As before, the gravity current delivers dense fluid into a ponded region at the bottom of the basin, and the ponded region thickens until it reaches the height of the source.

At this low Re_s, however, there are further differences from the runs with higher Re_s sources. The relatively homogeneous layer at the bottom of the ponded region is larger. At the lower Re_s, viscosity will stabilise the current more and allow a larger proportion of the fluid to be transported in the undiluted sublayer. This trend in the thickness of the homogeneous layer is discussed in more detail in section 5.3.1. The substantial homogeneous layer in the ponded region is not well accounted for by either of the model profiles. This is expected, because neither of the models account for an undiluted sublayer within the gravity current.

Above the homogeneous layer, the profile has a relatively constant gradient. This part of the profile is more closely matched by the peeling model than the persistently entraining model. The similarity of the last measured profile with the peeling model is, again, closer if it is plotted on an axis of cumulative volume, as in figure 5.23, where the small volume at the bottom vertex of the basin is not emphasised.

The profiles for the low flow runs are not layered at early times because the crashing against the back wall is less vigorous. The crashing produces a very dilute , continuously stratified layer at the top of the ponded region, over the range $0.3 < \eta < 0.5$ at $\tau = 0.068$. This layer is advected upwards as the top of the ponded region rises up the basin.

5.3.1 Trend in the homogeneous layer thickness

The trend in the thickness of the homogeneous layer was examined specifically. Two algorithmic measures of the thickness of the homogeneous layer were developed, the extreme curvature algorithm and the two line segment least-squares algorithm described in section 4.2.2. Both algorithms gave the same qualitative results. Because the extreme curvature algorithm was most robust it shall be used for this analysis. In brief, the algorithm identified the top of the homogeneous region from the point of extreme curvature in a filtered density profile. The profiles for all runs, including those outside the range of validity of the linear entrainment parameterisation (5.7), are shown in figure 5.24. The profile for each run was taken at the time that the ponded region reached the source unit (i.e., when the experiment ended).

For each profile, the top of the homogeneous region, as identified by the algorithm, is indicated by the green cross. The trend that the homogeneous layer gets thicker as Re_s reduces is clear across all the plots. In the $Re_s = 1500$ profile, the homogeneous layer is either very thin or does not exist. The algorithm, because of this, incorrectly identifies the height in this run and should be ignored. It is also worth noting that at Re_s of 130 and 110, the gravity currents were in the laminar regime, discussed in section 5.1.1. In these profiles, the homogeneous layer fills almost the whole of the ponded region. A relatively sharp transition to the density of fluid initially in the ambient occurs at the top of the ponded region. This is qualitatively different from the flows with higher Re_s.

The trend in the height of the homogeneous layer is shown figure 5.25. The thickness of the lower layer reduces as Re_s increases. Within the range $300 < Re_s < 1000$ the relationship is roughly linear, although the scatter and relatively few data points makes such details of the trend unclear. At $Re_s = 360$, the lowest value for which the linear trend for E in (5.7) is valid, the height of the interface above the bottom of the profiler is 0.08 m. The volume contained within the homogeneous layer when $Re_s = 360$ is 20% of the fluid in the ponded region. This is the run, of all runs for which (5.7) is valid, with the largest homogeneous layer.

5.3.2 Comparison of peeling model and persistently entraining model with observed profiles

Let us now consider how well the two models – persistently entraining and peeling – describe the experimental observations. The length scale of the ponded region for the two models is identical. The height of the ponded region only depends on the behaviour of the gravity current in the uniform region above the ponded layer, which is treated identically in the two models. This length scale compares very well with the models. The good agreement derives from the fact that the linear fit to the $E(Re_s)$ relationship which sets the height of the ponded region, shown in figure 5.10, is good.

A small amount of fluid at low density in the observed data usually rises above the height of the ponded region predicted by the models. For example, this is

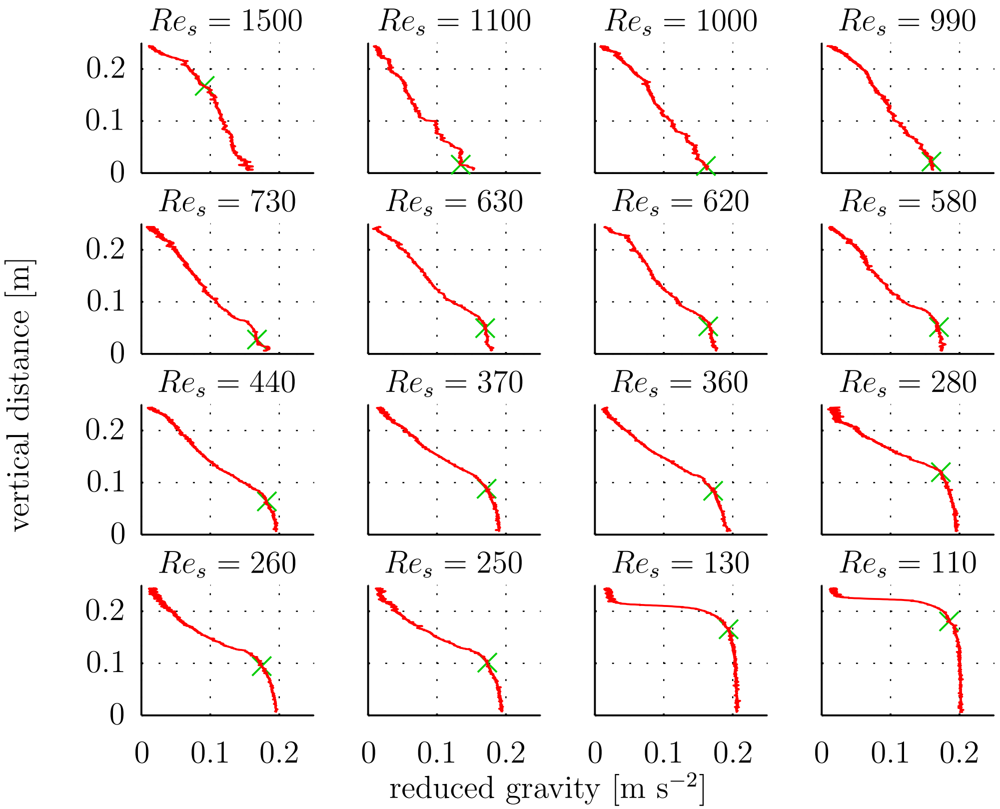

FIGURE 5.24: Density profile in the ponded region for sixteen runs with different source Reynolds numbers, Re_s. As Re_s decreases, the thickness of the homogeneous lower layer increases from having negligible thickness to spanning almost the whole ponded region. The green crosses show the location of the interface between the homogeneous lower layer and the more strongly stratified upper layer, identified by finding the point of maximum curvature.

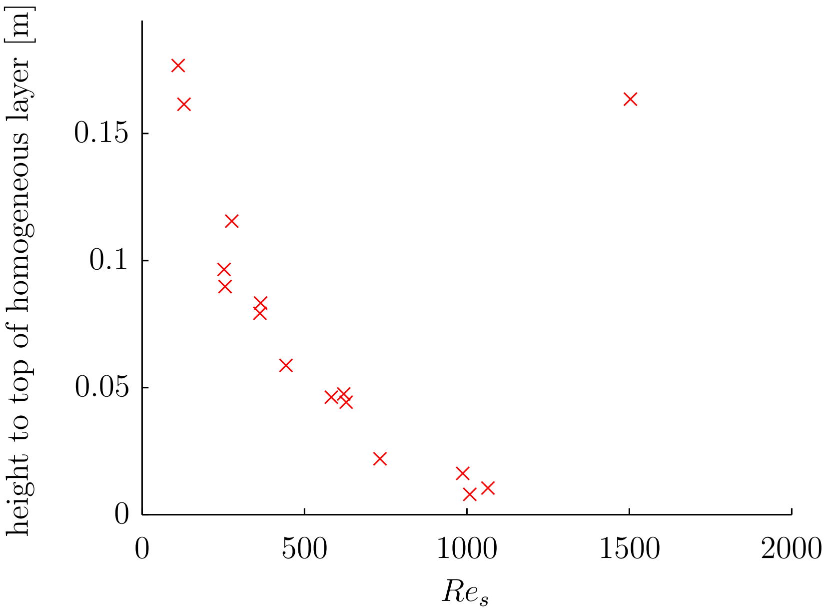

FIGURE 5.25: Trend in the height to the top of the homogeneous layer against source flow rate. The distance is measured from the bottom of the profiler.

clearly seen in the profile at $\tau = 0.39$ in figure 5.19 and at $\tau = 0.068$ in figure 5.21. This slight underprediction of the length scale is because the top of the ponded region used to find the linear relationship for $E(Re_s)$ was defined as the 10% concentration height, as discussed in 4.2.1. The fluid with density less than 10% of the source density is therefore above the top of the predicted ponded region, by this definition.

The density scale predicted by the peeling model is closer to the observed data than is the persistently entraining model in all cases. The persistently entraining model assumes that fluid at a single depth in the gravity current is all diluted to the same density by fluid entrained from the ambient. The experimental data show that much of the fluid remains denser than suggested by the persistently entraining model. The peeling model allows the fluid within the gravity current to have a range of densities, meaning that for the same buoyancy flux within the gravity current, the peak density is higher. Also, in the peeling model, the fluid in the gravity current is only diluted by entrainment where the ambient is uniform. Once fluid in the gravity current reaches the stratified ponded region, no further mixing occurs, making the density predicted by the peeling model greater.

One obviously incorrect feature of the peeling model is that some fluid is predicted to have density exceeding the source density. This happened because the top of the ponding region was sometimes modelled to reach slightly higher than the physical source. The peak density in the modelled gravity current rises quickly towards infinity at the virtual origin. Small errors in the dimensionless time scale used to calculate τ at the time of the last profiles cause the peak density to become greater than the source density. The volume of fluid with this density is very small, which can be seen more clearly when the density is plotted against the cumulative volume as in figure 5.23.

The form of the observed density profile at high Re_s runs is closer to the peeling model than to the persistently entraining model. The observed profile has a relatively uniform density gradient, which is similar to the peeling model. The density gradient predicted by the persistently entraining model over most of the ponded region, particularly at the bottom of the basin, is considerably lower than observed.The discontinuity in density at the top of the ponded region predicted by the persistently entraining model is not present in the observed profiles.

The initial stratification established by the gravity current colliding with the back wall is clearly not captured by the models. The models do not account at all for this mechanism. The volume of fluid in this initial ponded region is small and so is not significant. As the fluid is advected up to the wide part of the basin, this layer gets thinner still. The layers observed in this initial stratification promote efflux of fluid from the gravity current at the discontinuities in the ambient, leading the stratification to become continuous.

Relatively undiluted source fluid forms a layer at the bottom of the basin, which is not at all accounted for by the model assumptions. This layer becomes more significant at lower Re_s. In the lowest Re_s case compared against the models, $Re_s = 360$, this undiluted source fluid accounts for 20% of the volume delivered to the ponded region. The peeling model is a better model of the stratification above this homogeneous layer than the persistently entraining model, especially when plotted against cumulative volume.

It is impressive that the observations match so well with the peeling model, given the simplicity of the profiles of velocity and density and the limited support for assuming their linear form. This suggests that the peeling of fluid away from the stratified gravity current into the ponded region is the leading order mechanism occurring in the flow. A number of ways that the peeling model could be improved will be outlined in section 6.3. It should also be noted that the profiles from when the basin has filled, shown in figure 5.22, could be described reasonably well in a very simple way, with a straight line between a density of 0 at the source height and the source density at the bottom of the basin. Such a model would have broadly similar accuracy to the peeling model. This model would not, however, model the profile evolution at earlier times and nor would it be based on any known physical mechanism.

Considering both the similarity of the measured density profiles to the peeling model and evidence of intermediate depth intrusions from the dye visualisation in section 5.2, there is a strong case that, in all the experiments, the outer layers of the gravity current peeled away from the gravity current to enter the stratified ambient.

5.4 Summary and discussion

In this chapter we have seen that E is not constant over the range of source flows used in the experiments. Instead, E varies between 0.0002 at $Re_s = 110$ to 0.084 at $Re_s = 1500$. These values for E decrease if the threshold density for determining whether fluid was in the ponded region was increased. Visualisations of the gravity current with an opaque dye showed that the turbulent entrainment into the current goes through distinct laminar, transitional and turbulent regimes as Re_s increases. These regimes broadly matched the boundaries of regimes in the measured value of E, and observed by previous researchers (Baines, 2001; Cenedese & Adduce, 2008). In the turbulent regime for $300 < Re_s < 1100$, a linear relationship was a good approximation to the $E(Re_s)$ relationship.

Motions within the ponded region were visualised with pulses of differently coloured dyes. This showed that, at all Re_s tested, the gravity current did not transport all the fluid within it to the bottom of the ponded region as the persistently entraining model predicts. Instead, fluid moved directly to a range of depths in the ponded region. Some of the fluid in the gravity current was transported to the bottom of the basin. Other fluid from the outer layers of the gravity current peeled away across the depth of the ponded region to move into the ambient. The condition given by Baines (2005, 2008) for the effluxing gravity current behaviour to occur is that

$$C_D + 1.2 \times 10^{-4} Ri^{-1} - 0.2(QN^3/g')^{0.4} \sin\theta > 0, \tag{5.11}$$

where C_D is the drag coefficient and N the local buoyancy frequency. In the present experiments, these parameter values were typically $C_D = 0.006$ (as used by Baines (2005) for a smooth tank), $Ri = 0.1$, $Q = 0.001$ m^2 s^{-1}, $N = 1$ s^{-1}, $g' = 0.2$ m s^{-2} and $\theta = 8.6°$. These values meet the condition given by Baines (2005) for effluxing gravity current behaviour. The observed peeling is therefore in agreement with Baines' criteria. Conditions which meet Baines' criteria for entraining plumes rather than effluxing gravity currents have not been examined here, however, meaning that Baines' theory has not been thoroughly tested in these experiments.

The evolving density profile in the basin was measured with a conductivity probe across a series of experimental runs with increasing source flow rate and constant source density. These profiles were predicted better by the peeling model than the persistently entraining model. The observed density profiles showed that some fluid in the gravity current was transported to the bottom of the basin in an undiluted sublayer, which was hardly diluted at all by ambient basin fluid. Because this undiluted sublayer was not represented in the peeling model of the gravity current, runs at low Re_s, in which up to 20% of the gravity current fluid was transported in the unmixed sublayer, were predicted less well by the models than runs at higher Re_s.

For a current which is not bounded to a 2D channel but able to spread laterally on an unbounded slope, the form of the evolution of the current would change to account for the more 3D nature of the flow spreading laterally on the slope. This would change the functional form of the stratification that developed. The basic mechanisms discussed here would, however, still be active. Reducing the Reynolds number to the point where the flow is laminar would still reduce E through viscous damping. The upper layer of the stratified gravity current would still peel into a stratified ambient by the same mechanisms.

Gravity currents flowing along lake beds often have Reynolds numbers which exceed what can be examined in laboratory experiments by orders of magnitude, and the inclines are often lower than can easily be accommodated in the laboratory. The parameterisation of the entrainment coefficient found in this study is therefore limited in its direct applicability to geophysical settings. This is not, however, the objective of this study. The qualitative observation of the peeling mechanism across all the Reynolds numbers found here is significant and is likely to be applicable at high Reynolds numbers typical of geophysical settings. Our results also add further support to other researcher's findings that gravity currents falling through stratified ambients can efflux fluid into the ambient fluid across a range of intermediate depths.

Chapter 6

Conclusion

The investigations in this thesis have reviewed and developed models of various fluid dynamical processes that occur during the inflow of rivers into lakes. These models have been compared against observations, both in the field and in the laboratory, to assess how well the models approximate the actual inflow processes. Validating and developing these models is important, because they underlie both the broad conceptual understandings of inflow behaviour and the detailed parameterisations contained in lake simulation models used for water resource management. Specifically, we have shown that the entrainment occurring in the plunge region of an inflow may be much less than some previous studies suggested; we have found evidence that gravity currents can efflux fluid at intermediate depths in filling box models; and we have developed a simple model for the efflux process which matches the observed behaviour favourably relative to existing models.

6.1 Summary

Chapter 2 described measurements of an inflow made in Lake Iseo, Italy. The River Oglio inflow was tracked through the consecutive stages – plunge region, underflow and intrusion – of becoming an interflow. The river inflow was successfully identified within the lake from naturally existing differences between the chemical characteristics of the river water and lake water. Existing models for the location and dilution of the interflow in each of these stages were compared to the observations. The model for the plunge region based on lateral entrainment gave poor estimates of the maximum offshore extent of the plunge curve and the entrainment of lake water in the plunge region. A new model of plunging by gravitationally driven lateral slumping was found to give better prediction of the offshore extent of the plunge curve and the dilution in the plunge region. Gravitationally driven lateral slumping is likely to be important to the dynamics of many plunge region configurations. It explains the lower values in the wide range of plunge region mixing ratios measured in different studies (Rueda *et al.*, 2007).

The rest of the thesis considered the evolving stratification of a filling basin. The basin initially contains homogeneous light fluid and is fed by dense fluid from a gravity current. In chapter 3, models of the gravity current and evolving stratification in the basin were described. The four models covered a spectrum of different amounts of mixing in the basin fluid and the gravity current. Asymptotic solutions for the stratification generated by an entraining gravity current with top hat density and velocity profiles were derived and compared with a numerical solution. These solutions were adapted from previous work (Worster & Huppert, 1983) to a triangular basin. These expressions can be used in applications where closed form solutions are required, such as where fast, approximate computations of the stratification are required. Extending these asymptotic solutions to power law basins would be an interesting future project to allow this result to be applied to more general basin shapes.

A novel model was developed which, motivated by qualitative observations, permits fluid from a gravity current in a stratified ambient to peel away from the current and move to a level of neutral buoyancy. The peeling model leads to a larger density range within the basin, because the fluid in the gravity current is not mixed as much as in the entraining gravity current with top hat profiles.

In chapter 4, a method was described to measure the evolving density profile in experiments analogous to the scenario described by the theoretical models. The apparatus developed sought to minimise sources of mixing other than turbulent entrainment into the continuous flux gravity current. Methods of processing the profiles were described that locate the change in the density gradient in the profiles using either extremum in curvature or least squares error minimisation.

Chapter 5 described the experimental results and compared them to the theoretical models of gravity current fed basins. The entrainment coefficient, E, which collapsed experimental data to the theoretically predicted form was found to increase with increasing source Reynolds number, Re_s, because viscous damping was reduced. A satisfactory approximation to $E(Re_s)$ was made by a linear function over the range $300 < Re_s < 1100$. Dye visualization showed that fluid peeled away from the outer layer of the gravity current as it flowed through the stratified part of the ambient fluid in the basin. This is a significant observation, because it is contrary to the commonly used entraining model of a gravity current with top hat density and velocity profiles. The experimental observations of the evolving density profile in the basin more closely matched the peeling gravity current than the persistently entraining gravity current model. The continuous density profile predicted by the peeling gravity current model was observed. The simple assumption made in the peeling model of linear profiles of density and velocity in the gravity current were not good approximations for experiments below approximately $Re_s = 700$, where a significant undiluted sublayer was present in the gravity currents.

6.2 Relevance to field data

The laboratory experiments focused on the situation where evolution of the basin stratification is driven only by an underflow. In real lake settings, there are myriad other effects which can modify or dominate over the dynamics observed in the laboratory, including solar heating, wind mixing, non-linear density variation with temperature and internal waves within the basin (Imberger & Patterson, 1989). Focusing on the underflow process in isolation helps to understand field results both when an underflow is the sole dominant driver of the stratification evolution and when an underflow is just one of many contributing processes.

To relate the peeling mechanism observed in the laboratory experiments to the field observations, an obvious question is whether the peeling of fluid from the gravity current was observed in the Lake Iseo inflow. The signals from the inflow tracers, shown in figure 2.12, do not show any indication of intrusion within the uniform density epilimnion. This observation agrees with the laboratory and theoretical evidence that no efflux occurs from a gravity current in a uniform density ambient. The signals of the inflow are shown over a range of depths within the stratified metalimnion. This could be caused by peeling of fluid from the gravity current into the ambient, but it could also be caused by variation over time of the neutral buoyancy depth of the intrusion. Both the oscillations in isotherm depth from the basin scale waves and the variations in the inflow temperature could cause the intrusion signal to smear out over a range of depths, as observed in Lake Iseo. Field observations which distinguish between these mechanisms are required to further investigate efflux into stratified ambient fluids in lakes.

Detailed field observations showing peeling efflux from a gravity current have been made in some previous studies (Baines, 2008), but they have been difficult to interpret. Clearer observations have been made of efflux from gravity currents in ambients with two uniform density layers (Fischer & Smith, 1983; Cortés *et al.*, 2014*a*). The relative accessibility of gravity currents in lakes makes them ideal locations to observe the peeling phenomenon. Future studies should use sites in which: the underflow descends for a long distance through a strongly stratified ambient; variations in the isotherm depths in the lake and the inflow source density are minimal; and where the signal of the river water is clearly distinguishable from the lake water. Measurements of the water column should be made along the length of the underflow over the depths at which efflux into the ambient may occur.

It is important to ask what trends observed in the relatively low Re regimes achieved in the laboratory can be extrapolated to the field scale, where Re can be very large (e.g., $Re > 50\,000$). Intermediate depth efflux from gravity currents in stratified ambients was seen in section 5.2 to occur at all values of Re tested, including the highly turbulent runs at $Re = 900$. At $Re > 20\ 000$, often found in large scale geophysical inflows, stirring in the turbulent flow produces density variations over smaller scale (Dimotakis, 2000). There is no clear reason why this extension to smaller scales at high Re would prohibit the peeling mechanism that allows intermediate depth intrusions. It is reasonable, therefore, to assume that the peeling mechanism occurs in geophysical settings (Baines, 2008). Observations in controlled laboratory experiments at Re higher than achieved here would provide better evidence. Whilst it is difficult to access the high Re regime in laboratory settings, a laboratory experiment could in theory achieve the $Re \sim 20\,000$ regime at which the transition to fully turbulent mixing occurs without suffering errors from the end wall mixing which occurred at the highest flow rates in this study.

An experiment at Re observed in geophysical settings could be conducted with the following physical scales. To achieve $Re_s \sim 20\ 000$ requires a flow of 3 L s^{-1} in a tank 0.15 m wide. If we assume that Ri would be the same as in the present experiments, a gravity current of reduced gravity 0.5 m s^{-2} would flow with a thickness of 0.04 m. The free surface would need to be at least 0.2 m above the source to ensure the gravity current was a small proportion of the total depth of water. At $Re_s \sim 20\ 000$, E would be larger than in the experiments at $Re_s < 1100$ described in chapter 5. With larger E, the gravity current would be thicker. When the current is thicker relative to the depth of the basin, a greater proportion of the volume of fluid in the ponded region will be produced by the initial crashing of the gravity current against the back wall. This means the entrainment into the gravity current will not be the dominant source of mixed fluid in the experiment and measurements of entrainment in such experiments will have large errors. To ensure that the basin is deep enough relative to the thickness of the gravity current, $\tan\theta$ must be large enough relative to E, where θ is the angle of inclination of the tank. We do not currently have a good understanding of what the value of E is at $Re = 20\,000$. It will be larger than when $Re_s = 1100$, but E cannot increase without limit. The peak value is likely to be $E \sim 0.1$, in line with the data in figure 5.14. If $E = 0.1$, the tank would need to be inclined at $\theta > 15^\circ$ for the current to be less thick relative to the depth of the tank than was the case in the $Re_s = 1100$ experiment described in chapter 5. The variation of E as a function of Re for $Re > 1100$ is not well understood currently, and this should be explored at intermediate values of Re_s before carrying out an experiment at $Re = 50\ 000$. Further investigation of the mixing processes that occur when the gravity current hits the back wall would also enable an experiment at such large Re_s to be better designed.

With a source flow of 3 L s^{-1} the tank used in the present experiments would fill rapidly. Based on the time scale (3.14), the tank, inclined at 15° would fill in approximately 20 s. To measure 10 profiles, the probe would need to make a traverse every 2 s to get 10 profiles. This would be prohibitively quickly with the current equipment. A longer tank could be used to increase the filling time so that the probe could make more traverses. Alternatively, a photometric measurement method would give fast measurements of the concentration profile.

In some instances, limnological gravity currents do occur at low to moderate Re (i.e., $Re < 2000$), for example in river inflows in moderate flow conditions and in small turbidity currents in the benthic boundary layer of a lake Fernandez & Imberger (2006). In these cases, the reduction of E with reduced Re observed in section 5.1.2 may make significant differences to the amount of fluid entrained into the underflows. The dependence of E on Re may explain the huge variability in published data for the relationship between E and the Richardson number (Ellison & Turner, 1959; Wells *et al.*, 2010). Further experiments using the methodology of Baines (1983), in which entrainment is measured from the ambient flow required to keep an emptying filling box flow in a steady state, could provide the relationship between Re and E more precisely.

The occurrence of intermediate depth intrusions from underflows within stratified ambients has major practical implications for water resource management. Their occurrence means that underflows containing pathogens cannot be assumed to transport all the contaminated water to deep levels within the lake where there is less risk of human exposure (Antenucci *et al.*, 2005). When water resource managers would like to distribute nutrients and oxygen rich water from inflows into the interior of the lake (Morillo *et al.*, 2009), intermediate depth gravity current efflux may provide a mass flux pathway to deliver these tracers to all depths within a lake. The impacts of this pathway has not yet been included in underflow models (Dallimore *et al.*, 2003), but the simple model described in this work offers a starting point for further development and integration with modelling tools.

6.3 Further development of the peeling model

The peeling model described in section 3.4 gives a good first order description of the stratifications observed in the filling basin experiments. However, a number of improvements could be made to this model.

The mixing generated by the head of the gravity current as it runs down the incline and crashes against the back wall was not included in the model. This mixing is more significant in larger flow rate experiments, where the volume in the initial crashing phase is larger relative to the rest of the filling process, than at lower flow rates. The fluid produced by crashing of the head is potentially relevant to lakes, where gravity currents generated by inflows crash against the boundaries of the lake. There has only been a little work done to examine gravity currents crashing against obstacles and overturning (Baines & Turner, 1969; Rottman *et al.*, 1985; Lane-Serff *et al.*, 1995; Kaye & Hunt, 2007). Lane-Serff *et al.* (1995) mention that further investigation into both inclined gravity currents crashing against obstacles and the density of the fluid produced by the crash would be worthwhile, but there has been no further work on this, to my knowledge. The mixed fluid formed in the gravity current head could be incorporated into numerical models of peeling gravity currents as an initial condition, from which the filling process then continues. The parameterisations for such a model would be better if more experimental data were first gathered on the fluid density generated by the crashing of inclined gravity currents.

The profile of the gravity current used in the model could also be improved. These experiments found that, in the lower Re_s runs, a significant amount of fluid was transported by a relatively undiluted sublayer within the gravity current. The proportion of fluid transported by this sublayer increased as Re_s reduced. The profile of density and velocity within the gravity current could be altered to account for this sublayer. A simple way to consider different profiles would be to alter the linear gravity current profiles, (3.24) and (3.25), to quadratic profiles. The result would be that, in general terms, if more dense fluid were transported by the gravity current, the profile of the ambient in figure 3.16 would change to consist of a larger proportion of dense fluid than in the present results. If more light fluid were transported, the profile would contain a larger proportion of light fluid. This is qualitatively what was seen in the experiments at $Re_s = 370$ where the gravity current contained more dense fluid than assumed in the linear profile.

However, the size of the viscous sublayer transporting the undiluted source fluid will not evolve in the same self similar way assumed by these profiles for fully turbulent gravity currents. To predict the transport in the undiluted sublayer, a suitable scaling for the evolution of the viscous boundary layer would need to be incorporated into the model. Little work has been done so far to understand how such layers within a turbulent gravity current evolve.

Finally, the model could be extended to have a more realistic parameterisation of the efflux of fluid from a gravity current into a stratified ambient. The present assumption that no mixing occurs in the ponded region gives a lower bound on the mixing. Some potential parameterisations include a mixing length approach suggested by Odier *et al.* (2012) or an approach using empirical entrainment and detrainment constants suggested by Baines (2001). Research into efflux into stratified ambients is at an early stage. It is suspected that the wave field within the stratified fluid has an impact on the efflux (Baines, 2001). The wave field in the ponded region may therefore also need to be accounted for in the model. The success of the simple assumption used here that negligible mixing occurs in the ponded region is surprising. This assumption may be a sufficiently accurate approximation, but more understanding of efflux from a gravity current is required to know what the limitations are on the validity of the assumption of negligible mixing.

6.4 Significance of gravity current fed basins to other disciplines

The observations in these laboratory experiments are relevant to flows with similar mechanics in other domains. In oceanography, many gravity currents supply the dense water which fills basins in the ocean bathymetry. Gravity currents formed by cold, salty waters also form an important feature of the global meridional overturning circulation. These dense waters are produced at the ocean surface of the poles and run along the beds of the global ocean to become the North Atlantic Deep Water and the Antarctic Bottom Water. If significant efflux from these gravity currents occurs at intermediate depths along the gravity currents, the mean circulation pattern and ambient stratification will be very different from the classical case (Hughes & Griffiths, 2006) where all fluid in the gravity currents flows to the bottom of the basins. In flows in the oceans, other than close to the equator, the effect of the earth's rotation will influence the motion. The efflux mechanism should occur in gravity current in rotating, stratified ambients, indeed Baines (2008) suggests locations in the ocean where efflux may be observable. It will be interesting to see if data gathered in the forthcoming Overturning in the Subpolar North Atlantic Programme (OSNAP) (Schiermeier, 2013) gives any indication of efflux from gravity currents transporting dense water from the poles.

In building physics, air commonly flows through rooms as gravity currents and filling box models have been used extensively to predict the behaviour of ventilation systems (Linden, 1999; Hogg & Huppert, 2007). The flow in the triangular geometry considered in the laboratory experiments in chapter 5 is typical of that in an auditorium with raked seating on a slope or in a room with a sloped roof. Mid-depth intrusions will prevent a cold gravity current running down raked seating from all descending to the bottom of the room; instead supply air will be transported to a range of depths in the interior of the auditorium. Mid-depth intrusions from gravity currents will cause ventilation systems designed on the basis of gravity currents with top hat profiles to differ from the intended ventilation strategy.

6.5 Further work

The models and observations in this work suggest many fruitful avenues for further work. In regards to the plunge region, the comparison of the model predictions with field observations requires more data than the single field observation made here. A better field site would enable a more thorough comparison. Preferably, the site would have a lake with a river entering perpendicular to the shore, sharply diverging river banks where the river meets the shore and a river channel with little variation in depth. This configuration would be closer to the idealised model and would have the simplest dynamics. Observations of plunging behaviours of rivers at different Froude numbers, ranging from less than unity to considerably greater than unity, would enable the bounds on the validity of the lateral falling model to be established in practice. The influence of bottom topography is likely to play an important role and should be investigated in future studies. Current efforts are developing the lateral slumping model of a plunge region to account for sloping bottom topography. Work on the unsteady behaviour of plunge regions would be particularly interesting. These models could also very usefully be compared to controlled laboratory experiments. Recent work on the mixing and vortex dynamics in shear layers has suggested new dynamics, which would benefit greatly from validation against flows in the laboratory (White & Helfrich, 2013). This further analysis of the plunge region is necessary for the dominant dynamics to be identified and the mixing be more accurately predicted.

The results in section 5.3 imply that the form of the density profile (and presumably also the velocity profile) varied substantially at different Re. The profile in a gravity current also varies depending on the slope angle, form of the bottom roughness, and distance from a prescribed source condition (Ellison & Turner, 1959). Measurements of the structure of a current that span much of this parameter space have not yet been made. Experimental techniques which are beginning to be used by researchers in the field – such as planar laser induced fluorescence, LIDAR or nuclear magnetic resonance imaging – may make these measurements easier. Such measurements would be valuable to understanding the profiles, energy balance and mixing rates in gravity currents encountered in many important geophysical settings. Specific to the present study, this would improve the peeling gravity current model described in 3.4.

Present understanding of the efflux of fluid from a continuous flux gravity current into a stratified ambient is incomplete. It is an area of active research, with new parameterisations recently suggested (Baines, 2005; Odier *et al.*, 2012). Experiments to understand efflux from a gravity current at the interface of a two layer ambient would be the simplest to begin with, as have been carried out by Cortés *et al.* (2014*b*). Within this context it is important to explore the impact of different profiles within the gravity current on the fluxes between the current and ambient. It would also be useful to explore how motions in the ambient, such as selective withdrawal and internal waves in the ambient, affect these fluxes. It is important that numerical simulations of gravity currents in stratified ambients are carried out; they will allow the intermediate depth peeling mechanism to be characterised for more general scenarios.

Various extensions to the peeling model, described in section 6.3, could be pursued. The peeling model should also be integrated with larger scale, operational lake models. One dimensional models, such as the dynamic reservoir simulation model (DYRESM) developed by Imberger & Patterson (1981), would be good candidates for initial implementation. The lake model incorporating the intermediate depth gravity current efflux should then be validated against field observations. A relatively motionless body of water with substantial efflux from an inflowing gravity current would have a large signal to noise ratio for the intermediate depth efflux process. This would make a good site to investigate.

In summary, the path of the River Oglio as it formed the interflow in Lake Iseo was reasonably consistent with the expected mechanisms, except for the plunge region where a new mechanism was shown to compare well with the observed behaviour. In laboratory studies of underflows, the entrainment coefficient was found, over the range $100 < Re_s < 1100$, to be a linear function of Re_s. Gravity currents were found to peel away at intermediate depths in the stratified part of the ambient. A new model including this peeling transport made better approximations to the observations than did the pre-existing model. Further research is needed to better understand the impact of Re_s on the entrainment coefficient and to achieve a more thorough, quantitative understanding of efflux from gravity currents. The peeling efflux from gravity currents is a fundamental fluid dynamical mechanism that is significant in a variety of fields, beyond limnology. Understanding this efflux from gravity currents more clearly and knowing when it should be included in lake models could reduce the considerable uncertainty in predictions of inflow behaviour.

Appendix A

The Product-log Function

The product-log function $\mathcal{W}(x)$, a transcendental function, is the inverse of

$$f(x) = xe^x. \tag{A.1}$$

The function is also known as the Lambert-W function, after Johann Lambert, who initially investigated it (Lambert, 1758; Corless *et al.*, 1996). The name "product-log" highlights how the function corresponds to the logarithm. Rather than, as in the case of the logarithm, being the inverse of e^x, the product-log function is the inverse of xe^x. Unlike the logarithm, the product-log function asymptotically approaches $y(x) = x$ at $x = 0$ and is defined for $-e^{-1} < x < 0$. The principal branch of the function is plotted in figure A.1. The product-log function was numerically evaluated in this thesis using the matlab™ software package.

In the context of this thesis, only the part of the function over the domain $-e^{-1} \leq x \leq 0$ and in the range $\mathcal{W}(x) > -1$, shown in red in figure A.1, is physically relevant.

To derive (3.18), we substitute the expression (3.16) for q into (3.15) and integrate to give

$$\tau = \zeta_f - \ln(\zeta_f) - 1. \tag{A.2}$$

When rearranged to

$$-e^{-1-\tau} = -\zeta_f e^{-\zeta_f}, \tag{A.3}$$

of the functional form (A.1), this can be inverted to

$$\zeta_f = -\mathcal{W}(-e^{-1-\tau}). \tag{A.4}$$

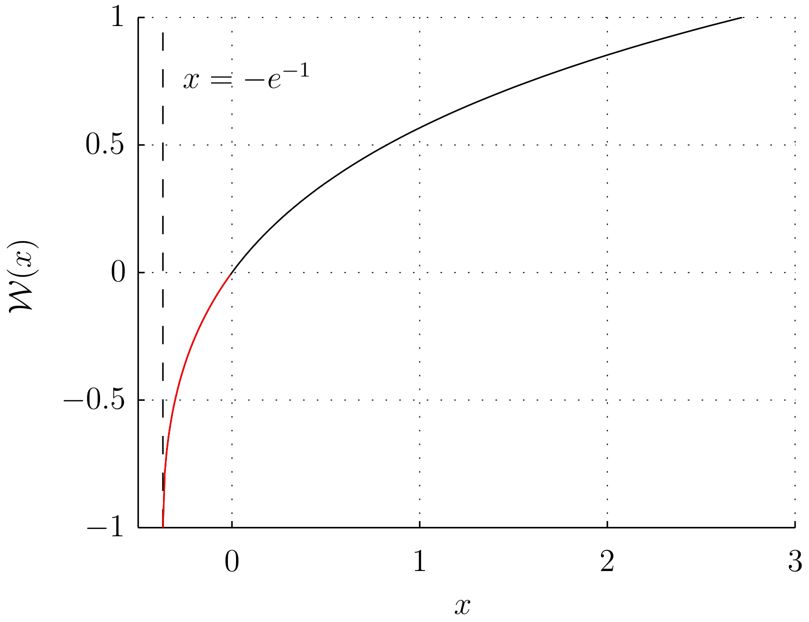

Figure A.1: The principal branch of the product-log function. The red line shows the part of the curve pertinent to this study.

Appendix B

Filling Box Model Code Listing

The listing below calculates the evolution of the density profile in a basin of constant width. The listing is written in matlab and may be processed by either matlab™ or octave software.

```
function []= fillingbox_evolution()
% A function implementing the Germeles (JFM 1975) integration scheme
% for the filling box stratification.

% Initiate time step sizes
total_time=5;
delta_tau=0.01;
total_time_steps=ceil(total_time/delta_tau);
% Set time steps to plot
index_snapshots=ceil([3 total_time/10/delta_tau 2*total_time/ ...
    10/delta_tau total_time/delta_tau])
```

```
% The first layer is calculated asymptotically
initial_plume_elements=1;
total_plume_elements=initial_plume_elements;
d_a=0;
zeta(1)=1;
f(1)=1;
q_2(1)=1;
m_2(1)=1;

% Do first time step to avoid crashing from having only one layer
total_plume_elements=total_plume_elements+1;
top_thickness=sqrt(q_2(end))*delta_tau;
top_d_a=d_a(end)+f(end)/(q_2(end)^(1/2));
zeta(1)=zeta(1)-top_thickness;
zeta(2)=1;
d_a(2)=top_d_a;

for ii=2:total_time_steps
    %% Calculate plume evolution

        % Calculate plume fluxes at the top of the ponded region
        q_2(1)=zeta(1)^2;
    m_2(1)=zeta(1)^2;
    f(1)=1;

        % iterate through the layers of the plume
    for i=2:total_plume_elements
        delta_zeta=zeta(i)-zeta(i-1);
        % calculate terms for the Runge-Kutta scheme
        zeta_halfstep=delta_zeta/2;
        q_2_halfstep=q_2(i-1) + zeta_halfstep*(2*m_2(i-1))^(1/2);
        m_2_halfstep = m_2(i-1) + ...
                        zeta_halfstep *(2*q_2(i-1)^(1/2)*f(i-1));
        f_halfstep = f(i-1) + zeta_halfstep * ...
                (-q_2(i-1)^(1/2)*(d_a(i)-d_a(i-1))/(delta_zeta));
        % calculate the next values in the iteration
        q_2(i) = q_2(i-1) + delta_zeta*(2*m_2_halfstep^(1/2));
        m_2(i) = m_2(i-1) + delta_zeta  ...
                        *(2*q_2_halfstep^(1/2)*f_halfstep);
        f(i)   = f(i-1) + delta_zeta ...
```

```
        *(-q_2_halfstep^(1/2)*(d_a(i)-d_a(i-1))/(delta_zeta));

    end



    %%  Find new stratification
    % Calculate parameters for new layer
        total_plume_elements    =total_plume_elements+1;
        top_thickness           =sqrt(q_2(end))*delta_tau;
        top_d_a                 =d_a(end)+f(end)/q_2(end)^(1/2);

    % Plot snapshot
     if sum(ii==index_snapshots)>0
           f_han=figure;
           plot(sqrt(q_2),zeta(1:total_plume_elements-1));
           set(gca,'YDir','reverse');
           hold on
           plot(sqrt(m_2),zeta(1:total_plume_elements-1),'r');
           plot(f,zeta(1:total_plume_elements-1),'g');
           plot(d_a,zeta(1:total_plume_elements-1),'c');
           legend({'volume flux','momentum','buoyancy flux'...
                      ,'density profile'});
           ylabel('dimensionless height, \zeta')
           title(['t=',num2str(ii*delta_tau)])
           ylim([0 1])
     end


    %% Set new layer depths
    if ii ~= total_time_steps % Not on final iteration
        zeta(1:total_plume_elements-2)= ...
            zeta(1:total_plume_elements-2)- ...
          sqrt(q_2(1:total_plume_elements-2))*delta_tau;
        zeta(total_plume_elements-1)=1-top_thickness;
        zeta(total_plume_elements)=1;
        d_a=[d_a,top_d_a];
    end
end
```

Appendix C

Development of the Controlled Lagrangian Drogue Profiler

In preparation for the field project, I contributed to the development of a new profiling instrument, the controlled lagrangian drogue (CLD). The CLD is a long term development project at the Centre for Water Research. Figure C.1 shows a picture of the instrument. In brief, this instrument is designed to continually measure profiles throughout a lake over deployments of approximately a month in duration. The only control over the location of the profiler is by altering the density of the profiler so that it sinks or rises to different depths within the stratified water column. The profiler is moved passively by the background current in the lake at the depth at which the profiler is located. The profiler periodically falls through the water column to take profile measurements and then communicates these measurement via Global System for Mobile Communication

(GSM) signals to a computer database. The measurements of the state of the lake can be interrogated by water resource managers as a decision support tool.

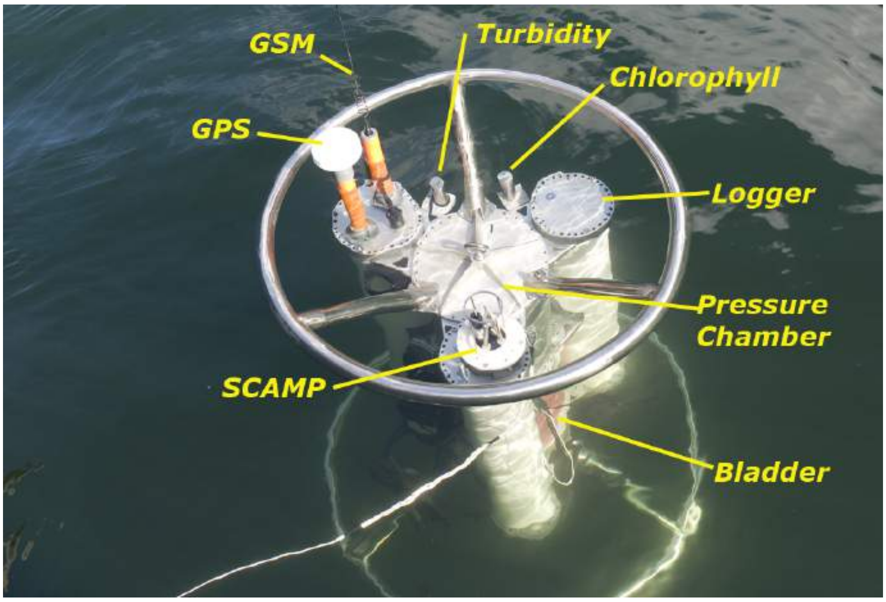

Figure C.1: Photograph of the controlled lagrangian drogue profiling instrument. The labels indicate the location of the communication, profiling and mechanical modules. Source: Jörg Imberger.

In this piece of work, I wrote a control algorithm to select the depth to which the CLD should sink in order to move towards the target destination. The script was written in java within the Aquatic Realtime Management System (ARMS) which manages the database of lake measurements. The relationship between ARMS and the other parts of the CLD system is shown in the system architecture schematic in figure C.2.

The main steps in the control algorithm were:

1. Receive present location data from the CLD via the CLD_Mon communication control software.
2. Run simulations of the lake motion over the next 24 hours using ELCOM (Hodges *et al.*, 2000) to forecast the paths taken by drogues floating at alternative depths in the water column.
3. Select which depth the CLD should dive to and the duration for which the CLD should hold that position in order to move closest to the target location.

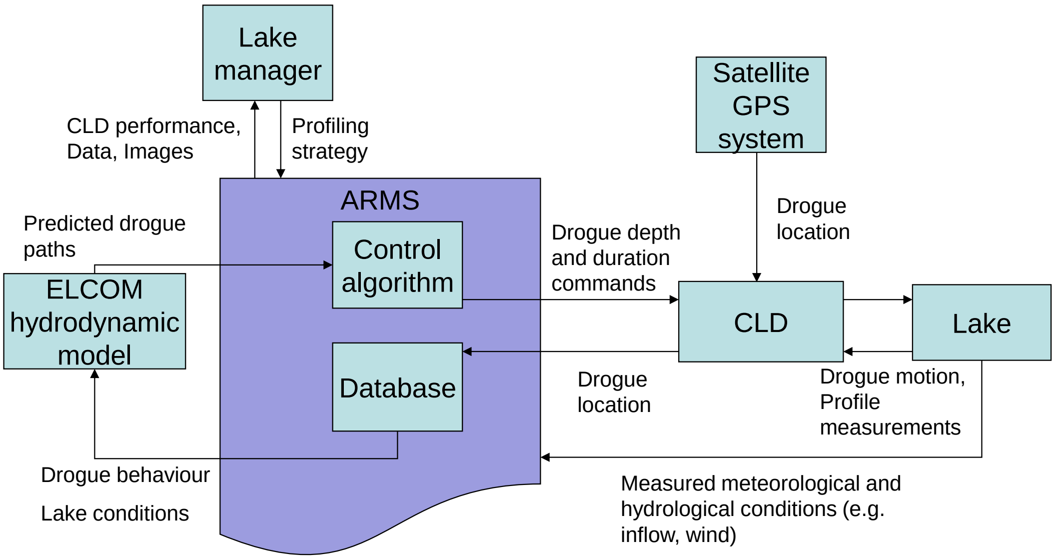

FIGURE C.2: Schematic of the CLD control system. The control algorithm discussed here is contained within the ARMS software.

4. Send dive depth and duration command to the CLD via the CLD_Mon control software.

The control system was implemented. Tests were carried out on the software using real meteorological data to drive the lake simulation to show that the instructions could successfully be sent to the CLD and that the CLD could move towards a target location. These tests, one of which is shown in figure C.3, demonstrated the software was successfully implemented and that the CLD could in principle successfully move towards a target using the control algorithm.

The mechanical system was tested in the Iseo field experiment by other members of the field operations team. It was decided that it was not safe to deploy the instrument under the control system described here until the behaviour of the mechanical systems were better validated. It was therefore not possible to test whether the control system could successfully move the CLD towards a target location in the field. It is important that the modelled motion of the CLD is compared with the actual motion after the dive command has been carried out. A major test will be whether the control algorithm can successfully direct the CLD towards the target despite errors between the simulated motion of the CLD and the actual motion of the CLD.

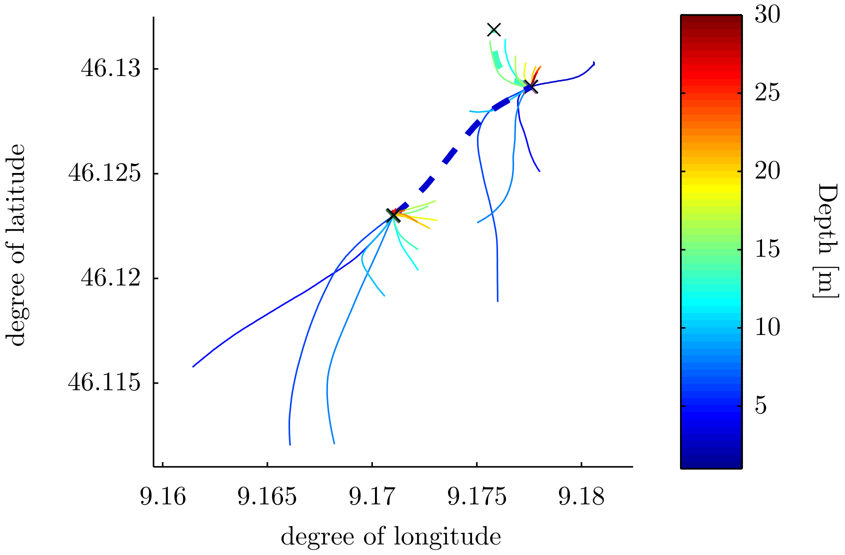

FIGURE C.3: Paths simulated for lagrangian drogues dropped to different depths (solid lines) and the path selected by the control algorithm (dashed lines) when targeting a location to the north. The CLD started at (9.17, 46.123), changed depth at (9.178, 46.129) and ended at (9.176,46.132), the locations indicated by the black crosses.

Acknowledgements

I would like to thank my supervisor Herbert Huppert who gave me the opportunity to do a PhD in the first place. His mentorship and insight have been invaluable. Jörg Imberger, my external supervisor, has taught me a great deal about lakes and field work. I am very grateful for the opportunity he has given me to work on these beautiful environments. My advisor, Stuart Dalziel, has been a wonderful source of ideas, laboratory know-how and support, for which I am also very thankful. I would also like to thank my examiners, Paul Linden and Gregory Lane-Serff. Their comments improved the manuscript substantially and opened fruitful new lines of enquiry.

I am very grateful to the engineering consultancy Arup for supporting this investigation, with both their expertise and finance. They generously allowed me to take sabbatical leave to pursue my studies. Particular thanks go to Gavin Davies, Jake Hacker and Edoardo Piano.

I have had many helpful discussions with many helpful people, including, Colm Caulfield, Paul Linden, Grae Worster, Mark Hallworth, Ben Maurer, Clelia Marti, Jason Antenucci, Chris Dallimore, Andrew Wells, and Marco Pilotti.

Fellow students have also given me much guidance and camaraderie: John Fletcher (whose knowledge of the product-log function was a life saver), Andy Crosby, Alan Jamieson, Jamie Partridge, Dimitry Foures, Julien Landel, Megan

Davies Wykes, Kat Daniels, Til Wagner, Nick Toberg, Anthony Anderson, Hugh Lund, Giulia Valerio, Sarah Laborde, Leticia de Vilhena, Daniel Machardo, Matthew Agarwala, Duncan Hewitt, Daisuke Takagi and Madeleine Golding.

As this PhD is the product of a long educational career, I also owe much thanks to the excellent teachers at Nottingham High School and Darley Abbey Old Vicarage School.

I would like to thank those who have developed the various tools I have used to produce this thesis. The software I have used includes DYRESM, Inkscape, Gimp, TeXnicCenter, Latex, Smallpdf.com, Zotero, Notepad++, Matlab and its various online libraries, SummatraPDF, PDF-XChange, Mathematica, Wolfram Alpha, and Digiflow.

The laboratory staff of the Batchelor Laboratory – David Page-Croft, Colin Hitch and John Milton – have contributed their expertise to this investigation. They have helped tremendously, lifted my spirits and made sure I don't flood the lab with too much mercury. I am also very grateful to the field team at the Centre for Water Research for their help in taking field measurements – Carol Lam, Greg Attwater, Lee Goodyear and Roger Head.

I am also grateful to people who have helped me read through for typos: Mum, Dad, Monica, Naomi and Eleanor Hadley-Kershaw. Any remaining errors, I must have added subsequently.

This being the closest I will ever get to making an acceptance speech at the Oscars, I must also take this opportunity to thank my family and my wife Monica. Without their enduring love and support, I would not have finished this PhD.

BIBLIOGRAPHY

ALAVIAN, V., JIRKA, G. H., DENTON, R. A., JOHNSON, M. C. & STEFAN, H. G. 1992 Density currents entering lakes and reservoirs. *Journal of Hydraulic Engineering* **118** (11), 1686–1691.

AMBROSETTI, W. & BARBANTI, L. 2005 Evolution towards meromixis of lake iseo (northern italy) as revealed by its stability trend. *Journal of Limnology* **64** (1), 1–11.

ANTENUCCI, J. P., BROOKES, J. D. & HIPSEY, M. R. 2005 A simple model for quantifying cryptosporidium transport, dilution and potential risk. *Journal of the American Water Works Association* **97** (1), 86–93.

BAINES, P. G. 2001 Mixing in flows down gentle slopes into stratified environments. *Journal of Fluid Mechanics* **443**, 237—270.

BAINES, P. G. 2005 Mixing regimes for the flow of dense fluid down slopes into stratified environments. *Journal of Fluid Mechanics* **538**, 245.

BAINES, P. G. 2008 Mixing in downslope flows in the ocean - plumes versus gravity currents. *Atmosphere-Ocean* **46** (4), 405–419.

Baines, W. D. 1983 A technique for the direct measurement of volume flux of a plume. *Journal of Fluid Mechanics* **132**, 247–256.

Baines, W. D. & Turner, J. S. 1969 Turbulent buoyant convection from a source in a confined region. *Journal of Fluid Mechanics* **37** (1), 51–80.

Balmforth, N. J. & Mandre, S. 2004 Dynamics of roll waves. *Journal of Fluid Mechanics* **514**, 1–33.

Bateman, I. 2011 Economic values from ecosystems. In *UK national ecosystem assessment: technical report*, pp. 1067—1152. Cambridge: UNEP-WCMC.

Benjamin, T. B. 1968 Gravity currents and related phenomena. *Journal of Fluid Mechanics* **31** (2), 209–248.

Bini, A., Corbari, D., Falletti, P., Fassina, M., Perotti, C. R. & Piccin, A. 2007 Morphology and geological setting of iseo lake (lombardy) through multibeam bathymetry and high-resolution seismic profiles. *Swiss Journal of Geosciences* **100** (1), 23–40.

Botelho, D. & Imberger, J. 2007 Dissolved oxygen response to wind-inflow interactions in a stratified reservoir. *Limnology and Oceanography* **52** (5), 2027–2052.

Boussinesq, J. 1903 *Théorie analytique de la chaleur*. Gathier-Villars.

Britter, R. E. & Linden, P. F. 1980 The motion of the front of a gravity current travelling down an incline. *Journal of Fluid Mechanics* **99** (3), 531–543.

Britter, R. E. & Simpson, J. E. 1978 Experiments on the dynamics of a gravity current head. *Journal of Fluid Mechanics* **88** (02), 223–240.

Budyko, M. I. 1969 The effect of solar radiation variations on the climate of the earth. *Tellus* **21** (5), 611–619.

Cáceres, M., Valle-Levinson, A., Sepúlveda, H. H. & Holderied, K. 2002 Transverse variability of flow and density in a chilean fjord. *Continental Shelf Research* **22** (11–13), 1683–1698.

Caulfield, C.-C. P. 1994 Multiple linear instability of layered stratified shear flow. *Journal of Fluid Mechanics* **258**, 255–285.

Caulfield, C. P. & Woods, A. W. 2002 The mixing in a room by a localized finite-mass-flux source of buoyancy. *Journal of Fluid Mechanics* **471**, 33—50.

Cenedese, C. & Adduce, C. 2008 Mixing in a density-driven current flowing down a slope in a rotating fluid. *Journal of Fluid Mechanics* **604**, 369–388.

Cenedese, C. & Adduce, C. 2010 A new parameterization for entrainment in overflows. *Journal of Physical Oceanography* **40** (8), 1835–1850.

Chen, J. C. 1980 Studies of gravitational spreading currents. Ph.D. thesis, California Institute of Technology.

Christodoulou, G. C. 1986 Interfacial mixing in stratified flows. *Journal of Hydraulic Research* **24** (2), 77–92.

Cooper, P. & Hunt, G. R. 2010 The ventilated filling box containing a vertically distributed source of buoyancy. *Journal of Fluid Mechanics* **646**, 39—58.

Corless, R. M., Gonnet, G. H., Hare, D. E. G., Jeffrey, D. J. & Knuth, D. E. 1996 On the LambertW function. *Advances in Computational Mathematics* **5** (1), 329–359.

Cortés, A., Fleenor, W. E., Wells, M. G., de Vicente, I. & Rueda, F. J. 2014*a* Pathways of river water to the surface layers of stratified reservoirs. *Limnology and Oceanography* **59** (1), 233–250.

Cortés, A., Rueda, F. J. & Wells, M. G. 2014*b* Experimental observations of the splitting of a gravity current at a density step in a stratified water body. *Journal of Geophysical Research: Oceans* **119** (2), 1038–1053.

Dallimore, C. J., Hodges, B. R. & Imberger, J. 2003 Coupling an underflow model to a three-dimensional hydrodynamic model. *Journal of Hydraulic Engineering* **129** (10), 748–757.

Dallimore, C. J., Imberger, J. & Hodges, B. R. 2004 Modeling a plunging underflow. *Journal of Hydraulic Engineering* **130** (11), 1068–1076.

DALLIMORE, C. J., IMBERGER, J. & ISHIKAWA, T. 2001 Entrainment and turbulence in saline underflow in lake ogawara. *Journal of Hydraulic Engineering* **127**, 937–948.

DALZIEL, S. B. 2008 DigiFlow user guide. *Tech. Rep.*. Dalziel Research Partners.

DIMOTAKIS, P. E. 2000 The mixing transition in turbulent flows. *Journal of Fluid Mechanics* **409**, 69–98.

ELDER, R. A. & WUNDERLICH, W. O. 1972 Inflow density currents in TVA reservoirs. In *Proceedings of the International Symposium on Stratified Flows*, pp. 220–236. Novosibirsk: IAHR.

ELLISON, T. H. & TURNER, J. S. 1959 Turbulent entrainment in stratified flows. *Journal of Fluid Mechanics* **6** (03), 423–448.

FERNANDEZ, R. L. & IMBERGER, J. 2006 Bed roughness induced entrainment in a high richardson number underflow. *Journal of Hydraulic Research* **44** (6), 725–738.

FERNANDEZ, R. L. & IMBERGER, J. 2008 Time-varying underflow into a continuous stratification with bottom slope. *Journal of Hydraulic Engineering* **134** (9), 1191–1198.

FISCHER, H. B., LIST, E. J., KOH, R. C. Y., IMBERGER, J. & BROOKS, N. H. 1979 *Mixing in inland and coastal waters*. Academic Press.

FISCHER, H. B. & SMITH, R. D. 1983 Observations of transport to surface waters from a plunging inflow to lake mead. *Limnology and Oceanography* **28** (2), 258–272.

FLEENOR, W. E. 2001 Effects and control of plunging inflows on reservoir hydrodynamics and downstream releases. Ph.D. thesis, University of California, Davis.

FORD, D. E. & JOHNSON, M. C. 1983 An assessment of reservoir density currents and inflow processes. Technical Report E-83-7. Ford, Thornton, Norton, and Associates, Ltd., and the Environmental Laboratory, Waterways Experiment Station, for the U. S. Army Engineer Waterways Experiment Station, Vicksburg, MS.

Fornarelli, R. & Antenucci, J. P. 2011 The impact of transfers on water quality and the disturbance regime in a reservoir. *Water Research* **45** (18), 5873–5885.

Fozdar, F. M., Parker, G. J. & Imberger, J. 1985 Matching temperature and conductivity sensor response characteristics. *Journal of Physical Oceanography* **15** (11), 1557–1569.

Fringer, O., Gerritsen, M. & Street, R. 2006 An unstructured-grid, finite-volume, nonhydrostatic, parallel coastal ocean simulator. *Ocean Modelling* **14** (3–4), 139–173.

Germeles, A. E. 1975 Forced plumes and mixing of liquids in tanks. *Journal of Fluid Mechanics* **71** (3), 601–623.

Håkanson, L. 1977 On lake form, lake volume and lake hypsographic survey. *Geografiska Annaler. Series A, Physical Geography* **59** (1/2), 1–30.

Hayashi, M. & van der Kamp, G. 2000 Simple equations to represent the volume–area–depth relations of shallow wetlands in small topographic depressions. *Journal of Hydrology* **237** (1–2), 74–85.

Hebbert, B., Imberger, J. & Loh, I. 1979 Collie river underflow into the wellington reservoir. *Journal of Hydraulics Division ASCE* **105**, 533–545.

Hodges, B. R., Imberger, J., Saggio, A. & Winters, K. B. 2000 Modeling basin-scale internal waves in a stratified lake. *Limnology and Oceanography* **45** (7), 1603–1620.

Hogg, C. & Huppert, H. 2007 Transient evolution of buoyancy driven exchange flows. In *Proceedings of Roomvent 2007*, p. 277.

Hogg, C. A. R., Marti, C., Huppert, H. & Imberger, J. 2013 Mixing of an interflow into the ambient water of lake iseo. *Limnology and Oceanography* **58** (2), 579—592.

Holford, J. M. & Linden, P. F. 1999 Turbulent mixing in a stratified fluid. *Dynamics of atmospheres and oceans* **30** (2), 173–198.

Hubner, J. 2004 Buoyant plumes in a turbulent environment. Ph.D. thesis, Cambridge University.

Hughes, G. & Griffiths, R. 2006 A simple convective model of the global overturning circulation, including effects of entrainment into sinking regions. *Ocean Modelling* **12** (1–2), 46–79.

Hunt, G. R. & Kaye, N. G. 2001 Virtual origin correction for lazy turbulent plumes. *Journal of Fluid Mechanics* **435**, 377–396.

Huppert, H. E. 2006 Gravity currents: a personal perspective. *Journal of Fluid Mechanics* **554**, 299.

Huppert, H. E. & Simpson, J. E. 1980 The slumping of gravity currents. *Journal of Fluid Mechanics* **99** (4), 785–799.

Imberger, J. 1972 Two-dimensional sink flow of a stratified fluid contained in a duct. *Journal of Fluid Mechanics* **53** (2), 329–349.

Imberger, J. 1985 Thermal characteristics of standing waters: an illustration of dynamic processes. *Hydrobiologia* **125**, 7–29.

Imberger, J. 2004 A lake diagnostic system for managing lakes and reservoirs. *Water Resources Impact* **6** (1), 7–10.

Imberger, J. & Boashash, B. 1986 Application of the Wigner–Ville distribution to temperature gradient microstructure: A new technique to study small-scale variations. *Journal of Physical Oceanography* **16** (12), 1997–2012.

Imberger, J. & Fandry, C. 1975 Withdrawal of a stratified fluid from a vertical two-dimensional duct. *Journal of Fluid Mechanics* **70** (2), 321–332.

Imberger, J. & Head, R. 1994 Measurement of turbulent properties in a natural system. In *Symposium on Fundamentals and Advancement in Hydraulic Measurements and Experimentation* (ed. C. A. Pugh), pp. 1–20. ASCE.

Imberger, J. & Ivey, G. N. 1991 On the nature of turbulence in a stratified fluid. part II: application to lakes. *Journal of Physical Oceanography* **21** (5), 659–680.

Imberger, J. & Patterson, J. 1981 A dynamic reservoir simulation model - DYRESM: 5. In *Transport Models for Inland and Coastal Waters: Symposium Proceedings*, pp. 310—361. Academic Press Inc.

Imberger, J. & Patterson, J. C. 1989 Physical limnology. In *Advances in applied mechanics* (ed. J. W. Hutchinson & T. Y. Wu), , vol. 27, pp. 303—475. Elsevier.

Imberger, J., Thompson, R. & Fandry, C. 1976 Selective withdrawal from a finite rectangular tank. *Journal of Fluid Mechanics* **78** (3), 489–512.

Ivey, G., Winters, K. & Koseff, J. 2008 Density stratification, turbulence, but how much mixing? *Annual Review of Fluid Mechanics* **40** (1), 169–184.

Johnson, T. R., Ellis, C. R. & Stefan, H. G. 1989 Negatively buoyant flow in a diverging channel. IV: entrainment and dilution. *Journal of Hydraulic Engineering* **115** (4), 437–456.

Johnson, T. R., Farrell, G. J., Ellis, C. R. & Stefan, H. G. 1987 Negatively buoyant flow in a diverging channel. i: Flow regimes. *Journal of Hydraulic Engineering* **113** (6), 716–730.

Kaye, N. B. & Hunt, G. R. 2007 Overturning in a filling box. *Journal of Fluid Mechanics* **576**, 297–323.

Killworth, P. D. & Carmack, E. C. 1979 A filling-box model of river-dominated lakes. *Limnology and Oceanography* **24** (2), 201–217.

Koh, R. C. Y. 1966 Viscous stratified flow towards a sink. *Journal of Fluid Mechanics* **24** (3), 555–575.

Lambert, J. H. 1758 Observations variae in mathesin puram. *Acta Helvetica, physico-mathematico-anatomico-botanico-medica* **3**, 128–168.

Lane-Serff, G. F. 1993 On drag-limited gravity currents. *Deep Sea Research Part I: Oceanographic Research Papers* **40** (8), 1699–1702.

Lane-Serff, G. F. & Baines, P. G. 2000 Eddy formation by overflows in stratified water. *Journal of Physical Oceanography* **30** (2), 327–337.

Lane-Serff, G. F., Beal, L. M. & Hadfield, T. D. 1995 Gravity current flow over obstacles. *Journal of Fluid Mechanics* **292**, 39–53.

Legg, S., Ezer, T., Jackson, L., Briegleb, B., Danabasoglu, G., Large, W., Wu, W., Chang, Y., Özgökmen, T. M., Peters, H., Xu, X., Chassignet, E. P., Gordon, A. L., Griffies, S., Hallberg, R., Price, J., Riemenschneider, U. & Yang, J. 2009 Improving oceanic overflow representation in climate models: The gravity current entrainment climate process team. *Bulletin of the American Meteorological Society* **90** (5), 657–670.

Linden, P. 2013 Gravity currents. In *2013 Program in Geophysical Fluid Dynamics: Buoyancy Driven Flows*. Woods Hole Oceanographic Institution.

Linden, P. F. 1973 The interaction of a vortex ring with a sharp density interface: a model for turbulent entrainment. *Journal of Fluid Mechanics* **60** (3), 467–480.

Linden, P. F. 1999 The fluid mechanics of natural ventilation. *Annual Review of Fluid Mechanics* **31** (1), 201–238.

Linden, P. F. & Simpson, J. E. 1986 Gravity-driven flows in a turbulent fluid. *Journal of Fluid Mechanics* **172**, 481–497.

Luketina, D. A. & Imberger, J. 1987 Characteristics of a surface buoyant jet. *Journal of Geophysical Research* **92** (C5), 5435–5447.

Luketina, D. A. & Imberger, J. 2001 Determining turbulent kinetic energy dissipation from batchelor curve fitting. *Journal of Atmospheric and Oceanic Technology* **18** (1), 100–113.

Machado, D. A. & Imberger, J. 2013 Modeling the impact of natural and anthropogenic nutrient sources on phytoplankton dynamics in a shallow coastal domain, western australia. *Environmental Fluid Mechanics* **14** (1), 87–111.

Maltby, E. & Ormerod, S. 2011 Freshwaters - openwaters, wetlands and floodplains. In *UK national ecosystem assessment: technical report*, pp. 295—360. Cambridge: UNEP-WCMC.

Manins, P. C. 1976 Intrusion into a stratified fluid. *Journal of Fluid Mechanics* **74** (03), 547–560.

Marquardt, D. W. 1963 An algorithm for least-squares estimation of nonlinear parameters. *Journal of the Society for Industrial and Applied Mathematics* **11** (2), 431—441.

Marti, C. L., Mills, R. & Imberger, J. 2011 Pathways of multiple inflows into a stratified reservoir: Thomson reservoir, australia. *Advances in Water Resources* **34** (5), 551–561.

Moler, C. 2004 *Numerical Computing With MATLAB*, 1st edn. SIAM.

Monaghan, J. J. 2007 Gravity current interaction with interfaces. *Annual Review of Fluid Mechanics* **39** (1), 245–261.

Morillo, S., Imberger, J., Antenucci, J. P. & Copetti, D. 2009 Using impellers to distribute local nutrient loadings in a stratified lake: Lake como, italy. *Journal of Hydraulic Engineering* **135** (7), 564—574.

Morton, B. R., Taylor, G. I. & Turner, J. S. 1956 Turbulent gravitational convection from maintained and instantaneous sources. *Proceedings of the Royal Society of London. Series A, Mathematical and Physical Sciences* **234** (1196), 1–23.

Mosello, R., Ambrosetti, W., Arisci, S., Bettinetti, R., Buzzi, F., Calderoni, A., Carrara, E., De Bernardi, R., Galassi, S., Garibaldi, L., Leoni, B., Manca, M., Marchetto, A., Morabito, G., Oggioni, A., Pagnotta, R., Ricci, D., Rogora, M., Salmaso, N., Simona, M., Tartari, G., Veronesi, M. & Volta, P. 2010 Evoluzione recente della qualità delle acque dei laghi profondi sudalpini (maggiore, lugano, como, iseo e garda) in risposta alle pressioni antropiche e alle variazioni climatiche. *Biologia Ambientale* **24** (1), 167–177.

Odier, P., Chen, J. & Ecke, R. 2012 Understanding and modeling turbulent fluxes and entrainment in a gravity current. *Physica D: Nonlinear Phenomena* **241** (3), 260–268.

Oglethorpe, R. L. F., Caulfield, C. P. & Woods, A. W. 2013 Spontaneous layering in stratified turbulent Taylor–Couette flow. *Journal of Fluid Mechanics* **721**, R3.

Osborn, T. R. 1980 Estimates of the local rate of vertical diffusion from dissipation measurements. *Journal of Physical Oceanography* **10** (1), 83–89.

Pawlowicz, R. 2008 Calculating the conductivity of natural waters. *Limnology and Oceanography: Methods* **6**, 489–501.

Pilotti, M., Valerio, G. & Leoni, B. 2013 Data set for hydrodynamic lake model calibration: A deep prealpine case. *Water Resources Research* **49** (10), 7159–7163.

Princevac, M., Fernando, H. J. S. & Whiteman, C. D. 2005 Turbulent entrainment into natural gravity-driven flows. *Journal of Fluid Mechanics* **533**, 259–268.

Richardson, L. F. 1922 *Weather Prediction by Numerical Process*, 2nd edn. Cambridge: New York : Cambridge University Press.

Rottman, J. W., Simpson, J. E., Hunt, J. & Britter, R. 1985 Unsteady gravity current flows over obstacles: Some observations and analysis related to the phase II trials. *Journal of Hazardous Materials* **11**, 325–340.

Roughsey, D. 1988 *The rainbow serpent : story and art by Dick Roughsey*. Gareth Stevens Publishing.

Rueda, F. J., Fleenor, W. E. & de Vicente, I. 2007 Pathways of river nutrients towards the euphotic zone in a deep-reservoir of small size: Uncertainty analysis. *Ecological Modelling* **202** (3-4), 345–361.

Rueda, F. J. & MacIntyre, S. 2009 Flow paths and spatial heterogeneity of stream inflows in a small multibasin lake. *Limnology and Oceanography* **54** (6), 2041–2057.

Rueda, F. J. & MacIntyre, S. 2010 Modelling the fate and transport of negatively buoyant storm-river water in small multi-basin lakes. *Environmental Modelling and Software* **25**, 146–157.

Salmaso, N., Mosello, R., Garibaldi, L., Decet, F., Brizzio, M. C. & Cordella, P. 2003 Vertical mixing as a determinant of trophic status in deep lakes: A case study from two lakes south of the alps (lake garda and lake iseo). *Journal of Limnology* **62**, 33–41.

Schiermeier, Q. 2013 Oceans under surveillance. *Nature* **497** (7448), 167–168.

Serruya, S. 1974 The mixing patterns of the jordan river in lake kinneret. *Limnology and Oceanography* **19** (2), 175–181.

Sherman, F. S., Imberger, J. & Corcos, G. M. 1978 Turbulence and mixing in stably stratified waters. *Annual review of fluid mechanics* **10** (1), 267–288.

Shin, J. O., Dalziel, S. B. & Linden, P. F. 2004 Gravity currents produced by lock exchange. *Journal of Fluid Mechanics* **521**, 1–34.

Šimek, K., Comerma, M., García, J.-C., Nedoma, J., Marcé, R. & Armengol, J. 2010 The effect of river water circulation on the distribution and functioning of reservoir microbial communities as determined by a relative distance approach. *Ecosystems* **14** (1), 1–14.

Simpson, J. E. 1987 *Gravity currents in the environment and the laboratory*, 1st edn. Ellis Horwood and Sons.

Smetana, B. 1874 *Vltava*. Eulenburg.

Smith, H. G., Sheridan, G. J., Lane, P. N., Nyman, P. & Haydon, S. 2011 Wildfire effects on water quality in forest catchments: A review with implications for water supply. *Journal of Hydrology* **396** (1–2), 170–192.

Spigel, R. H., Howard-Williams, C., Gibbs, M., Stephens, S. & Waugh, B. 2005 Field calibration of a formula for entrance mixing of river inflows to lakes: Lake Taupo, North Island, New Zealand. *New Zealand Journal of Marine and Freshwater Research* **39** (4), 785–802.

Stefan, H. G. & Johnson, T. R. 1989 Negatively buoyant flow in a diverging channel. III: onset of underflow. *Journal of Hydraulic Engineering* **115** (4), 423–436.

Tavoularis, S. 2005 *Measurement in Fluid Mechanics*. Cambridge University Press.

Thoreau, H. D. 1854 *Walden; Or, Life in the Woods: Bold-faced Ideas for Living a Truly Transcendent Life*. Sterling Publishing Company, Inc.

Turner, J. S. 1968 The influence of molecular diffusivity on turbulent entrainment across a density interface. *Journal of Fluid Mechanics* **33** (4), 639–656.

Turner, J. S. 1973 *Buoyancy Effects in Fluids*. Cambridge University Press.

Turner, J. S. 1986 Turbulent entrainment: The development of the entrainment assumption, and its application to geophysical flows. *Journal of Fluid Mechanics* **173**, 431–471.

Valerio, G., Pilotti, M., Marti, C. L. & Imberger, J. 2012 Influence of bathymetry and wind field on basin-scale internal wave structure in a stratified lake: Lake iseo, italy. *Limnology and oceanography* **57** (3), 772–786.

Vilhena, L. C., Hillmer, I. & Imberger, J. 2010 The role of climate change in the occurrence of algal blooms: Lake burragorang, australia. *Limnology and Oceanography* **55** (3), 1188–1200.

da Vinci, L. 1508 Studies of water passing obstacles and falling.

Wåhlin, A., Darelius, E., Cenedese, C. & Lane-Serff, G. 2008 Laboratory observations of enhanced entrainment in dense overflows in the presence of submarine canyons and ridges. *Deep Sea Research Part I: Oceanographic Research Papers* **55** (6), 737–750.

Wells, M., Cenedese, C. & Caulfield, C. P. 2010 The relationship between flux coefficient and entrainment ratio in density currents. *Journal of Physical Oceanography* **40** (12), 2713–2727.

Wells, M. G. & Wettlaufer, J. S. 2007 The long-term circulation driven by density currents in a two-layer stratified basin. *Journal of Fluid Mechanics* **572**, 37—58.

White, B. L. & Helfrich, K. R. 2013 Rapid gravitational adjustment of horizontal shear flows. *Journal of Fluid Mechanics* **721**, 86–117.

Wong, A. 1998 Stratification and circulation caused by turbulent plumes. Ph.D. thesis, Australian National University.

Wong, A. B. D., Griffiths, R. W. & Hughes, G. O. 2001 Shear layers driven by turbulent plumes. *Journal of Fluid Mechanics* **434** (1), 209–241.

Woods, A. W. 2010 Turbulent plumes in nature. *Annual Review of Fluid Mechanics* **42**, 391–412.

Worster, M. G. & Huppert, H. E. 1983 Time-dependent density profiles in a filling box. *Journal of Fluid Mechanics* **132**, 457–466.

Yeates, P. S., Gómez-Giraldo, A. & Imberger, J. 2013 Observed relationships between microstructure patches and the gradient richardson number in a thermally stratified lake. *Environmental Fluid Mechanics* **13** (3), 205–226.